

ÉCOLE DE TECHNOLOGIE SUPÉRIEURE  
UNIVERSITÉ DU QUÉBEC

THESIS PRESENTED TO  
ÉCOLE DE TECHNOLOGIE SUPÉRIEURE

IN PARTIAL FULLFILMENT OF THE REQUIREMENTS FOR  
THE DEGREE OF DOCTOR OF PHILOSOPHY  
Ph.D.

BY  
Andrei Vladimir POPOV

DESIGN OF AN ACTIVE CONTROLLER FOR DELAYING THE TRANSITION FROM  
LAMINAR FLOW TO TURBULENT FLOW OVER A MORPHING WING IN WIND  
TUNNEL

MONTREAL, FEBRUARY 19 2010

© Copyright 2010 reserved by Andrei Vladimir Popov

**BOARD OF EXAMINERS (THESIS PH.D.)**

THIS THESIS HAS BEEN EVALUATED  
BY THE FOLLOWING BOARD OF EXAMINERS

Ms. Ruxandra Botez, Thesis Supervisor  
Département de génie de la production automatisée à l'École de technologie supérieure

Mr. Patrick Terriault, President of the Board of Examiners  
Département de génie mécanique à l'École de technologie supérieure

Mr. Stephane Halle, Member of the Board of Examiners  
Department of mechanical engineering at École de technologie supérieure

Mr. Youmin Zhang, External Member of the Board of Examiners  
Department of mechanical and industrial engineering at Concordia University

THIS THESIS WAS PRESENTED AND DEFENDED  
BEFORE A BOARD OF EXAMINERS AND PUBLIC  
FEBRUARY 2, 2010  
AT ÉCOLE DE TECHNOLOGIE SUPÉRIEURE

## ACKNOWLEDGMENTS

I would like to thank to my thesis supervisor, Dr. Ruxandra Botez, for the opportunity to work on this project and for her constant encouragement and support in finalizing this challenging work in the CRIAQ 7.1 project.

Thanks are also due to Dr. Teodor Lucian Grigorie for his collaboration in this work as well as to other students from LARCASE working together on this project: Mathieu Roux, Pierre Attal, Michel Labib, Julien Fays and Samuel Courchesne.

Many thanks are due to Dr. Patrick Terriault and Dr. Vladimir Brailovski as well as to their students from LAMSI, Daniel Coutu, Thomas George and Emeric Morellon, for their numerical and experimental collaboration in this project. I would also like to thank Dr. Mahmoud Mamou and Dr. Youssef Mebarki from the NRC-IAR (The National Research Council of Canada Institute for Aerospace Research) for their collaboration in infrared testing, and to Dr. Octavian Trifu from Ecole Polytechnique for his advice in aerodynamics.

We would like to thank to George Henri Simon for initiating the CRIAQ 7.1 project, as well as Philippe Molaret from Thales Avionics and Eric Laurendeau from Bombardier Aeronautics, for their collaboration in this work.

Thanks to Bombardier Aerospace, Thales Avionics, the NRC-IAR (National Research Council Institute for Aeronautical Research), the CRIAQ (Consortium for Research and Innovation in Aerospace in Quebec) and the NSERC (National Sciences and Engineering Research Council) for the funding of the global CRIAQ 7.1 project.

# **CONCEPTION D'UN CONTRÔLEUR ACTIF POUR LE RETARD DE LA TRANSITION DE L'ÉCOULEMENT LAMINAIRE AU TURBULENT SUR UNE AILE À GEOMÉTRIE DU PROFIL VARIABLE DANS LE TUNNEL À VENT**

Andrei Vladimir POPOV

## **RÉSUMÉ**

L'industrie aérospatiale est motivée par la réduction de la consommation de combustible pour les avions de transport à longue croisière, principalement par la réduction de la traînée. L'objectif principal de ce projet est de concevoir un système de contrôle actif pour la géométrie du profil d'aile d'une aile d'avion pour permettre la réduction de la traînée. La réduction de la traînée peut être obtenue par la modification du point de transition entre l'écoulement laminaire et écoulement turbulent, qui doit être positionnée le plus proche possible du bord de fuite du profil de l'aile. La position du point de transition à un rôle très important dans ce projet, et en conséquence ce travail se concentre sur le contrôle de la position du point de transition sur le profil de l'aile, comme effet du contrôle de la déflexion de la peau flexible installée sur l'extrados de l'aile.

Ce travail présente la modélisation, la réalisation, l'instrumentation et les essais expérimentaux d'une aile avec géométrie variable du profil du début de la conception jusqu'aux essais sur le banc et dans la soufflerie. Plusieurs essais en soufflerie pour plusieurs valeurs de nombre Mach et angles d'incidence ont été réalisés dans le tunnel de 2 m × 3 m appartenant à l'Institut de Recherche Aérospatiale - Conseil National de Recherche du Canada. Une aile rectangulaire avec une envergure finie et un profil d'aile variable due à une peau flexible installée sur l'extrados du profil a été instrumenté avec des capteurs Kulite. Le nombre de Mach a été varié de 0.2 jusqu'au 0.3 et avec l'angle d'incidence de  $-1^{\circ}$  jusqu'au  $2^{\circ}$ .

Les signaux de pression ont été mesurés, analysés et comparés par la valeur moyenne du coefficient de pression et la déviation standard avec les valeurs obtenues par le code CFD XFOil. Les valeurs mesurées ont été analysées par un logiciel maison conçu à l'aide de Matlab/Simulink pour détecter la magnitude du bruit dans la couche limite de l'écoulement et localiser la position du point de transition sur l'extrados de l'aile. Cette analyse a été nécessaire pour détecter les ondes Tollmien-Schlichting, apparaissant suite à la transition entre l'écoulement laminaire et turbulent.

La peau flexible changeait sa forme grâce à deux actionneurs pour réaliser la forme du profil optimisé correspondante à chaque condition du l'écoulement de l'air dans soufflerie. Les deux actionneurs en alliages à mémoire de forme, ayant un comportement non-linéaire, ont été contrôlés par un contrôleur avec plusieurs méthodes de contrôle. Cette méthodologie présentée dans ce travail et les résultats obtenus montrent la validité du concept en temps réel dans les conditions expérimentales.

**Mots-clés** : aile, variable, laminaire, turbulent, transition, control, tunnel à vent

# DESIGN OF AN ACTIVE CONTROLLER FOR DELAYING THE TRANSITION FROM LAMINAR FLOW TO TURBULENT FLOW OVER A MORPHING WING IN WIND TUNNEL

Andrei Vladimir POPOV

## ABSTRACT

The aerospace industry is motivated to reduce fuel consumption in large transport aircraft, mainly through drag reduction. The main objective of the global project is the development of an active control system of wing airfoil geometry during flight in order to allow drag reduction. Drag reduction on a wing can be achieved through modifications in the laminar-to-turbulent flow transition point position, which should be situated as close as possible to the trailing edge of the airfoil wing. As the transition point plays a crucial part in this project, this work focuses on the control of its position on the airfoil, as an effect of controlling the deflection of a morphing wing airfoil equipped with a flexible skin.

The paper presents the modeling and the experimental testing of the aerodynamic performance of a morphing wing, starting from the design concept phase all the way to the bench and wind tunnel tests phases. Several wind tunnel test runs for various Mach numbers and angles of attack were performed in the  $6 \times 9 \text{ ft}^2$  wind tunnel at the Institute for Aerospace Research at the National Research Council Canada. A rectangular finite aspect ratio wing, having a morphing airfoil cross-section due to a flexible skin installed on the upper surface of the wing, was instrumented with Kulite transducers. The Mach number varied from 0.2 to 0.3 and the angle of attack between  $-1^\circ$  and  $2^\circ$ . Unsteady pressure signals were recorded and analyzed and a thorough comparison, in terms of mean pressure coefficients and their standard deviations, was performed against theoretical predictions, using the XFOIL computational fluid dynamics code.

The acquired pressure data was analyzed through custom-made software created with Matlab/Simulink in order to detect the noise magnitude in the surface airflow and to localize the transition point position on the wing upper surface. This signal processing was necessary in order to detect the Tollmien-Schlichting waves responsible for triggering the transition from laminar to turbulent flow.

The flexible skin needed to morph its shape through two actuation points in order to obtain an optimized airfoil shape for several flow conditions in the wind tunnel. The two shape memory alloy actuators, having a non-linear behavior, drove the displacement of the two control points of the flexible skin towards the optimized airfoil shape. This thesis presents the methodology used and the results obtained from designing the controller of the two shape memory actuators as well as the methods used for morphing wing control in the wind tunnel tests designed to prove the concept and validity of the system in real time.

**Keywords:** wing, morphing, laminar, turbulent, transition, control, wind tunnel

## TABLE OF CONTENTS

	Page
INTRODUCTION .....	1
CHAPTER 1 STATE OF THE ART .....	6
1.1 Aerodynamic methods for laminar flow improvement.....	6
1.2 Morphing wings equipped only with actuators.....	8
1.3 Materials and actuators: use in the morphing wing design.....	10
1.4 Integrated morphing wing studies.....	12
1.5 Integrated morphing aircraft studies .....	13
CHAPTER 2 OBJECTIVES AND ORIGINALITY .....	23
2.1 The morphing wing model concept and its function.....	23
CHAPTER 3 THEORY DEVELOPPED.....	29
3.1 Modeling the wind tunnel parameters and pressure and forces acting on the morphing wing airfoil estimation.....	29
3.1.1 Validation of the XFOil CFD code by use of experimental data from wind tunnel tests on the original airfoil WTEA .....	22
3.1.2 Aerodynamic analysis of the modified airfoils by use of XFOil.....	33
3.1.3 Computation of the aerodynamic characteristics in wind tunnel and estimation of the forces acting on the flexible skin during tests.....	37
3.2 Modeling the dynamic pressure signal and transition position measured by use of optical sensors .....	41
3.2.1 Modeling the turbulent flow by Gaussian distribution .....	41
3.2.2 Equivalences between noise level and velocity RMS in the wind tunnel.....	43
3.2.3 Modeling and simulation of the optical sensors measurements.....	48
3.3 Shape memory alloys (SMA) actuators modeling and control function design .....	53
3.4 Controller simulation in closed loop using airflow pressure distribution.....	61
CHAPTER 4 ARTICLE 1: TRANSITION POINT DETECTION FROM THE SURFACE PRESSURE DISTRIBUTION FOR CONTROLLER DESIGN .....	71
4.1 Introduction.....	73
4.2 Experimental setup.....	75
4.3 Theoretical considerations .....	76
4.4 Results obtained for a NACA 4415 airfoil.....	82
4.5 Results obtained for the WTEA-TE1 airfoil .....	85
4.6 Conclusions.....	90

CHAPTER 5	ARTICLE 2: CLOSED-LOOP CONTROL SIMULATIONS ON A MORPHING WING .....	93
5.1	Introduction.....	96
5.2	Closed-loop controller design.....	102
5.3	Results and discussion .....	114
5.4	Conclusions.....	120
CHAPTER 6	ARTICLE 3: VARIATIONS IN OPTICAL SENSOR PRESSURE MEASUREMENTS DUE TO TEMPERATURE IN WIND-TUNNEL TESTING.....	124
6.1	Introduction.....	126
6.2	Experimental setup description.....	127
6.3	Wind-tunnel data post-processing details .....	129
6.4	Results analysis .....	134
6.5	Transition detection.....	136
6.6	Conclusions.....	140
CHAPTER 7	ARTICLE 4: DRAG REDUCTION BY IMPROVING LAMINAR FLOW PAST MORPHING CONFIGURATIONS .....	142
7.1	Introduction.....	145
7.2	Experimental setup description.....	146
7.3	Wind tunnel data post-processing details.....	148
7.4	Results and discussion .....	152
7.5	Transition detection validation.....	153
CHAPTER 8	ARTICLE 5: CONTROL OF A MORPHING WING IN BENCH TESTS .....	158
8.1	Introduction.....	160
8.2	Experimental setup description.....	161
8.3	Data analysis .....	164
8.4	Conclusion .....	166
CHAPTER 9	ARTICLE 6: MODELING AND TESTING OF A MORPHING WING IN OPEN LOOP ARCHITECTURE .....	168
9.1	Morphing wing structure, objectives and testing conditions .....	171
9.2	Experimental set-up .....	175
9.3	Results and conclusions .....	180
CHAPTER 10	ARTICLE 7: CLOSED LOOP CONTROL VALIDATION OF A MORPHING WING USING WIND TUNNEL TESTS .....	193
10.1	Introduction.....	195
10.2	Experimental setup description.....	198
10.3	Experimental results obtained in the wind tunnel.....	209

10.4	Conclusion .....	216
CHAPTER 11 ARTICLE 8: REAL TIME MORPHING WING OPTIMIZATION IN A SUBSONIC WIND TUNNEL .....		
11.1	Introduction.....	221
11.2	Experimental setup description.....	224
11.3	Simulation and experimental results obtained in the wind tunnel .....	230
11.4	Conclusion .....	237
CONCLUSION.....		
		240

## LIST OF TABLES

		Page
Table 3.1	Pressure values estimation of optical sensors .....	49
Table 3.2	Minimum SPL detectable by optical sensors .....	50
Table 3.3	Frequencies of the transitional pressure signal .....	53
Table 3.4	Aerodynamic cases.....	62
Table 4.1	The relative errors, as a fraction of the airfoil chord, for the transition point prediction calculated by the PCHIP versus the Xfoil method.....	88
Table 4.2	The relative errors, as a fraction of the airfoil chord, for the transition point prediction with the Spline versus the Xfoil method.....	89
Table 6.1	Airflow cases dependent of angles of attack $\alpha$ , Mach numbers $M$ , Reynolds numbers $Re$ and static temperatures wind on $T_{static}$ .....	132
Table 6.2	Optical sensor readings with respect to temperature and pressure variations given by the manufacturer.....	134
Table 6.3	Relative errors between OS and PT measured results for 21 airflow cases...	137
Table 6.4	Mean error between OS measured and Xfoil calculated results for 21 airflow cases.....	139
Table 8.1	Test flow conditions for 35 wing airfoils .....	161
Table 9.1	Test flow conditions for 35 wing airfoils .....	174
Table 10.1	Test flow conditions for 35 wing airfoils .....	199

## LIST OF FIGURES

		Page
Figure 2.1	Mechanical schematic of the morphing wing model .....	23
Figure 2.2	Open loop control schematic of the system .....	24
Figure 2.3	Close loop control schematic of the system .....	24
Figure 3.1	The normalized coordinates of the original laminar airfoil WTEA .....	30
Figure 3.2	Validation of the numerical values (continuous line) obtained by XFOIL using experimental values (dots) obtained during wind tunnel tests for the original airfoil WTEA for the flow case Mach number = 0.2 and Reynolds number = 6 million .....	31
Figure 3.3	Validation of the numerical values (continuous line) obtained by XFOIL using experimental values (dots) obtained during wind tunnel tests for the original airfoil WTEA for the flow case Mach number = 0.25 and Reynolds number = 2 million .....	32
Figure 3.4	Modified airfoils obtained by combining the original airfoil WTEA with B-Spline curves with a single control point A in the middle of the interval 7% and 65% of the chord .....	33
Figure 3.5	Pressure distributions around the modified airfoils for one airflow case characterized by Mach number $M = 0.3$ , angle of attack $\alpha = -1^\circ$ and Reynolds number $Re = 3.36$ million .....	34
Figure 3.6	Transition point position variation for different vertical displacements of control point A and different angles of attack for the airflow case of $M = 0.3$ and $Re = 3.36$ million .....	35
Figure 3.7	Lift coefficient variation for different vertical displacements of control point A and angles of attack for the airflow case of $M = 0.3$ and $Re = 3.36$ million .....	35
Figure 3.8	Drag coefficient variation for different vertical displacements of control point A and angles of attack for the airflow case of $M = 0.3$ and $Re = 3.36$ million .....	36

Figure 3.9 Slenderness factor variation for different vertical displacements of control point A and angles of attack for the airflow case of  $M = 0.3$  and  $Re = 3.36$  million.....36

Figure 3.10 Pressure distributions for the modified airfoil with a control point A vertical displacement of +5 mm .....39

Figure 3.11 Local dynamic pressure over the flexible skin estimation by calculating the area integral under the  $Q$  values plot.....39

Figure 3.12 Turbulent signal of wind flow recorded in 1 sec sampled at 5 kHz (up), and the same signal at 3 seconds later (down) [7] .....43

Figure 3.13 Image of the transition from laminar to turbulent flow evidenced by fluorescent oil in UV light on the upper surface of a wing model with NACA 4415 airfoil in IAR-NRC wind tunnel .....46

Figure 3.14 Validation of the wind tunnel tests transition detection using XFOIL code, which predicts the  $x_{tr}$  position and the estimated frequencies of the turbulent flow .....47

Figure 3.15 The dynamic pressure distribution on the airfoil upper surface.....48

Figure 3.16 Measurements using microphones in wind tunnel of the transition occurrence over an airfoil [11].....52

Figure 3.17 Wing model design realised in CATIA by LAMSI team [12].....54

Figure 3.18 Optical and Kulite sensors distribution on the flexible skin, view from below realised in CATIA .....54

Figure 3.19 Mechanical principle of the SMA actuators.....55

Figure 3.20 The SMA S-function numerical model used in Simulink.....56

Figure 3.21 Schematic of the PID controller, SMA actuator and mechanical system .....57

Figure 3.22 Schematic of the PID controller, where  $P=1800$ ,  $I=400$ ,  $D=0$  .....58

Figure 3.23 Test of the numerical model for a step of 0, 2, 4, 6, 8 mm in the absence of aerodynamic forces .....59

Figure 3.24 Controller bench test performed in closed loop using the potentiometer signal as feedback for actuator position .....60

Figure 3.25	Control schematic of the wing model in wind tunnel conditions (the plant) using the optical sensors pressure signal as feedback signal. ....	61
Figure 3.26	Model of the flexible skin using B-Splines compared to the finite element results obtained in Nastran-Patran, the reference airfoil and optimised airfoil for the case C149 .....	64
Figure 3.27	Results simulation for the airflow condition case C131 with the two actuators at the zero positions (0 mm). .....	65
Figure 3.28	Results simulation for the airflow condition case C131 with the two actuators at the same positions as the two optimised airfoil control points .....	67
Figure 3.29	Results simulation for the airflow condition case C131 with two actuators controlled by a PID controller, so that the mean pressure coefficient is maintained at the same value as the optimised pressure coefficient corresponding to the 6 <sup>th</sup> and the 13 <sup>th</sup> optical sensors selected in the menu on the right of the figure.....	68
Figure 4.1	Closed-loop flow control (with optical sensors and feedback) of the morphing wing design in a wind tunnel .....	75
Figure 4.2	Pressure distribution and Xfoil predicted transition point on the NACA 4415 airfoil at $M = 0.191$ , $Re = 2 \times 10^6$ , and $\alpha = 0$ deg.....	77
Figure 4.3	Schematic of the velocity distributions in the laminar separation bubble.....	78
Figure 4.4	$C_p$ distributions on a NACA 4415 airfoil at $M = 0.3$ and $Re = 3 \times 10^6$ , obtained using the Xfoil code.....	80
Figure 4.5	$C_p$ distributions that correspond to a WTEA-TE1 reference airfoil and to its modified shapes using a single control point, which creates a bump or depression on the airfoil.....	82
Figure 4.6	$C_p$ distributions in the vicinity of the transition point interpolated using the Spline and PCHIP methods .....	84
Figure 4.7	Second derivative of the $C_p$ distribution interpolated using the Spline and PCHIP methods .....	84
Figure 4.8	$C_p$ distributions on the upper and lower surface of the WTEA-TE1 airfoil at a) $\alpha=0$ deg and at b) $\alpha=1$ deg.....	85
Figure 4.9	$C_p(x)$ at a) $\alpha = 0$ deg and at b) $\alpha = 1$ deg by use of Spline and PCHIP methods .....	86

Figure 4.10	Second derivative of $C_p$ at a) $\alpha = 0$ deg and at b) $\alpha = 1$ deg by use of Spline and PCHIP methods .....	86
Figure 5.1	Controller closed loop scheme .....	98
Figure 5.2	WTEA-TE1 reference airfoil and its modified airfoils shapes .....	99
Figure 5.3	Details of block 2: determination of the pressure coefficients vs. the chord and transition point position [8]. .....	100
Figure 5.4	Pressure coefficients vs. the chord computed by XFOIL and the transition point position calculated by the new algorithm for Mach 0.2 and $\alpha = -2$ deg .....	101
Figure 5.5	Pressure coefficients vs. the chord computed by XFOIL and the transition point position calculated by the new algorithm for Mach 0.2 and $\alpha = 0$ deg .....	101
Figure 5.6	Pressure coefficients vs. the chord computed by XFOIL and the transition point position calculated by the new algorithm for Mach 0.2 and $\alpha = 2$ deg .....	102
Figure 5.7	Details of block 4: SMA.....	104
Figure 5.8	SMA model scheme .....	104
Figure 5.9	SMA cycle.....	105
Figure 5.10	Identification of the SMA's transfer functions .....	107
Figure 5.11	Temperature and actuator displacement vs time with the SMA model compared with the corresponding transfer functions .....	108
Figure 5.12	Displacement of the actuator vs. time with the ZN method.....	109
Figure 5.13	Actuator displacements vs. time with the IMC method for several $\tau_c$ .....	110
Figure 5.14	Displacement of actuator vs. time with the ZN and IMC methods.....	112
Figure 5.15	Algorithm for SMA control improvement .....	113
Figure 5.16	Displacement of the actuator vs. time with the new algorithm.....	114
Figure 5.17	Details of block 3: controller.....	115

Figure 5.18	First simulation type results .....	116
Figure 5.19	Second simulation type results .....	118
Figure 5.20	Third simulation type results .....	120
Figure 6.1	Positions of the sensors on the upper surface airfoil during a wind-tunnel test .....	129
Figure 6.2	Gage pressure signals recorded by optical sensors and pressure taps during 29 s .....	130
Figure 6.3	Differential pressures between gage pressures measured by optical sensors OS and gage pressures measured by pressure taps PT .....	131
Figure 6.4	Static air temperatures variations during 21 runs in the Wind Tunnel.....	131
Figure 6.5	Pressure coefficients distribution plotted over the wind-tunnel model airfoil 's upper surface.....	136
Figure 6.6	Visualization of relative errors of optical sensors versus pressure taps during 21 runs in the wind tunnel.....	138
Figure 7.1	Schematics of the flexible skin mechanical actuation, showing the mechanical principle of morphing.....	147
Figure 7.2	Measured by Kulite transducers vs. theoretical XFOil $C_p$ values over the upper surface of the reference airfoil .....	149
Figure 7.3	FFT spectral decomposition of the 16 Kulite sensors channels .....	150
Figure 7.4	Measured by Kulite transducers vs. theoretical XFOil pressure coefficient values over the upper surface of the optimized airfoil .....	151
Figure 7.5	FFT spectral decomposition of the 16 Kulite sensors channels .....	152
Figure 7.6	Temperature map using infrared camera on the upper surface of the model for a flow of $Re = 2.55 \times 10^6$ , $Mach = 0.224$ and $\alpha = -0.53$ deg.....	154
Figure 7.7	Measured by Kulite transducers vs. theoretical XFOil $C_p$ values over the upper surface of the model for airflow of $Re = 2.55 \times 10^6$ , $Mach = 0.224$ and angle of attack = - 0.53 deg .....	155

Figure 7.8	Temperature map using infrared camera on the upper surface of the model for a flow of $Re = 2.55 \times 10^6$ , $Mach = 0.225$ and $\alpha = 0.97$ deg .....	156
Figure 7.9	Measured by Kulite transducers vs. theoretical XFOIL pressure coefficient values over the upper surface of the model for airflow of $Re = 2.55 \times 10^6$ , $Mach\ number = 0.225$ $\alpha = 0.97$ deg .....	156
Figure 8.1	Schematics of the flexible skin mechanical actuation.....	162
Figure 8.2	SMA control architecture during the bench test.....	162
Figure 8.3	Simulink controller schematics .....	163
Figure 8.4	Theoretical reference and optimized airfoils compared to scanned airfoils in bench test.....	164
Figure 8.5	Time histories and temperature displacement diagram of case C127 morphing airfoil in bench test .....	165
Figure 8.6	Time histories and temperature displacement diagram of case C135 morphing airfoil in bench test .....	166
Figure 9.1	Closed-loop morphing wing system.....	173
Figure 9.2	Structure of the actuating system with SMAs.....	175
Figure 9.3	$dY_1$ and $dY_2$ as functions of $M$ for various $\alpha$ .....	176
Figure 9.4	Model of the flexible structure designed by LAMSI .....	177
Figure 9.5	SMA control architecture and sensor acquisition systems of the test in a wind tunnel for the morphing wing model.....	178
Figure 9.6	Pressure sensor distributions on the morphing wing airfoil.....	180
Figure 9.7	PID controller results for run 33 .....	182
Figure 9.8	Self-tuning fuzzy controller results for run 42 .....	183
Figure 9.9	Ladder command for SMA actuators using self-tuning fuzzy controller.....	184
Figure 9.10	Airflow case C124, $M=0.275$ and $\alpha = 2^\circ$ .....	185
Figure 9.11	Airflow case C114, $M = 0.225$ and $\alpha = 2^\circ$ .....	186

Figure 9.12	Airflow case C129, Mach number = 0.3, $\alpha = -1$ deg, reference (original) airfoil .....	188
Figure 9.13	Airflow case C129, $M = 0.3$ , $\alpha = -1^\circ$ optimized (morphed) airfoil.....	189
Figure 9.14	2-D Wing Model in normalized coordinates (chord $c = 0.5\text{m}$ ). Morphing portion of the wing at $0 < x/c < 0.7$ . Region measured by IR highlighted in red at $0.69 < y/c < 1.46$ . The rigid part of the wing, made of aluminum, is not used in the IR data. Flow is from left to right .....	190
Figure 9.15	Infrared images at $M = 0.3$ , $\alpha = -1^\circ$ for two wing shapes: a) Reference and b) Optimized shape C129. Transition location indicated with the red arrow. Flow is from left to right .....	191
Figure 9.16	Infrared images at $M = 0.275$ , $\alpha = 0^\circ$ for two wing shapes: a) Reference and b) Optimized shape C124. Transition location indicated with the red arrow. Flow is from left to right.....	191
Figure 10.1	Cross section of the morphing wing model.....	196
Figure 10.2	Two examples of optimized airfoil shapes for the aerodynamic cases C127 ( $M=0.275$ , $\alpha=1.5^\circ$ ) and C130 ( $M=0.3$ , $\alpha=-0.5^\circ$ ).....	198
Figure 10.3	Schematics of the flexible skin mechanical actuation.....	199
Figure 10.4	Architecture of the morphing wing model control system.....	200
Figure 10.5	FFT decomposition of the twelve channels pressure signals showing the transition development in the boundary layer over the morphing wing upper surface .....	203
Figure 10.6	Graphical User Interface (GUI) where all the aerodynamic and morphing shape information is centralized together with the control buttons of the software .....	204
Figure 10.7	Open loop control using optimized airfoils database and actuator positions as feed-back.....	208
Figure 10.8	Closed loop control using optimized airfoils database and $C_p$ values as feed-back .....	209
Figure 10.9	Reference airfoil versus C226 airfoil results for $M = 0.275$ , and $\alpha = 1^\circ$ .....	211

Figure 10.10	C232 airfoil results obtained in a) Open loop, b) Closed loop control .....	212
Figure 10.11	C232 airfoil results obtained at $M = 0.3$ and $\alpha = 0.5^\circ$ in a) Open loop, b) Closed loop .....	215
Figure 10.12	C232 infrared results obtained at $M = 0.3$ and $\alpha = 0.5^\circ$ in a) Reference, b) Open loop control, c) Closed loop control.....	216
Figure 11.1	Cross section of the morphing wing model.....	222
Figure 11.2	Schematics of the flexible skin mechanical actuation.....	225
Figure 11.3	Architecture of the morphing wing model control system.....	226
Figure 11.4	Graphical User Interface (GUI) where all the aerodynamic and morphing shape information are centralized together with the control buttons of the software .....	228
Figure 11.5	Optimization logic schematic.....	230
Figure 11.6	Optimization in simulation using XFOIL code a) and b) vs. optimization in real time during wind tunnel tests c) and d) for the same airflow conditions $M = 0.25$ and $\alpha = 0.5^\circ$ .....	233
Figure 11.7	Optimization simulation result of $x_{tr} = 0.497$ for $dY_1 = 3.3$ mm and $dY_2 = 7.2$ mm.....	234
Figure 11.8	Optimization result of $x_{tr}/c = 0.635$ ( $x_{tr} = 317.5$ mm) for $dY_1 = 2.6$ mm and $dY_2 = 5.1$ mm during wind tunnel test for $M = 0.25$ and $\alpha = 0.5^\circ$ .....	235
Figure 11.9	Optimization time history during wind tunnel test for $M = 0.25$ and $\alpha = 0.5^\circ$ .....	236
Figure 11.10	Infrared results obtained at $M = 0.25$ and $\alpha = 0.5^\circ$ in a) Reference, b) After optimization.....	237

## ABREVIATIONS

CFD	Computational fluid dynamics
CRIAQ	Consortium for Research and Innovation in Aerospace in Quebec
ETS	École de technologie supérieure
FFT	Fast Fourier transform
IAR-NRC	Institute for Aerospace Research - National Research Council Canada
IMC	Internal method of control
LAMSI	Laboratory of shape memory alloys and intelligent systems
LARCASE	Laboratory of research in control avionics and aero-servo-elasticity
LFC	Laminar flow control
LVDT	Linear variable differential transducer
NSERC	National Sciences and Engineering Research Council of Canada
PID	Proportional integrative derivative controller
RMS	Root mean square, standard deviation of a noised signal
SMA	Shape memory alloy
SPL	Sound pressure level
WTEA-TE	Wind tunnel experimental airfoil with modified trailing edge
ZN	Ziegler-Nichols method

## SYMBOLS AND MEASURING UNITS

<i>a</i>	Speed of sound
<i>b</i>	Span of wing model
<i>c</i>	chord of wing airfoil
<i>e</i>	Error
<i>f</i>	Frequency
ft	Foot
<i>i</i>	Current in the shape memory alloy
<i>k</i>	Adiabatic coefficient of air
kHz	Kilo Hertz
kS/s	Kilo samples per second
lb	Pounds
lbf	Pounds force
m	Meter
m/s	Meter per second
<i>p</i>	Static pressure
<i>p<sub>abs</sub></i>	Absolute pressure
<i>p<sub>gage</sub></i>	Gage pressure
<i>p<sub>0</sub></i>	Total pressure (stagnation pressure)
<i>p<sub>1</sub></i>	Inflow static pressure
psi	Pounds per square inch
<i>q</i>	Dynamic pressure
<i>u</i>	Local airflow velocity in <i>x</i> direction
<i>v</i>	Local airflow velocity in <i>y</i> direction
<i>x</i>	Stream wise distance from airfoil leading edge
<i>y</i>	Perpendicular distance on the upper surface of the airfoil
<i>A</i>	Amplitudes of perturbations
<i>C<sub>p</sub></i>	Pressure coefficient = $(p - p_{\infty}) / q_{\infty} = (p - p_{\infty}) / 0.5\rho U_{\infty}^2$
<i>F</i>	Applied force on the shape memory alloy
<i>G</i>	Transfer function
GPa	Giga Pascal
<i>K</i>	Static gain of the proportional integral derivative
<i>K<sub>c</sub></i>	Critical gain of the proportional integral derivative
<i>K<sub>d</sub></i>	Derivative gain of the proportional integral derivative
<i>K<sub>i</sub></i>	Integral gain of the proportional integral derivative
<i>K<sub>p</sub></i>	Proportional gain of the proportional integral derivative
<i>L</i>	Length reference
<i>M</i>	Mach number
<i>N</i>	Natural logarithm of rapport between amplified perturbation and initial perturbation in laminar flow <i>N</i> factor = $\ln(A/A_0)$
<i>N<sub>cr</sub></i>	<i>N</i> critical, the value of <i>N</i> when transition between laminar and turbulent flow occurs
Pa	Pascal (N/m <sup>2</sup> Newton per square meter)
<i>Re</i>	Reynolds number

$T_c$	Critical period of the shape memory alloy model
$T_i$	Initial temperature in the shape memory alloy
$U$	Input of a transfer function
$U_\infty$	Free stream airflow speed in wind tunnel
$V$	Airflow speed
$Y$	Exit of a transfer function
$\alpha$	Angle of attack of the wing
$\mu$	Air viscosity
$\rho$	Air density
$\sigma$	Turbulence intensity
$\tau$	Turbulence level
$\tau_c$	Controller delay of the proportional integral derivative controlling the shape memory alloy model
$\tau_1$	Time delay of the proportional integral derivative controlling the shape memory alloy model
$\tau_2$	Time delay of the proportional integral derivative controlling the shape memory alloy model
$\tau_3$	Dead time of the proportional integral derivative controlling the shape memory alloy model

## INTRODUCTION

Today, aeronautical transport is evolving at a very fast pace, as compared to the beginning of the aviation era; aeronautical traffic tripled during the last fifteen years, and by 2025, is projected to double from today's levels. This traffic is expected to see an estimated +3.0% increase in the number of passengers per year, to approximately 1 billion by 2016; will be accompanied by a load factor increase of 81.7% as compared to today's values by 2025 [1]. This evolution will need the new technologies development in the design and building of modern aircraft equipped with active control systems.

During the same time period, fuel cost increases will lead to a slowdown in the aerospace industry, which in turn will stimulate research to find technological solutions; this will specifically involve designing new fuel economy consumption methods. A new green trend has indeed started to spread out from the automobile industry into the aircraft industry, in which research is being carried out to reduce fuel consumption by reducing drag, which is directly related to the airflow type around the aerodynamic aircraft body design. The drag reduction concept is connected to the laminar flow and to the displacement of the transition point between laminar and turbulent flows towards the trailing edge.

Numerous studies, which will be detailed in the Chapter 1, show that the transition between laminar and turbulent flows is influenced by the shape of the wing airfoil, which will be our main focus in this research project. Aerodynamic studies from the beginning of the aviation history show that for a certain flight condition characterized by a given Mach number and a given Reynolds number, the airflow around a wing airfoil is laminar at the leading edge, but becomes turbulent at a certain point due to air viscosity. A turbulent flow is not desired because of its negative effect in terms of drag increase, which, over time, leads to high fuel consumption, and consequently, increased operating costs.

This research thesis is realized as part of a major project initiated and financially supported by following government and industry associations: the Consortium for Research and

Innovation in Aerospace in Quebec (CRIAQ), the National Sciences and Engineering Research Council of Canada (NSERC), Bombardier Aerospace, Thales Avionics and the National Research Council Canada Institute for Aerospace Research (NRC-IAR).

The project aims to realize a theoretical and experimental aerodynamic wind tunnel study of a rectangular wing equipped with a flexible skin, smart actuators and optical sensors, able of changing its shape using an active controller, in order to move the position of transition from laminar to turbulent flow.

This multidisciplinary project is realized by several collaborating teams from the École de technologie supérieure, the Laboratory of Memory Alloys and Intelligent Systems (LAMSI), the Laboratory of Research in Avionics and Aero-Servo-Elasticity (LARCASE), École Polytechnique, the National Research Council Canada Institute for Aerospace Research (NRC-IAR), Thales Avionics and Bombardier Aerospace.

The teams were each assigned the following responsibilities in the project, respectively: the LAMSI team was charged with designing and manufacturing the actuators and flexible skin as well as the model internal structure; the École Polytechnique team had the responsibility of designing the optimized airfoils for each airflow condition using CFD codes in order to analyze the transition from laminar to turbulent flow; the NRC-IAR team had to organize and run the wind tunnel tests, while the LARCASE team was responsible for the integration and validation of the control and monitoring systems of the morphing wing model.

As a member of the LARCASE team, my thesis will focus on the aspects of the research involving the integration and functional validation of the various mechanical and electrical systems that composed the morphing wing model.

The thesis includes the chapters on the: 1) *state-of-the-art* in the morphing aircraft research domain, 2) *objectives* and *originality*, and 3) collection of *eight articles* published in the

chronological order (from the oldest to the newest), in which the research work performed to reach the project objectives is shown.

The eight articles are: the first three articles published in the AIAA Journal of Aircraft, two articles presented at two aeronautical conferences and the last three articles accepted for publication and in print in the AIAA Journal of Aircraft.

These articles are written in collaboration with my colleagues at the LARCASE laboratory and members of other teams. My contribution as main author, as well as the contributions of colleagues of the other teams to each article is specified in the introductory part of each article. Dr Botez is the co-author of these papers, as PhD advisor.

The thesis concludes with a short list of recommendations to be followed in future research on morphing aircraft control.

In the first article, a new theoretical method of detecting the transition between laminar to turbulent flows is presented. The method uses a new algorithm based on interpolation methods programmed in Matlab, to localize the transition where the discontinuities in the pressure plot appear, for small angles of attack. It was intended, at that time, to use this new method in the future controller, as feedback information on the transition point position on the wing model upper surface.

In the second article, a new simulation method for the shape memory alloys actuators control through a PID controller is presented. This new method was functional in simulation and was further tested with hardware in the loop, on bench tests, and successfully presented in the fifth article.

In the third article, a new method for optical sensors calibration with temperature variations is presented. This new method could be applied in the case when the optical sensors do not have temperature compensation to be used in wind tunnel tests. The optical sensors were

intended to give feedback information about the transition point position on the upper surface of the wing model, but they were abandoned later in the project due to technological reasons that are discussed in the fourth article introduction.

In the fourth article, a laminar-to-turbulent flow transition detection method is presented, and the way in which the signals were post processed in order to obtain the flow state information on the boundary layer. This method was finally implemented in the software controller as feedback information about transition point position and pressure information on the wing model upper surface.

In the fifth article, the bench test results are presented using the new control method developed. It was found that aerodynamic optimized theoretical airfoils are same as the scanned airfoils obtained on the real wing model during bench tests. The controller software tested on the bench was further used in the following wing tunnel tests, as shown in the last three articles.

The wind tunnel tests results are presented in the sixth article, and proved that the morphing wing concept would be feasible, and would provide great potential for the aerospace industry future. The wing model was controlled using the open loop control method. The shape memory actuators, high sensitivity pressure sensors and software controllers formed a system to be integrated and validated in the wind tunnel for the first time in this article.

In the following two articles, different control strategies are discussed, that can be used in the future morphing wing aircraft controllers. In the seventh article, the wind tunnel tests results of the wing model controlled using the closed-loop control method, are shown. The closed-loop control method results were compared and thus validated with the open loop control method results, and were validated using the infrared thermography.

A new optimization method is shown in the eighth article, for the closed loop controller, and the wing model as real time hardware-in-the-loop in running wind tunnel conditions. The experimental results were successfully validated with simulation results.

### **Reference**

- [1] Nan Shellabarger, 2008, “National Forecast Overview 2008-2025”, Director Aviation Policy and Plans, Federal Aviation Administration.  
[http://www.faa.gov/news/conferences\\_events/aviation\\_forecast\\_2008/agenda\\_presentation/media/nan\\_shellabarger.pdf](http://www.faa.gov/news/conferences_events/aviation_forecast_2008/agenda_presentation/media/nan_shellabarger.pdf) . Consulted November 6, 2009.

# **CHAPTER 1**

## **STATE OF THE ART**

In this chapter, a brief state of the art in the morphing aircraft research domain is presented. Firstly the laminar flow improvement literature will be described using only aerodynamics knowledge, then morphing wing control methods using only actuators, followed by materials and actuation use in the morphing wing design, and finally the integrated morphing wing and aircraft studies realised until now.

### **1.1 Aerodynamic methods for laminar flow improvement**

To modify the laminar flow around a wing airfoil, it was necessary to change the airfoil shape; therefore one of the methods for airfoil changes was developed at Kentucky University, which consisted of deflecting the wing upper surface using adaptive actuators [1, 2, 3, 4, 5, 6] .

It was shown that the actuators activated oscillatory motions of a certain frequency to the boundary layer flow over the upper surface. These actuators were made of piezo-electric materials which changed their shapes when connected to an electrical current differential voltage. The wind tunnel tests showed that the displacement of the transition point to the trailing edge resulted in the drag decrease and in the lift increase [2].

Another method for changing the airfoil shape involved the use of a bump, which was inflated with air. This method was conceived by researchers at Stuttgart University [7, 8]. In this method, the airfoil geometry was modified in order to decrease the negative effects of shockwaves in transonic flow. The results obtained by the airfoil optimization showed a 70% decrease in the wave drag and a 15% decrease in the wing total drag.

At the German Aerospace Research Center (DLR), researchers simulated the changes of the airfoil shape using an inflated bump [10, 11]. The results obtained showed a 10% drag

reduction for Mach numbers between 0.72 and 0.77. A basic theory was developed for changing the airfoil shape in transonic flow.

Another method for changing the airfoil shape was studied by the Aerospace Company Embraer [12, 13, 14, 15]. In this case, the leading and trailing edges changed their shapes by curving the camber line. The results obtained by Embraer were promising as they showed a reduction in drag value by up to 24%.

A 1991 study conducted at NASA's Langley laboratory evaluated the application of the hybrid laminar flow control (HLFC) on subsonic aircrafts and bi-motor aircraft transporters [9, 16]. The study was realized by using the FLOPS optimizing flight system as well as a CFD code. The researchers studied the laminar flow over the upper surface of the wing, and over the vertical and horizontal stabilizers. They also studied the advantages of the laminar flow over the nacelles.

The "chordwise air collection" method was designed in 1984 [17], in fact, laminar flow control (LFC) over the upper surface of the wing was realized by the boundary layer suction, thereby moving the transition position at 85% of the chord.

A numerical algorithm was developed for optimizing the suction distribution, by maintaining the transition at a desired location (chord %) and maintaining the energy spent at a minimum [18]. Three steps were considered: 1. Boundary layer computation; 2. Transition prediction, and 3. Optimization of the suction distribution while maintaining the transition location at a certain desired percentage of the chord. In the third step, the gradient method was used. Optimized wings were conceived by reducing the kinetic energy of the perturbation and drag values while, the lift and pitch moment coefficients were maintained at desired values [19].

At the German Aerospace Research Center (DLR), the DoAL3 airfoil was designed for aircraft wings, at moderate Mach numbers,  $M = 0.45-0.6$ , and at Reynolds numbers, up to  $Re = 14 \times 10^6$ . Transition measurements were performed in the Brunswick Wind Tunnel (TWB)

at Mach number of 0.48. The effects of Reynolds number and the thermal transfer on the laminar flow separately were studied, and the numerical results were validated by experiments.

A controller was developed at Southampton University, with the aim of maintaining the desired turbulence level over a flat plate equipped with a suction porous panel. The pressure fluctuations were measured with microphones at the boundary layer over the flat plate, and the signal was conditioned and filtered to remove the background noise of the wind tunnel fan, then the turbulence level was estimated by computing the RMS (Root Mean Square) pressure signal. The controller used the error between the RMS values of the measured pressures and the desired RMS values at the spots where the microphones were installed, thus maintaining the transition on the specified area over the flat plate [20].

## 1.2 Morphing wings equipped only with actuators

Three devices were able of modifying wing structure on a test bed aircraft [21]. The first device was the *Hyper-Elliptic Cambered Span* (HECS) wing mechanism – used to increase loiter time. During cruise, induced drag accounted for 50% of the total aircraft drag. Compared to a planar elliptic wing of the same span, the HECS wing provided a lift-to-drag ratio (L/D) increase of as much as 15%, with a 10% increase in surface area. The second device was the *oblique joint* mechanism, located at the root of a standard planar elliptical airfoil, and capable of independently rotating each wing on an aircraft through variations of dihedral, sweep and incidence angles, by use of three sequential motors per wing that can be operated independently. The third device employed a Stewart platform concept as a constrained version of the 6 degrees of freedom mechanism commonly used, with a central pivot preventing translational motion and allowing rotation about the center of the top and bottom plate using 3 Haydon Switch and Instrument ½ stroke linear actuators. Compliant skin materials were also discussed.

A strain energy model took into account the actuation cost of a morphing airfoil, where a multi-objective optimization found trade-off solutions between low-energy/high drag and

high energy/low drag morphing airfoils [22]. The aerodynamic work term was added to the strain energy model to compute the total energy required for the airfoil shape change. The effect of the morphing airfoil's relative stiffness on the multi-objective solutions was presented.

Stabilators were used for various applications such as primary and secondary flight control, buffet-load alleviation, flutter testing, active flow reattachment and vortex generation. Although most of the adaptive aerostructures applications were found in UAV's, missiles and munitions [23].

Closed-loop control of the morphing platform (*wing-shape control*) and simultaneously enforced prescribed closed loop aircraft dynamics (*flight control*) were modeled [24]. The *N-MAS wing* designed by NextGen Aeronautics was considered. The flight control law actively used the leading edge morphing wing sweep angle as an actuator to assist in manoeuvres while guaranteeing aircraft stability. An aircraft model (morphing wing, aircraft body, and control surface locations) was developed using CAD drawings, mass and geometry specifications and NACA airfoil designations. The Simulink model included variable Center of Gravity- (CG) and DATCOM-derived aerodynamic coefficients as a function of the wing configuration and angle of attack. The morph between the two modes of *Loiter* and *Dash* was modeled by a first-order transfer function, and hence the morph rate was governed by the transfer function time constant.

The empirical structural weights for various wing geometries were obtained by implementing two finite element-based structural optimization methods: 1) an aggregate and 2) a simultaneous analysis [25]. These methods were applied on a morphing wing with two degrees of freedom: the wing sweep and the root chord length. Two linear actuators were used: one positioned along and parallel to the forward spar and the other one positioned along and parallel to the wing root chord. These geometrical variations produced four configurations with changes in *area*, *aspect ratio* and *sweep*: the *high lift configuration* for the largest area and minimal sweep angle; the *loiter configuration* for the maximum aspect

ratio and minimum sweep angle; the *dash/cruise configuration* for the maximum sweep and minimal area; and the *manoeuvre configuration* for the maximum area at the maximum sweep.

### 1.3 Materials and actuators use in the morphing wing design

Various types of materials were used in the morphing wing design, such as:

*Computational materials* with high performance, such as continuous fibre-reinforced polymer matrix composites and piezoelectric films from high temperature polyimides [26], *advanced piezoelectric materials*, such as piezoelectric polymers, high displacement piezoelectric ceramic actuators and ferroelectric thin film micro-actuators and *integrated and graphite reinforced composites*.

*Morphing actuators' failure compensations*, called *effectors*, were investigated as they replaced control surfaces such as ailerons or rudders on a morphing wing [27].

Flexible material structures enabled large rigid body deformations of aircraft structures while maintaining their aerodynamic shapes. Matrix material was selected to be a Shape Memory Polymer SMP embedded with a reinforcing fibre [28, 29].

An adaptive actuator failure compensation control scheme was completed for the state tracking of a morphing aircraft model with unknown morphing actuator failures [30].

A device allowed most of the energy required to twist or deform a wing to be stored in discrete springs. When the device was used, sufficient energy was provided to control the wing position. Lightweight actuators were used to perform wing twisting and other structural distortions, and reduce the onboard mass of the wing-twist system [31].

Post-Buckled and Pre-compressed PBP piezoelectric actuators induced roll control on a subscale morphing wing. Aerodynamic wing loading was modeled using Theodorsen's

theory of disturbed flow. Bench tests showed a maximum deflection of more than +/- 3 degrees up to a break frequency of 34 Hz. Application of PBP actuators led to savings in *Operating Empty Weight (OEW)* of 3.5% and an increase in break frequency from 3 to 34 Hz [32].

Strain actuators embedded in the structure or strategically distributed modern miniaturized actuators were conceived and verified [33].

*Shape memory alloys (SMA)* used in morphing flaps actuation were developed in ultra-light and scaled models made of balsa wood and nylon sticks, due to favourable characteristics of high strength and low weight. The SMA actuators were controlled using robust non-linear controllers [34, 35].

Wind tunnel studies on morphing wing flaps prototypes using SMA wires (NiTiNol) were performed at the Missouri University of Science and Technology. The trailing edge was morphed by means of six NiTiNol wires that could pull the flaps assembly upon electrical activation, while ten springs acted to regain the initial wing configuration when the SMA wires cooled down [36].

Another morphing flap actuated using SMAs was developed at Nanyang Technological University, Singapore using four SMA wires anchored in four different chord points. A wing prototype with flexible skin made of fibreglass composite and rubber sheet was manufactured and tested [37].

Torsion bars and wires using SMA (NiTiNol) for the roll control of a morphing wing model aircraft were tested in wind tunnel and during flight at the Virginia Polytechnic Institute and State University [38].

The “Hingeless Wing” concept using SMA wires was investigated at the Aerospace Engineering Department (DIAS) at University “Federico II” of Naples, in collaboration with the Italian Aerospace Research Center (CIRA) [39], and independently at the University of Catania (Italy) [40].

#### **1.4 Integrated morphing wing studies**

Mission Adaptive Compliant (MAC) Wing Technology allowed linearly varying flap deflections along the wing span. The main benefits consisted of allowing the flap to reshape the wing lift distribution closer to an elliptical distribution, thus minimizing induced drag and wing root bending moment, and thereby saving weight [41].

Northrop Grumman Corporation (NGC) has built and tested two 16% - scale wind tunnel models (conventional and smart) of a fighter aircraft under the DARPA/AFRL/NASA Smart Wing Phase I project [42]. Hinge-less, contoured TE control surfaces with embedded SMA wires and span-wise wing twists effected by SMA torque tube mechanisms were compared to the conventional hinged control surfaces. Benefits were expressed in terms of increased pitching and rolling moments, and improved pressure distributions. Successful results were expressed in terms of: 5 degrees of span-wise twist and an 8-12% increase in rolling moment using a single SMA torque tube, 12 degrees of deflection and 10% increase in rolling moment, and in demonstration of optical techniques for span twist and deflected shape measurements.

A symmetric wing structure was created with two tapered graphite/epoxy composite plates and a steel body. Four pairs of SMA wires were attached to the wings’ bottom surfaces in the chord-wise direction. Lift and drag forces were measured at various angles of attack. Dynamic vibration signals were measured by Fiber Bragg Grating FBG sensors at the wing root and were used to monitor aeroelastic unstable flutter phenomena, at various angles of attack [43].

A wing structure comprised of an optimized internal layout of cables and struts was able to change its shape. Cables were used as actuators' tendons, while struts provided rigidity to the wing. In addition to achieving continuous morphing by changing cable lengths, this structure had the advantages of being light weighted and having a distributed actuation. Topology optimization was used to optimally place cables and struts in a *bay* or in a wing section. The *Non-dominated Sorting Genetic Algorithm II* (NSGA II) was used for modeling the NASA HECS and the NextGen TSCh wings [44].

An integrated multi-disciplinary optimization procedure for morphing wing optimization was mainly based on 'off-the-shelf' analysis codes. It allowed the computation of the minimum structural weight of morphing wings (for which *swept angle and aspect ratio* change). This optimization was performed with a general-purpose optimization code, called Optimus, distributed by Noesis Solutions. For aeroelasticity studies, MSC/Nastran and ALIS (for steady and unsteady linear aerodynamics) codes were used. Two approaches were presented: *sequential* and *fully integrated*. An LMS Virtual Lab Morphing tool was also used [45].

Wings roll performances were achieved by use of *articulated conformal control surfaces*. Analysis results were compared to experimental results obtained for a 16% scale model of a fighter wing equipped with embedded smart materials used to deform a control surface. The control surface design was found suitable for low-rate applications such as *takeoff* and *landing* configurations [46].

## **1.5 Integrated morphing aircraft studies**

Lockheed Martin has built an Unmanned Combat Air Vehicle UCAV for Morphing A/C studies. Its configuration had two folds that allowed the radical morphing of the span and wetted area. The multi-role aerodynamic performance was defined by a combination of cruise/loiter efficiency and dash/penetration capability in a single vehicle, and by significantly increasing the mission performance with respect to the conventional platforms. Both inboard and outboard flaps were required for manoeuvring and pitch/yaw stability [47].

An articulated large-scale half span wind tunnel model-validated morphing system operation under realistic flight loads was realized [48].

Four application fields of the SMA's technology on an aircraft have been investigated: vibration/acoustic control, shape control, multi-functional smart structures, and morphing structures. Tail-buffet suppression, flutter damping, engine-vibration control, smart wing, smart skin, adaptive Micro Air Vehicle (MAV), vortex wake control and biology-inspired aircraft were reviewed. The best technology application would be a reconfigurable configuration for which performances would be adjusted and optimized under varying conditions [49].

The MFX-1, created under a DARPA sponsored program called Next Generation Morphing A/C Structures (N-MAS) and realized by Next-Gen Aeronautics, had a 9.3 ft wing span, a length of 6.8 ft, V-tails, non-retractable landing gear with a steerable nose wheel, three on-board cameras with one download link and a GPS system. It was powered by a single jet engine with 45 lbs of maximum thrust. Other key features included: independently activated ailerons, flaps, rudders, GPS, MEMS gyros and accelerometers as flight control system sensors, altitude telemetry, airspeed, GPA headings, and battery conditions, maximum flight time of 20 minutes and a parachute flight termination/recovery system. The primary purposes of these tests were to (1) demonstrate in-flight operation at sub-scale, and stability and control of the MFX-1; and (2) test flight test procedures including communications and pilot skills for N-MAS aircraft.

During the first test, a fixed wing was flown, which provided good training for the flight test crew. During the second test, performed on the morphing wing, multiple checks of the morphing wing actuation and power systems were performed prior to flight to reduce the overall test risk [50]. The flight took place at altitudes between 400 and 600 ft, and at speeds between 100 and 120 knots. The remote pilot had no cues except aircraft views from the ground. Onboard recorded data included GPS location and altitude; and three video cameras, mounted on the twin tails of the aircraft and in its nose, provided flight pictures to be

downloaded after landing. The wing area changed 40%, the wing span changed 30%, and the wing sweep varied from 15° to 35° to successfully morph during flight, of less than 15 seconds. During Phase II of the NMAS program, a 200 lb, autonomous, twin-jet morphing UAV had a larger and improved wing design which rapidly morphed during manoeuvres required for agile Hunter-Killer operations.

The probabilistic modeling of actuator failure and stochastic robust control provided a novel and flexible means of failure compensation for a morphing tailless, delta-wing fighter aircraft operating arrays of large numbers of actuation devices [51]; Lateral equations of motion were linearised at Mach number  $M = 0.6$  and altitude  $H = 15,000$  ft. The equilibrium trim angle of attack was approximately 4.4 degrees. Control moments required at the trim condition were generated by conventional hinged surface actuators. The shape-change effectors/device arrays were used to stabilize and manoeuvre the vehicle at the trim condition. Among the four distributed arrays of shape-change devices on each wing, three are situated on the upper surface and one is on the lower wing surface. There were a total of 156 devices, 78 on each wing [51].

NextGen developed an in-plane morphing geometry concept. Flexible elastomeric skins with out-of-plane stiffeners accommodated the wing motion while transmitting air pressure loads to the wing substructure. Wind tunnel testing of a full-scale wing for a 2400 lb vehicle and flight testing of a subscale UAV were performed. The following issues were identified: the need to address multiple geometries and flight envelopes to account for morphing shape changes; the in-plane wing flexibility resulting from its mechanism restraint by linear actuators. Another half-span wind tunnel model was tested in the NASA Transonic Dynamics Tunnel for aeroelasticity studies [52].

The Miniature Trailing Edge effector (MiTE) was a small trailing edge device located at 1-5% chord, deflected vertically into the flow. A stable separation region ahead of the flap and a pair of counter-rotating vortices aft were realized. Aerodynamic analysis results provided a database for the development of the aerodynamic wind tunnel test model. The

aeroservoelastic test model successfully proved an Active Flutter Suppression concept for an UAV [53].

An aeroelastic numerical code took into account the *morphing energy* coupled of a 3D beam finite elements model in a co-rotational framework to a lifting line aerodynamic code. The morphing energy was calculated by the sum of actuation moments, applied at the beam nodes, multiplied by the required angular rotations of the beam elements. The code results were validated with Nastran Aeroelasticity Module. This code was tested for a *sweep morphing manoeuvre*, and it was demonstrated that sweep morphing improved aircraft aerodynamic performances such as the lift-to-drag ratio (L/D) values [54].

The Flight Test results of a Mission Adaptive Compliant Wing (MAC-Wing) variable geometry Trailing Edge Flap with a Natural Laminar Flow NLF airfoil have been described. The MAC-Wing technology provided light-weight, low power, variable geometry reshaping of the upper and lower flap surface with no discontinuities. The airfoil-flap system was optimized to maximize the laminar boundary layer extent over a broad lift coefficient range for endurance aircraft applications. The expanded laminar bucket capability allowed the endurance aircraft to extend their range, by 15% or more, by optimizing the lift-to-drag ratio (L/D) throughout the mission. The wing was tested at full-scale dynamic pressure, Mach number, and reduced-scale Reynolds numbers on Scaled Composites' Knight Aircraft. Laminar flow regime occurred up to 60% chord of the wing during tests. Significant fuel and weight savings as well as high control authority were verified by tests and analyses. Fifteen Dantec Dynamics hot film sensors measured the boundary layer transition position [41].

The MORPHEUS wind tunnel model of a Morphing Air Vehicle (MAV) was designed for the following five purposes: quasi-steady aerodynamic modeling of an aircraft with large planform changes, optimization studies to achieve efficient flight configurations, transient aerodynamic modeling of high rate planform changes, planform manoeuvring evaluations as control effectors, and gimballed flight control simulation of a morphing aircraft [55].

In the Air-to-Air Fighter (AAF) model consisting of a propulsion subsystem (PS) and an Airframe Subsystem – Aerodynamics (AFS-A), the morphing wing was allowed to change its sweep, length, root and tip chord lengths within set constraints for its AAF mission of 19 flight segments. Using *minimum fuel burned* as an objective, the most efficient wing configuration and the overall aircraft system operation were achieved for each segment of the mission [56].

A DARPA-sponsored wind tunnel test model of a Lockheed Martin morphing concept was designed and tested. The wind tunnel model incorporated the key features representatives of a full scale vehicle model: out-of-plane morphing through a coordinated actuation system integrated with seamless skins and a composite support structure that encompassed the actuator system along the wing fold hinge lines, structural layout and materials featured in the full scale vehicle design, and a first-time thermo-polymer actuator integral to a leading edge device for smooth contour between the inner wing and fuselage when fully morphed. The model was instrumented with strain gauges, accelerometers and pressure transducers; data was acquired and correlated with aircraft design and analysis methods [57].

Following our detailed bibliographical research, it was realized that until now, nobody realized a fully automated morphing wing controller for the laminar flow improvement and further for transition delay using pressure sensors and Smart Material Actuators to morph its upper surface.

## References

- [1] Munday, D., Jacob, J., 2002, *Active control separation on a wing with oscillating camber*, AIAA Journal of Aircraft, vol. 39 (1), Paper AIAA 2001–0293.
- [2] Jacob, J. D., 1999, *Aerodynamic flow control using shape adaptive surfaces asme*, Paper No. DETC99/VIB-8323, ASME 17th Biennial Conference on Mechanical Vibration and Noise, Symposium on Structronics, Mechatronics, and Smart Materials, Las Vegas, Nevada, September.  
<http://www.engr.uky.edu/~fml/papers/VIB-8323.pdf>, Consulted on November 6, 2009.

- [3] Munday, D., Jacob, J., 2001, *Low speed morphing wing flow control*, University of Kentucky, Lexington, KY.  
<http://www.engr.uky.edu/~fml/research/wing-2001.pdf>, Consulted on November 6.
- [4] Munday, D., Jacob, J. D., and Huang, G., 2002, *Active flow control of separation on a wing with oscillatory camber*, 40th AIAA Aerospace Sciences Meeting, Reno, NV. Paper AIAA-2002-0413  
<http://www.engr.uky.edu/~fml/papers/AIAA-2002-0413.pdf>, Consulted on November 6, 2009.
- [5] Munday, D., Jacob, J. D., Hauser, T., and Huang, G., 2002, *Experimental and numerical investigation of aerodynamic flow control using oscillating adaptive surfaces*, AIAA Paper No. 2002-2837, 1st AIAA Flow Control Conference, St. Louis.  
<http://www.engr.uky.edu/~fml/papers/AIAA-2002-2837.pdf>, Consulted on November 6, 2009.
- [6] Jacob, J. D., 1998, *On the fluid dynamics of adaptive airfoils*, University of Kentucky, Lexington,  
<http://www.engr.uky.edu/~fml/papers/imece-paper.pdf>. Consulted on November 6, 2009.
- [7] Lutz, T., Sommerer, A., Wagner, S., 2000, *Design of adaptive transonic airfoils by means of numerical optimisation*, University of Stuttgart, Germany.
- [8] Wadehn, W., Sommerer, A., Lutz, Th., Fokin, D., Pritschow, G., Wagner, S., 2002, [\*Structural concepts and aerodynamic design of shock control bumps\*](#), Proceedings 23rd ICAS Congress, Toronto, Canada, September 8 - 13, ICAS Paper 66R1.1.
- [9] Pinkerton, J. L., Moses, R. W., 1997, *A feasibility study to control airfoil shape using THUNDER*, Langley Research Center, Hampton, Virginia, NASA Technical Memorandum 4767.
- [10] Sobieczky, H., Geissler, W., 1999, *Active flow control based on transonic design concepts*, DLR German Aerospace Research Establishment, AIAA Paper 99-3127.
- [11] Sobieczky, H., Geissler, W., Hannemann, M., 1998, *Expansion shoulder bump for wing section viscous/wave drag control*, FLOWCON IUTAM Symposium on Mechanics of Passive and Active Flow Control, Gottingen, Germany.
- [12] Martins, A.L.; Catalano, F.M., 1996, *Aerodynamic optimization study of a mission adaptive wing for transport aircraft*, ICAS-96, Sorrento, Italy.
- [13] Martins, A.L., Catalano, F.M., 1998, *Viscous drag optimization for a transport aircraft mission adaptive wing*, ICAS-98-31499 Melbourne, Australia.

- [14] Catalano, F.M., Greco Jr, P.C., Martins, A.L., 2002, *Viscous and wave drag optimization for a transport aircraft mission adaptive wing*, Aircraft Laboratory – University of São Paulo-Brazil and Embraer, ICAS Congress.
- [15] Martins, A. L., Catalano, F. M., 2003, *Drag optimization for transport aircraft mission adaptive wing*, Journal of the Brazilian Society of Mechanical Sciences, vol. 25, no. 1.
- [16] Arcara, P.C., Jr., Bartlett, D.W., McCullers, L.A., 1991, *Analysis for the application of hybrid laminar flow control to a long-range subsonic transport aircraft*, SAE Technical Paper Series, 912113, 1991, pages 1-15, Aerospace Technology Conference and Exposition, Sep 23-26, Long Beach, CA, USA.
- [17] Allison, D.O., Dagenhart, J.R., 1978, *Design of a laminar-flow-control supercritical airfoil for a swept wing*, CTOL Transport Technology, pages 395-408.
- [18] Hackenberg, P., 1995, *Numerical optimization of the suction distribution for laminar flow control aerofoils*, Doctoral Thesis, University of Southampton (United Kingdom).
- [19] Pralits, J., 2003, *Optimal design of natural and hybrid laminar flow control on wings*, Doctoral Thesis, Technical Report from Royal Institute of Technology, Stockholm, Sweden.
- [20] Rioual, J.-L., Nelson, P. A., Fisher, M. J., 1994, *Experiments on the automatic control of boundary-layer transition*, Journal of Aircraft. Vol. 31, No. 6, pp 1416-1418.
- [21] Manzo, J., Garcia, E., Wickenheiser, A., M., 2004, *Adaptive structural systems and compliant skin technology of morphing aircraft structures*, Proceedings of SPIE: International Society for Optical Engineering, Vol. 5390, pp. 225–234.  
[http://spie.org/x648.html?product\\_id=540348](http://spie.org/x648.html?product_id=540348) [retrieved 8 January 2010]
- [22] Namgoong, H., Crossley, W., A., Lyrintzis, A., S., 2006, *Morphing airfoil design for minimum aerodynamic drag and actuation energy including aerodynamic work*, AIAA Paper 2006-2041, pp. 5407–5421.
- [23] Barrett, R., 2007, *Improvements to commercial and general aviation via adaptive aerostructures*, Paper AIAA-2007-7873, 7<sup>th</sup> AIAA Aviation Technology, Integration and Operations Conference (ATIO), 18-20 September, pp. 1-9.
- [24] Gandhi, N., Jha, A., Monaco, J., Seigler, T., M., Ward, D., Inman, D., J., 2007, *Intelligent control of a morphing aircraft*, Paper AIAA-2007-1716, pp. 166-182.
- [25] Skillen, M. D., Crossley, W. A., 2005, *Developing response surface based wing weight equations for conceptual morphing aircraft sizing*, Paper AIAA-2005-1960, pp. 2007-2019.

- [26] Simpson, J., O., Wise, S., A., Bryant, R., G., Cano, R., J., Gates, T., S., 1998, *Innovative materials for aircraft morphing*, SPIE, Vol. 3326, pp. 240-249.
- [27] Tao, G., Tang, X., D., Chen, S., H., Fei, J., T., Joshi, S., M., 2006, *Adaptive failure compensation of two-state aircraft morphing actuators*, IEEE Transactions on Control Systems Technology, Vol. 14(1), pp. 157-164.
- [28] Pastor, C., Sanders, B., Joo, J., J., McCarty, R., 2006, *Kinematically design flexible skins for morphing aircraft*, IMECE 2006-13771, pp. 89-95.
- [29] Keihl, M., M., Bortolin, R., S., Sanders, B., Joshi, S., Tidwell, Z., 2005, *Mechanical properties of shape memory polymers for morphing aircraft applications*, Smart Structures and Materials 2005: Industrial and commercial applications of smart structures technologies, edited by E. V. White, Proceedings of SPIE, Vol. 5762, pp. 143-151.
- [30] Chen, S., Tao, G., Fei, J., Joshi, S., M., 2004, *Adaptive compensation of morphing actuator failures*, Proceedings of the 2004 ACC, Boston, Massachusetts, June 30 - July 2, pp. 1805-1810.
- [31] Clingman, D., Ruggeri, R., 2004, *Mechanical strain energy shuttle for aircraft morphing via wing twist or structural deformation*, Smart Structures and Materials 2004: Industrial and Commercial Applications of Smart Structures Technologies, edited by E. H. Anderson, Proceedings of SPIE, Vol. 5388, pp. 288-296.
- [32] Vos, R., De Breuker, R., Barrett, R., Tiso, P., 2007, *Morphing wing flight control via postbuckled precompressed piezoelectric actuators*, Journal of Aircraft, Vol. 44(4), pp 1060-1067.
- [33] Rodriguez, A. R., 2007, *Morphing aircraft technology survey*, Paper AIAA-2007-1258.
- [34] Alasty, A., Alemohammad, S., H., Khiabani, R., H., Khalighi, Y., 2004, *Maneuverability improvement for an ultra light airplane model using variable shape wing*, AIAA Atmospheric Flight Mechanics Conference and Exhibit, Providence, Rhode Island, AIAA Paper 2004-4831.
- [35] Song, G., Ma, N., 2007, *Robust control of a shape memory alloy wire actuated flap*, Smart materials and Structures, Vol. 16, pp. N51-N57.
- [36] Benavides, J., C., Correa, G., 2004, *Morphing wing design using Nitinol wire*, Missouri University of Science and Technology, Intelligent System Center, <http://isc.mst.edu/reu/2004indprojects/2004-6.html>, Consulted on February 9, 2010

- [37] Seow, A., K., Liu, Y., Yeo, W., K., 2008, *Shape memory alloy as actuator to deflect a wing flap*, 49<sup>th</sup> AIAA/ASME/ASCE/AHS/ASC Structures, Structural Dynamics and Materials Conference, April 7-10, Schaumburg, IL, AIAA Paper 2008-1704.
- [38] Mason, H., W., Robertshaw, H., Inman, D., J., 2004, *Recent Experiments in aerospace and design engineering education*, 42<sup>nd</sup> AIAA Aerospace Sciences meeting and Exhibit, January 5-8, Reno, Nevada, AIAA Paper 2004-0415.
- [39] Barbarino, S., Pecora, R., Lecce, L., Concilio, A., Ameduri, S., 2008, *Airfoil morphing architecture based on shape memory alloys*, Proceedings of SMASIS 2008, Conference on Smart Materials, Adaptive Structures & Intelligent Systems, October 28-30, Ellicott City, Maryland, Paper SMASIS 2008-480.
- [40] Mirone, G., 2007, Design and demonstrators testing of adaptive airfoils and hinge-less wings actuated by shape memory alloy wires, *Smart Structures and Systems*, Vol. 3(1), pp. 89-114.
- [41] Hetrick, J.A., 2007, *Flight testing of mission adaptive compliant wing*, Paper AIAA-2007-1709, 48<sup>th</sup> AIAA/ASME/ASCE/AHS/ASC Structures, Structural Dynamics and Materials Conference, 23-26 April, pp. 1-18.
- [42] Scherer, L. B., Martin, C. A., West, M., Florance, J., P., Wieseman, C., D., Burner, A., W., and Fleming, G., A., 1999, *DARPA/AFRL/NASA smart wing second wind tunnel test results*.  
<http://www.tpub.com/content/nasa1999/NASA-99-6spie-lbs/index.htm>, Consulted on November 6, 2009.
- [43] Yang, S.-M. , Han, J.-H., Lee, I., 2006, *Characteristics of smart composite wing with SMA's and optical fibre sensors*, *International Journal of Applied Electromagnetics and Mechanics*, Vol. 23, pp. 177-186  
<http://iospress.metapress.com/content/br4kaakbahwu2xf0/> Consulted on January 8, 2010.
- [44] Bharti, S, Frecker, M., Lesieutre, G., Ramrakhyani, D. 2004, *Active and passive material optimization in a tendon actuated morphing aircraft structure*, *Smart Structures and Integrated Systems Congress*, San Diego, CA, 15-18 March, Proceedings of Society of Photo-Optical Instrumentation Engineers, SPIE Proceedings, Vol. 5360, pp. 247-257.
- [45] Ricci, S., Terraneo, M., 2006, *Application of MDO techniques to the preliminary design of morphed aircraft*, AIAA-2006-7018, pp. 1263-1276.
- [46] Sanders, B., Eastep, F., E., Foster, E., 2003, *Aerodynamic and aeroelastic characteristics of wings with conformal control surfaces for morphing aircraft*, *Journal of Aircraft*, Vol. 40(1), pp. 94-99.

- [47] Love, M., H., Zink, P., S., Stroud, R., L., Bye, D., R., Chase, C., 2004, *Impact of actuation concepts on morphing aircraft structures*, Paper AIAA-2004-1724, pp. 2355-2366.
- [48] Bye, D. R., McClure, P.D., 2007, *Design of a morphing vehicle*, Paper AIAA-2007-1728, pp. 321-336.
- [49] Koma, A., Y, Zimcik, D., G., 2003, *Applications of smart structures to aircraft for performance enhancement*, CASJ, Vol. 49(4), pp. 163-172.
- [50] Flanagan, J. S., Strutzenberg, R., C., Myers, R., B., Rodrian, J., E., 2007, *Development and flight testing of a morphing aircraft, the NextGen MFX-1*, AIAA Paper AIAA-2007-1707, pp. 73-75.
- [51] Ataei-Esfahani, A., Wang, Q., 2007, *Robust failure compensation for a morphing aircraft model using a probabilistic approach*, IEEE Transactions on Control Systems Technology, Vol. 15(2), pp. 324-331, March 2007.
- [52] Andersen, G. R., Cowan, D., L., 2007, *Aeroelastic modeling, analysis and testing of a morphing wing structure*, Paper AIAA-2007-1734, pp. 359-373.
- [53] Kroo, I., Prinz, F., Eaton, J., 1999, *UAV aero-elastic control using redundant micro-actuators*, AFOSR CONTRACT No. F49620 – 99 – 1 - 0129.
- [54] De Breuker, R, Abdalla, M., Gurdal, Z., Lindner, D., 2007, *Energy-based aeroelastic analysis of a morphing wing*, Proceedings of SPIE, Vol. 6523, pp. 1-12.
- [55] Neal, D. A., Farmer, J., Inman, D., 2006, *Development of a morphing aircraft model for wind tunnel experimentation*, Paper AIAA-2006-2141, pp. 6443-6456.
- [56] Smith, K., Butt, J., von Spakovsky, M., R., Moorhouse, D., 2007, *A study of the benefits of using morphing wing technology in fighter aircraft systems*, Paper AIAA-2007-4616, pp. 1497-1508.
- [57] Love, M. H., Zink, P., Stroud, R., Bye, D., Rizk, S., White, D., *Demonstration of morphing technology through ground and wind tunnel tests*, Paper AIAA-2007-1729, pp. 337-348.

## CHAPTER 2

### OBJECTIVES AND ORIGINALITY

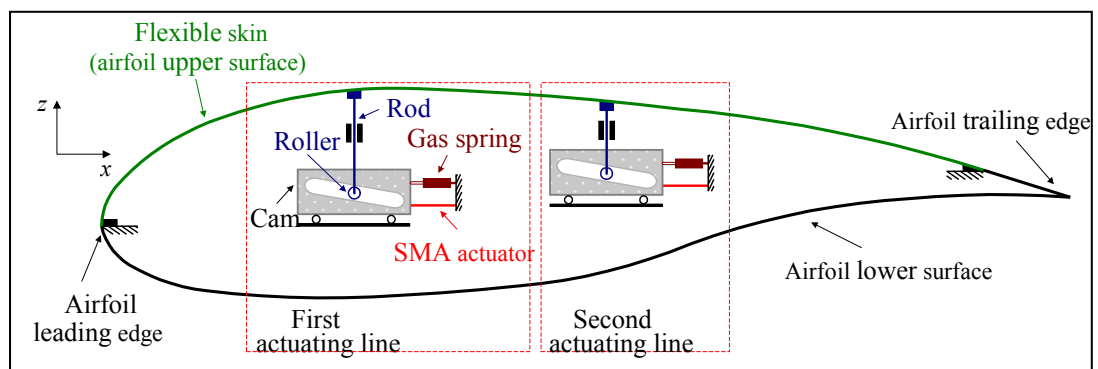
#### 2.1 The morphing wing model concept and its function

The main objective of the project is to modify the shape of the wing shape, upper flexible skin in real time in order to maintain the laminar flow on the upper surface during subsonic flight. This objective will be validated numerically by modeling and simulation in Matlab/Simulink, and experimentally, by wind tunnel tests.

The originality of this thesis consists in the integration of smart actuators and pressure sensors (optical and Kulite) with the flexible skin; it also involves the modification of the airfoil during flight using a controller for maintaining the maximum laminar flow on the wing surface.

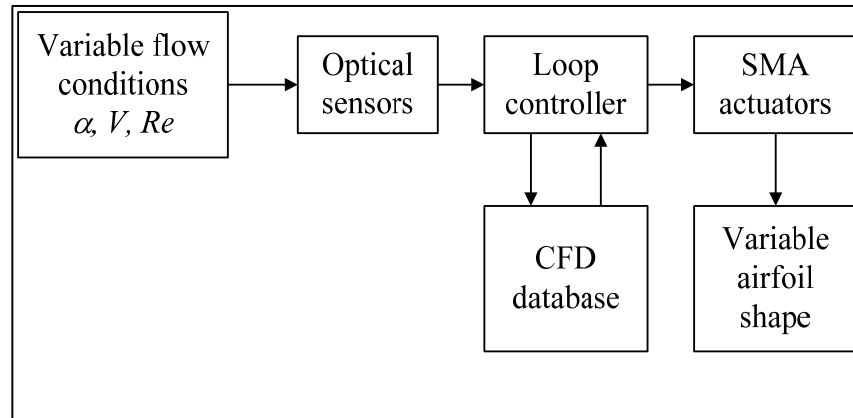
To achieve this main objective, my research aimed to develop an active controller able to change the aerodynamic airfoil shape in order to move the transition point location as close as possible to its trailing edge.

Figure 2.1 shows the mechanical schematic of the morphing wing model manufactured at ÉTS by the LAMSI team in collaboration with the IAR-NRC team.



**Figure 2.1 Mechanical schematic of the morphing wing model.**

Figures 2.2 and 2.3 show the logic schematics of the open and closed loop controllers.



**Figure 2.2** Open loop control system schematics

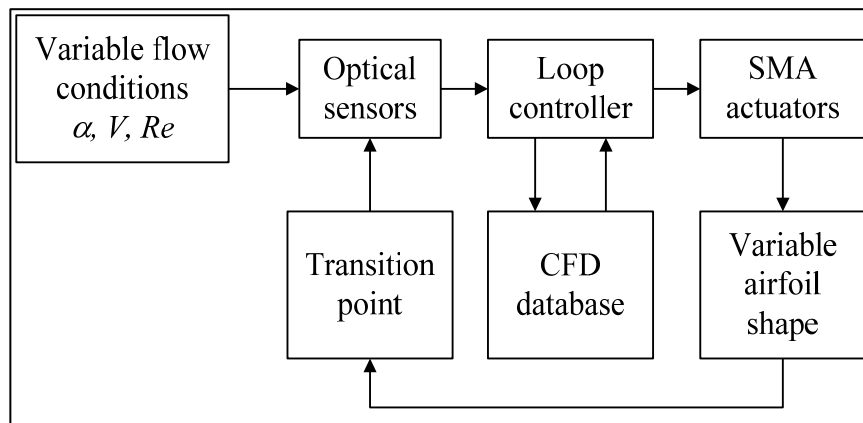


**Figure 2.3** Closed loop control system schematics

To control the transition point position through morphing of the airfoil shape, it is necessary an actuation system to change the flexible skin shape as shown in Figure 2.1. The actuators used shape memory alloys which regained their initial shape, by heating these alloys with electrical current. In our project, the actuators consisted of SMA wires that changed their lengths by heating or cooling, and by connecting or disconnecting the SMA wires to an

electrical power supply. The role of power supply command is given by a controller, which receives information about the external airflow state from a set of several optical pressure sensors. The controller compares the information received from optical sensors with the information stored in a database in the computer memory. If the controller executes the command from the information stored in the database, then the control strategy is defined as open loop, because of the fact that the controller gives no feedback about the airflow state. If the controller receives information from the sensors about the airflow state and compares it with the information stored in the database, then decisions can be made and actuators states can be adjusted and we further define the control strategy as closed loop.

My contribution in this project consists in two research objectives: to realize the main objective which is the design and the manufacturing of a closed-loop controller of the whole mechanical and electrical systems integrated into a fully automated functional system.

My first objective was to develop and test a system of sensors that receives information about the airflow state, process the valuable information and send it finally to the controller, which will make the decisions on the command of actuators states.

In the first article, a new method of detecting the boundary layer transition was developed, in which new algorithms were designed for a hypothetically array of pressure signals given by an array of pressure sensors installed on the wing upper surface. The conclusion of the article is that a minimum of 84 sensors are needed to be distributed on the 60% of the chord to detect discontinuities in pressure coefficients distributions that indicate the transition occurrence; in fact, sensors would have had 3.5 mm space intervals between them on the real wing model, or a density of 7.25 per inch chord length.

One of the most original concepts in this project was the idea of using optical sensors to read the pressure distribution over the wing model, which originated from the industrial partner Thales Aerospace. It was decided that only 16 optical sensors need to be used and 16 kulite sensors, due to financial, manufacture and available space in the prototype. In fact, the

optical sensors dimensions, their installation methods on the flexible skin and the interference between sensors and SMA wires actuators have not allowed the use a higher number of sensors on the model wing.

For this main reason (allowed number of sensors), the new method of transition detection from an array of pressure signals described in the first article was abandoned in the development of the transition detection sensory system, but still this method is original and it can be further used in subsonic flows transition detection and in shock waves detection in transonic and supersonic flows. This method is highly sensitive and requires a higher sensors density per chord length in transition detection; this method is also more robust and precise and requires a less density of sensors per chord length in shock waves detection, because the step discontinuity in the pressure coefficients distribution is higher and easier detectable.

The optical sensors were tested in the IAR-NRC wind tunnel and the signal processing methodology was described in the third article. The post-processing work of the recorded data in the wind tunnel was performed in collaboration with the Dr. M. Mamou from IAR-NRC and with the other members of the LARCASE team (Dr. Lucian Grigorie and Dr. Ruxandra Botez). The new method for pressure values corrections recorded by the optical sensors with the temperature variations in the airflow is original as my main contribution, and it can still be used in the future implementation of optical sensors (which do not have temperature corrections) on wind tunnel models or on real aircraft.

The use of optical sensors in parallel with thermocouples was preferred, and a second type of optical sensors from another company. The idea of using optical sensors was abandoned after this second try due to technological challenges and limitations as shown in the 3<sup>rd</sup> and 4<sup>th</sup> article. In fact, the second company was not able to provide the optical sensors to meet all necessary specifications values: high sampling rate for transition detection, resolution and precision.

The idea of a 16 sensors array distributed on the 70 % of the chord on the wing model remained, but only kulite sensors were installed in the following wind tunnel tests; obtained results were presented in articles 4, 6, 7 and 8.

Regarding the wind tunnel testing, the installation of the wing model in wind tunnel and the electrical supplies of actuators belong to LAMSI, IAR-NRC and LARCASE teams; in fact, LARCASE team has done the wind tunnel testing plan writing and scheduling, the sensors and controller data post-processing and installation on the wing model, and the planning of the cabling systems related to the model integration in the wind tunnel.

My main contributions are seen in the research work on the real time signal processing and its use in the controller, the control schematics architecture, the software design, simulation and visualization in real time during wind tunnel tests shown in the 4<sup>th</sup>, 6<sup>th</sup>, 7<sup>th</sup> and 8<sup>th</sup> articles.

The second objective of my research was the development of the mechanical-electrical SMA actuators controller. The mechanical and electrical design and manufacture of the entire wing model belongs to LAMSI team. The Simulink/Matlab model subroutine that simulates numerically the behavior of a SMA wire belongs to Dr. Patrick Terriault from LAMSI.

The design and simulation of the controller, presented in the 2<sup>nd</sup> article and the development of the controller presented in the 5<sup>th</sup> and 6<sup>th</sup> articles are my main contributions. The work performed during bench tests presented in the 5<sup>th</sup> article and the work performed in wind tunnel tests presented in the 6<sup>th</sup> article was done in collaboration with Dr. Teodor Grigorie at LARCASE team. The PID controller presented in the 6<sup>th</sup> article was designed by me, and the self-tuning fuzzy controller was designed by Dr. Grigorie using my simulation programs and controller architecture design. Dr. Botez is co-author of these articles, as supervisor.

The infrared measurements performed in the wind tunnel tests were the main contributions of Dr. Mamou and Dr. Mebarky from IAR-NRC in the articles 4, 6, 7 and 8.

The aerodynamic data base consisted, in pairs of actuators coordinates, which was used by the controller during bench and wind tunnel tests, and it was presented in the articles 5 and 6, as collaborative work done by both teams: École Polytechnique and LAMSI teams.

The open loop, closed loop and real time optimization control methods using high sampling rate and sensitivity pressure sensors for detecting and controlling the position of laminar-to-turbulent transition as described in the articles 6, 7 and 8 are original and never published in other scientific journals and conferences, as attested by the reviewers. These methods can be used with any types of pressure or temperature sensors such as microphones or hot films sensors respectively, and can control any type of electro-mechanical or hydraulic actuators, linear or rotary actuators, SMA wires or piezo-electric actuators, or any other types of “smart actuator”.

## CHAPTER 3

### THEORY DEVELOPPED

#### **3.1 Modeling the wind tunnel parameters and pressures and forces acting on the morphing wing airfoil estimation.**

The following section presents the methodology applied on the reference airfoil provided by IAR-NRC [1], [2]. This methodology was applied on all modified airfoils. The sub-sections of this methodology are summarized as follows:

- The original airfoil was studied using the Xfoil CFD code to obtain the aerodynamic coefficients (lift, drag and pressure) and the transition point position as a chord percentage. Simulation results were validated with the experimental values obtained by IAR-NRC in the wind tunnel tests using the original airfoil wing model.
- The morphed airfoil was obtained by defining the flexible skin as a *B*-spline curve and the new contour of the airfoil obtained by unifying the *B*-spline with the original airfoil, which was studied using the Xfoil CFD code in order to obtain the aerodynamic coefficients (lift, drag and pressure) and the transition point position as a chord percentage.
- The pressure coefficient distribution was used to calculate the forces concentrated at the actuating points, estimating the force magnitude and variation domain of the SMA actuators.

##### **3.1.1 Validation of the Xfoil CFD code by use of experimental data from wind tunnel tests on the original airfoil WTEA.**

The first step in the project was to choose an original laminar airfoil, whose shape had to be modified in order to obtain the transition point as close to the trailing edge as possible. This choice was made in collaboration with the IAR-NRC; that provided the coordinates of the laminar airfoil WTEA (see figure 3.1) and the experimental results obtained by wind tunnel tests for two flow cases:

- Mach number = 0.2 and Reynolds number = 6 million;
- Mach number = 0.25 and Reynolds number = 2 million.

Figure 3.1 shows the coordinates of the theoretical airfoil optimized for laminar flow conditions in transonic speed (Mach number = 0.7) and experimental coordinates obtained by scanning the aluminum manufactured wing model used in the wind tunnel.

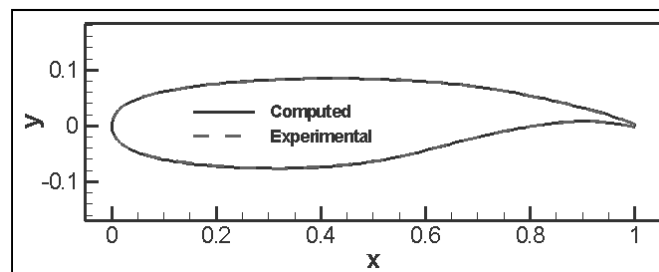


**Figure 3.1 The normalized coordinates of the original laminar airfoil WTEA.**

The aerodynamic analysis of the original laminar airfoil was obtained by using the airfoil experimental coordinates in the CFD code XFOIL [3, 4].

Figure 3.2 and 3.3 show the numerical results ( $C_L/C_D$  the polar curve,  $C_L/\alpha$  curve,  $x_{tr}$  transition point position on the chord and  $C_p$  distribution) versus experimental results obtained in wind tunnel tests for the two flow cases provided by IAR-NRC.

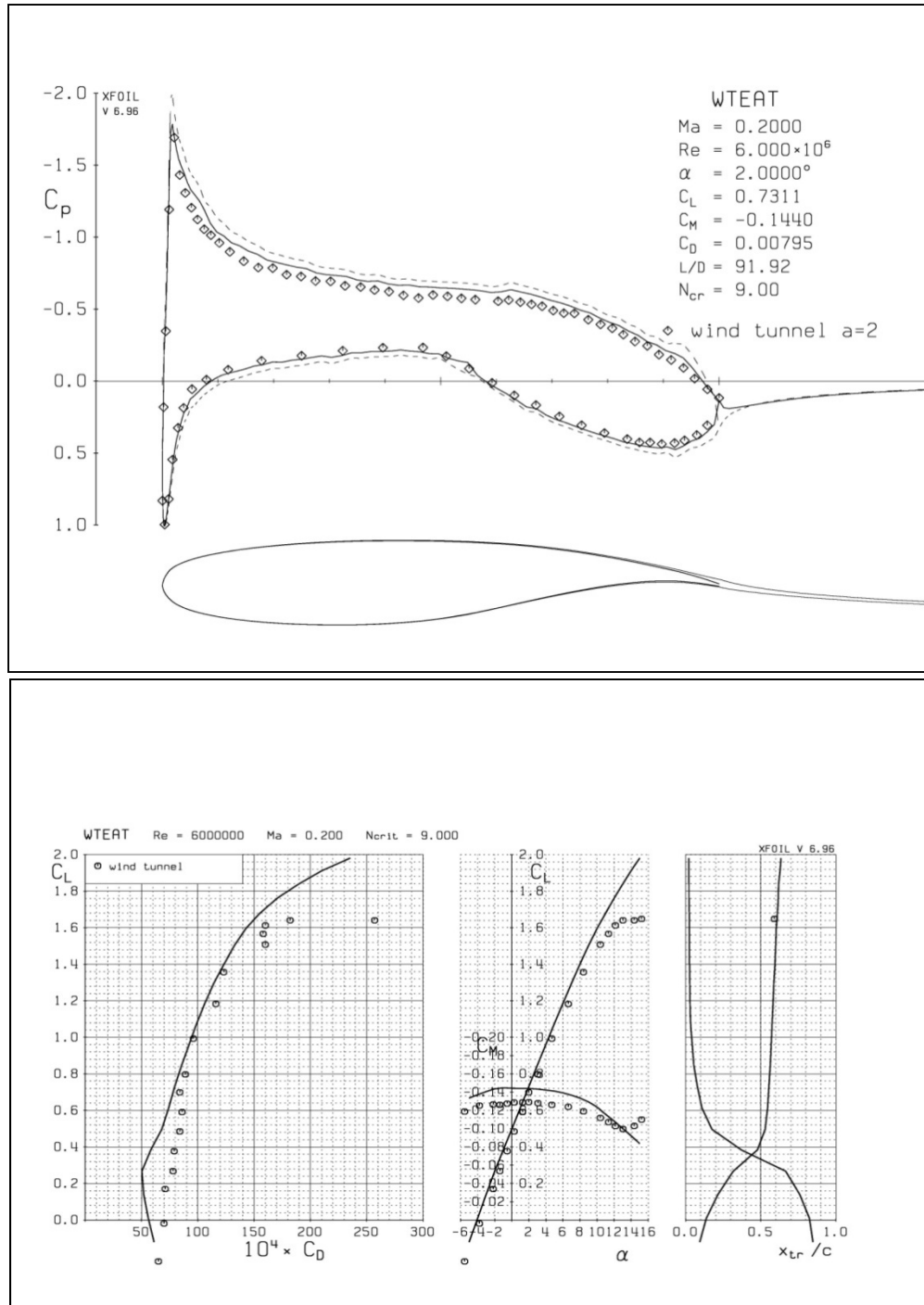


**Figure 3.2** Validation of the numerical values (continuous line) obtained by XFOIL using experimental values (dots) obtained during wind tunnel tests for the original airfoil WTEA for the flow case Mach number = 0.2 and Reynolds number = 6 million.

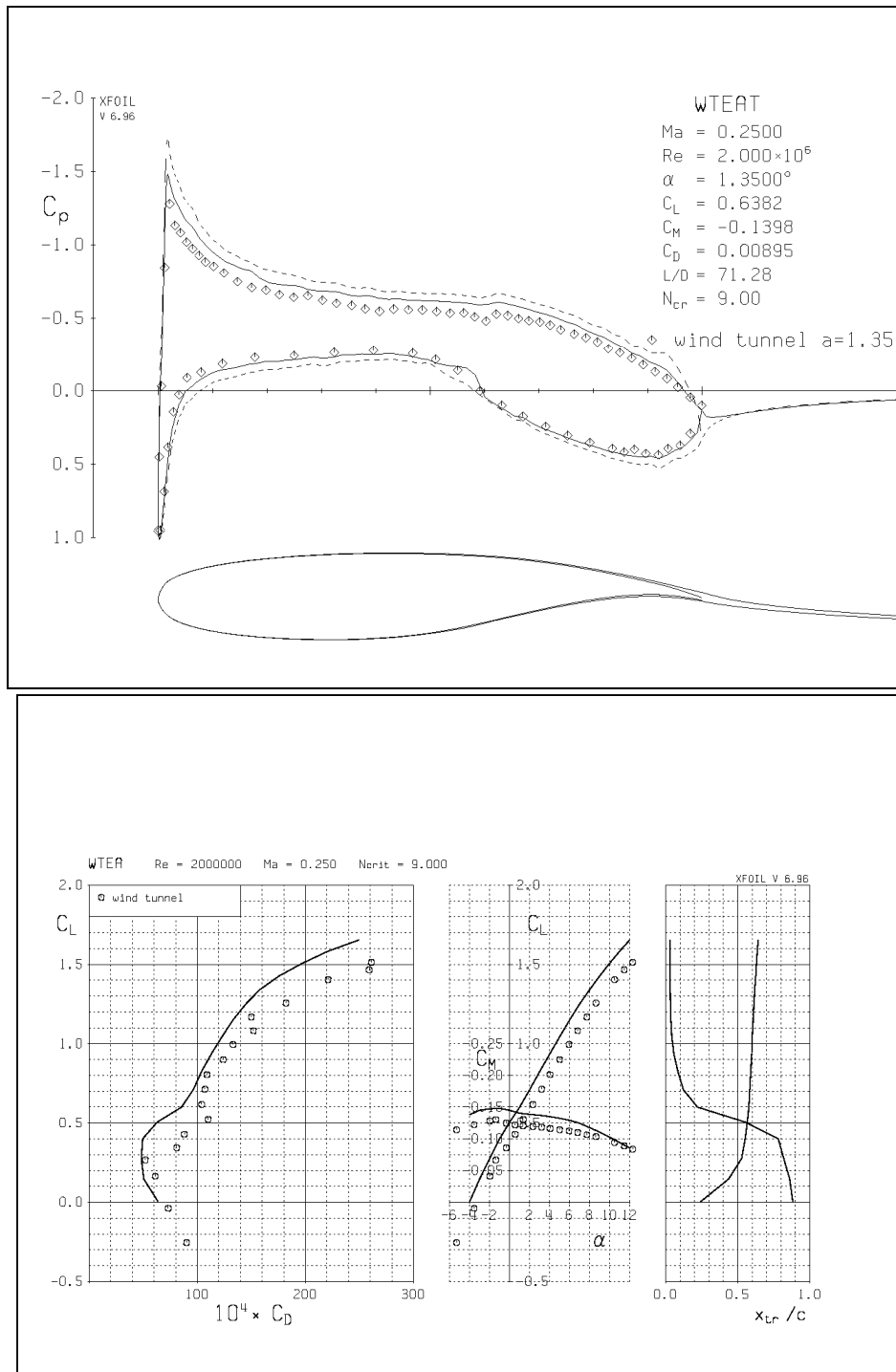


**Figure 3.3** Validation of the numerical values (continuous line) obtained by Xfoil using experimental values (dots) obtained during wind tunnel tests for the original airfoil WTEA for the flow case Mach number = 0.25 and Reynolds number = 2 million.

### 3.1.2 Aerodynamic analysis of the modified airfoils by use of XFOil

Given the peak pressure distribution in the leading edge area and the challenges in the technological manufacture of the composite flexible skin, the École Polytechnique team decided to define the flexible skin area between 7% and 65% of chord on the wing upper surface.

The LAMSI team decided to modify the original airfoil WTEA using B-spline curves, with one control point and two fixed points (the joints of the flexible skin on the wing fixed structure). In the control point A, which was defined at the middle of the interval  $[0.07\ c\ 0.65\ c]$ , as shown in Figure 3.4, an actuator capable of changing the vertical point position, was to be installed. The modified airfoils with a 50 cm chord obtained for several vertical displacements of  $\pm 20$ ,  $\pm 16$ ,  $\pm 12$ ,  $\pm 8$ ,  $\pm 5$ ,  $\pm 3$ ,  $\pm 1.5$ ,  $\pm 0.5$  and 0 mm are shown in Figure 3.4. The idea behind studying the morphing airfoil with a single control point was to estimate the preliminary forces values that act upon the actuator for different airflow conditions.

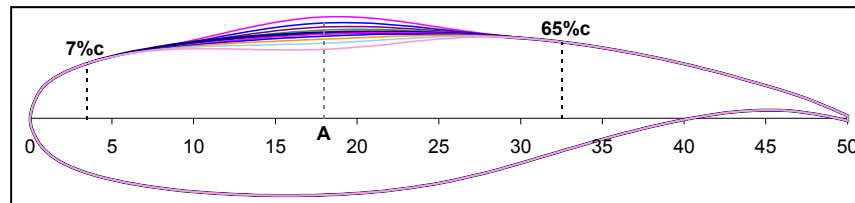


**Figure 3.4** Modified airfoils obtained by combining the original airfoil WTEA with B-Spline curves with a single control point A in the middle of the interval 7% to 65% of the chord.

The LARCASE team built an automatic control system in closed loop. To that end, a database of modified airfoils for different airflow conditions characterized by angles of attack  $\alpha = -2^\circ$ ,  $-1^\circ$ ,  $1^\circ$ ,  $2^\circ$  and  $3^\circ$  and Mach number constants between  $M=0.1$  and  $0.3$  was conceived. This database (containing pressure coefficients  $C_p$ , aerodynamic coefficients  $C_L$  and  $C_D$  and transition position on the chord  $x_{tr}$ ) was used in designing the controller. The final database was built by the LAMSI and École Polytechnique teams using more complex

computational methods, but for the purpose of the design of the controller in the appropriate time, the LARCASE team built its own codes and database using XFOil, which were validated with experimental results, as shown in paragraph 3.1.1.

An aerodynamic analysis was performed for various combinations of Mach numbers and angles of attack using XFOil to obtain the effect of the airfoil changing shape on the boundary layer flow and the transition trigger. Figure 3.5 shows an example of pressure distribution calculated by XFOil for Mach number  $M = 0.3$ , angle of attack  $\alpha = -1^\circ$  and Reynolds number  $Re = 3.36$  million.

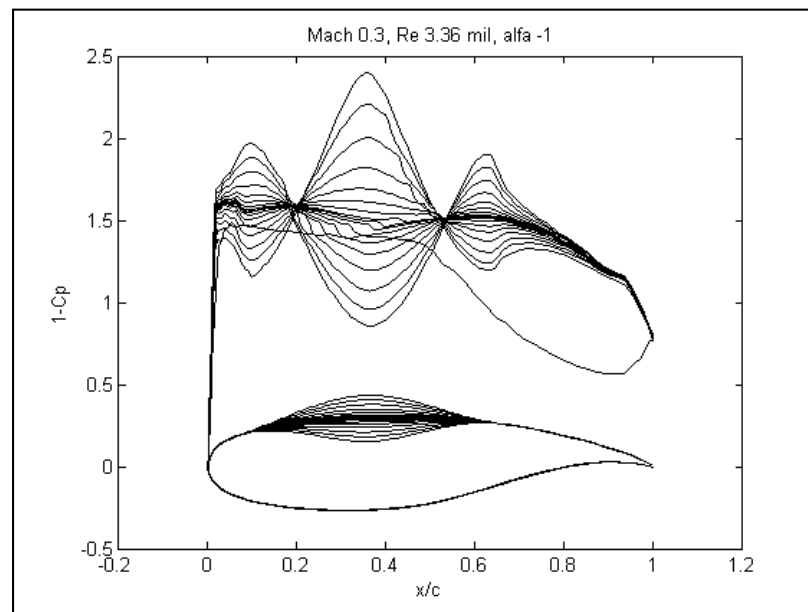


**Figure 3.5** Pressure distributions around the modified airfoils for one airflow case characterized by Mach number  $M = 0.3$ , angle of attack  $\alpha = -1^\circ$  and Reynolds number  $Re = 3.36$  million.

We plotted the variations of the transition point position  $x_{tr}$  calculated with XFOil (Figure 3.6), the lift coefficient (Figure 3.7), the drag coefficient (Figure 3.8) and the slenderness factor (Figure 3.9) with the vertical displacement of the control point A. These variations were calculated for the modified airfoils for the airflow conditions Mach number  $M = 0.3$  and Reynolds number  $Re = 3.36 \times 10^6$ .

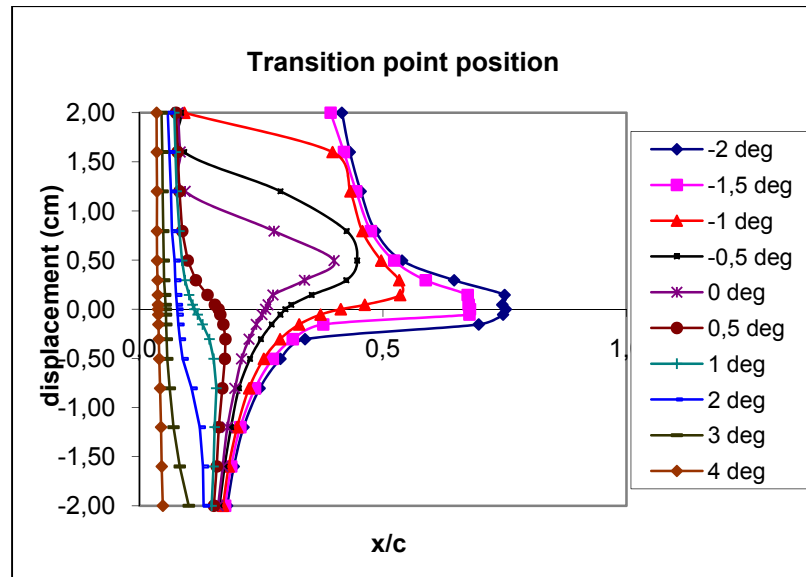


**Figure 3.6** Transition point position variation for different vertical displacements of control point A and different angles of attack for the airflow case of  $M = 0.3$  and  $Re = 3.36$  million.

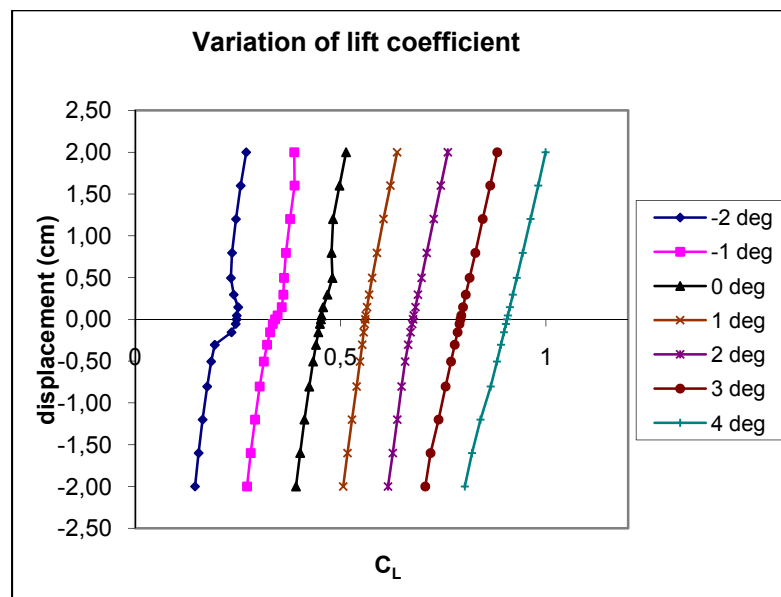


**Figure 3.7** Lift coefficient variation for different vertical displacements of control point A and angles of attack for the airflow case of  $M = 0.3$  and  $Re = 3.36$  million.

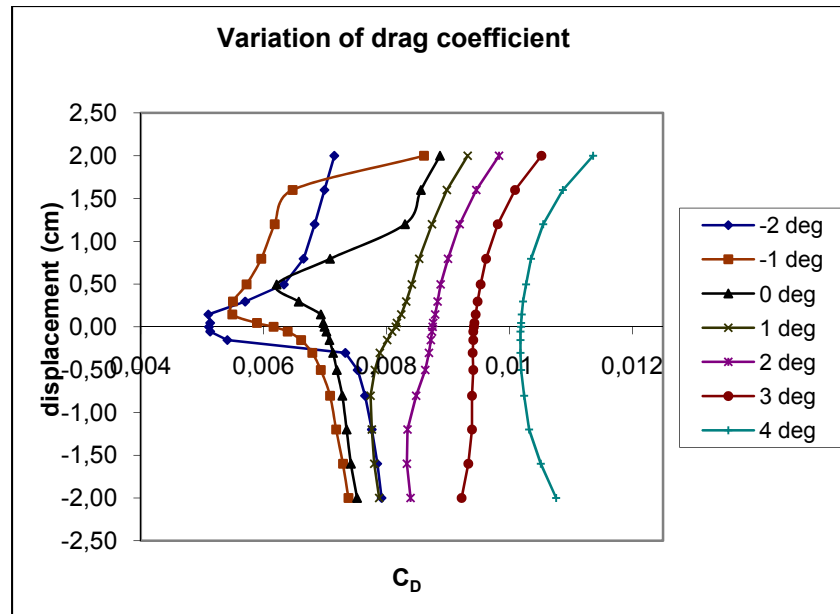


**Figure 3.8** Drag coefficient variation for different vertical displacements of control point A and angles of attack for the airflow case of  $M = 0.3$  and  $Re = 3.36$  million.

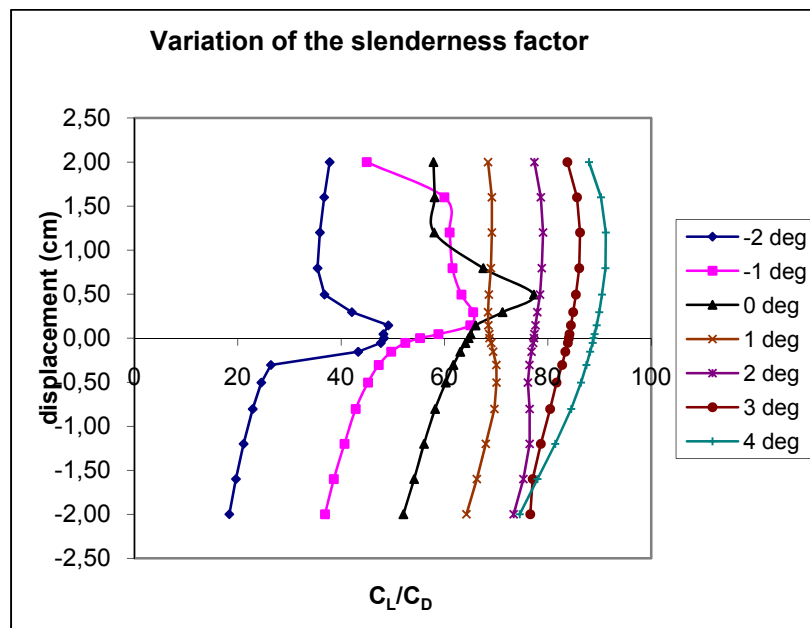


**Figure 3.9** Slenderness factor variation for different vertical displacements of control point A and angles of attack for the airflow case of  $M = 0.3$  and  $Re = 3.36$  million.

Results shown in Figures 3.6 to 3.9 showed that the morphing effect of 5 mm displacement at  $0^\circ$  angle of attack has a reduction of drag coefficient of 0.001 (from 0.007 to 0.006 see Figure 3.8) which is due to a movement of transition point of 15% of the chord (from  $0.25c$  to  $0.4c$ ; see Figure 3.6). This shape change resulted in the improvement of the slenderness factor by 20% (from 65 to 78 see Figure 3.9).

The next section details the computation of wind tunnel aerodynamic characteristics used in our validations.

### 3.1.3 Computation of the aerodynamic characteristics in wind tunnel and estimation of the forces acting on the flexible skin during wind tunnel tests.

To compute the pressure distribution and aerodynamic coefficients on the original and modified airfoils, we need to simulate the same airflow conditions (pressure, airspeed and temperature) that exist in the non pressurized  $3 \text{ m} \times 2 \text{ m}$  subsonic wind tunnel at IAR-NRC.

The airflow conditions in this type of wind tunnel are always the same as the standard atmosphere, with the exception of several corrections factors, next explained.

The static air temperature considered in the wind tunnel was  $T_{0wt} = 15^\circ\text{C} = 288.15 \text{ K}$ , the air density  $\rho_{0wt} = 1.225 \text{ kg/m}^3$  and the total pressure  $p_T = 101.35 \text{ kPa}$ . For an airspeed equivalent to Mach number  $M = 0.3$ , the airflow temperature needs to be corrected using the following formula [5]:

$$T_{wt} = \frac{T_{0wt}}{1 + \frac{(k-1)}{2} M^2} = 283.06 \text{ K} \quad (3.1)$$

where  $k = 1.4$  is the air adiabatic coefficient. The airspeed is obtained with the following equation [5]:

$$V = M \cdot a = M \sqrt{kRT_{wt}} = 101.2 \text{ m/s} \quad (3.2)$$

where  $R = 287.0529 \frac{\text{Nm}}{\text{kgK}}$  is the gas constant and  $a$  is the speed of sound in the air.

The same types of corrections were made to the air density  $\rho_{wt}$  and air viscosity  $\mu_{wt}$  as follows [5]:

$$\rho_{wt} = \frac{\rho_{0wt}}{\left(1 + \frac{k-1}{2} M^2\right)^{\frac{1}{k-1}}} = 1.172 \text{ kg/m}^3 \quad (3.3)$$

$$\mu_{wt} = 1.458 \cdot 10^{-6} \frac{T_{wt}^{1.5}}{T_{wt} + 110.4} = 1.7647 \cdot 10^{-5} \text{ Pa} \cdot \text{s} \quad (3.4)$$

The following values were used in computing the dynamic pressure of the upstream wind  $Q_\infty$  and Reynolds number  $\text{Re}$  [5]:

$$Q_\infty = \frac{\rho_{wt} V^2}{2} = 5996.9 \text{ Pa} \quad (3.5)$$

$$\text{Re} = \frac{\rho V}{\mu} c = 3.36 \cdot 10^6 \quad (3.6)$$

where  $c = 0.5 \text{ m}$  is the airfoil chord of the wing model that will be tested in wind tunnel.

The dynamic pressure value in wind tunnel is needed for estimating the forces acting on the flexible skin during tests. Figure 3.10 shows an example of a pressure coefficient distribution plot on the surface of the airfoil. The dynamic pressure distribution from Figure 3.11 is

calculated with the equation (3.9) where the  $C_p$  distribution from Figure 3.10 and the value of  $Q_\infty$  calculated with the equation (3.5) are used. The pressure is calculated on the flexible skin region between 7% and 65% of the chord.

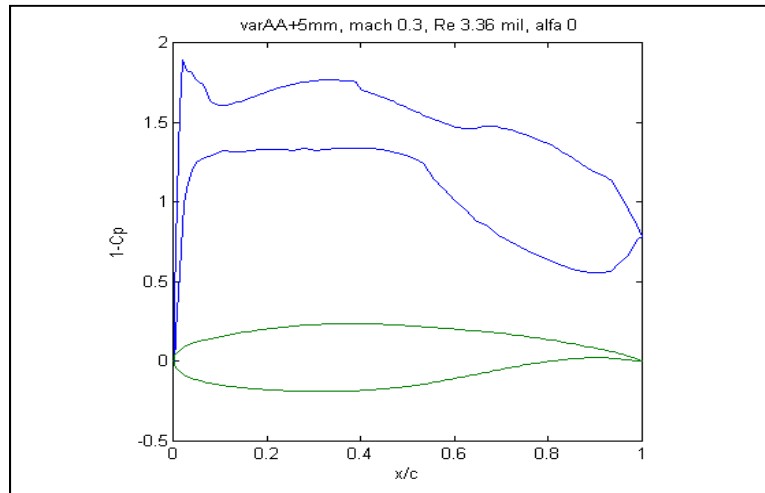


**Figure 3.10** Pressure distributions for the modified airfoil with a control point A vertical displacement of +5 mm.

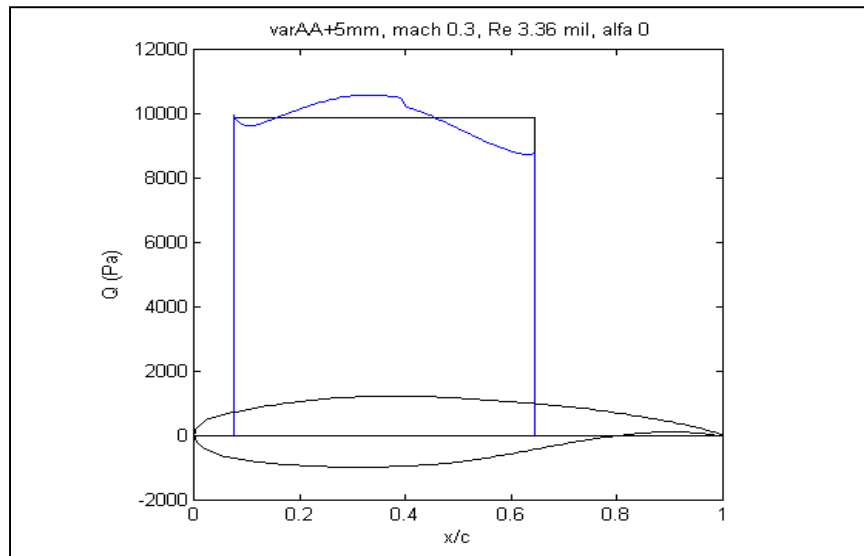


**Figure 3.11** Local dynamic pressure over the flexible skin estimation by calculating the area integral under the  $Q$  values plot.

The pressure coefficient is defined with the following equation [5]:

$$C_p = \frac{p - p_\infty}{Q_\infty} \quad (3.7)$$

Where  $Q_\infty$  is calculated by equation (3.5),  $p$  is the static pressure on the flexible skin surface and  $p_\infty$  is static pressure of the airflow far upstream.

The pressure that acts on the flexible skin is the difference between static pressure on the surface of the skin and the static pressure inside the cavity of the airfoil, where the air is considered static and the pressure is the same as standard air pressure.

In this type of wind tunnel, the total pressure of the airflow is generally equal to the static air atmospheric pressure, and therefore the pressure inside the cavity is equal to the total pressure outside the flexible skin.

This assumption was proven to be wrong in the wind tunnel tests because the wing model was not sealed, and in fact, there was an air flux between the outside and inside of the flexible skin, which reduced its estimated value by 50%.

The total pressure definition is shown in the following equation (3.8):

$$p_T = p_\infty + Q_\infty \quad (3.8)$$

The pressure variation  $\Delta p$  was calculated by use of equations (3.7) and (3.8):

$$\begin{aligned} \Delta p &= p - p_{atm} = p - p_T = p_\infty + Q_\infty C_p - p_\infty - Q_\infty \\ \Delta p &= Q_\infty (C_p - 1) \end{aligned} \quad (3.9)$$

Finally, the total force acting on the flexible skin was calculated using the equivalent area under the  $Q$  distribution plot equation, as shown in Figure 3.11. This force is considered as applied in the middle of the interval  $x = 7\% - 65\%$ , which corresponds to the area gravity center formed by the flexible skin pressure as follows:

$$F = \sum \Delta p_i \cdot \Delta x_i \quad (3.10)$$

We estimated the force value applied on the flexible skin of 2879 N/m of the span length of the airfoil modified with a control point vertical displacement of 5 mm in airflow conditions with Mach number = 0.3, Reynolds number = 3.36 million and angle of attack  $\alpha = 0^\circ$ . For a total span of 1.2 m, the total suction force acting on the flexible skin has a value of 3455 N.

These estimated values were used by the LAMSI team to design the flexible skin's SMA actuators characteristics. This method was implemented in the simulation under the Matlab/Simulink environment in order to simulate the acting force on the SMA theoretical model, given to us by Prof. Patrick Terriault from LAMSI.

### **3.2 Modeling the dynamic pressure signal and transition position measured using optical sensors**

The transition from laminar flow to turbulent flow must be measured and localized on the airfoil skin, and to that end, a set of sensors had to be installed on the flexible skin. The challenges encountered arose from the fact that normally, the theory built around turbulence uses the velocity of the air particles as a physical means, while the optical sensors technology obliged us to use the local pressure of air particles. The following theoretical considerations explain the mathematical reasons behind physical phenomena of the air flowing past the airfoil and the physical means that are measured by sensors.

### 3.2.1 Modeling the turbulent flow by Gaussian distribution

It is well known that turbulent flow is always characterized by the random numbers law with a Gaussian distribution characteristic. The mean value of velocity  $U$  and the instant value of velocity  $\tilde{U}$  are recorded in a time interval  $T$ :

$$U = \frac{1}{T} \int_0^T \tilde{U} dt \quad (3.11)$$

$$\tilde{U} = U + u \quad (3.12)$$

where  $u$  is the instant fluctuation of velocity with respect to the mean value [6]. The mean value of the velocity fluctuations is zero if the airflow is stationary:

$$\bar{u} = \frac{1}{T} \int_0^T u dt = 0 \quad (3.13)$$

To measure the quantity or the magnitude of these fluctuations, the root mean square (RMS) is used. The RMS of the velocity fluctuations are defined as follows:

$$u_{RMS} = \sqrt{\overline{u^2}} = \sqrt{\frac{1}{T} \int_0^T u^2 dt} \quad (3.14)$$

The RMS of velocity fluctuations has the physical meaning of the standard deviation of the randomly velocity values recorded as a Gaussian distribution. While turbulence is not purely random, however, the Gaussian distribution is respected [6].

In Figure 3.12, a typical record of turbulent signal sampled at 5 kHz in the Onera S1 wind tunnel is shown, as is the Gaussian distribution of the same signal at different times [7].

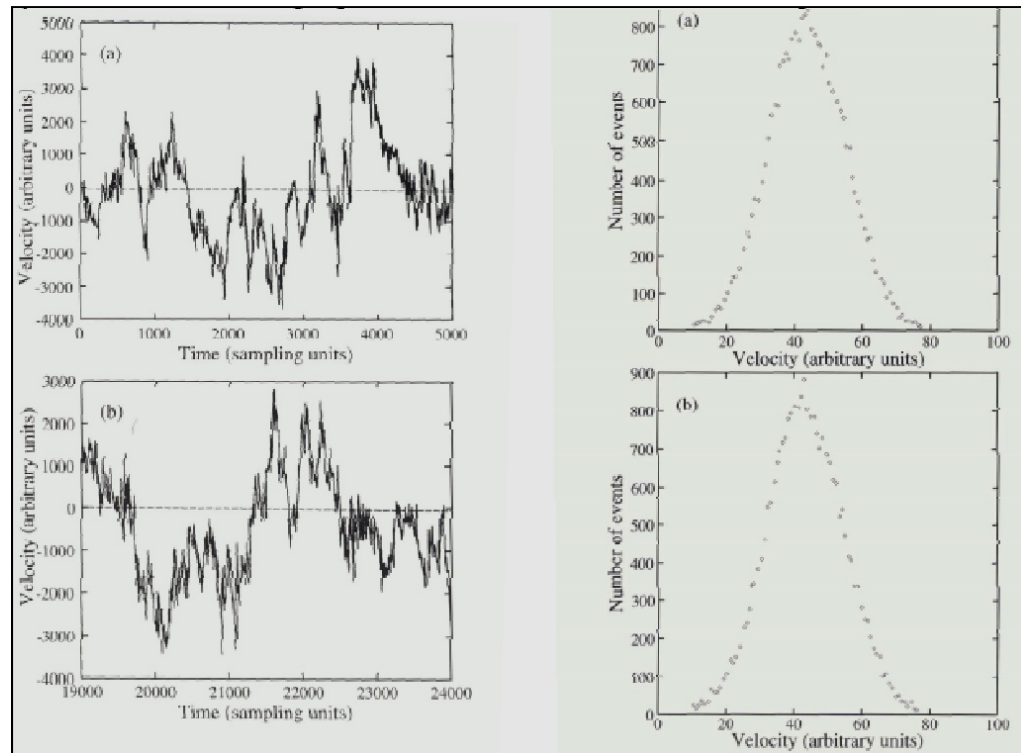


**Figure 3.12** Turbulent signal of wind flow recorded in 1 sec sampled at 5 kHz (up), and the same signal at 3 seconds later (down) [7].

### 3.2.2 Equivalences between noise level and velocity RMS in the wind tunnel

The airflow on the boundary layer over an airfoil has a certain kinetic energy while flowing in laminar layers. Because of friction encountered with the airfoil wall, some of the energy is lost through heat convection, leading to the air heating. This lost kinetic energy has an effect on the potential energy of the flow, which is represented by the stagnation pressure as well as on the flow which become turbulent. The kinetic energy lost by the airflow due to turbulent flow occurrence is equal to the increase in stagnation pressure.

The mean kinetic energy of the turbulent flow in volume unit is defined by equation [6]:

$$\begin{aligned}\overline{ke} &= \frac{1}{2} \rho \left[ \overline{(U+u)^2 + (V+v)^2 + (W+w)^2 - (U^2 + V^2 + W^2)} \right] \\ \overline{ke} &= \frac{1}{2} \rho (\overline{u^2} + \overline{v^2} + \overline{w^2}) \equiv \frac{1}{2} \rho \overline{q^2}\end{aligned}\quad (3.15)$$

The turbulent flow intensity is defined as:

$$\sigma = \frac{1}{U_\infty} \sqrt{\frac{1}{T} \int_0^T \frac{1}{3} (u^2 + v^2 + w^2) dt} \quad (3.16)$$

Where  $U, V, W$  are the mean values of the velocity vectors in all three space directions  $x, y, z$  and  $u, v, w$  are the instant velocity fluctuations.

In a wind tunnel the mean value of instant velocity fluctuations are equal in all three space directions, while the turbulence intensity  $\sigma$  has the same value as the RMS of the kinetic energy given by the following equation [6]:

$$\sigma (\%) = \frac{100}{U_\infty} \sqrt{\frac{\overline{q^2}}{3}} \equiv \frac{100}{U_\infty} \sqrt{\overline{u^2}} = 100 \frac{u_{RMS}}{U_\infty} \quad (3.17)$$

We estimated that for an airflow of  $U_\infty=101$  m/s ( $M = 0.3$ ) in the IAR-NRC 2 m  $\times$  3 m wind tunnel, which has a turbulence intensity  $\sigma = 0.16\%$  the magnitude of fluctuations are  $u_{\infty RMS} = 0.16$  m/s which is equivalent to a  $p_{\infty RMS} = 6.5$  Pa. This value was estimated in terms of sound decibel dB Sound Pressure Level (SPL), using equation (18), [8]:

$$p_{\text{dB(SPL)}} = 20 \cdot \log_{10} \left( \frac{p_\infty}{2 \cdot 10^{-5} \text{ Pa}} \right) = 110 \text{ dB(SPL)} \quad (3.18)$$

This value is equivalent to the value obtained in the Virginia Technology Stability Wind Tunnel, where the noise level of the wind tunnel was recorded at 109 dB(SPL) for an intensity turbulence level of 0.10% [9].

The estimations are also required to validate the simulations of the wind tunnel conditions using XFOIL. Figure 3.14 shows an image result of the preliminary wind tunnel test performed in the IAR-NRC 2 m × 3 m wind tunnel. The tested wing model had an NACA 4415 airfoil with a chord  $c = 1.5$  ft (0.4572 m) and a span  $b = 3.87$  ft (1.2 m). The wind speed during testing was  $U_\infty = 65$  m/s, Mach number  $M = 0.191$ , Reynolds number  $Re = 2$  million at static atmosphere temperature  $T = 15^\circ\text{C}$  and the angle of attack was  $\alpha = 0^\circ$ . The test was performed in order to visually detect the transition location on the airfoil chord for several angles of attack values and to determine the optimum position of the optical sensors on the upper surface of the wing.

Figure 3.15 shows the results of the wind tunnel test simulation using XFOIL code. The results are expressed in terms of  $C_p$  coefficients and normalized frequencies and amplitudes of turbulent spectra around the airfoil. Critical value  $N_{crit}$  used by XFOIL for calculating the transition position is defined by the empirical equation [10]:

$$N_{crit} = -8.43 - 2.4 \ln \sigma = 7 \quad (3.19)$$

where  $\sigma$  is the turbulent flow intensity.

After the estimation of the pressure fluctuations values in the upstream airflow, we considered these as initial oscillations that amplify when in contact with the airfoil wall as a result of friction. Using this hypothesis, we estimated that the pressure signal amplitudes  $A$  in transition by use of the decision equation of XFOIL code for transition position [3], [4]:

$$A = A_0 \cdot e^N \quad (3.20)$$

Where  $A_0$  is the initial amplitude and  $N=N_{crit}$ .

The estimated values of the velocity fluctuations amplitudes in transitional flow are multiplied by the value  $e^7=1097$ , which means they are 1000 times greater than the background wind tunnel turbulence level.

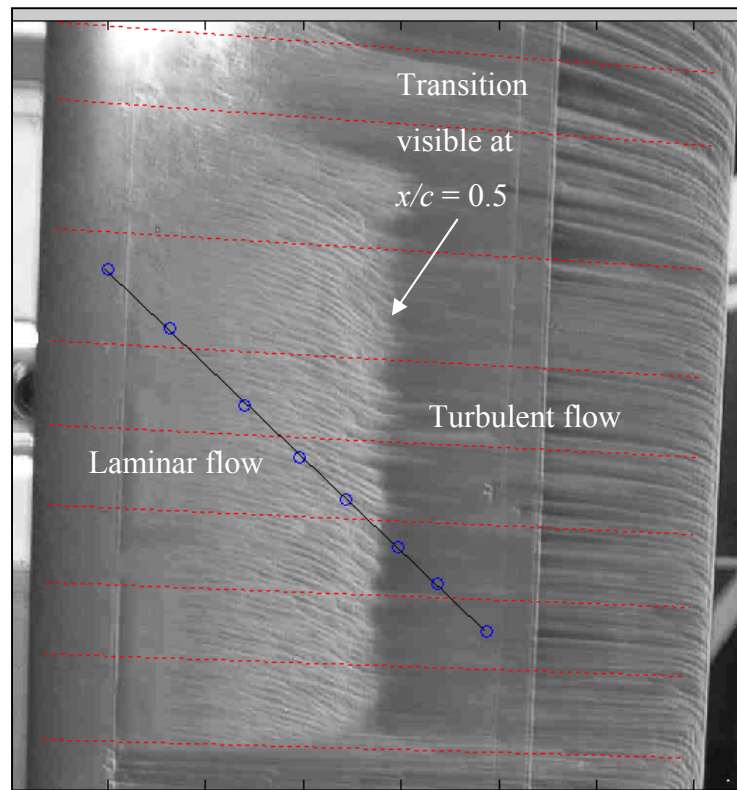


**Figure 3.13** Image of the transition from laminar to turbulent flow evidenced by fluorescent oil in UV light on the upper surface of a wing model with NACA 4415 airfoil in the IAR-NRC wind tunnel.

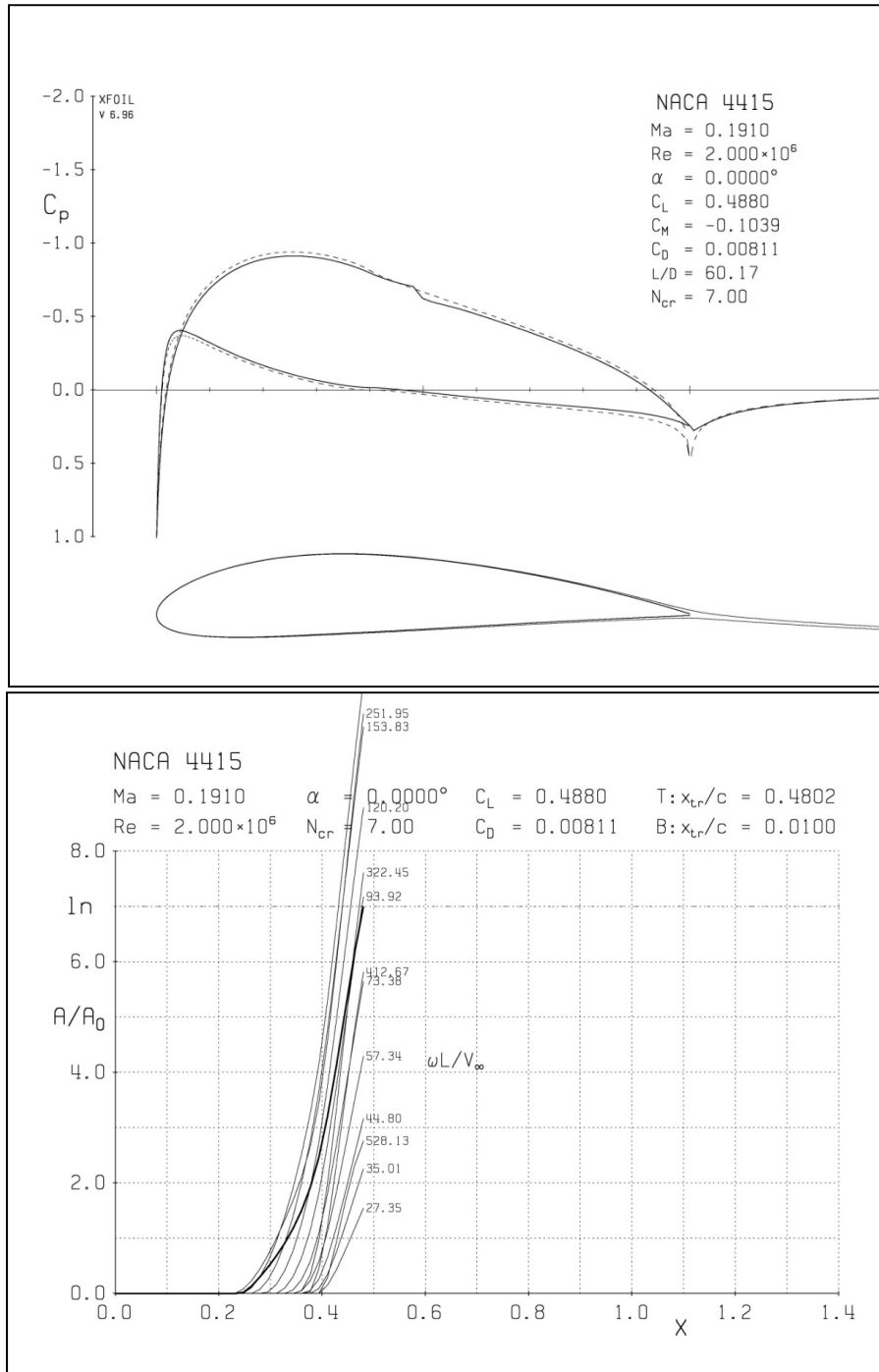


**Figure 3.14** Validation of the wind tunnel tests transition detection using XFOil code, which predicts the  $x_{tr}$  position and the estimated frequencies of the turbulent flow

### 3.2.3 Modeling and simulation of the optical sensors measurements

Now that we have estimated the noise level in the laminar, transition and turbulent flow, we will further estimate the characteristics of optical sensors needed to measure the flow states in order to gain information about their dynamics.

We suppose that the test will be performed at the incidence of 2 degrees, and on the model, one sensor will be installed at the 20% position of the chord in the laminar flow and another at the 55 % position of chord in the turbulent flow (see Figure 3.16).

Figure 3.16 shows the dynamic pressure distribution on the upper surface of the airfoil and the value of the dynamic pressure measured by these optical sensors:

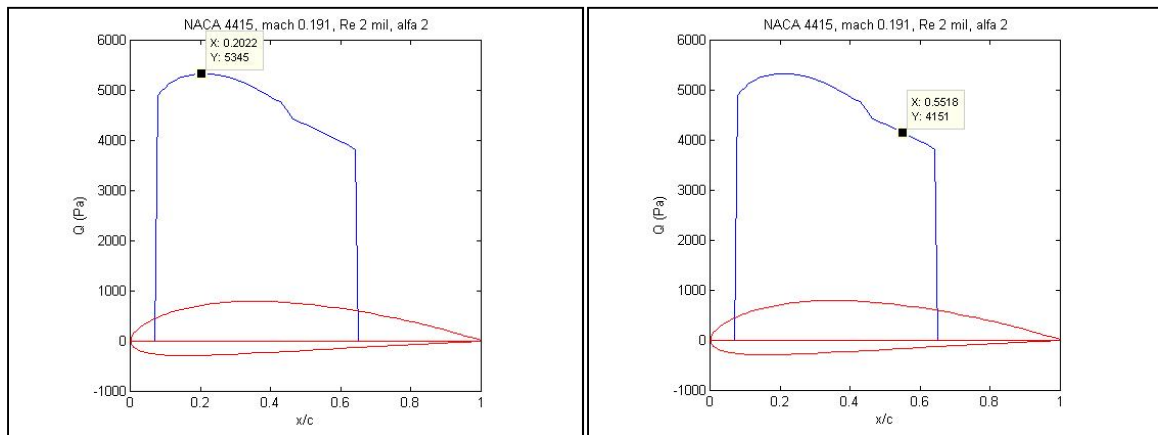


**Figure 3.15** The dynamic pressure distribution on the airfoil upper surface

The sensor in the **laminar flow** measures a dynamic pressure of 5345 Pa which corresponds to a flow velocity of about 94 m/s (calculated with a corrected value  $\rho = 1.2029 \text{ kg/m}^3$  for Mach number = 0.191).

The sensor installed downstream of the transition point, measures the fluctuations of the dynamic pressure of the **turbulent flow**.

To carry out a computer simulation, we need to have an idea of the magnitudes of the fluctuations. For moderate flow velocities not much higher than 100 m/s, relevant values of turbulent fluctuations are roughly 10% of average velocity, and are between 0.01 and 10 m/sec. Turbulence frequencies vary from 1 Hz to 10 kHz [6].

$$\begin{aligned} U &= 83 \text{ m/s} & Q &= 4151 \text{ Pa} \quad (0.602 \text{ psi}) \\ u_{\max} &= 8.3 \text{ m/s} & q_{\max} &= 41.5 \text{ Pa} \quad (0.006 \text{ psi}) \end{aligned} \quad (3.21)$$

where  $u_{\max}$  and  $q_{\max}$  are the maximum values of fluctuations. The maximum oscillation value of velocity should be 10% of the flow speed, which corresponds to a maximum pressure oscillation of 1% of the mean pressure value. The values measured by the sensor should be found in the interval  $[Q - q_{\max} \div Q + q_{\max}] \equiv [4110 \div 4190] \text{ Pa}$  or approximately 0.6 psi.

A rough estimation of the pressure values that sensors should measure is shown in Table 3.1:

Table 3.1 Pressure values estimation of optical sensors

<b>Mach</b>	<b>Air speed</b> $U_{\infty}$	<b>Dynamic pressure</b> $q$	<b>static pressure</b> $p (C_p = 0)$	<b>Speed fluctuations</b> $\Delta V$	<b>Pressure fluctuations</b> $\Delta p = \Delta q$
0.2	68 m/s 223 ft/s	0.42 psi	14.28 psi	6.8 m/s	0.004 psi
0.3	105 m/s 344 ft/s	0.98 psi	13.7 psi	10.5 m/s	0.0098 psi

Two types of optical sensors provided by two companies, FISO and OPSENS, were compared in this study:

- OPSENS OPP A/B
  - Range: 0 to 15 psia (absolute pressure reading)
  - Resolution: <0.01% full scale (0.0015 psi)
  - Sampling rate : 1000 Hz
- FISO FOP-MS
  - Range: 0 to 5 psid (differential pressure reading)
  - Resolution: 0.1% full scale (0.005 psi)
  - Sampling rate : 1000 Hz

The problem which arises is determining what is the smallest turbulent signal the sensor is capable to sense. In other words, what is the smallest amplitude of oscillation of a random signal when the sensor does not read any peak? Table 3.2 show the minimum signal level the sensors are capable of measuring, by the sensor characteristics:

Table 3.2 Minimum SPL detectable by optical sensors

<b>Resolution</b>	<b>Minimum SPL (dB)*</b>
34 Pa (0.005 psi)	124 dB
10.3 Pa (0.0015 psi)	114 dB

\* NOTE: The Sound Pressure Level is defined as the magnitude of the sound level with respect to the minimum pressure felt by human hearing of 2e-5 Pa.

The definition of decibel (dB) is:

$$X_{dB} = 20 \cdot \log_{10} \left( \frac{A}{A_0} \right) = 10 \cdot \log_{10} \left( \frac{A^2}{A_0^2} \right) \quad (3.22)$$

Where  $A$  is the amplitude of signal oscillations and  $A_0$  is the reference amplitude.

By this definition we estimate that the noise of the turbulent signal should be roughly 20-30 dB above the background noise level which we'll consider the laminar flow signal. The values estimated in Table 3.2 compared with the values of background noise estimated by the equation (3.18) show that these sensors would be at the minimum limit of turbulent signal detection.

Measurements in wind tunnel using microphones showed that the sound pressure signal must be analyzed through spectral decomposition by FFT in order to remove the background noise that covers the meaningful signal which shows the occurrence of Tolmienn-Schlichting waves. The Tolmien-Schlichting waves appear in the 1 kHz frequency band and are responsible for inducing the turbulent flow. It was proved experimentally that transition occurrence is directly linked to the occurrence of Tolmien-Schlichting waves, which have different frequency bands according to the airflow type. As shown in Figure 3.17, for a sensor installed in the position where the air flow is laminar, the signal spectra shows a small spectral distribution like a hump in a frequency band between 500 Hz and 1500 Hz. The hump increases in width band and in high (magnitude of the oscillation signal) while the transitional flow becomes turbulent and remains turbulent until the hump disappears, which shows that the airflow is fully turbulent [11].

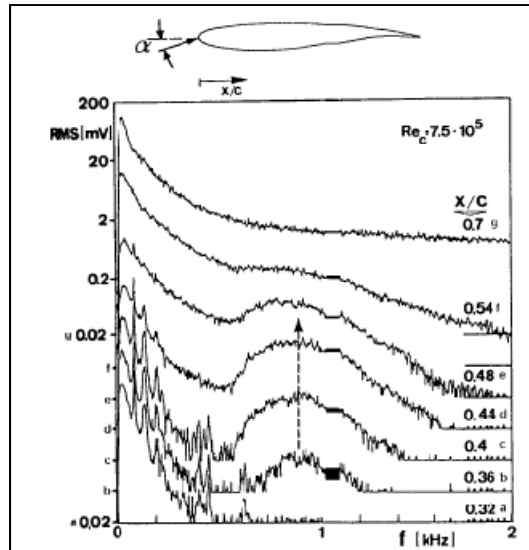


**Figure 3.16** Measurements using microphones in wind tunnel of the transition occurrence over an airfoil [11]

The XFOIL code was used to simulate the possible frequencies that the transition signal would have. As shown in Figure 3.15, XFOIL calculates the normalized frequencies that we converted using equation (3.23) in order to estimate the actual values of turbulent oscillations.

$$\nu = \omega L / V_\infty = 2\pi f c / U_\infty \quad (3.23)$$

where  $\nu$  is the normalized frequency calculated by XFOIL,  $V_\infty = U_\infty$  is the upstream air speed measured in m/s and  $L = c$  is the chord of the airfoil measured in m and  $f$  is the frequency measured in Hz ( $s^{-1}$ ).

Table 3.3 shows the estimated values of the frequency turbulent signal likely to occur during transition for the same aerodynamic cases as those shown in Figure 3.15.

Table 3.3 Frequencies of the transitional pressure signal

<b>M=0.2, alpha = -1</b>	<b>M=0.2, alpha = 0</b>	<b>M=0.2, alpha = 1</b>
610 Hz	661 Hz	720 Hz
780 Hz	846 Hz	922 Hz
999 Hz	1083 Hz	1180 Hz
1278 Hz	1386 Hz	1510 Hz
1636 Hz	1774 Hz	1932 Hz
2094 Hz	2271 Hz	2470 Hz
2680 Hz	2906 Hz	3160 Hz

Studying the measured signal allowed us to choose the right type of sensors for the detection of the laminar-to-turbulent signal. The Nyquist-Shannon theorem requires that when measuring a signal with a frequency  $f$ , the sampling acquisition rate should be double i.e.  $2f$ , which means that sensors with a 1000 Hz sampling rate would detect frequency signals only up to 500 Hz. As will be shown in the following chapters, the optical sensors proved to be blind to the detection of the Tollmien-Schlichting waves in wind tunnel tests due to either the resolution was too rough, or acquisition sampling rate was too rough.

### **3.3 Shape memory alloys (SMA) actuators modeling and control function design**

The wing model tested in the wind tunnel was a rectangular wing with a reference airfoil WTEA, a 0.5 m chord and a 0.9 m span. The wing model was equipped on its upper surface with a flexible skin made of composite materials (layers of carbon and Kevlar fibres in a resin matrix), two line actuators made of shape memory alloys wires, as shown in Figure

3.17, and 32 pressure sensors (16 optical sensors and 16 Kulite sensors) distributed on the flexible skin chord-wise and span-wise, as shown in Figure 3.18. The sensors were positioned on two diagonal lines at an angle of 15 degrees from the center line.

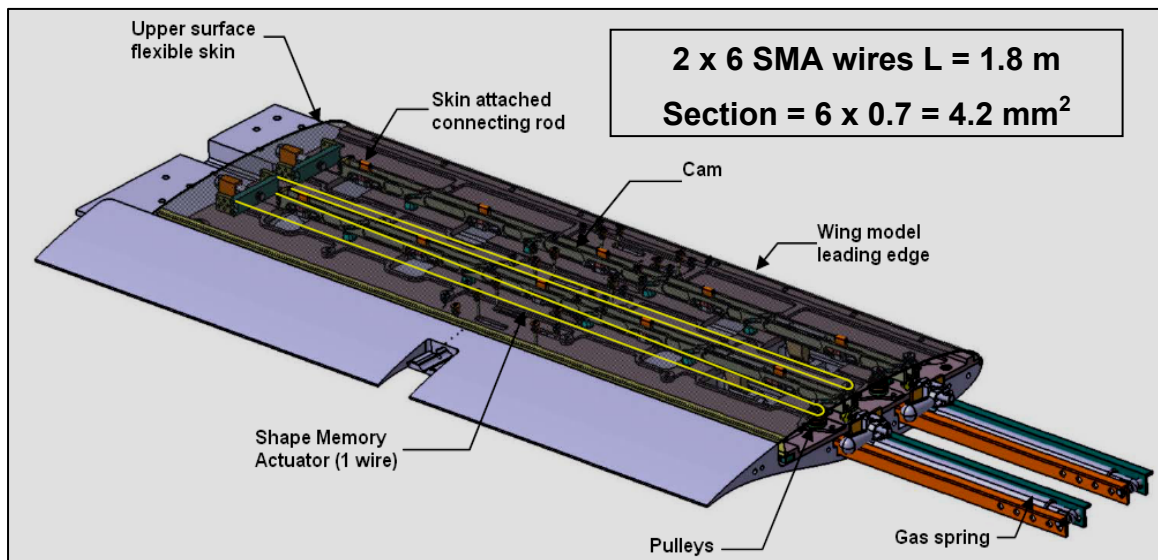


**Figure 3.17** Wing model design realised in CATIA by LAMSI team [12]

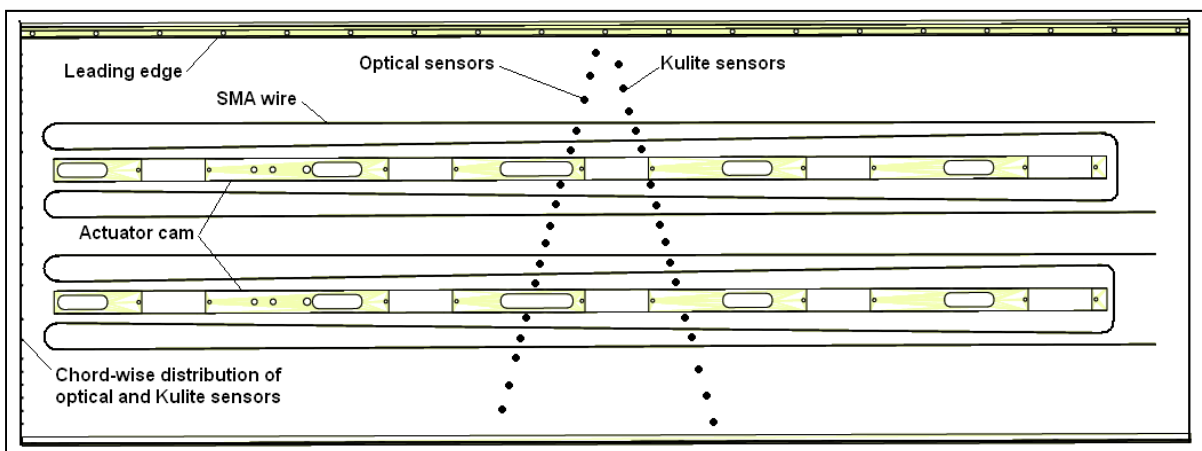


**Figure 3.18** Optical and Kulite sensors distribution on the flexible skin, view from below realised in CATIA

The mechanical principle of the SMA actuators is shown in Figure 3.19. The flexible skin is installed between 0 and 70% of chord (0 – 0.350 m) and is deformed by use of two rods

linked to the flexible skin in the points situated at 25.3% and 47.6% of chord, respectively (0.126 m and 0.238 m distance from the leading edge).

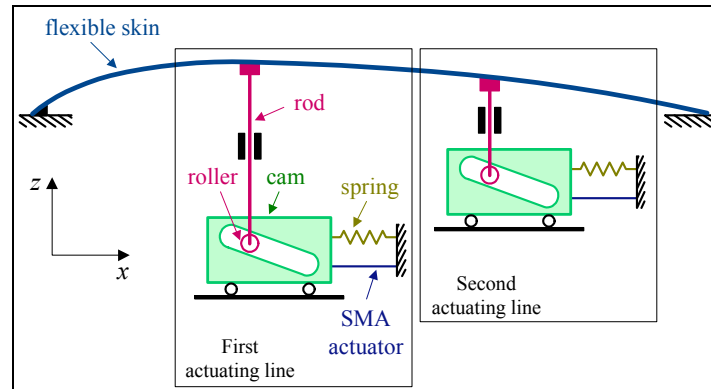


**Figure 3.19 Mechanical principle of the SMA actuators**

The vertical displacement of each actuator was converted into a horizontal displacement at a rate of 1 to 3, which means that the 24 mm horizontal stroke was converted into an 8 mm vertical stroke [12].

In this section, we describe our contribution to the control modeling of the actuators designed by the LAMSI team for the purpose of simulating the system. The shape memory alloy actuators use the Ni-Ti alloys, which are characterized by the ability to change their shapes when heated and regaining their initial shape when cooled. These properties are used in practice by inducing an electrical current through the alloy, which produces the required heat. The actuator is made of several SMA wires that will increase its length when heated and decrease its length when cooled. In order to model the control function, we need to model the equivalent SMA transfer function. The SMA actuator is modeled in Simulink using an S-function numerical finite element model built by Dr. Patrick Terriault (LAMSI team) using the theoretical Likatchev model [13]. We consider as input parameters  $I$ , the electrical current intensity,  $F$ , the force applied to the wire, and the initial temperature of the SMA wire. The outputs of the S-function were the displacement of the actuator, the temperature of the alloy during operation, and the material transformation phase, which is not used in our application, as shown in Figure 3.20.

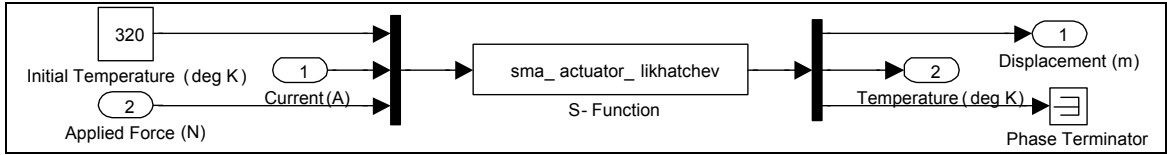


**Figure 3.20 The SMA S-function numerical model used in Simulink.**

The aerodynamic force varies with the airflow characteristics (Mach number, Reynolds number and  $\alpha$ -angle of attack). The aerodynamic forces acting on the two points of the actuators' links with the flexible skin are calculated by integrating the static pressure distribution over the upper surface of the flexible skin. The pressure distribution is calculated using the pressure coefficient definition formula, considering that the pressure inside the wing box is equal to the stagnation pressure, while the pressure coefficients corresponding to a certain airflow condition given by the Mach number, Reynolds number and  $\alpha$ -angle of attack are calculated using the XFOIL code software.

$$\delta p = Q_{\infty} \cdot C_p \quad (3.24)$$

$$F_{aerodynamic1} = \int_{\frac{x_1+x_2}{2}}^0 \delta p \cdot dx \quad (3.25)$$

$$F_{aerodynamic2} = \int_{0.7c}^{\frac{x_1+x_2}{2}} \delta p \cdot dx \quad (3.26)$$

where  $x_1$  and  $x_2$  are the actuators positions on chord.

Since the aerodynamic force is a suction force, it tends to lift the skin and to shorten the SMA wire. The elastic force of the flexible skin acts against the aerodynamic force. A gas spring is needed in order to counteract the aerodynamic force, such that the resultant force that acts on the SMA wire is given by equation (3.28). The SMA wire is loaded by the gas spring even if there is no aerodynamic force applied on the flexible skin. The gas spring has a preloaded force of 1500 N and a linear elastic coefficient of 2.95 N/mm [12].

$$F_{SMA} = F_{spring} + F_{skin} - F_{aerodynamic} \quad (3.27)$$

$$F_{SMA} = (F_{pretension} + k_{spring} \cdot \delta_{horizontal}) + k_{skin} \cdot \delta_{vertical} - F_{aerodynamic} \quad (3.28)$$

Figure 3.21 shows the schematic of the PID controller, the SMA actuator model and the model of the mechanical system that converts the horizontal stroke of the actuator into a vertical stroke of the flexible skin. The PID controller supplies the current necessary to heat the SMA wire, and through the feedback of the displacement signal, interrupts the current in order to let the SMA wire cool down. To maintain a certain desired displacement, the controller will cycle the current, keeping the SMA wire at a certain length by cycling the martensitic-austenitic transformation. The schematic of the controller is shown in Figure 3.22. The first switch will cycle the current according to the differential signal from the displacement sensor, which is compared to the desired displacement. The second switch acts as a temperature limiter; in the physical model, the temperature must be kept under 85 deg C in order to avoid interference with the operation of the optical sensors. Finally, the current saturation simulates the physical limits of the power supplies, which are manually set to 10 A and 20 V.

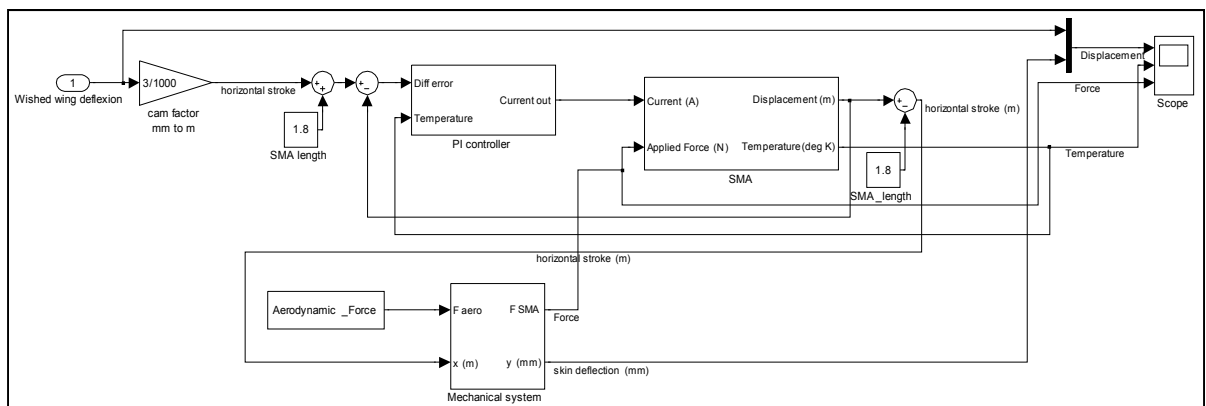


**Figure 3.21 Schematic of the PID controller, SMA actuator and mechanical system.**

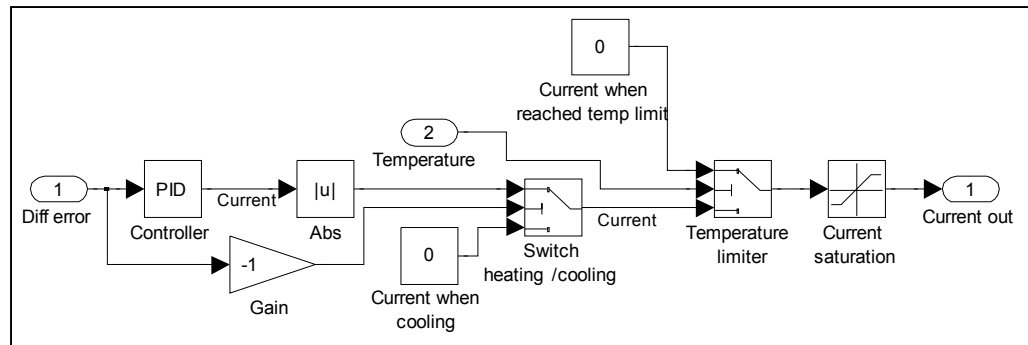
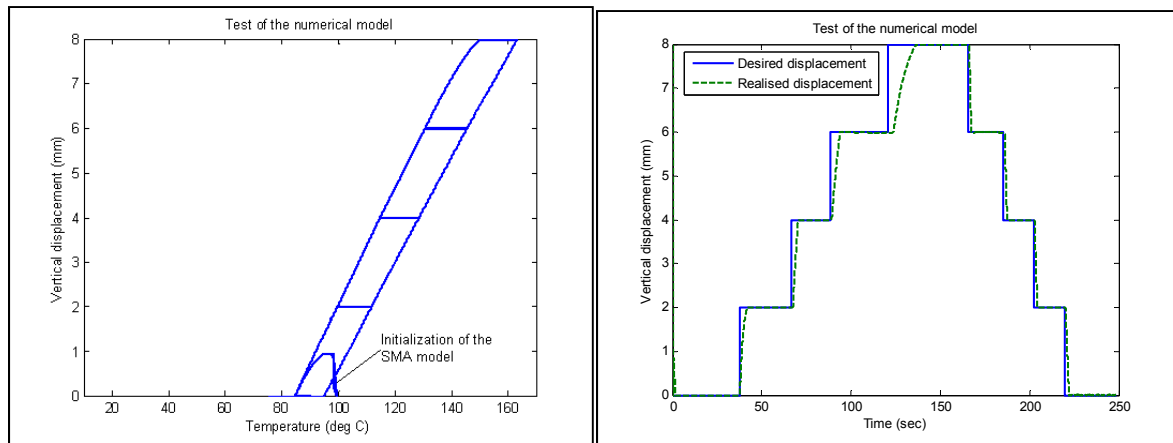


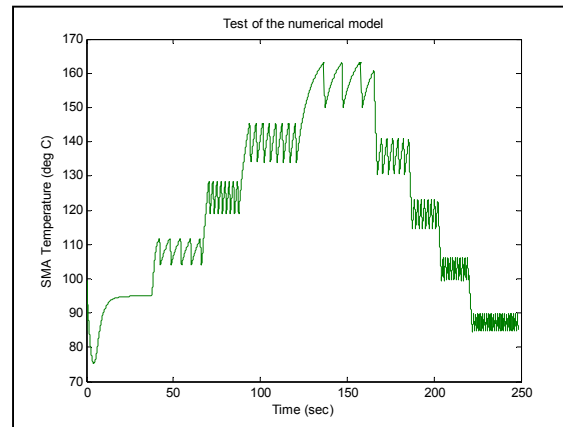
**Figure 3.22 Schematics of the PID controller, where  $P=1800$ ,  $I=400$ ,  $D=0$ .**

The results of the simulation are shown in Figure 3.23. The test of the simulation program was performed by requesting a series of steps inputs of 0, 2, 4, 6 and 8 mm in ascending and descending order as shown in Figure 3.23.b. As shown in Figures 3.23.a. and 3.23.b. the temperature required for the actuator to reach the commanded displacement of 8 mm is 160 degrees Celsius. This temperature is obtained thanks to the SMA's Likhatchev numerical model and to the mechanical force that simulates the gas spring. The less the aerodynamic force is applied, the greater is the force that acts on the SMA and the more current is required to change the wire displacement. To see the behaviour of the controller and the actual SMA actuator, we performed a series of preliminary tests in laboratory conditions, as shown below:



a).

b).



c).

**Figure 3.23** Test of the numerical model for a step of 0, 2, 4, 6, 8 mm in the absence of aerodynamic forces.

The experimental tests were performed in the LAMSI facility with the physical wing model installed on the bench. The physical SMA actuators were connected to two AMREL SPS100-33 power supplies controlled by Matlab/Simulink through a Quanser Q8 communication board with 8 input and 8 output channels. The input channels of the Quanser board were used for a thermocouple connected to a wire of the SMA actuator, an input signal from the potentiometer that senses the actuator position and an input signal from a laser beam installed above the actuator which detects the vertical displacement of the SMA actuator. The sampling rate of the acquired signals was set at 0.01 seconds. The gas springs that maintained the SMA wires in tension had a preloaded value of 225 lbs (1000 N) since there

was no aerodynamic force in the laboratory condition. The tests were performed using the configuration with the signal of the potentiometer measuring the horizontal displacement of the actuator used in closed loop in order to obtain the desired position of the actuator (Figure 3.24).

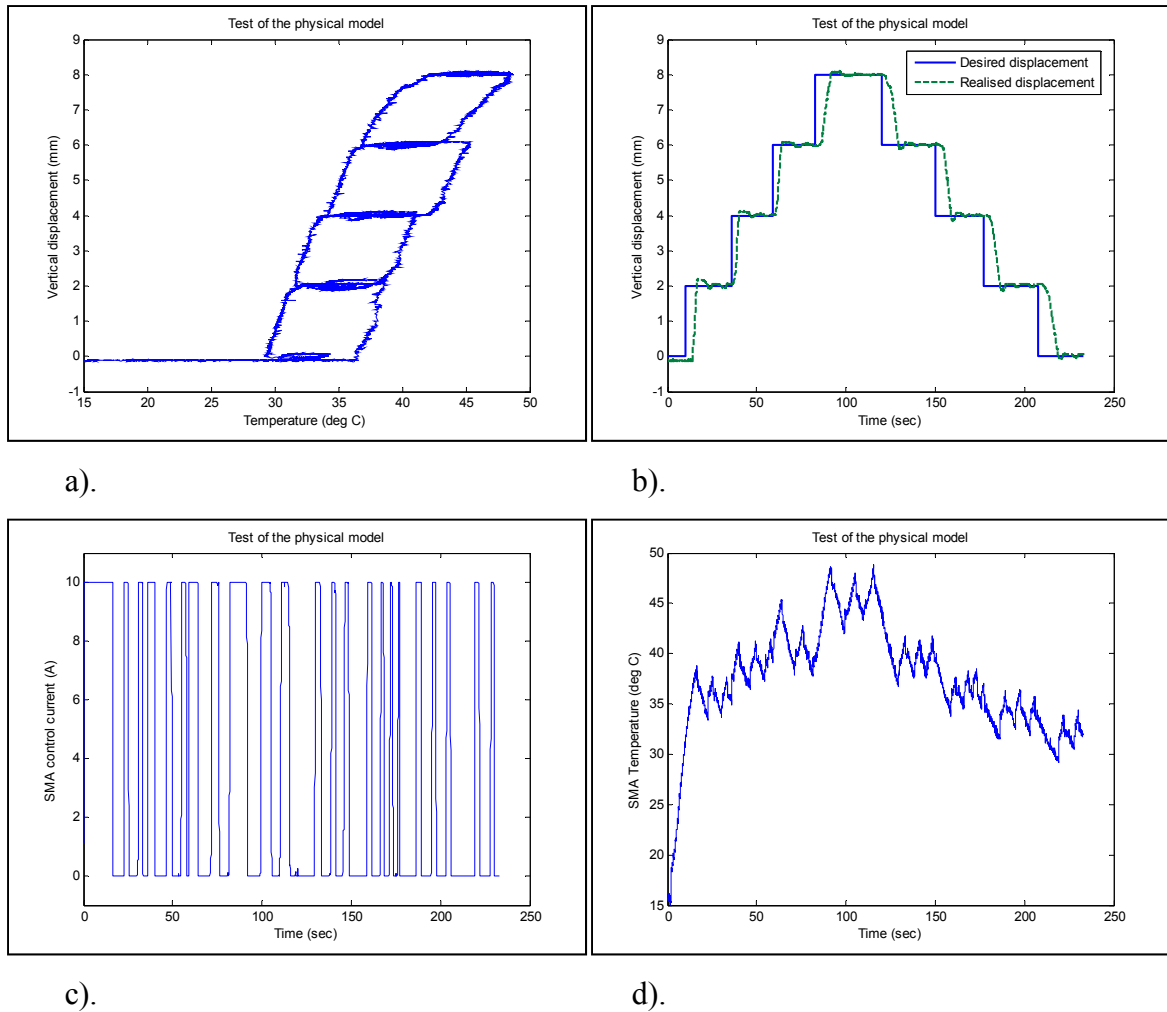


**Figure 3.24** Controller bench test performed in closed loop using the potentiometer signal as feedback for actuator position

The errors obtained in this configuration were slightly higher than 0.1 mm in the beginning of step command, but after several cycles, the errors drop below 0.1 mm (see Figure 3.24.b).

The next stage of bench tests was analysed in Chapter 8. The controller was connected with the two actuators in parallel using potentiometer position signals as feedback, and the actuator displacement and flexible skin displacement in laboratory conditions (no aerodynamic force action) was measured using the laser beam. The airfoil measured during the bench test was compared with the theoretical airfoil calculated by the École Polytechnique team [14]. The expected measurements using the laser beam was not highly precise, but nonetheless gave an approximate estimate of the airfoil shape when the SMA actuators acted.

### 3.4 Controller simulation in closed loop using airflow pressure distribution

In this section, we present the schematic of the controller that was used in the wind tunnel tests. The final objective of the project is to build a controller that uses the pressure signals provided by optical sensors in order to change the airfoil shape during wind tunnel tests. The schematic of the system is shown in Figure 3.26.

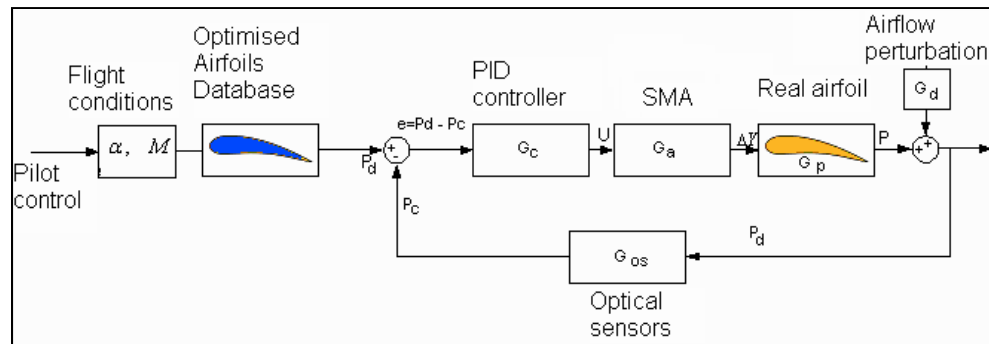


**Figure 3.25 Control schematic of the wing model in wind tunnel conditions (the plant) using the optical sensors pressure signal as feedback signal**

As seen in Figure 3.26, the system is initialized by the pilot (the user) to set the flight conditions expressed by the angle of attack  $\alpha$  and airspeed (Mach number)  $M$ . For such a case there is only one optimal airfoil and one desired  $P_d$  pressure distribution in the controller database.

The controller is used to minimize the error  $e = P_d - P_c$  between the desired pressure value and the pressure value measured by the optical sensor. The controller uses the error  $e$  as input and sends a control signal  $U$  to the actuators; the actuators change the airfoil by moving the control points of each actuator by the value  $\Delta Y$ , which changes the aerodynamic pressure distribution over the airfoil  $P$ . This pressure distribution is perturbed by external influences such as wind gusts  $G_d$ . The real pressure is then measured by optical sensors  $P_c$  and used by the controller, closing the loop.

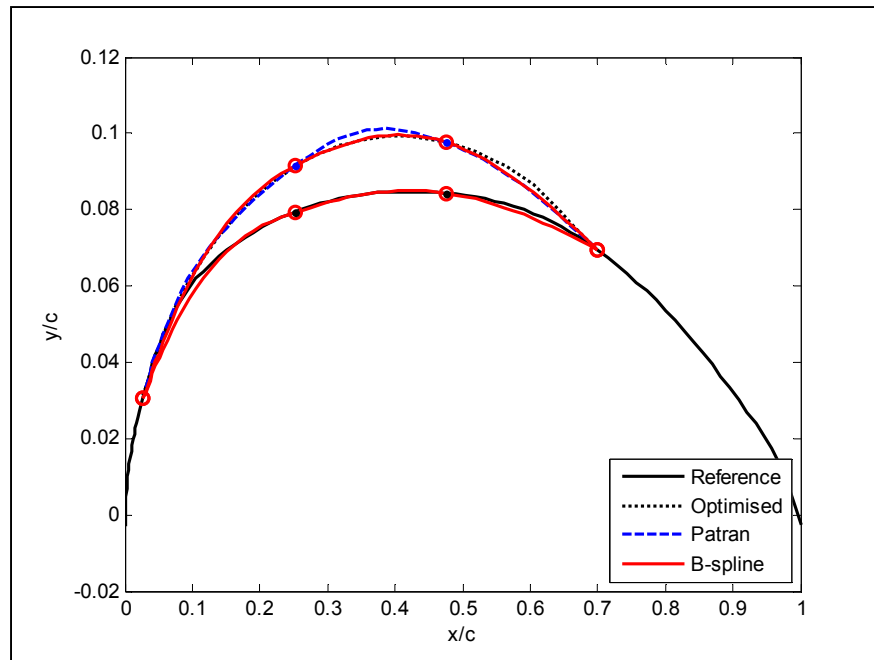
The system input is given by the selection of the flight conditions (Mach number and  $\alpha$  angle of attack). The Mach number is defined as a series (0.2, 0.225, 0.25, 0.275, 0.3), limited by the maximum airspeed of the wind tunnel, which occurs when Mach = 0.35. The angles of attack are limited in the range where the flow is still laminar and are defined as a series of -1, -0.5, 0, 0.5, 1, 1.5, 2 degrees. The combinations of Mach numbers and angles of attack give 49 combinations of cases, as shown in Table 3.4.

Table 3.4 Aerodynamic cases

Mach	Re ( $\times 10^6$ )	Angle of attack (degrees)						
		-1.00	-0.50	0.00	0.50	1.00	1.50	2.00
0.200	2.2932	C101	C102	C103	C104	C105	C106	C107
0.225	2.5679	C108	C109	C110	C111	C112	C113	C114
0.250	2.8384	C115	C116	C117	C118	C119	C120	C121
0.275	3.1044	C122	C123	C124	C125	C126	C127	C128
0.300	3.3654	C129	C130	C131	C132	C133	C134	C135

For each of the 35 cases, the École Polytechnique team calculated an optimised airfoil that was capable of keeping the transition point as close as possible to the trailing edge of the airfoil [14]. Because the optimised airfoil is a theoretical airfoil that was obtained through inverse design, there is no guarantee that this airfoil can be obtained in reality through

technological processes. We performed a series of simulations using the finite element method in Nastran-Patran to verify the differences between the optimised airfoil and the airfoil that will be obtained in wind tunnel conditions under aerodynamic force loading, with the same actuator displacements imposed. The Nastran-Patran simulations of the flexible skin shape behaviour under the aerodynamic loads were performed by Mr. Samuel Courchesne, internship student and member of LARCASE team, based on structural data given by Mr. Daniel Coutu, PhD student and member of LAMSI team. The structural work performed in Nastran-Patran at LARCASE gave same results as the structural work performed by the LAMSI team using ANSYS commercial software [15]. In addition, aeroelasticity studies in Nastran-Patran were also performed by Mr. Courchesne, and it was found that flutter could occur at Mach number of 0.55, much higher than Mach number of 0.3. Figure 3.26 shows a comparison between the theoretical optimised airfoil and the finite element model results. In my simulation, I needed a simplified model that could be used in a fast iterative algorithm. For that reason, to simulate the morphing of the flexible skin, I used a B-Spline model that approximates the reference airfoil and the optimised airfoil for the all 35 cases considered. The B-Spline is a convenient approximation that generates an infinite number of curves of actuators intermediary positions in the 0–8 mm range.



**Figure 3.26 Model of the flexible skin using B-Splines compared to the finite element results obtained in Nastran-Patran, the reference airfoil and optimised airfoil for the case C149.**

The closed-loop controller may be intended to reach any of the following objectives:

1. The realised airfoil in wind tunnel conditions should have the same actuator displacements as the optimised airfoil,
2. The realised airfoil in wind tunnel conditions should have the same or nearly the same mean pressure distribution as the optimised airfoil,
3. The realised airfoil in wind tunnel condition should have the same or nearly the same RMS pressure distribution (that indicates the noise level on the boundary layer) as the optimised airfoil.

In the first case, the controller uses the database of optimised airfoils in our simulation as the desired position for the actuators, and compares it with the realised position signal of the SMA actuator. The optical sensors and Kulite sensors are used to monitor the pressure distribution and the RMS pressure distribution on the boundary layer. In this case the controller is considered to work in an open loop. The simulation results realized in Simulink

are shown in Figure 3.27. The  $C_p$  distribution for each of the airfoils (reference, optimised and realised airfoils) was calculated using XFOIL software on the modified airfoil shapes modelled using  $B$ -splines, which was coupled with the Matlab/Simulink simulation.

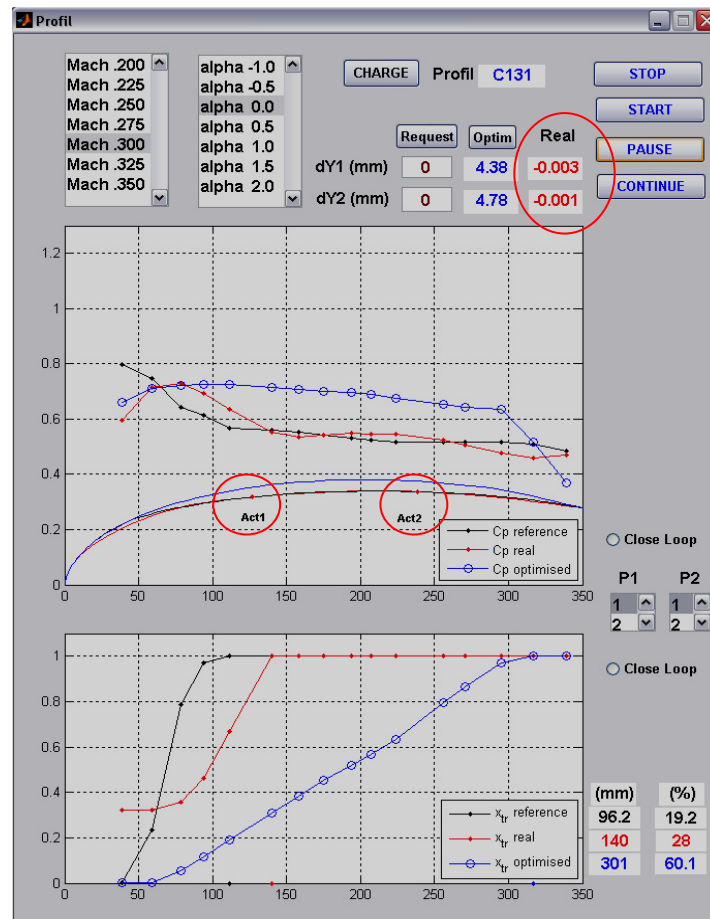


**Figure 3.27 Results simulation for the airflow condition case C131 with the two actuators at the zero positions (0 mm).**

The upper plot of the Figure 3.28 shows the reference airfoil (black), the optimised airfoil (blue) and the realised airfoil (red), which in this case, is the  $B$ -spline model of the flexible skin. The upper plot also shows the  $C_p$  distribution corresponding to the chosen airflow conditions for each of the airfoils, calculated using XFOIL. The lower plot shows the  $N_{cr}$  distribution calculated by XFOIL for each of the three airfoils: reference, optimised and realised. In the upper left corner, we can see the airflow conditions, and in the lower right

corner, we see the calculated transition point positions in mm and % of chord. The pressure distributions (normalised mean values and RMS) are obtained by an array of 16 points which corresponds to the processed signals of the optical sensors.

Figure 3.29 shows the results of the simulation when the “Optim” button is pressed, when the controller receives a signal to put the SMA actuators in the calculated positions of 4.38 mm for SMA actuator #1 and 4.78 mm for SMA actuator #2, respectively. The airfoil realised is very close to the optimised one and has a  $C_p$  distribution very close to the optimised  $C_p$  distribution. The transition point position is positioned near the trailing edge, but it is not obtained at the maximum position possible.

To obtain a better transition point position, we controlled the mean pressure measured by optical sensors in a closed loop. Each SMA actuator is controlled in a closed loop by a PI controller that maintains the pressure coefficient measured by a selected optical sensor at the same value as the desired pressure calculated on the optimised airfoil. Figure 3.30 shows the results simulation for the airflow condition case C131 when the “Close loop” button is selected, for the control pressure position of SMA actuator #1 is selected the optical sensor #6, and for the control pressure position of SMA actuator #2 is selected the optical sensor #13. The transition is obtained in a better position than during the previous open loop control.

In these simulations, we used the  $N_{cr}$  values calculated by XFOIL but in the wind tunnel, the *RMS* pressure values measured by the pressure sensors were used. The values plotted on the figure are normalized such that value 0 represents the laminar flow and value 1 represent the  $N_{cr}/7$  value, which is the transition to turbulent flow value.

The next step in the controller design is the building of an optimizer that will find the best transition point position without using a data base of previously calculated airfoils. The work was carried out, and is presented in Chapter 11.



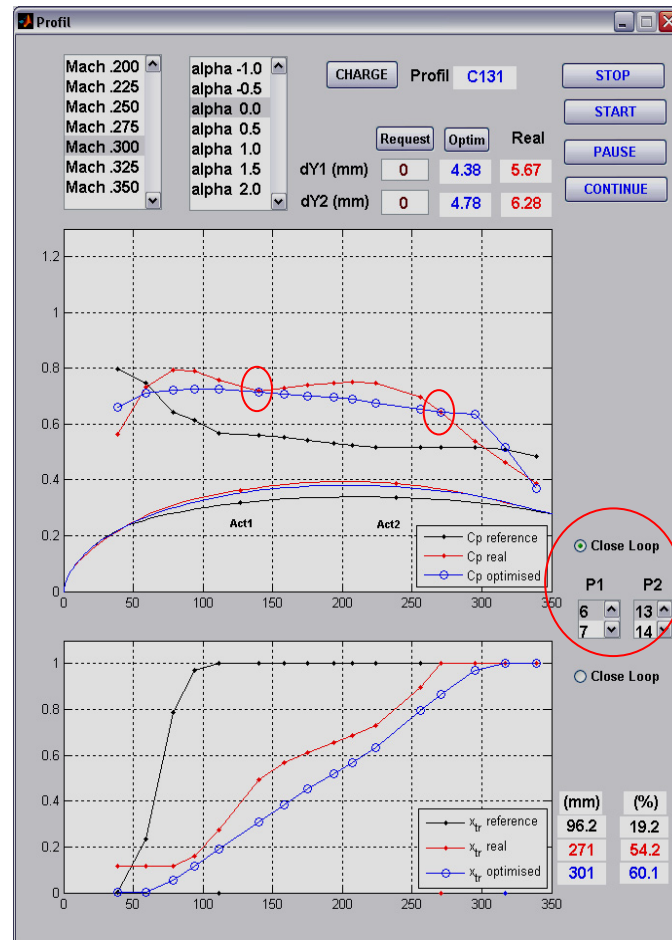


**Figure 3.29** Results simulation for the airflow case C131 with two actuators controlled by a PID controller, so that the mean pressure coefficient is maintained at the same value as the optimized pressure coefficient corresponding to the 6<sup>th</sup> and the 13<sup>th</sup> optical sensors selected in the menu on the right of the figure.

After the realization of the software program in Simulink/Matlab simulating all the mechanical, electrical and aerodynamic systems, then we needed to test and validate it on the real wing model (hardware in the loop), during bench tests, and later, in wind tunnel tests, using real pressure values measured by pressure sensors instead of those calculated by XFOIL. The testing methodology with the hardware-in-the-loop and the obtained results in bench tests and wind tunnel tests using the software designed and tested by me are presented in articles 4, 5, 6, 7 and 8.

## References

- [1] Khalid, M., 1993, *Navier Stokes Investigation of Blunt Trailing Edge Airfoils using O-Grids*, AIAA Journal of Aircraft, vol. 30 (5), pp. 797-800.
- [2] Khalid, M., and Jones, D.J., 1993, *A CFD investigation of the blunt trailing edge airfoils in transonic flow*, Inaugural Conference of the CFD Society of Canada, June 14-15, Montreal.
- [3] Drela, M., 2003, *Implicit implementation of the full  $e^N$  transition criterion*, AIAA 2003-4066.
- [4] Drela, M., Giles, M., B., 1987, *Viscous-inviscid analysis of transonic and low Reynolds number airfoils*, AIAA Journal, vol. 25, no.10, pp 1347-1355.
- [5] Paraschivoiu, I., *Subsonic aerodynamics*, 2003, École Polytechnique de Montréal, ISBN 2-553-01130-X
- [6] Kuethe, A., M., Chow, C.-Y., 1997, *Foundations of aerodynamics: bases of aerodynamic design*, 5th ed., John Wiley & Sons, Inc. N.Y.
- [7] Hinze, J., O., 1975, *Turbulence an introduction to its mechanism and theory*, McGraw-Hill Book Co. Inc., N.Y.
- [8] SPL definition [http://en.wikipedia.org/wiki/Sound\\_pressure](http://en.wikipedia.org/wiki/Sound_pressure). Consulted November 6, 2009.
- [9] Larssen, J.,V., William, J., D., 1999, *Acoustic properties of the Virginia Tech. Stability Wind Tunnel*, Department of Aerospace and Ocean Engineering, Virginia Polytechnic Institute and State University, Blacksburg, Virginia, December 6th, 1999, 24061 *VPI-AOE-263*  
<http://www.aoe.vt.edu/research/facilities/stab/files/vpi-aoe-263.pdf>.  
Consulted on November 6, 2009.
- [10] Mack, L. M., 1977, *Transition and laminar instability*, Jet Propulsion Laboratory Publication 77-15, Pasadena, CA.
- [11] Nitsche, W., Mirow, P., Dorfler, T., 1989, *Investigations on flow instabilities on airfoils by means of piezofoil-arrays*, Laminar-Turbulent Transition IUTAM Symposium, Toulouse, France.
- [12] Georges, T., Morellon, E., Terriault, P., Brailovski, V., 2008, *Design des actionneurs AMF : application au cas de l'aile flexible*, LAMSI report, May.

- [13] Terriault, P., Viens, F., Brailovski, V., 2006, *Non-isothermal Finite Element Modeling of a Shape Memory Alloy Actuator Using ANSYS*, Computational Materials Science, No. 36, pp. 397-410.
- [14] Trifu, O., 2008, *Optimization of the WTEA-TE1 airfoil with modification #1 applied on 10% of its upper side*, Ecole Polytechnique report, May.
- [15] Coutu, D., Brailovski, V., Terriault, P., Fischer, C., 2007, *Experimental validation of the 3D numerical model for an adaptive laminar wing with flexible extradors*, Proceedings of 18<sup>th</sup> International Conference of Adaptive Structures and Technologies, October 3-5, Ottawa, ON, Canada.

## CHAPTER 4

### ARTICLE 1

#### TRANSITION POINT DETECTION FROM THE SURFACE PRESSURE DISTRIBUTION FOR CONTROLLER DESIGN

Andrei Vladimir Popov, Ruxandra Mihaela Botez, and Michel Labib  
École de Technologie Supérieure, Montréal, Quebec H3C 1K3 Canada  
This article was published in the AIAA Journal of Aircraft, Vol.45, No. 1,  
January-February 2008.  
DOI: 10.2514/1.31488

#### Article presentation

This article contains a theoretical study of the method for detecting the laminar-to-turbulent transition location on the suction surface of an airfoil. The article enters into the physical details of aerodynamic laws of the boundary layer and demonstrates that the transition can be localized by the detection of the pressure step increase in the pressure distribution, as shown in the Section 3.2, *Modeling the dynamic pressure signal and transition position measured using optical sensors*. We demonstrated that using 84 sensors installed on the upper surface of the airfoil, we can detect the pressure distribution to a sufficiently accurate degree. Then, by using a mathematical interpolation and double derivation between the measured values, the occurrence of the discontinuity in the pressure distribution can be detected automatically by a software program. For the simulation of the pressure distribution, the XFOIL code was used, and the method seemed to be good enough for such an application, although under experimental conditions, it was shown to be unsuitable for use due to wide fluctuations seen in the pressure values measured by the sensors.

The new method nevertheless still has the potential to be implemented, for the automatic detection of pressure step when shock waves occur in transonic flow, because the pressure step has a much larger value than the local pressure variations in the experimental measurements. In laminar-to-turbulent transition in subsonic flow, the pressure step value is

too small to be detected by such a method, which is the reason why it was abandoned, and not implemented in this project. Another reason why it was dropped was because it was not possible to fit more than sixteen (16) optical sensors inside the wing cavity due to their dimensions and their optical fibers, which were connected to the acquisition system. The density of the sensors in the chord length unit was an important prerequisite to be respected for the implementation and feasibility of this method.

## **Résumé**

Dans cet article, une méthode de détection de la transition entre l'écoulement laminaire et turbulent sur l'extrados de l'aile à partir de la distribution des pressions est présentée. La localisation de la transition est effectuée pour deux types de profils laminaires de référence: NACA 4415 et WTEA-TE1, ainsi que 17 profils WTEA-TE1 modifiés, obtenus en déplaçant la surface flexible de l'extrados en utilisant un mécanisme de contrôle dans un seul point. La deuxième dérivée du profil de distribution de pression est calculée en utilisant deux types d'interpolation : polynôme d'interpolation piecewise cubique Hermite et polynôme d'interpolation cubique Spline. À l'aide de ces deux méthodes, on détermine la location de la transition dans le point où la courbure du profil de distribution de pression est maximale. Les résultats obtenus par ces méthodes sont validés avec le logiciel XFOIL, qui est utilisé pour calculer la position théorique du point de transition. Les avantages de ces méthodes nouvelles pour le design d'un contrôleur en temps réel sont présentés.

## **Abstract**

A method for the detection of the location of laminar-to-turbulent transition on the suction surface of an airfoil from the surface pressure distribution is examined. The location of transition is determined for two reference laminar airfoil types: NACA 4415 and WTEA-TE1, as well as for 17 modified WTEA-TE1 airfoil shapes, obtained by displacing the flexible wing upper surface using a single point control mechanism. The second derivative of the pressure distribution is calculated, using two interpolation schemes: piecewise cubic Hermite interpolating polynomial and Spline, from which it is determined that transition may

be identified as the location of maximum curvature in the pressure distribution. The results of this method are validated using the well-known XFOIL code, which is used to theoretically calculate the transition point position. Advantages of this new method in the real-time control of the location of the transition point are presented.

#### **4.1 Introduction**

The modern era of aviation opened a new horizon of research in the morphing adaptive wing concept, encouraged by rising fuel costs and environmental concerns. Adaptive wings, which have the potential to revolutionize the aerospace industry and would be highly beneficial from both commercial and military standpoints, target the enhancement of airfoil efficiency in off-design regimes via drag reduction and lift augmentation, leading to improvements in aircraft performance. Adaptive wing technology may be implemented on mainly two different scales: 1) the large scale through the use of flaps, spoilers, ailerons, etc. and 2) the small scale through boundary-layer control. Although the prospect of cost effectively designing commercial and/or military vehicles with extensive adaptive wing technology may be unlikely in the immediate future, various research into adaptive technology at both the small and large scales are being conducted, especially in the area of boundary-layer control [1].

Several authors have studied this concept from both theoretical and experimental perspectives, and several airfoil shape optimization techniques have been developed; however, implementation into an aircraft structure has yet to be considered [1–3]. The main objective of this type of control is to reduce drag by modifying the location of the laminar-to-turbulent flow transition point on the wing upper surface for a range of operating flow conditions characterized by the Mach number, Reynolds number, and angle of attack. The in-flight modification of aircraft wings can be done to maintain laminar flow over the wing surface as flight conditions change, which will reduce drag and therefore fuel consumption. Although advances have been made in the development of laminar flow airfoils, there are several problems which require careful attention if further improvements are to be realized in the development of a wing with laminar flow over a large portion of its surface. One

important concern is the formation and behaviour of the laminar separation bubble, predominantly present at low Reynolds numbers, which plays an important part in determining the character of the boundary layer and the stall characteristics of the airfoil.

Studies of the separation of the laminar boundary layer, ensuing transition of the separated shear layer, and the subsequent reattachment and redevelopment of the turbulent boundary layer have already been realized to predict and understand this complex flow phenomenon from both theoretical [4–6] as well as experimental [7] standpoints. An excellent tool is the XFOIL freelicensed software which is a boundary-layer solver developed by Drela [8, 9]. This software implements the  $e^N$  method for transition point detection coupled with a viscous/inviscid flow panel-method solver. The optimal airfoil shapes were represented with a parameterized curve equation, allowing the system to learn the map from the flight-condition parameter values to the curve parameter values [1].

A complex system, however, would adjust the airfoil shape based on the location of the transition point determined from the measured surface pressure distribution. As seen in Fig. 4.1, for various airfoil types and flow conditions (angles of attack  $\alpha$ , speeds  $V$ , and Reynolds numbers  $Re$ ), the controller would receive the airfoil upper surface  $C_p$  distributions from the optical sensors, compare it to a computational fluid dynamics (CFD) generated database in which transition points will be given for various airfoil types as a function of the  $C_p$  distribution, and determine the transition point once a match is found. The controller would subsequently analyze the transition point position and modify the airfoil shape accordingly using memory alloy actuators for real-time variable flow conditions. The overall aim of the controller will be to reduce the drag force on the airfoil upper surface in the vicinity of the trailing edge, given the same set of airflow conditions (angle of attack, airspeed, and Reynolds number) and the same lift force, through changes in the transition point position.

The work presented in this paper is concerned with only a small part of the closed-loop flow control design shown in Fig. 4.1. Focus was placed on the relationship between the transition point positions provided by the CFD database and the chord wise pressure coefficient distributions.

This relationship will be extremely helpful in real-time controller future design because it will allow for the detection of the transition point position on modified intermediate airfoil shapes only from experimental pressure coefficient distributions. The main advantage of this work is that controller design and real-time simulation of the entire system will therefore be easier to implement.

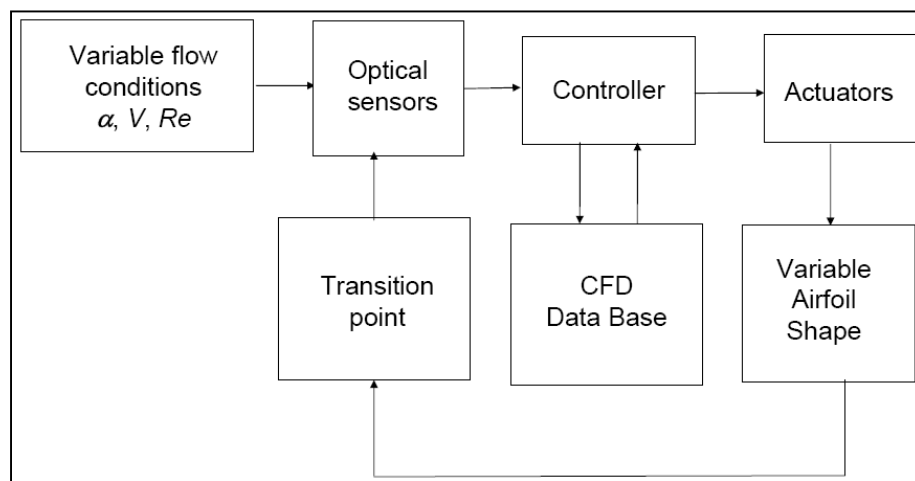


**Figure 4.1** Closed-loop flow control (with optical sensors and feedback) of the morphing wing design in a wind tunnel.

## 4.2 Experimental setup

The wind tunnel to be used for this experiment is the NRC–IAR (National Research Council—Institute for Aeronautical Research) 2 m × 3 m subsonic wind tunnel, which has a maximum airspeed of 140 m/s ( $M = 0.41$ ) and a turbulence level of 0.16%. The design properties of the wing model are the wing trailing edge airfoil (WTEA) shape, a chord of 0.5 m and a span of 1.2 m. The WTEA is an airfoil optimized for laminar flow in transonic speed (Mach between 0.75–0.8) but due to the limitations of the actual wind tunnel, the Mach range is situated between 0.2 and 0.4. The differences in the air data values for both wind tunnels are considered in the XFOIL code simulations. In fact, the results expressed in terms of pressure coefficient distributions versus the chord in XFOIL were found to be the same as the

results obtained experimentally in the transonic wind tunnel. In the work here presented, we compare only the results obtained with XFOIL with results obtained with the MATLAB interpolation programs.

### 4.3 Theoretical considerations

The results obtained by wind-tunnel tests were also obtained by use of the XFOIL code, which uses the  $e^N$  method for transition point detection coupled with a viscous/inviscid flow panel-method solver [8,9]. The  $N_{crit}$  number introduced into the XFOIL code was calculated using Mack's correlation [8] using the wind-tunnel freestream turbulence level  $\tau$ .

$$N_{crit} = -8.43 - 2.4 \ln \tau \quad (4.1)$$

In Fig. 4.2, the pressure coefficients distribution and the predicted transition point are shown for the NACA 4415 airfoil. It was observed that the transition occurs when there is an increase of the pressure in the boundary layer, which is clearly visible in the  $C_p$  plots generated by XFOIL code. The increase of pressure was explained by Galbraith and Coton [10] as a separation bubble which appeared in the boundary layer. This separation bubble occurred at low Reynolds numbers and was studied in detail by Arena, O'Meara, and Mueller [4, 7].

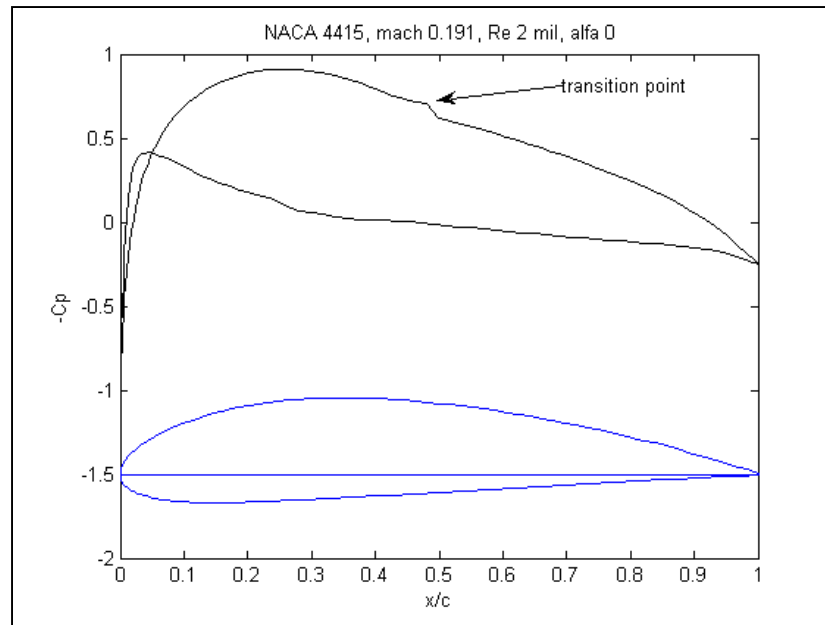


**Figure 4.2** Pressure distribution and XFOIL predicted transition point on the NACA 4415 airfoil at  $M = 0.191$ ,  $Re = 2 \times 10^6$ , and  $\alpha = 0$  deg.

In the low Reynolds number range, an adverse-pressure gradient in the leading-edge flow causes the laminar boundary layer to separate, forming a free shear layer, which, for slightly higher Reynolds number, subsequently undergoes transition to turbulence, and culminates with the incipient reattachment of the turbulent shear layer. This region, delimited upstream and downstream by the laminar separation and turbulent reattachment points is termed a laminar separation bubble. A further increase in Reynolds number, in the medium to high Reynolds number range ( $5 \times 10^5$  to  $10^7$ ), promotes transition in the free shear layer causing the reattachment point to migrate toward the leading edge forming a shortened bubble. The laminar flow separation, transition, and turbulent reattachment occur over a small percentage of the chord and are followed by an attached turbulent boundary layer. Eventually, a sufficiently high enough Reynolds number caused the laminar boundary layer to undergo transition before separation so that the bubble disappeared. This phenomenon is typical for most large transport aircraft, for which the Reynolds numbers based on the wing chord are on the order of  $10^7$  [10].

In the case of our research project, we consider a medium Reynolds number ( $2-4 \times 10^6$ ) with laminar boundary layers in the flow. However, the laminar boundary layer is very sensitive to adverse-pressure gradients and tends to separate much earlier than a turbulent boundary layer. Thus, in a typical aerodynamic context with a changeover from favourable to adverse-pressure gradient, a region of laminar flow typically ends with a transitional laminar separation bubble soon after the flow encounters the adverse pressure gradient according to Rist and Augustin [11]. The basic setup of a laminar separation bubble is sketched in Fig. 4.3.

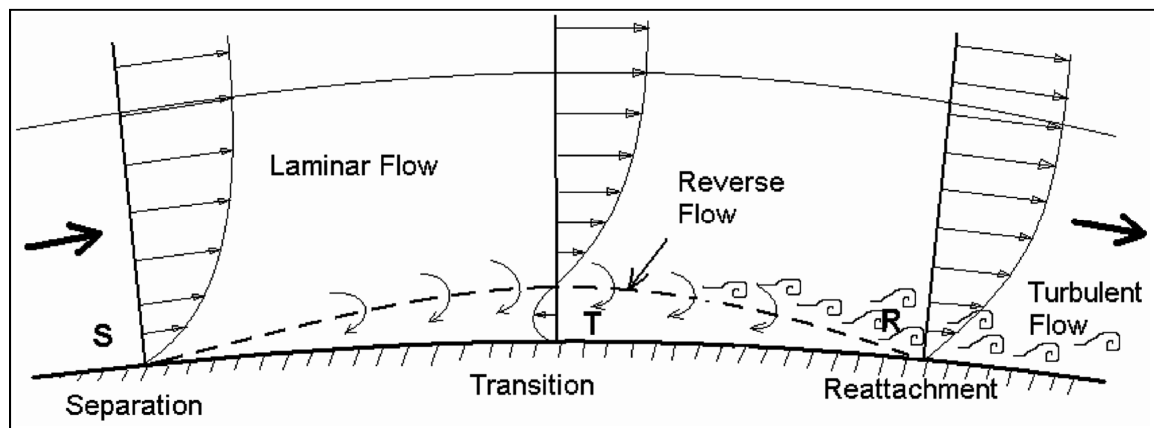


**Figure 4.3 Schematic of the velocity distributions in the laminar separation bubble.**

The laminar boundary layer separates from the wall at a point  $S$ , transition to turbulence takes place at  $T$ , and the turbulent flow reattaches at  $R$ . The latter occurs because of an increased momentum exchange normal to the wall under the action of the larger turbulence eddies. With some oversimplification, the reattachment process can be thought to be due to a turbulent wedge that spreads from a point in the detached shear layer. The actual transition process starts by amplification of small-amplitude disturbances, which are already present in the upstream laminar flow or which are ingested from the freestream via a process called “receptivity.” Once large enough, higher frequencies occur and the shear layer disintegrates into structures of different size [11]. For a detailed study of transition prediction using numerical computational methods and simulations of the laminar separation bubble in low Reynolds number flows, please refer to the paper of Mamou et al. [12].

The laminar-to-turbulent transition point is defined somewhere between the laminar separation and the turbulent reattachment points. Several semi-empirical methods have been developed to determine the transition point location; the most commonly used is the  $e^N$  method, which is implemented in XFOIL code [8]. Based on experimental observations and linearized stability theory, this method indicates transition when the amplification ratio of any small disturbance in the laminar boundary layer reaches an amplification factor  $e^N$  [9]. Figure 4.4 shows pressure coefficient distributions obtained using the XFOIL code for a NACA 4415 reference airfoil at  $M = 0.3$ ,  $Re = 3 \times 10^6$ , and a range of angles of attack, where the correspondent laminar separation, transition, and turbulent reattachment points are shown in the  $C_p$  plots.

The transition point position can be detected in Fig. 3 as the point characterized by a high gradient in the local pressure, which can be explained with the following boundary equation of motion [4]:

$$\rho \left( \frac{\partial u}{\partial t} + u \frac{\partial u}{\partial x} + v \frac{\partial u}{\partial y} \right) = - \frac{\partial p}{\partial x} + \frac{\partial}{\partial y} \left( \mu \frac{\partial u}{\partial y} \right) \quad (4.2)$$

The viscosity of the fluid imposes the “no-slip condition” at the airfoil surface, that is,  $u = v = 0$  at  $y = 0$ , thus, the flow Eq. (1) reduces to

$$\mu \left( \frac{\partial^2 u}{\partial y^2} \right)_{y=0} = \frac{\partial p}{\partial x} \quad (4.3)$$

When the pressure gradient is positive, the flow decelerates until it becomes reversed flow. Immediately downstream of the separation point, identified when  $(\partial u / \partial y)_{y=0} = 0$ , the schematic streamlines near the surface in Figure 4.3 show a strong curvature, which is associated with a strong pressure gradient normal to the surface. The streamlines may deflect

back toward the surface to form a turbulent boundary layer, or they may deflect further away to form a highly unsteady turbulent shear layer.

Figure 4.4 shows a typical screen plot of XFOIL, where  $C_p$  distribution plot and numerical results are shown for a series of simulations where angle of incidence varies from  $-5^\circ$  to  $7.5^\circ$ . In the figure are printed in the table, the transition positions calculated by XFOIL on upper and lower surface of the airfoil for each airflow condition.

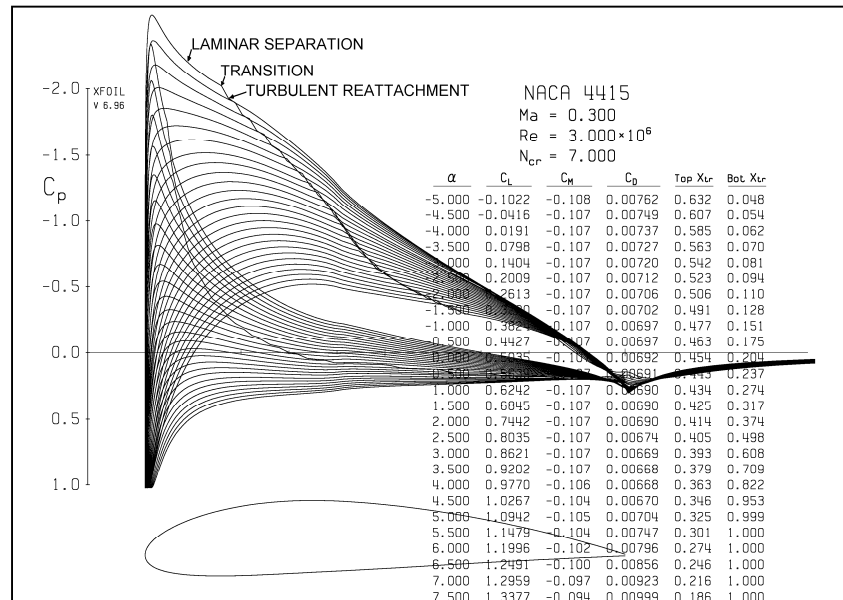


**Figure 4.4**  $C_p$  distributions on a NACA 4415 airfoil at  $M = 0.3$  and  $Re = 3 \times 10^6$ , obtained using the XFOIL code.

The laminar-to-turbulent transition point is defined somewhere between the laminar separation and the turbulent reattachment points. Several semi-empirical methods have been developed to determine the transition point location; the most commonly used is the  $e^9$  method, which is implemented in XFOIL code [8]. Based on experimental observations and linear stability theory, this method indicates transition when the amplification ratio of any small disturbance in the laminar boundary layer reaches an amplification factor  $e^9 = 8100$  [9].

The method proposed in this paper is based on the transition point position, defined as the point where the velocity streamline curvature  $(\partial^2 u / \partial y^2)_{y=0}$  is maximal along  $x$ , which corresponds to its first derivative with  $x$ . To obtain this maximum derivative  $\partial / \partial x (\partial^2 u / \partial y^2)_{y=0}$ , we derive Eq. (4.2) with respect to  $x$  and then we obtain Eq. (4.4), from which we can see that this first derivative corresponds to the second pressure derivative with respect to  $x$ , which should be a maximum:

$$\mu \frac{\partial}{\partial x} \left( \frac{\partial^2 u}{\partial y^2} \right)_{y=0} = \frac{\partial^2 p}{\partial x^2} \quad (4.4)$$

The maximum in the second derivative of the pressure corresponds to the maximum curvature of the pressure plot, which is associated with the beginning of transition.

A CFD database used by the controller, as described above, was constructed with the aid of the XFOIL CFD solver for various flow conditions. This database consists of a collection of airfoil wing shapes, along with their corresponding pressure coefficient ( $C_p$ ) versus chord distributions and location of the transition point.

Figure 4.5 shows the CFD database with several pressure coefficient distributions for the reference WTEA-TE1 airfoil shape (16% thick supercritical airfoil with 68% of the chord in a laminar flow state optimized for transonic speed) and its modified airfoils. The reference airfoil is modified (up and down on the upper airfoil surface) through the use of a single control point (which corresponds to the actuator position) located at 36% of its chord; and thus 16 new modified airfoils with positive and negative deflections of the original airfoil upper surface are obtained.

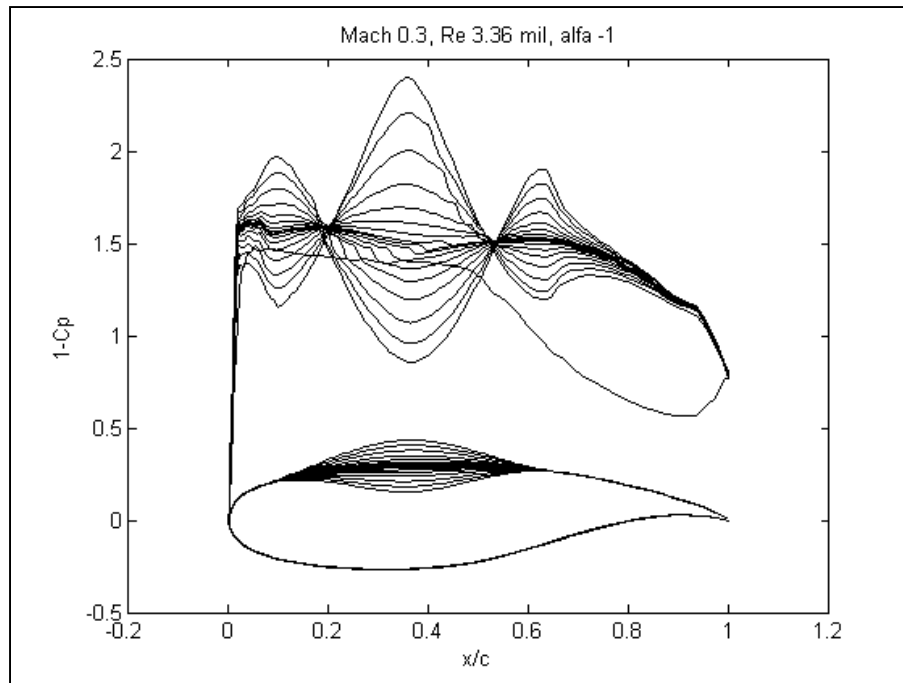


**Figure 4.5**  $C_p$  distributions that correspond to a WTEA-TE1 reference airfoil and to its modified shapes using a single control point, which creates a bump or depression on the airfoil.

#### 4.4 Results Obtained for a NACA 4415 Airfoil

In this section, the results obtained for the reference NACA 4415 airfoil are presented. The XFOIL code is used to simulate the airfoil behaviour at a speed of 65 m/s, corresponding to  $M = 0.191$  and  $Re = 2 \times 10^6$  at a temperature  $T = 15^\circ\text{C}$  with a chord of 0.4572 m (1.5 ft). To determine the curvature (second derivative) of the  $C_p$  distribution, two interpolation methods are used: Spline and PCHIP (piecewise cubic Hermite interpolating polynomial) [13]. The PCHIP method finds the values of an underlying interpolating function  $p(x)$  at intermediate points, such that on each subinterval  $x_k \leq x \leq x_{k-1}$ ,  $p(x)$  is the cubic Hermite interpolant to the given values and their slopes at the two endpoints  $x_k$  and  $x_{k-1}$ . The function  $p(x)$  interpolates between the points values, and its first derivative  $p'(x)$  is continuous. The second derivative  $p''(x)$  may be discontinuous, as there might be jumps in the  $x_k$  points. The slopes at these points are chosen in such a way that  $p(x)$  preserves the data shape and respects its monotonicity, which is to say that on the interval in which the data is monotonic or has a

local extreme, the same interval  $p(x)$  is monotonic or has a local extreme. The Spline method constructs the interpolation polynomial in almost the same manner as the PCHIP. With Spline, the slopes at the  $x_k$  points are chosen differently, so that the second derivative should be continuous, which results in a smoother result. The Spline method produces a more accurate result if the data consist of smooth function values while the PCHIP method has no overshoots and less oscillation if the data are not smooth, an advantage for the pressure distribution interpolations in the vicinity of the transition point, characterized by a sudden pressure increase.

Figure 4.6 which display the  $C_p$  distribution interpolated in the vicinity of the transition point using both the Spline and the PCHIP methods, clearly indicates that the step in the pressure at the point of transition is more accurately interpolated by the PCHIP method than by the Spline function. Figure 4.7, which illustrates the second derivative of the  $C_p$  distribution, shows the maximum value of the  $C_p$  second derivative (equivalent to the minimum value of the negative  $C_p$  second derivative) determined from both methods of interpolation. The locations of transition determined under these conditions from the PCHIP and Spline interpolation methods are within 0.06 and 0.04% of the airfoil chord, respectively, compared to the transition position obtained directly from the XFOIL code, suggesting a fairly high accuracy in the determination of the transition point.

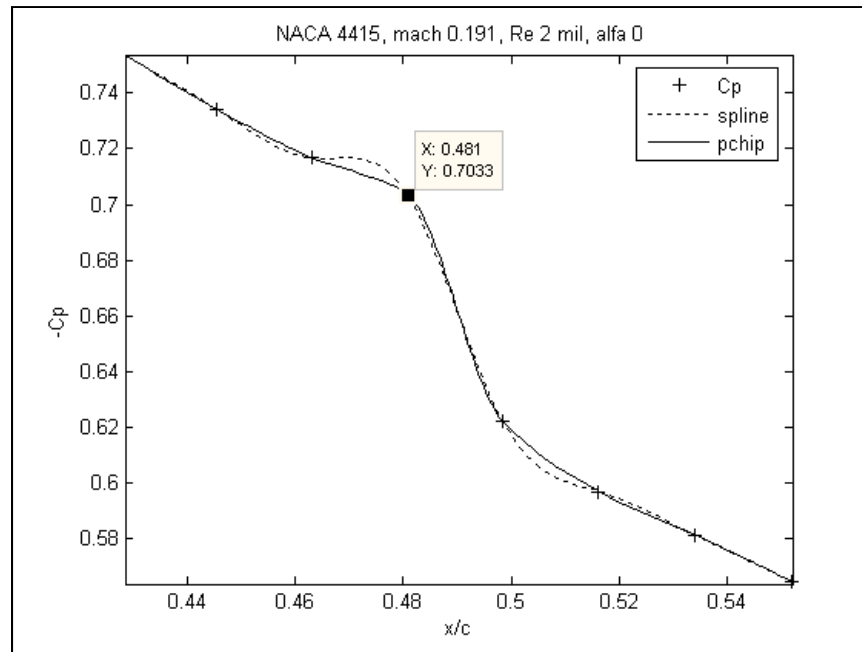


**Figure 4.6**  $C_p$  distributions in the vicinity of the transition point interpolated using the Spline and PCHIP methods.

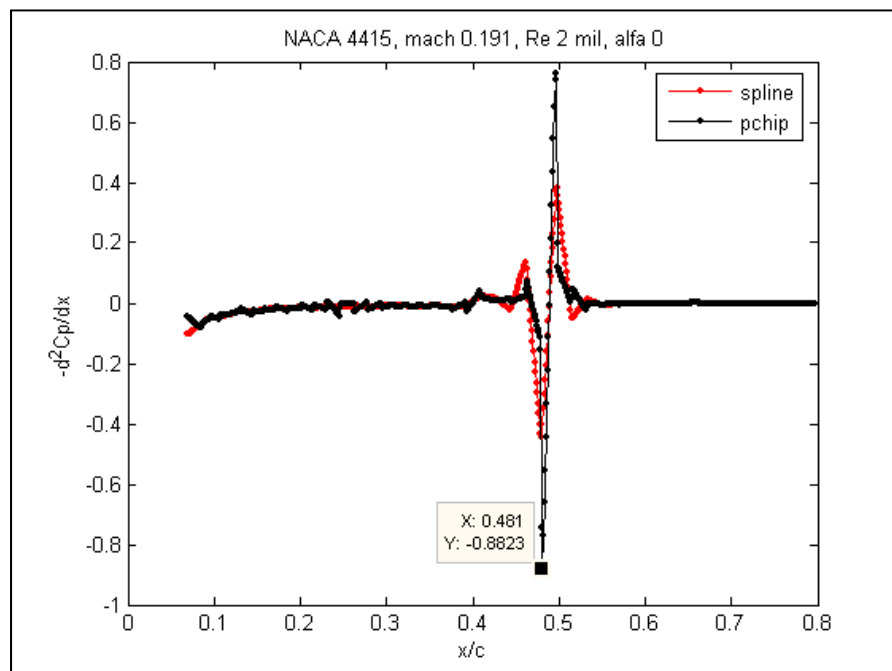


**Figure 4.7** Second derivative of the  $C_p$  distribution interpolated using the Spline and PCHIP methods.

#### 4.5 Results Obtained for the WTEA-TE1 Airfoil

The two interpolation methods presented above were applied to a set of 17 airfoil shapes derived through modifications to the reference WTEA-TE1 airfoil (the notation TE1 stands for an airfoil configuration with a blunt trailing edge). The simulation conditions are  $M = 0.3$ ,  $Re = 3.36 \times 10^6$ , and temperature  $T = 15^\circ\text{C}$ . The values of airfoil deflections at the control point here considered are  $\pm 20, \pm 16, \pm 12, \pm 8, \pm 5, \pm 3, \pm 1.5, \pm 0.5$ , and 0 mm, while the airfoil chord was equal to 0.5 m. The angle of attack was set to various values: -2, -1, 0, 1, and 2 deg. Therefore, a total of 85 cases (5 angles of attack multiplied by 17 airfoil deflections) was obtained for which the transition point position was calculated.

The WTEA-TE1 airfoil surface pressure coefficients calculated with the XFOIL code are presented in Figs. 4.8 for two angles of attack  $\alpha = 0$  deg and  $\alpha = 1$  deg. Figures 4.9 and 4.10 show the pressure coefficient distributions  $C_p(x)$  and second derivatives versus the airfoil chord obtained for two angles of attack  $\alpha = 0$  deg and  $\alpha = 1$  deg by both interpolation methods, Spline and PCHIP. The location of transition predicted by XFOIL was found to be 0.2040, respectively, 0.1118, and based on the maximum pressure curvature criterion, is also identified in Figs. 4.9 and 4.10. The error associated with the determination of the transition point, relative to the theoretically determined value identified in Fig. 4.10, was 0.1% $c$  at  $\alpha = 0$  deg and below 0.1% $c$  at  $\alpha = 1$  deg.

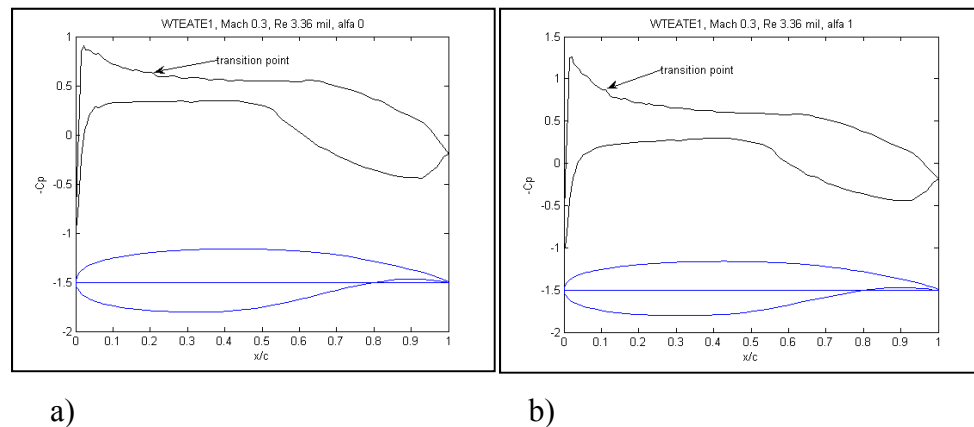


**Figure 4.8**  $C_p$  distributions on the upper and lower surface of the WTEA-TE1 airfoil at a)  $\alpha=0$  deg and at b)  $\alpha=1$  deg.

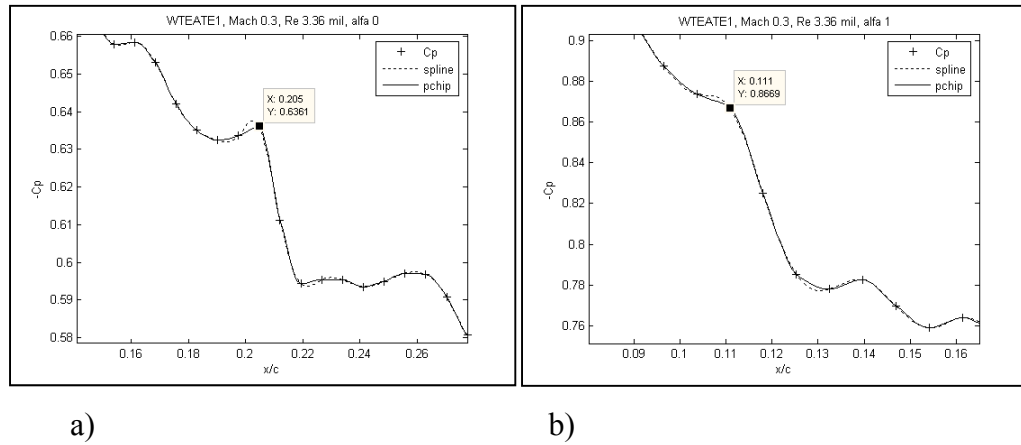


**Figure 4.9**  $C_p(x)$  at a)  $\alpha = 0$  deg and at b)  $\alpha = 1$  deg by use of Spline and PCHIP methods.

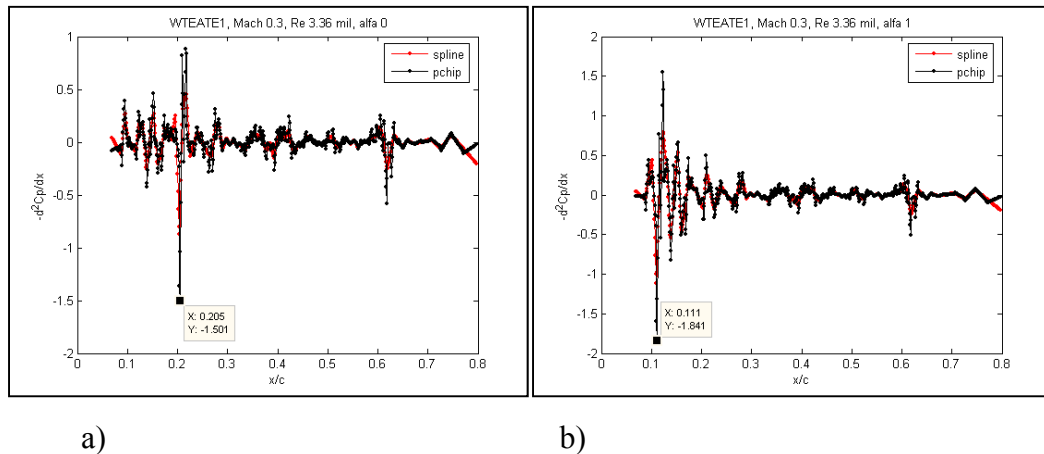


**Figure 4.10** Second derivative of  $C_p$  at a)  $\alpha = 0$  deg and at b)  $\alpha = 1$  deg by use of Spline and PCHIP methods.

Tables 4.1 and 4.2 show the relative errors of the transition point positions, as a fraction of the airfoil chord, calculated by the PCHIP method versus XFOIL code (Table 4.1) and by the Spline method versus XFOIL code (Table 4.2) obtained for the two reference wing airfoils, NACA 4415 and WTEA-TE1, and for the 17 modified airfoils of the WTEA-TE1 for five angles of attack. The total mean error calculated with the PCHIP method versus XFOIL code was found, from Table 4.1, to be  $0.23\%c$  and the total mean error calculated with the Spline method versus XFOIL code was found, from Table 4.2, to be  $0.33\%c$ , from which it can be concluded that the PCHIP method gives better results in this application. The maximum errors are shown in Tables 4.1 and 4.2 in bold figures. Note that the WTEA-TE1 has a

different shape than the 0 mm displacement airfoil because for the latter Spline curves were used to define the upper surface between 0.07 and 0.65  $x/c$ .

The precision with which the location of the transition point is determined is dictated by the density of the pressure sensors distributed along the airfoil chord. In the current investigation, the XFOIL software is used to simulate the  $C_p$  distribution at 84 and 37 points for the WTEA and NACA 4415 airfoils, respectively, within the 7–65% chord interval, where a flexible skin should be equipped with smart actuators. For both the NACA 4415 and WTEA airfoils considered in this paper, the location of the transition point as a function of the pressure coefficient distribution was determined with a high precision of 0.1% of a chord between 7 and 80% of the chord, given the current measurement resolution.

Table 4.1 The relative errors, as a fraction of the airfoil chord, for the transition point prediction calculated by the PCHIP versus the XFOIL method

<b>PCHIP method</b>	<b>-2 deg</b>	<b>-1 deg</b>	<b>0 deg</b>	<b>1 deg</b>	<b>2 deg</b>
NACA4415	0.0061	0.0057	0.0006	0.0051	<b>0.0092</b>
WTEA-TE1	0.0030	0.0003	0.001	0.0008	<b>0.0038</b>
20.0 mm	0.0017	0.0008	0.0003	0.0007	0.0019
16.0 mm	0.0016	0.0053	0.0003	0.0035	0.0042
12.0 mm	0.0027	0.0017	0.0011	0.0006	0.0009
8.0 mm	0.0014	0.0007	0.0006	0.0016	0.0026
5.0 mm	0.0010	0.0002	0.0044	0.0035	0.0001
3.0 mm	0.0014	0.0019	0.0031	0.0018	0.0002
1.5 mm	0.0018	0.0058	0.0052	0.0037	0.0023
0.5 mm	0.0054	0.0051	0.0029	0.0013	0.0032
0 mm	<b>0.0091</b>	0.0053	0.0015	0	0.0006
-0.5 mm	0.0042	0.0037	0.0041	0.0014	0.0017
-1.5 mm	0.0044	0.0016	0.001	0.0053	0.0005
-3.0 mm	0.0014	0.0022	0.0014	0.0019	0.0033
-5.0 mm	0.0027	0.0022	0.0003	0.0006	0.0006
-8.0 mm	0.0030	0.0032	0.0001	0.0001	0.004
-12.0 mm	0.0029	0.0003	0.0002	0.0006	0.002
-16.0 mm	0.0028	0.0039	0.0025	0.0008	0.0007
-20.0 mm	0.0019	0.0011	0.0024	0.0026	0.0014
<b>Mean error</b>	0.0031	0.0027	0.0017	0.0019	0.0023

Table 4.2 The relative errors, as a fraction of the airfoil chord, for the transition point prediction with the Spline versus the XFOIL method

<b>Spline method</b>	-2 deg	-1 deg	0 deg	1 deg	2 deg
NACA4415	0.0051	0.0047	0.0004	0.0041	<b>0.0102</b>
WTEA	<b>0.0740</b>	0.0003	0.0000	0.0018	0.0082
20.0 mm	0.0007	0.0018	0.0087	0.0003	0.0009
16.0 mm	0.0026	0.0033	0.0007	0.0045	0.0032
12.0 mm	0.0037	0.0007	0.0021	0.0016	0.0019
8.0 mm	0.0004	0.0007	0.0016	0.0194	0.0006
5.0 mm	0.0000	0.0008	0.0034	0.0145	0.0011
3.0 mm	0.0014	0.0009	0.0021	0.0008	0.0012
1.5 mm	0.0008	0.0048	0.0042	0.0027	0.0033
0.5 mm	0.0044	0.0041	0.0019	0.0023	0.0012
0 mm	<b>0.0071</b>	0.0007	0.0005	0.0010	0.0004
-0.5 mm	0.0032	0.0027	0.0031	0.0014	0.0007
-1.5 mm	0.0054	0.0016	0.0020	0.0033	0.0005
-3.0 mm	0.0004	0.0012	0.0004	0.0019	0.0033
-5.0 mm	0.0017	0.0032	0.0007	0.0016	0.0004
-8.0 mm	0.0020	0.0022	0.0009	0.0009	0.0030
-12.0 mm	0.0039	0.0013	0.0008	0.0004	0.0020
-16.0 mm	0.0038	0.0039	0.0015	0.0008	0.0003
-20.0 mm	0.0029	0.0001	0.0034	0.0026	0.0004
<b>Mean error</b>	0.0065	0.0021	0.0020	0.0035	0.0023

## 4.6 Conclusions

A method for the detection of the location of laminar-to-turbulent transition on the suction surface of an airfoil from the surface pressure distribution was examined. It was found, through validation using the XFOIL code, that the transition point may be identified via the maximum curvature of the surface pressure distribution. This technique identified the location of the transition point with a mean accuracy of 0.23 or 0.33% of the airfoil chord, depending on whether the PCHIP or Spline interpolation method was implemented. This method does not, however, replace the theoretical  $e^N$  method or other boundary-layer numerical methods. Indeed, it is based on the results obtained by these methods, expressed in terms of pressure coefficient distribution versus the airfoil chord.

This method is advantageous in its real-time applicability, such as in the controller of a morphing wing model, which would measure the pressure distribution, compute the second derivative, and then identify the position of transition to be used as the indicator on how to modify the wing shape. There are limitations, however, to this method related to the range in which the transition point can be located; the method does not work well in the vicinity of the leading edge suction peak, necessitating its elimination. In addition, accurate determination of the location of the transition point is dependent on a sufficient density of pressure measurements along the airfoil chord.

Future work will involve experimental verification of the theoretically based results presented above. The effect of transition point position on the wing drag reduction will be determined, and, in this way, a controller to modify in real time the airfoil geometry will be developed.

## References

- [1] Jacob, J. D., "On the Fluid Dynamics of Adaptive Airfoils," Proceedings of 1998 ASME International Mechanical Engineering Congress and Exposition, ASME, Fairfield, NJ, Nov. 1998, pp. 167–176.
- [2] Driver, J., and Zingg, D. W., "Optimized Natural-Laminar-Flow Airfoils," AIAA Paper 2006-0247, Jan. 2006.
- [3] Zingg, D. W., Diosady, L., and Billing, L., "Adaptive Airfoils for Drag Reduction at Transonic Speeds," AIAA Paper 2006-3656, June 2006.
- [4] Arena, A. V., and Mueller, T. J., "Laminar Separation, Transition, and Turbulent Reattachment Near the Leading Edge of Airfoils," AIAA Journal, Vol. 18, No. 7, 1980, pp. 747–753.
- [5] Khrabrov, A., and Oi, M. V., "Effects of Flow Separation on Aerodynamic Loads in Linearized Thin Airfoil Theory," Journal of Aircraft, Vol. 41, No. 4, 2004, pp. 944–948.
- [6] Khabrov, A., and Greenwell, D., "Influence of Steady Pitch Rate on 2-D Airfoil Aerodynamic Characteristics at Incidence," Journal of Aircraft, Vol. 43, No. 5, 2006, pp. 1552–1555. doi:10.2514/1.19198.
- [7] O'Meara, M. M., and Mueller, T. J., "Laminar Separation Bubble Characteristics on an Airfoil at Low Reynolds Numbers," AIAA Journal, Vol. 25, No. 8, 1987, pp. 1033–1041.
- [8] Drela, M., "Implicit Implementation of the Full  $e^n$  Transition Criterion," AIAA Paper 2003-4066, 2003.
- [9] Drela, M., and Giles, M. B., "Viscous-Inviscid Analysis of Transonic and Low Reynolds Number Airfoils," AIAA Journal, Vol. 25, No. 10, 1987, pp. 1347–1355.
- [10] Galbraith, R. A., and Coton, F. N., "Two-Dimensional, Incompressible Aerofoil Design and Analysis," Computational Methods in Viscous Aerodynamics, edited by T. K. S. Murthy and C. A. Brebbia, Computational Mechanics Publications, Ashurst Lodge, Southampton, U.K., 1990, pp. 331–367.
- [11] Rist, U., and Augustin, K., "Control of Laminar Separation Bubbles Using Instability Waves," AIAA Journal, Vol. 44, No. 10, 2006, pp. 2217–2223. doi:10.2514/1.17518.
- [12] Mamou, M., Yuan, W., and Khalid, M., "Transition Prediction in Low Reynolds Airfoil Flows Using Finite Element/Difference Solvers Coupled with the  $en$  Method: A Comparative Study," AIAA Paper 2006-3176, June 2006.

- [13] Fritsch, F. N., and Carlson, R. E., "Monotone Piecewise Cubic Interpolation," SIAM Journal on Numerical Analysis, Vol. 17, No. 2, 1980, pp. 238–246. doi:10.1137/0717021.

## CHAPTER 5

### ARTICLE 2

#### CLOSED-LOOP CONTROL SIMULATIONS ON A MORPHING WING

Andrei Vladimir Popov, Michel Labib, Julien Fays, and Ruxandra Mihaela Botez  
École de Technologie Supérieure, Montréal, Québec H3C 1K3, Canada

This article was published in Journal of Aircraft, Vol.45, No. 5, September-October 2008.

DOI:10.2514/1.37073

#### Article presentation

The article contains a theoretical study of the closed-loop controller design for a hypothetical morphing wing with a single actuator, as shown in the Section 3.1.2, *Aerodynamic analysis of the modified airfoils using XFOil*. The article analyses the SMA theoretical model by using the Likhatchev numerical model developed by Dr. Patrick Terriault from the LAMSI team, and shows the methodology used to design a PID controller by combining this model with the XFOil code model. The two system simulations, the SMA numerical model and XFOil aerodynamic model, are combined using interpolation tables in Matlab/Simulink, while the PID controller is implemented in the simulation by closing the loop. The article shows and discusses the results obtained in the simulation of the integrated system. This simulation was the first step in developing a real-time controller to be used for controlling the real SMA actuators in the wind tunnel test. The next step was implementing the controller in simulation software which simulates aerodynamic forces using XFOil, but directly controls the SMA actuators in bench tests. The simulation software and preliminary bench test were shown in Section 3.3, *Shape memory alloy actuators modeling and function design*, and Section 3.4, *Controller simulation in closed loop using airfoil pressure distribution*. The physical realisation and results of the bench tests are shown and discussed in the Chapter 8, *Morphing wing control validation during bench tests*.

## Résumé

L'objet principal de ce projet est de développer un système de contrôle actif d'une aile pour la réduction de la traînée. Cette réduction de la traînée peut être réalisée en modifiant la position du point de transition entre l'écoulement laminaire et turbulent, qui doit se déplacer vers le bord de fuite du profil de l'aile. Parce que le point de transition a un rôle majeur dans ce projet, cet article focalise sur le contrôle de la position du point de transition sur le profil, en changeant la géométrie de l'aile équipée avec une peau flexible. Le profil de référence est le profil laminaire WTEA-TE1 sur lequel une peau flexible est installée. La géométrie du profil est modifiée à l'aide d'un seul point de contrôle, dans lequel l'actionneur est installé. Le nombre de Mach, l'angle d'incidence, et la déflexion du point de contrôle nous permettent de calculer les pressions et points de transition à chaque étape. Les variables d'entrée sont les déflexions et les angles d'incidence. Si les variables d'entrée changent, la position du point de transition change aussi.

Un modèle d'alliage à mémoire de forme a été conçu dans l'environnement de programmation Matlab/Simulink. La contribution majeure a été la conception d'un contrôleur en boucle fermée pour l'actionneur d'alliage à mémoire de forme à cause de son comportement non-linéaire. Plusieurs contrôleurs proportionnel-dérivée-intégrative (PID) ont été conçus pour contrôler l'alliage à mémoire de forme en boucle fermée. Trois simulations ont été effectuées pour valider ce contrôle. La première simulation maintient l'angle d'incidence constant pendant que déflexions successives du point de contrôle sont effectués. La deuxième simulation considère plusieurs échelons pour les déflexions mais ajoute un mouvement sinusoïdal pour l'angle d'incidence. Cette simulation est plus proche du régime de vol de croisière. Pour la troisième simulation, les deux angles d'incidence et déflexion sont modélisées comme des ondes sinusoïdales. Les sorties (déflexions et positions du point de transition) sont bien contrôlées et les résultats sont très bons.

On a conclu que cette méthode originale de contrôle est excellente pour le contrôle du point de transition de l'écoulement laminaire en turbulent sur une aile à géométrie variable.

## Abstract

The main objective of the project is to develop a system for the active control of wing airfoil geometry during flight to allow drag reduction. Drag reduction on a wing can be achieved by modifications in the laminar to turbulent flow transition point position, which should move toward the trailing edge of the airfoil wing. As the transition point plays a crucial part in this project, this paper focuses on the control of its position on the airfoil, as an effect of the deflection control on a morphing wing airfoil equipped with a flexible skin. The reference airfoil is the laminar WTEA-TE1 airfoil, on which a flexible skin is located; its geometry is modified by the use of a single point control, where it is assumed that one actuator acts. The Mach number, angle of attack, and deflection allow us to calculate the pressures and transition point positions at each step. The varying inputs are the deflections and the angles of attack. As they both change, the transition point position changes accordingly.

A model of a shape memory alloy has been carried out in the MATLAB<sup>®</sup>/Simulink environment. Hence, the challenge is to perform the control with a shape memory alloy in the closed loop, as it has a nonlinear behaviour. Several controllers, such as a proportional integral derivative controller, a proportional controller, and variable gains, are therefore necessary to control the shape memory alloy and the entire closed loop. Three simulations have been carried out to validate the control. The first simulation keeps the angle of attack constant and is performed for successive deflections. The second simulation considers different steps for the deflection but adds a sinusoidal component for the angle of attack; this simulation is closer to the cruise flight regime. During the third simulation, both the angle of attack and the deflection are modeled as a sinusoidal wave. The outputs (the deflection and the transition point position) are well controlled and the results are very good.

Hence, it is concluded that this original method of control is suitable for the control of the transition point position from the laminar to turbulent region on a morphing wing airfoil.

## 5.1 Introduction

Increases in fuel prices are burning issues that represent the main challenges in the aeronautical field. In the aerospace industry, these issues may be solved by fuel consumption reduction, translated in drag reduction, through a most efficient wing design. To achieve this design, there is the need to obtain a larger part of the laminar flow on the wing, which is equivalent to the transition point displacement toward the trailing edge.

One method of laminar flow improvement studied wing geometry modification by inflating and deflating installed bumps at a certain frequency. Munday et al. [1] used piezoelectric actuators to inflate and deflate bumps on the upper surface of wings in a wind tunnel to determine the transition point displacement. Turbulent flow was thus delayed and the lift coefficient was increased by up to 7%. The flow active control was therefore achieved by modifying the wing geometry.

Another laminar flow study method concerned wing geometry modification by installation and optimization of a bump on the upper surface of the airfoil to improve shock wave control in transonic flow [2]. Optimization of this bump gave a 70% reduction in friction drag and a 15% reduction in the total drag on the wing. Because the bump optimization required a high number of iterations during the numerical aerodynamic analysis, the Euler 2-D code with a boundary-layer correction was chosen to save time. The flow around the optimized wing geometry was studied using a Navier–Stokes code. Sobieczky and Geissler [3] simulated the behaviour of a wing configured with one bump at the leading edge and a second bump at the trailing edge of the upper surface for Mach numbers ranging from 0.72 to 0.77. The results showed a drag reduction of 10%. Yet another method is the modification of the geometry by leading and trailing edge variations.

Martins and Catalano [4] studied drag reduction on adaptive wings for a transport aircraft manufactured by Embraer Aircraft Company. The camber of the adaptive wing airfoil was modified to deform the leading and the trailing edge of the airfoil. The panel method with a boundary-layer correction was used. The transition point moved at 40% from the airfoil

chord (instead of 10%), and the friction drag was reduced by 24%. Powers and Webb [5] performed various flight tests at the NASA Dryden Flight Research Center on an F-111 aircraft. Their results were useful for numerical aerodynamics code validation and showed an increase in the lift coefficient dependent on the wing airfoil geometry modification.

Fibre Bragg gratings (FBGs) were applied to measure dynamic strains inside a subscale wing during a real-time wind-tunnel test [6]. Two recoated FBGs were embedded in the wing skin. The FBG sensor system included a wavelength-swept fibre laser with a wavelength indicator and fast signal processing modules. The agreement among the three sensor types inside the subscale wing (FBG, electric strain gauge, and lead zirconate titanate) was confirmed in a bench test. The optical fibre strain sensors had excellent resolution in the time domain and could detect a frequency response of up to 100 Hz.

In [6], two 16% scale wind-tunnel models, the first one conventional and the other incorporating smart wing design features, were designed and manufactured at NASA for Langley's 16 ft Transonic Dynamic Tunnel. Two series of tests were conducted to evaluate the advantages of the smart wing concept. A key objective of the Smart Wing Phase 1 program was to identify and reduce the risks involved with the integration of smart materials into an actual flight vehicle. The following topics were studied: 1) model design and static testing requirements, 2) design and manufacturing of the shape memory alloy (SMA) control surfaces, 3) system integration, and 4) post-test analysis and planned improvements. Lessons learned from the Phase 1 efforts were discussed along with plans for the Smart Wing Phase 2 program [7].

From the existing literature, there is no controller design using SMAs to move the transition point closer to the trailing edge to improve the laminar flow on a wing. To achieve this goal for the first time, a new algorithm was conceived to determine the transition point positions from the detection of a sudden increase in pressure.

This algorithm, presented in a previous paper [8], used the XFOIL code results obtained in terms of lift, drag, pressure coefficients, and transition point positions vs. the laminar airfoil chord to determine the transition point positions from the pressure distribution simulated with the XFOIL code. It was concluded, because intermediate pressure coefficients for intermediate airfoils could be calculated adequately by use of this new algorithm, that the transition point positions could be determined from wind-tunnel pressure measurements in real time in which airfoil shapes change for various flow conditions characterized by Mach numbers, Reynolds numbers, and angles of attack. A computational fluid dynamics (CFD) database was built for a range of airflow parameters and, by use of this new algorithm, the transition point position was calculated for intermediate wing airfoils and airflow parameters.

In this paper, the design aspects of a laminar flow controller on a wing equipped with flexible skin (localized at 7–65% of the airfoil chord) and an SMA were presented. The wing model built upon the concept shown in this paper, equipped with optical pressure sensors, a controller, and shape memory actuators will be tested in the near future in the wind tunnel. Figure 5.1 shows the scheme of the controller closed loop.

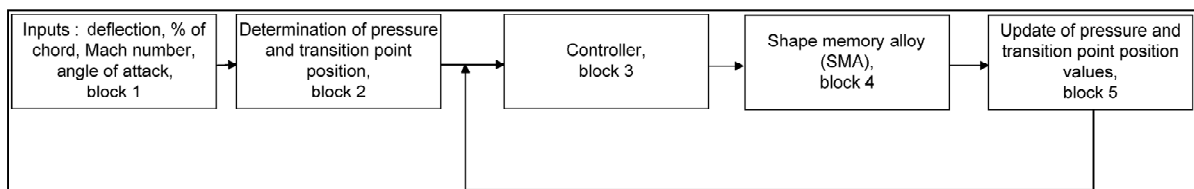


**Figure 5.1** Controller closed loop scheme

For a range of Mach numbers  $M$ , angles of attack, and Reynolds numbers  $Re$  (block 1 in Fig. 1), the upper surface of the airfoil is modified by use of an actuator located at a certain percentage of the chord where its corresponding deflection is obtained. The transition point positions were found from the detection of a sudden increase of pressure by use of the new algorithm [8] and shown in block 2 in Fig. 5.1.

Then, the controller (block 3 in Fig. 5.1) sends a command to the smart actuators (block 4 in Fig. 5.1) located on the flexible airfoil skin to change the wing shape and, therefore, to move the transition point closer to the trailing edge, thus increasing the laminar flow region on the wing airfoil. As a consequence, the laminar flow region becomes more substantial than the turbulent flow region on the upper wing surface and drag coefficients are reduced, which lowers fuel consumption.

The reference airfoil considered in this paper is the laminar WTEA-TE1 airfoil, with its chord of 50 cm. The airfoil coordinates and its data expressed in terms of lift, drag, pressure coefficients, and transition point position vs. the chord were validated experimentally in the wind tunnel and numerically with the XFOil code.

This reference airfoil is modified by use of a single control point localized at 36% of the chord, where it is assumed that one actuator acts, thus creating a deflection from -2 to +2 cm of the upper surface airfoil. Seventeen different airfoils are obtained by Spline interpolation modifying the control point position while maintaining the tangency condition to the fixed points located at 7 and 65% of chord, which are shown in Fig. 5.2.

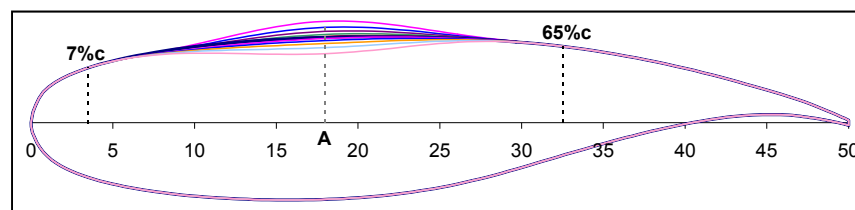


**Figure 5.2** WTEA-TE1 reference airfoil and its modified airfoils shapes.

Details of block 2 (see Fig. 5.1) are shown in Fig. 5.3. The controller simulation and validation are performed here for the following airflow conditions: angles of attack,  $\alpha = -2$  to  $+2$  deg; Reynolds number  $Re = 2.29 \times 10^6$ ; and Mach number,  $M = 0.2$  (see Figs. 5.4– 5.6). These airflow conditions were chosen due to the wind-tunnel airflow limitations. The maximum Mach number in the considered wind tunnel is  $M = 0.35$ .

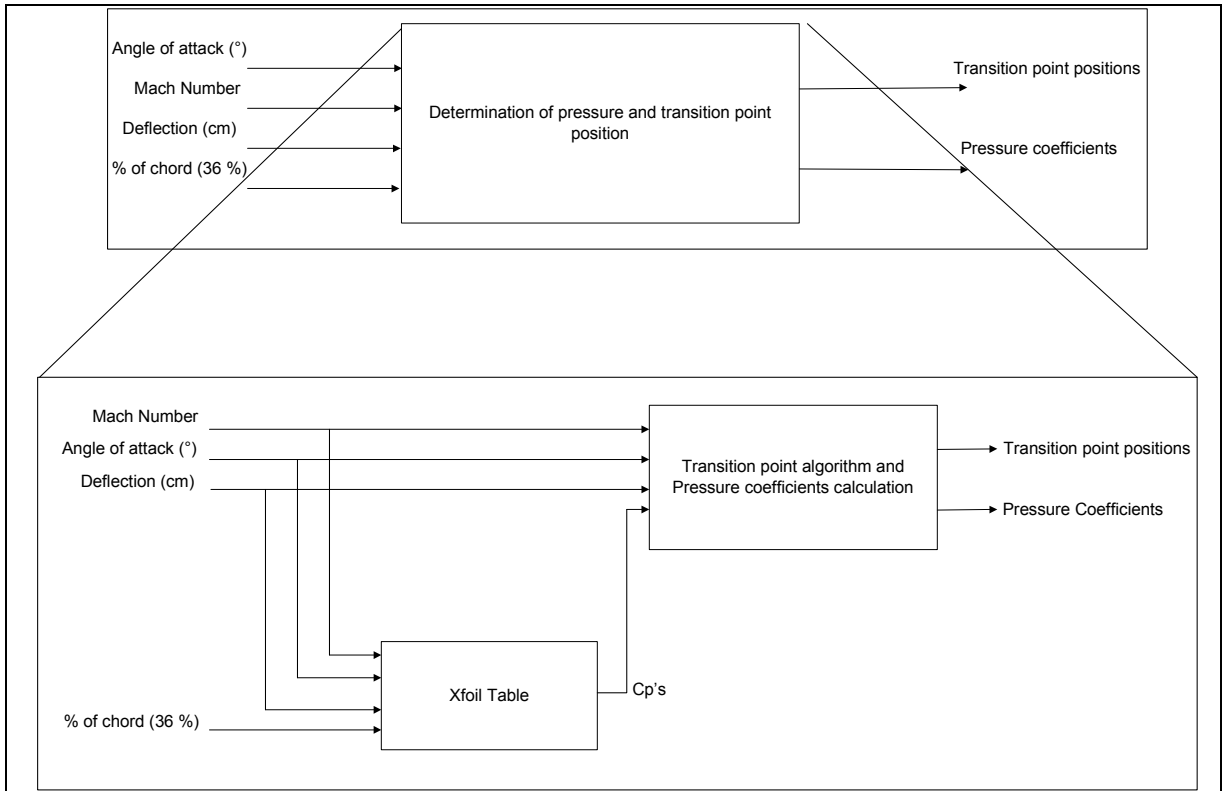


**Figure 5.3** Details of block 2: determination of the pressure coefficients vs. the chord and transition point position [8].

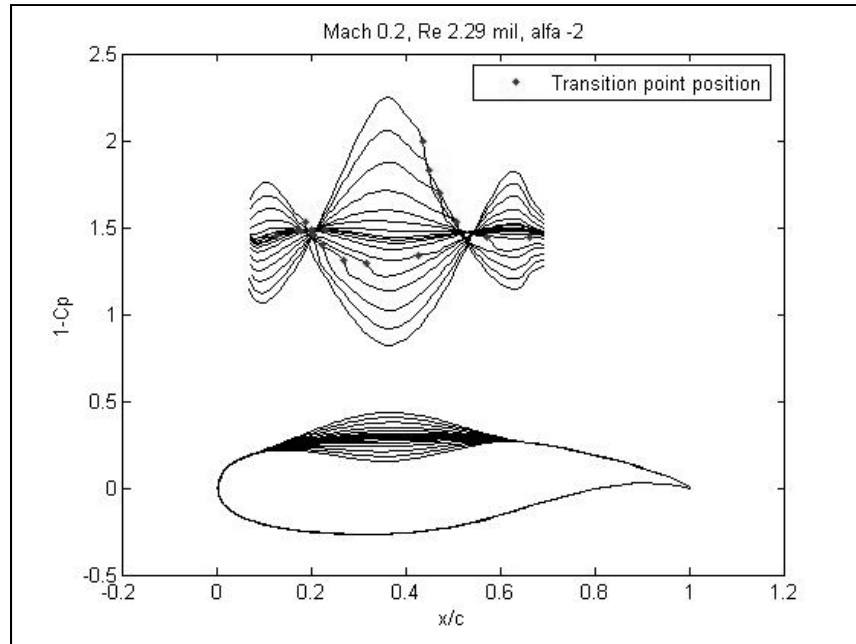


**Figure 5.4** Pressure coefficients vs. the chord computed by XFOIL and the transition point position calculated by the new algorithm for Mach 0.2 and  $\alpha = -2$  deg.

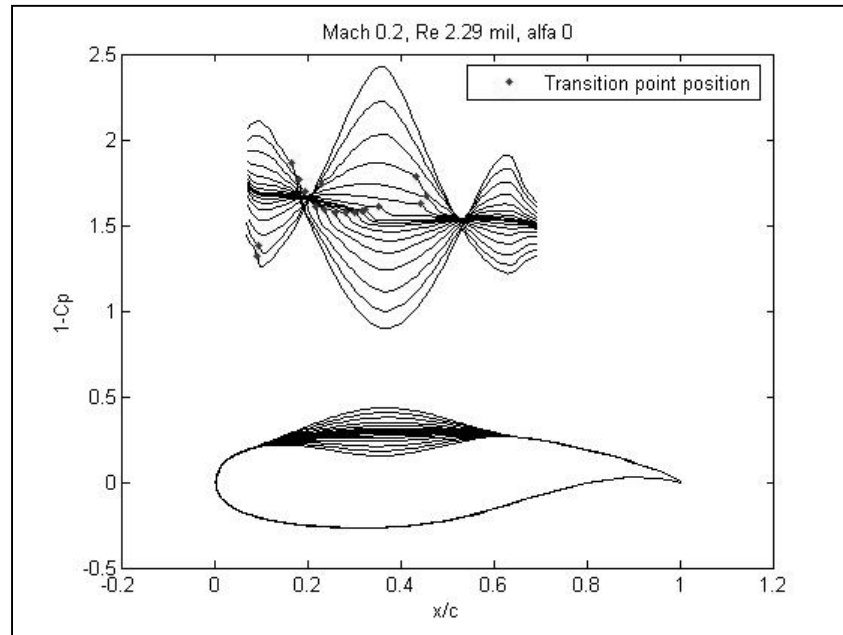


**Figure 5.5** Pressure coefficients vs. the chord computed by XFOIL and the transition point position calculated by the new algorithm for Mach 0.2 and  $\alpha = 0$  deg.

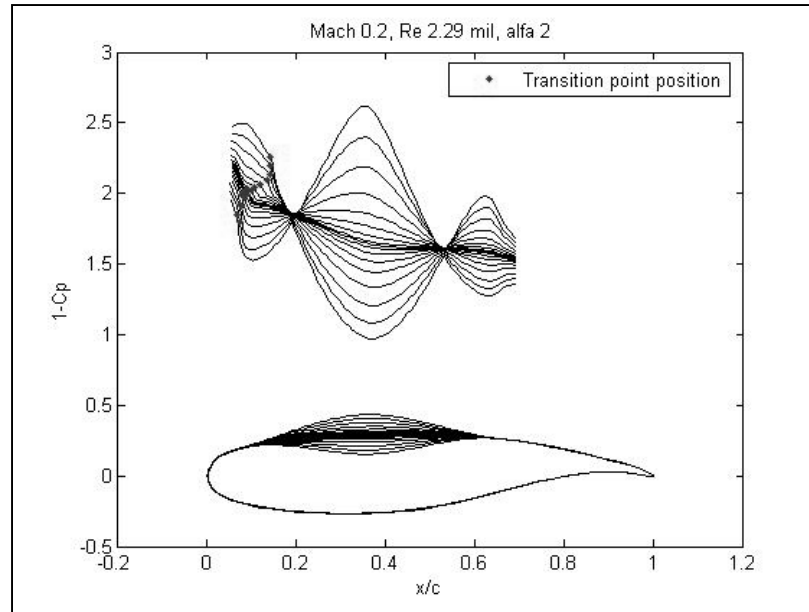


**Figure 5.6** Pressure coefficients vs. the chord computed by Xfoil and the transition point position calculated by the new algorithm for Mach 0.2 and  $\alpha = 2$  deg.

## 5.2 Closed-Loop Controller Design

The controller goal mainly concerns the displacement of the transition point position closer to the trailing edge to produce a higher laminar flow region on the airfoil and, therefore, to control the airfoil deflection for all airflow conditions. The closed loop is composed of three main blocks, as shown in Fig. 5.1: update of pressure and transition point position values, block 5; SMA, block 4; and controller, block 3. Each block is detailed in the following subsections.

### A. Block 2: Determination of Pressure and Transition Point Position

Block 2 receives the values of the four inputs (shown in block 1 in Fig. 5.1) and calculates the values of the pressure coefficients vs. the chord and transition point positions for airflow conditions with the new algorithm [8].

### **B. Block 5: Update of Pressure and Transition Point Position Values**

Block 5 (in Fig. 5.1) is the same as block 2. Block 5 inputs are the angles of attack, the Mach numbers, and the percentage of the chord. The new value of deflection is obtained in block 5 with respect to block 2, for which the deflection is defined as the input. In block 5, the actual deflection is calculated as the output of the SMA block. Hence, block 5 realizes an update of the pressure and the transition point position. The actual pressure and the actual transition point position are therefore obtained at each simulation step.

### **C. Block 4: Shape Memory Alloy**

The SMA block contains the model of the SMA, as shown in Fig. 5.7. The goal of block 4 is to control the airfoil deflection located at 36% of the airfoil chord, created with an SMA. The proportional integral derivative (PID) controller sends a command to the SMA to change the airfoil shape, so that the transition point can move toward the trailing edge. The SMA's functioning principle is shown in Fig. 5.8. The shape memory actuators are manufactured from a Ti–Ni alloy wire. These alloys have the property of exhibiting martensitic transformation when they are deformed at a low temperature phase, and they recover their original shape after heating. In Fig. 5.8, an SMA wire loaded with a mass suspended at the ambient temperature is shown schematically. The load changes the internal forces between the atoms, forcing them to change their positions in the crystals and consequently forcing the wires to lengthen, which is called the SMA activation or the initial phase.

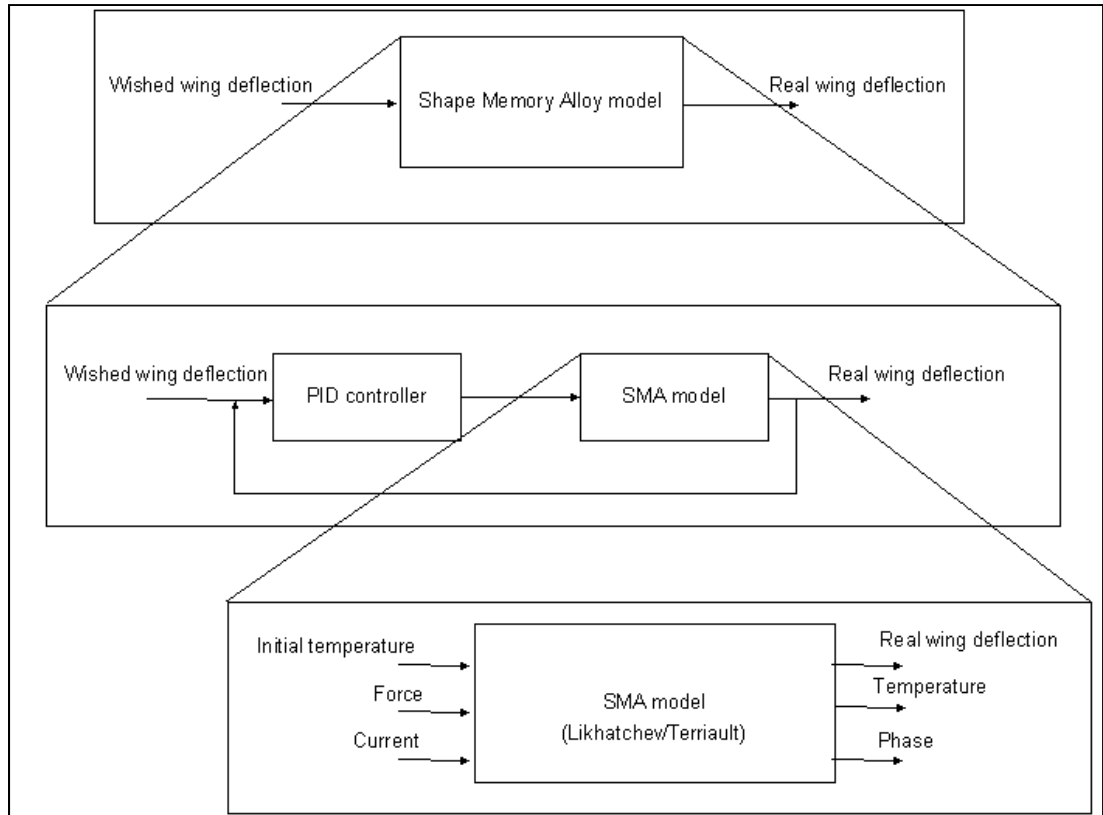


**Figure 5.7** Details of block 4: SMA.

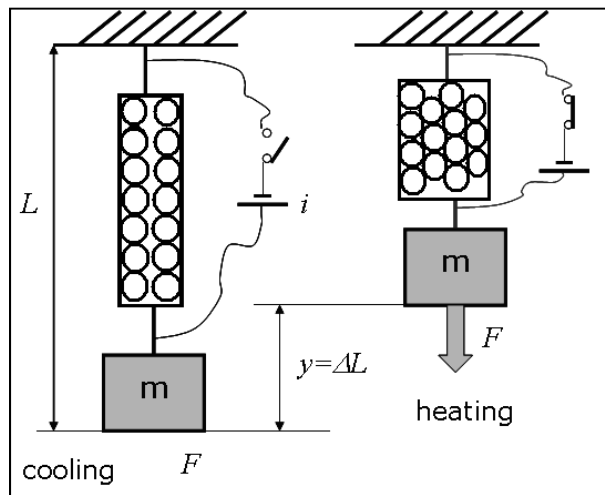


**Figure 5.8** SMA model scheme

When the wire is heated by use of a current, the generated heat by the current resistivity causes the atoms in the crystalline structure to realign and force the alloy to recover its original shape. After that, any change in the internal temperature of the alloy will modify the crystalline structure accordingly and then the exterior shape of the wire. This property of changing the length of the wire as a function of the electrical current that passes through the wire is used for actuation purposes. In this paper, a theoretical SMA model developed by Terriault [9] is used.

The three inputs of this model are the initial temperature  $T_i = 380$  K (see Fig. 6), the current intensity  $i$  of the SMA, and the applied force  $F$  on the SMA. The model simulates the behaviour of an SMA wire length of 0.081 m, which is stretched by a force of 400 N. The wire changes its length by the amount of heat produced by the current that passes through it. The model outputs are the final temperature and the SMA displacement. An SMA has a nonlinear behaviour [10], due to the several phases characterizing its functioning, as shown in Fig. 5.9.

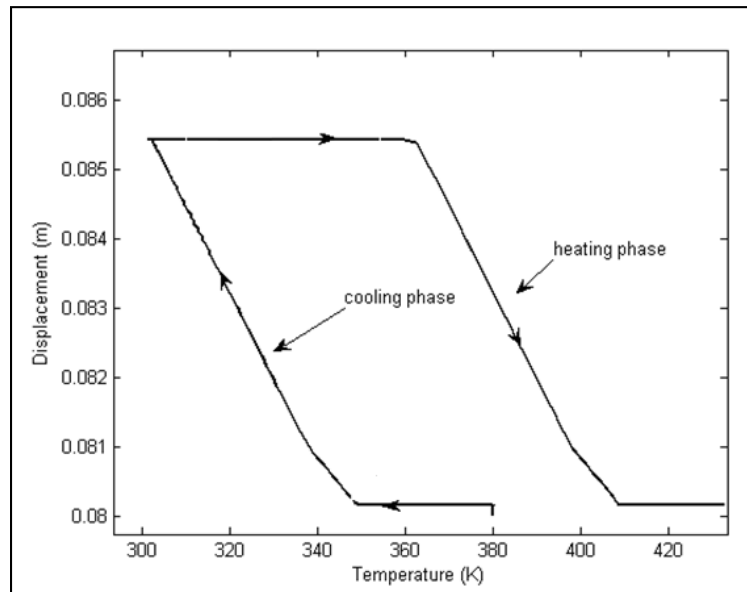


**Figure 5.9** SMA cycle

In this paper, a PID controller is designed to control the SMA. To use the shape-changing characteristics, the SMA needs to be initialized by an external force, which obliges it to go initially through the transformation phase and further to revert to the initial phase through the cooling phase. Before these two phases, the control cannot be realized, due to the intrinsic behaviour of the SMA.

Two methods are used to design the PID controller: the Ziegler–Nichols (ZN) method and the internal model control (IMC) method. These methods are described in Sections 5.6.C.1 and 5.6.C.2.

#### 1. **Ziegler–Nichols Method** [11]

A second-order transfer function  $\frac{K}{(\tau_1 s + 1)(\tau_2 s + 1)} e^{\theta s}$  is obtained to approximate as much as possible the SMA open-loop model behaviour. Hence, we realize an identification of its terms: the static gain  $K$ , the time delay  $\tau_1$ , the time delay  $\tau_2$ , and the dead time  $\theta$ . This step is illustrated in Fig. 5.10.

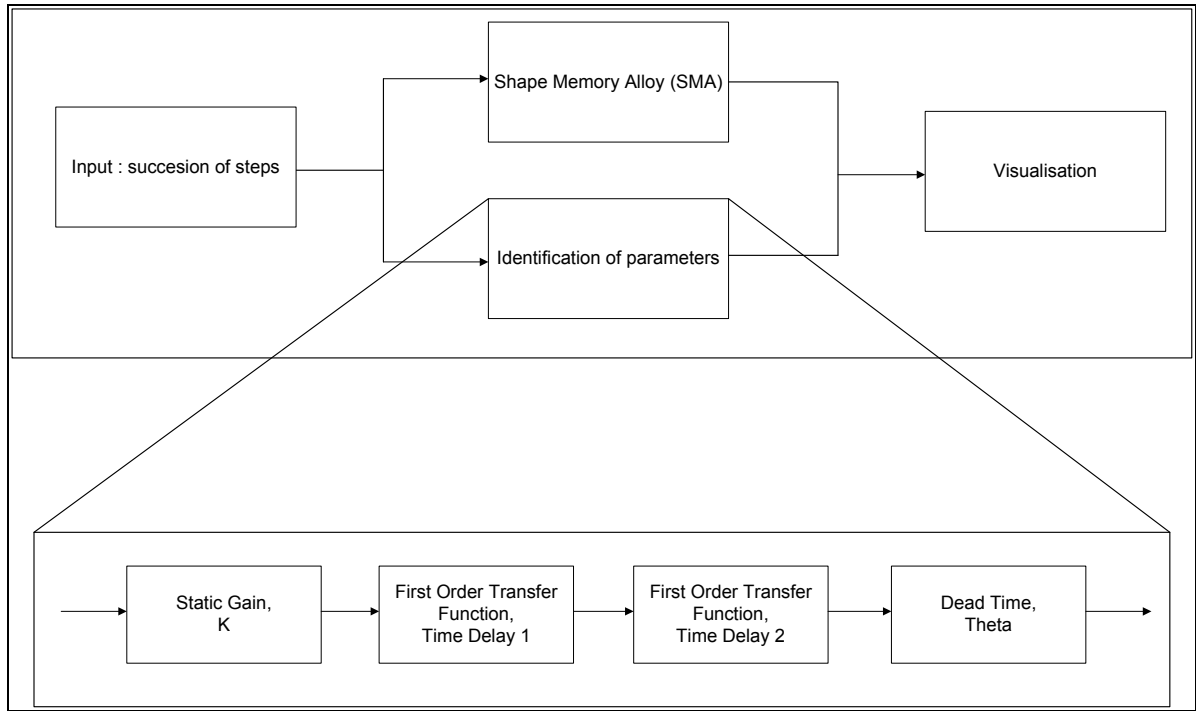


**Figure 5.10 Identification of the SMA's transfer functions.**

The SMA has two phases associated with its behaviour: a *cooling phase* and a *heating phase*. The following two transfer functions were found through parameter identification:

$$TF_{cooling} = \frac{0.0053}{(12s+1)(18s+1)} e^{13s} \text{ and } TF_{heating} = \frac{0.0053}{(3s+1)(10s+1)} e^{17s} \text{ corresponding to Fig. 5.11.}$$

These transfer functions will be used to identify the parameters of the PID controller using the Ziegler–Nichols method.

This method allows for the determination of satisfactory values for each of the three gains ( $K_p$ ,  $K_i$ , and  $K_d$ ) present in the PID controller.  $K_p$  is the proportional gain,  $K_i$  is the integral gain, and  $K_d$  is the derivative gain. To find the values of  $K_p$ ,  $K_i$ , and  $K_d$ , the first step is to determine the values of the critical gain  $K_c$  and the oscillating period  $T_c$ . Gains  $K_i$  and  $K_d$  are set to zero, and only  $K_p$  is used. Gain  $K_p$  is increased until the output starts to oscillate; when

the output starts to oscillate, the critical gain  $K_c$  is found. We measure the value of  $K_c$ , as well as the period of oscillations  $T_c$ .

The second step is to use the values of  $K_c$  and  $T_c$  to find the correct values of  $K_p$ ,  $K_i$ , and  $K_d$ . The following relationships are used to determine these gains [11]:

$$K_p = 0.6 K_c, \quad K_i = 2(K_p/T_c), \quad K_d = K_p(T_c/8) \quad (5.1)$$

Then,  $K_p = 171$ ,  $K_i = 6.22$ , and  $K_d = 1175.60$  are obtained.

The displacement of the actuator vs. the temperature is shown in Fig. 5.11, whereas the displacement of the actuator vs. the time is shown in Fig. 5.12.

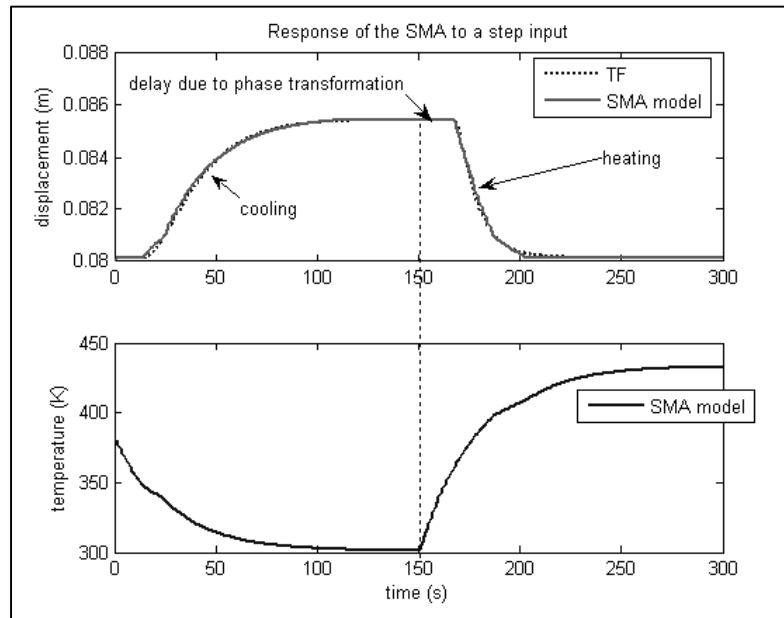


**Figure 5.11** Temperature and actuator displacement vs. time with the SMA model compared with the corresponding transfer functions.

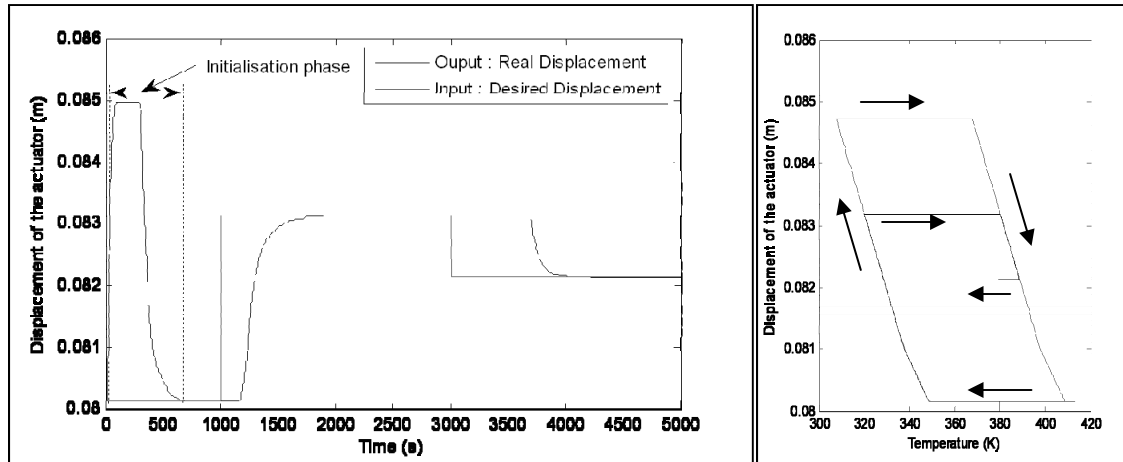


**Figure 5.12 Displacement of the actuator vs. time with the ZN method.**

The input is expressed as two successive steps. From  $t = 0$  to 1000 s, the input remains at 0.0801 m. From  $t = 1000$  to 3000 s, the first step input goes from 0.0801 to 0.0831 m. Then, from  $t = 3000$  to 5000 s, the second step input goes from 0.0831 to 0.0822 m.

*Initialization phase:* This phase corresponds to the first 1000 s. It was found that the input and the output are not the same during this period of time. This difference comes from the intrinsic behaviour of the SMA. Indeed, as seen in Fig. 5.6, the working point has to go through both the transformation and cooling phases before the action of any control on the SMA. This period of time cannot be avoided, and the control cannot be achieved until the working point reaches the end of the cooling phase. Once this period of time is over, the control can act precisely and give satisfactory results. A precision of 0.12% and a time response of 681 s at 0.5% of the input were found.

The precision is defined as

$$precision(\%) = \frac{|output - input|}{|input|} 100 \quad (5.2)$$

*First step:* At  $t = 1000$  s, the input goes from 0.0801 to 0.0831 m. We found a precision of 0.02% and a time response of 374 s.

*Second step:* At  $t = 3000$  s, the input goes from 0.0831 to 0.0822 m. We found a precision of 0.03% and a time response of 748 s.

## 2. Internal Model Control Method

The IMC [12] is another method to determine the values of the PID parameters. Two steps are followed in this method. The second step of the IMC method is to evaluate the  $K_p$ ,  $K_i$ , and  $K_d$  gains by use of Eqs. (5.3) in a closed loop. The closed loop shown in Fig. 5.7 is considered, not the one shown in Fig. 5.1.

$$K_p = \frac{\tau_1 + \tau_2}{K(\theta + \tau_c)}, \quad K_i = \frac{1}{K(\theta + \tau_c)}, \quad K_d = \frac{\tau_1 \tau_2}{K(\theta + \tau_c)} \quad (5.3)$$

The presence of the new term  $\tau_c$  is noticed, which is the controller time delay, and is used in this method as an additional degree of freedom. Its value is modified to find the best control of the SMA model. The actuator displacement vs. the temperature and the actuator displacement vs. the time are shown in Fig. 5.13 for several values of  $\tau_c$ .

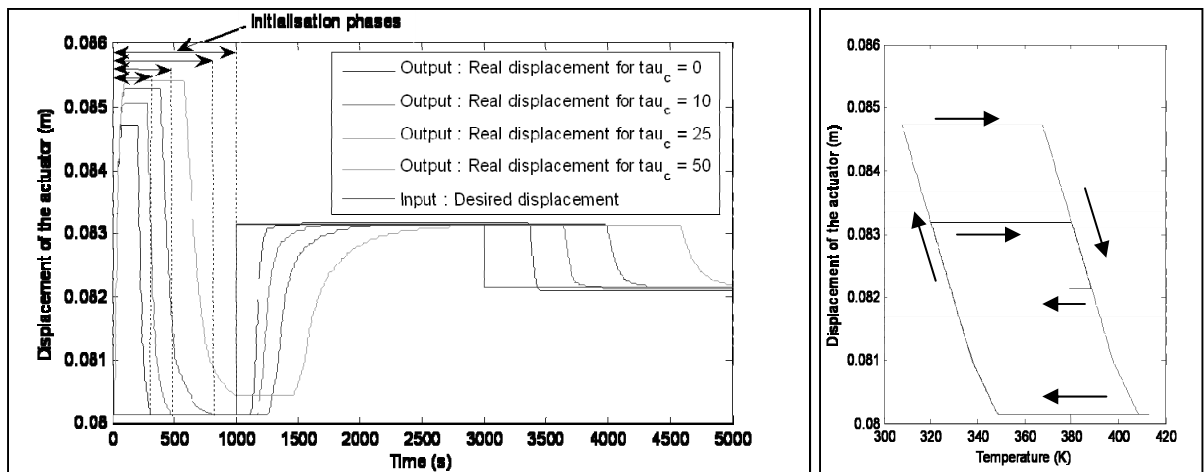


**Figure 5.13** Actuator displacements vs. time with the IMC method for several  $\tau_c$ .

The same successive steps as the ones used for the ZN method are then enforced. The best value following different cases of  $\tau_c$  is noticed in the case in which  $\tau_c = 0$ , showing the shortest time delay and shortest time response. Gains  $K_p = 144.28$ ,  $K_i = 11.10$ , and  $K_d = 332.96$  are hence obtained.

*Initialization phase:* This phase corresponds to the first 1000 s. The input and the output are not the same during this period. The difference between them comes from the intrinsic behaviour of the SMA. Indeed, as seen in Fig. 5.9, the working point has to go through both the transformation and cooling phases before the action of any SMA control. This phase cannot be avoided, and the control cannot be achieved until the working point reaches the end of the cooling phase. Once this period is over, the control can act precisely and give satisfactory results. It was found a precision of 0.07% and a time response of 297 s.

*First step:* At  $t = 1000$  s, the input goes from 0.0801 to 0.0831 m. We notice a precision of 0.09% and a time response of 208 s.

*Second step:* At  $t = 3000$  s, the input goes from 0.0831 to 0.0822 m. We notice a precision of 0.23% and a time response of 381 s.

### 3. Comparison of Results Obtained with Both Methods

To choose between these two methods, we can compare the obtained results on the same graph (see Fig. 5.14). It is clear that the parameters  $K_p$ ,  $K_i$ , and  $K_d$  found with the IMC method for  $\tau_c = 0$  are better than the ones found with the ZN method.

Even though the precision is a bit better with the ZN method, the time delay and time response is by far better with the IMC method, as shown in Table 5.1. It was decided to use the IMC method for the design of the PID controller.

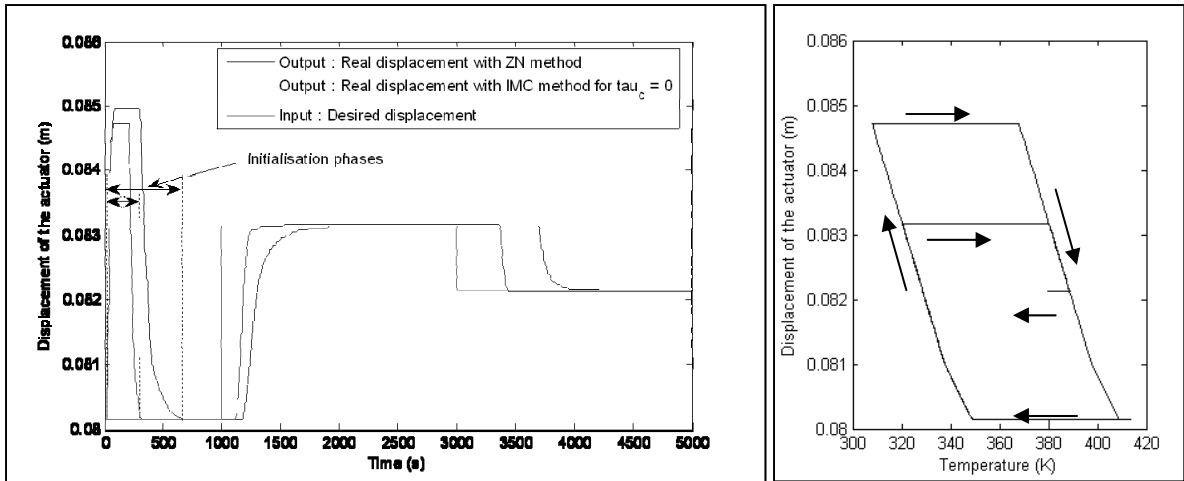


**Figure 5.14 Displacement of actuator vs. time with the ZN and IMC methods.**

#### 4. Control improvement

Even though the controller works properly, it was decided to reduce the time response during the cooling phase. Indeed, the controller designed with the IMC method has a dead time  $\theta$ , which creates a long time response, especially in the cooling phase. The idea here is to disconnect the controller action during the cooling phase, which means when the desired deflection is physically higher than the actual deflection. The controller action was disconnected with the instruction  $i = 0$  A in the SMA by use of the algorithm shown in Fig. 5.15.

The oscillations that appear are caused by the inertia of the SMA's heat transfer during the cooling and heating phase. Indeed, with a current of 0 A, the sign of the quantity “desired deflection minus actual deflection” continuously changes. Therefore, a switch was done continuously in our algorithm (Fig. 5.15), thus creating oscillations.

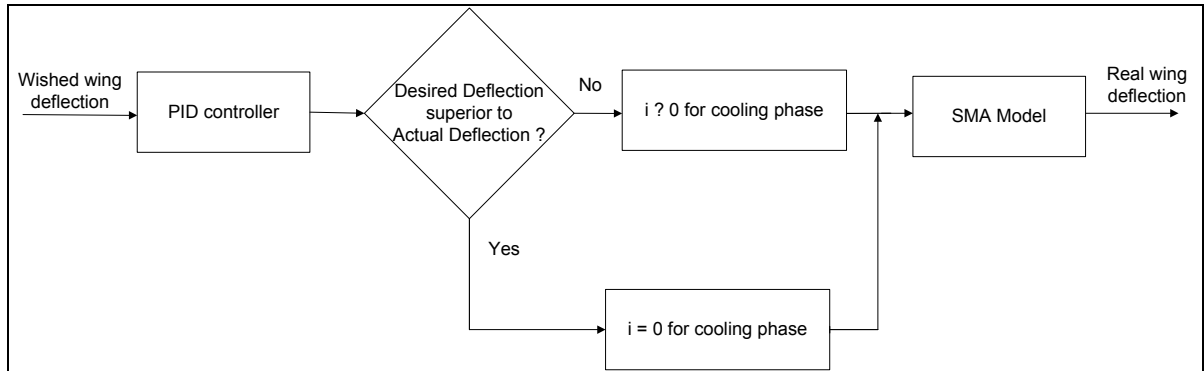


**Figure 5.15 Algorithm for SMA control improvement.**

The goal of the “desired deflection superior to actual deflection” block is to control the airfoil deflection. It is located in the whole closed loop (Fig. 5.1), whereas the PID designed in the previous paragraph is only located in the SMA block.

Two types of closed-loop dynamics exist (Fig. 5.1). On one hand, we have a very fast dynamic in block 2 of Fig. 5.3, with our real-time algorithm that should react as fast as possible. On the other hand, in block 4 of Fig. 5.4, we have a very slow dynamic with very high time responses. For this reason, the PID controller located in the SMA block is not capable of controlling the whole closed loop of Fig. 5.1. It was thus necessary to create a controller block located before the SMA block in the closed loop to deal with those two dynamics. This controller block is composed of two types of gains: a fixed proportional gain and a variable gain. The proportional gain reduces the inertia of the system created by the SMA model. The variable gain adjusts the controller as a function of the deflection value entered as the input (block 1 in Fig. 5.1). Results expressed in terms of actuator displacement variation with time are represented in Fig. 5.16.

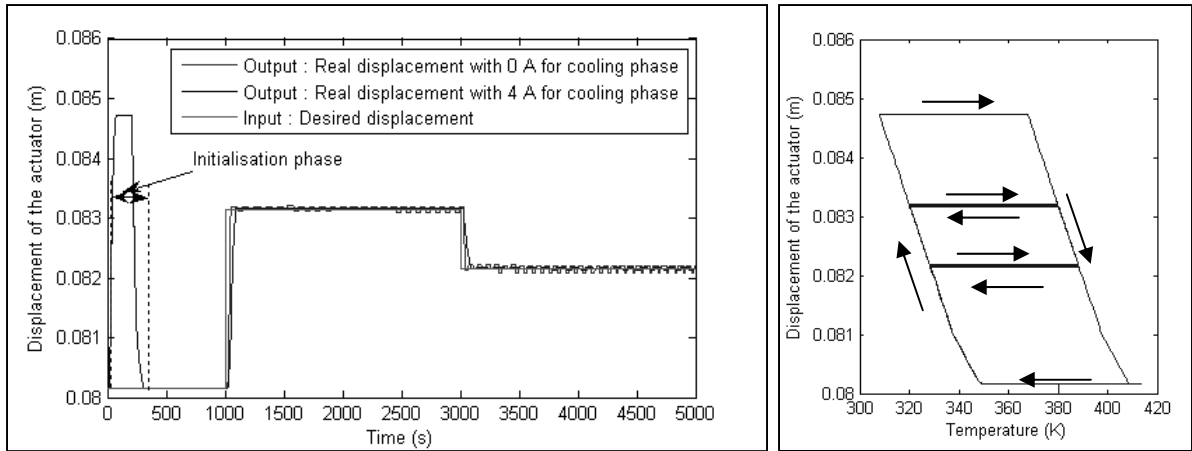


**Figure 5.16 Displacement of the actuator vs. time with the new algorithm.**

### 5.3 Results and Discussion

Three different types of simulations, one with a step input and a constant  $\alpha$  and two with a step input and a sinusoidal  $\alpha$ , were performed to validate the controller design (two located in the controller block and one in the SMA block) for the following airflow conditions: Mach number  $M = 0.2$ , temperature  $T = 288.15$  K, and Reynolds number  $Re = 2.29 \times 10^6$ . The point at which the actuator acts was located at 36% of the chord of the airfoil. The results obtained from these three types of simulations are represented and discussed in terms of airfoil deflections and transition point positions vs. time in Sections. 5.6. A–5.6.C. Three phases are present in these simulations: the initialization phase, the first deflection, and the second deflection. Details of the controller shown in block 3 are given in Fig. 5.17.

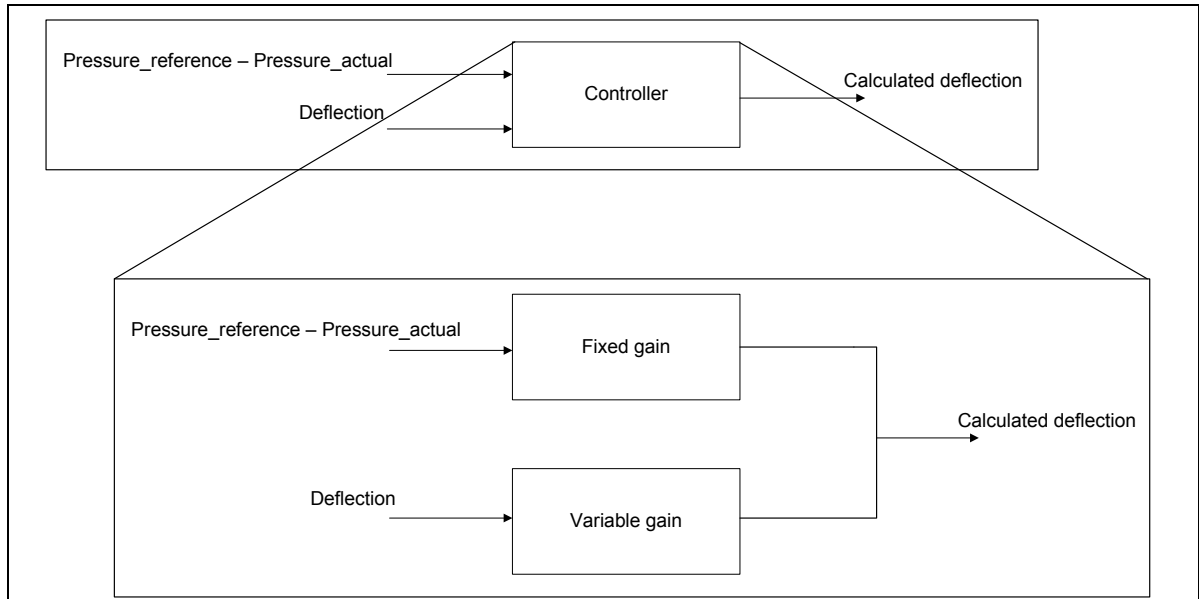


**Figure 5.17** Details of block 3: controller.

### A. First Simulation Type

During the first simulation, the angle of attack  $\alpha = 0$  deg, whereas the airfoil deflection time variation is as follows: 1) from  $t = 0$  to 500 s, the deflection remains at 0 mm; 2) from  $t = 500$  to 1000 s, the deflection varies from 0 to 20 mm; and 3) from  $t = 1000$  to 1500 s, the deflection varies from 20 to 10 mm. Results are shown in Fig. 5.18.

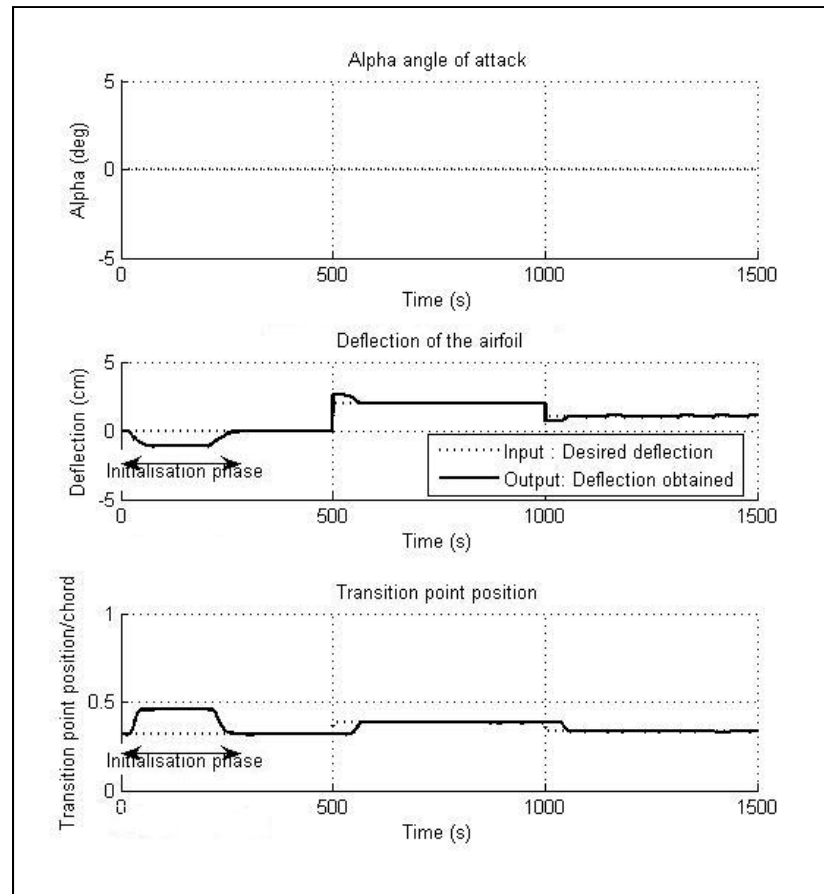


**Figure 5.18 First simulation type results.**

*Initialization phase:* During the initialization phase, more precisely, during the first 500 s, the airfoil deflection input remains at 0 cm. It is seen that, during the first 200 s, the input is different from the output. During this time period of 200 s, the SMA has to go through both the transformation and cooling phases (see Fig. 5.6). This time period cannot be avoided as it is intrinsic to the SMA numerical model and actually lasts 200 s. The control cannot be achieved until the working point has reached the end of the cooling phase. This initialization phase does not exist in the practical experiments and is a bug of the simulation model. Following this 200 s time period, it is seen that the transition point position and the airfoil deflection are well controlled, as both of them match well with the input. The transition point position was found to be at 31% of the chord by use of the transition point position algorithm

(block 2 in Fig. 5.1). A precision of 0.03% for the airfoil deflection and of 0.04% for the transition point position was found.

*First airfoil deflection:* At  $t = 500$  s, a deflection from 0 to 2 cm is enforced, which corresponds to the displacement of the transition point position from 31 to 38% of the chord according to the algorithm described in [8]. The transition point and the deflection are controlled efficiently, as the time response is fast. Even though there is an overshoot, the time response and the precision are satisfactory for both the airfoil deflection and the transition point position. A precision of 0.5% for the airfoil deflection and of 0.02% for the transition point position is found. The time response is 56 s for the deflection.

*Second airfoil deflection:* At  $t = 1000$  s, a second airfoil deflection from 2 to 1 cm is given, which corresponds to a displacement of the transition point position between 38 and 33%. The system time response and the precision are satisfactory. A precision of 4.7% for the deflection and of 1.5% for the transition point position are obtained. The time response is 53 s for the airfoil deflection.

## **B. Second Simulation Type**

In this simulation, the angle of attack is modeled as a sinus function with a 2 deg amplitude and with a frequency of 0.01 rad/s, whereas the airfoil deflection varies with time as follows: 1) from  $t = 0$  to 500 s, the deflection remains at 0 mm; 2) from  $t = 500$  to 1000 s, the deflection varies from 0 to 20 mm; and 3) from  $t = 1000$  to 1500 s, the deflection varies from 20 to 10 mm.

The choice of the sinusoidal wave input for the angle of attack is justified by the fact that it corresponds to the small variations of the angle of attack around 0 deg in the cruise regime, where the angle of attack may be continuously varying. The obtained results are shown in Fig. 5.19.

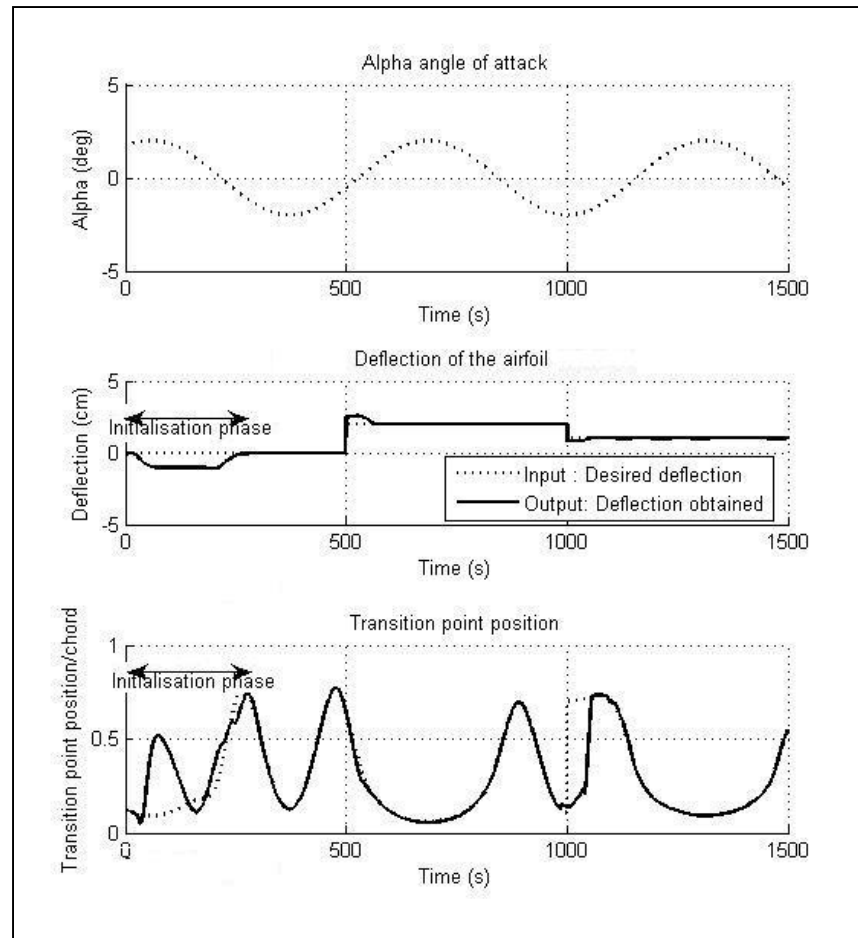


**Figure 5.19** Second simulation type results

It was found that the airfoil deflection is well controlled. The variation of the angle of attack in the second simulation with respect to its variation in the first simulation has no influence on the airfoil deflection control, as this airfoil deflection remains the same as during the first simulation. Only the transition point position oscillates and varies continuously due to the angle of attack sine wave variation. The transition point position is very sensitive to small variations of the angle of attack (see Figs. 5.4–5.6), which explains the oscillations of the transition point position in Fig. 5.19.

*Initialization phase:* During the first 500 s, the input deflection remains at 0 cm. During this phase, the transition point position (as the output) does not fit its input, due to the nonlinear

behaviour of the SMA. After the 200 s of initialization, the transition point position control is well achieved. The position of the transition point varies very much, from 7 to 75% of the airfoil chord; it fills the whole range of values accepted for the transition point. We found a precision of 0.03% for the deflection and of 0.04% for the transition point position.

*First deflection:* At  $t = 500$  s, a deflection from 0 to 2 cm is enforced. A small overshoot is seen in Fig. 5.18. A precision of 0.5% for the airfoil deflection and of 0.12% for the transition point position is found. The time response is 56 s for the airfoil deflection.

*Second deflection:* At  $t = 1000$  s, a deflection from 2 to 1 cm is given to the airfoil. A precision of 4.7% for the airfoil deflection and of 0.02% for the transition point position are found. The time response is 53 s for the airfoil deflection.

### C. Third Simulation Type

The goal of this third simulation is to highlight that changing the shape of the airfoil concretely allows the displacement of the transition point position toward the trailing edge. In this simulation, the angle of attack is modeled as sinusoidal functions with 2 deg amplitude and a frequency of 0.01 rad/s, whereas the deflection has the same frequency but is in anti-phase to the alpha oscillations and has amplitudes of 0.5 cm. Results are shown in Fig. 5.20.

*Initialization phase:* During this phase, the transition point position and the deflection do not fit the respective inputs, due to the nonlinear behaviour of the SMA. After the 200 s of initialization, the control is well achieved. The position of the transition point varies from 9 to 55% of the chord. The deflection varies from -1.5 to 0 cm.

*After the initialization phase:* During the next 1250 s, the control is satisfactory. It is noticed that the change of the shape of the airfoil allows us to move the transition point position toward the trailing edge. For small negative angles of attack, amplitude of the deflection of 0.5 cm is the optimum for maintaining the transition point the furthest to the trailing edge.

From Figs. 5.6 and 5.20, it can be seen that for positive angles of attack the transition point position is minimally influenced by the deflection of the airfoil shape.

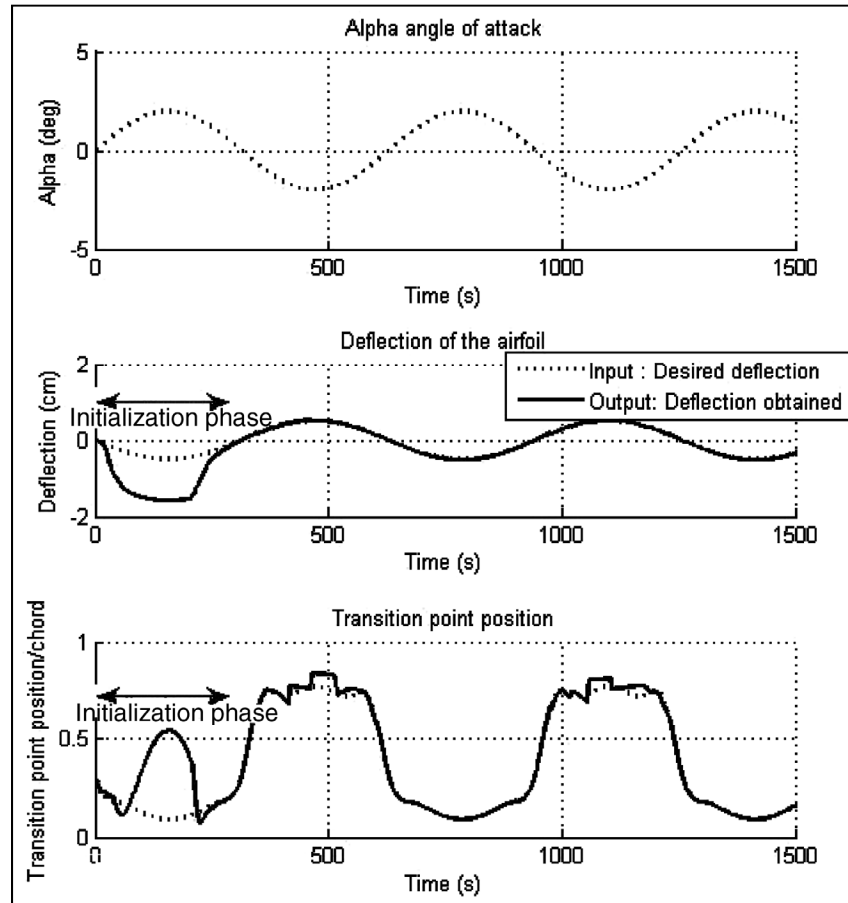


**Figure 5.20** Third simulation type results

#### 5.4 Conclusions

This paper presents an easy implementation of controlling the deflection on a morphing wing airfoil equipped with actuators, sensors, and flexible skin, which ultimately has an effect on the transition point position. The realization of the control has been carried out in two steps. The first step was to control the SMA block (block 4 in Fig. 5.1). The SMA has a nonlinear behaviour with a slow dynamic. The IMC method was preferred to the ZN method as it provided better results. Once the closed loop inside the SMA block has been controlled, then the whole closed loop is controlled. The whole closed loop has a very fast dynamic, because

of the real-time controller located in the determination of the pressure coefficients vs. chord and transition point position block (block 2 in Fig. 5.1). For this reason, a controller block (block 3 in Fig. 5.1) is necessary. The proportional gain reduces the inertia of the system created by the SMA model. The variable gain adjusts the control as a function of the deflection value entered as the input (block 1 in Fig. 5.1).

The simulations validated our choice of design, as fast and precise responses are obtained. The main advantage of this new and original method is its simplicity and its incorporation in experimental applications, such as in the controller of a morphing wing model. It is the first time that such a controller design concept is presented.

### **Acknowledgments**

We would like to thank Patrick Terriault for the modeling of the shape memory alloy in the MATLAB/Simulink environment. We would also like to thank Mahmoud Mamou and Mahmoud Khalid from the National Research Council of Canada Institute for Aerospace Research for the WTEA-TE1 airfoil modeling. We would like to thank George-Henri Simon and Philippe Molaret from Thales Avionics and also Eric Laurendeau from Bombardier Aeronautics for their collaboration on this paper. We would like to thank aerospace companies Thales Avionics, Bombardier Aerospace, and the Consortium of Research in the Aerospace Industry in Quebec for the funds that allowed the realization of this research as well as their collaboration in this work.

### **References**

- [1] Munday, D., Jacob, J. D., Hauser, T., and Huang, G., 2002, *Experimental and Numerical Investigation of Aerodynamic Flow Control Using Oscillating Adaptive Surfaces*, AIAA Paper 2002-2837.
- [2] Wadehn, W., Sommerer, A., Lutz, T., Fokin, D., Pritschow, G., and Wagner, S., 2002, *Structural Concepts and Aerodynamic Design of Shock Control Bumps*, ICAS Paper 66R1.1, Sept.

- [3] Sobieczky, H., and Geissler, W., 1999, *Active Flow Control Based on Transonic Design Concepts*, AIAA Paper 99-3127.
- [4] Martins, A. L., and Catalano, F. M., 2003, *Drag Optimization for Transport Aircraft Mission Adaptive Wing*, Journal of the Brazilian Society of Mechanical Sciences and Engineering, Vol. 25, No. 1, pp. 1–8.  
doi:10.1590/S1678-58782003000100001.
- [5] Powers, S. G., and Webb, L. D., 1997, *Flight Wing Surface Pressure and Boundary-Layer Data Report from the F-111 Smooth Variable-Camber Supercritical Mission Adaptive Wing*, NASA TM-4789.
- [6] Lee, J.-R., Ryu, C.-Y., Koo, B.-Y., Kang, S.-G., Hong, C.-S., and Kim, C.-G., 2003, *In-Flight Health Monitoring of a Subscale Wing Using a Fibre Bragg Grating Sensor System*, Smart Materials and Structures, Vol. 12, No. 1, Feb., pp. 147–155.  
doi:10.1088/0964-1726/12/1/317.
- [7] Martin, C. A., Bartley-Cho, J. D., and Flanagan, J. S., 1999, *Design and Fabrication of Smart Wing Wind Tunnel Model and SMA Control Surfaces*, Conference of Smart Structures and Materials 1999: Industrial and Commercial Applications of Smart Structures Technologies, Vol. 3674, Society of Photo-Optical Instrumentation Engineers, pp. 237–248.  
doi:10.1117/12.351562.
- [8] Popov, A., Botez, R. M., and Labib, M., 2008, *Transition Point Detection from the Surface Pressure Distribution for Controller Design*, Journal of Aircraft, Vol. 45, No. 1, pp. 23–28.  
doi:10.2514/1.31488.
- [9] Brailovski, V., Prokoshkin, S., Terriault, P., and Trochu, F. (eds.), 2003, *Shape Memory Alloys: Fundamentals, Modeling and Applications*, École de Technologie Supérieure, Montreal, ISBN 2-921145-42-1.
- [10] Song, G., Kelly, B., and Agrawal, B. N., 2000, *Active Position Control of a Shape Memory Alloy Wire Actuated Composite Beam*, Smart Materials and Structures, Vol. 9, No. 5, pp. 711–716.  
doi:10.1088/0964-1726/9/5/316.
- [11] Ziegler, J. G., and Nichols, N. B., 1942, *Optimum Settings for Automatic Controllers*, Transactions of the American Society of Mechanical Engineers, Vol. 64, No. 8, pp. 759–768.

- [12] Rivera, D. E., Morari, M., and Skogestad, S., 1986, *Internal Model Control: PID Controller Design*, *Industrial and Engineering Chemistry Process Design and Development*, Vol. 25, No. 1, pp. 252–265.  
doi:10.1021/i200032a041.

## CHAPTER 6

### ARTICLE 3

#### VARIATIONS IN OPTICAL SENSOR PRESSURE MEASUREMENTS DUE TO TEMPERATURE IN WIND-TUNNEL TESTING

Andrei Vladimir Popov and Ruxandra Mihaela Botez  
École de Technologie Supérieure, Montréal, Québec H3C 1K3, Canada  
Mahmoud Mamou, National Research Council, Ottawa, Ontario K1A 0R6, Canada  
and Lucian Teodor Grigorie, École de Technologie Supérieure,  
Montréal, Québec H3C 1K3, Canada

This article was published in AIAA Journal of Aircraft, Vol. 46, No.4, July-August 2009.  
DOI: 10.2514/1.40715

#### Article presentation

The article shows the results of the first wind tunnel tests performed in the project on June 15<sup>th</sup> 2007, at the NRC-IAR 2 m × 3 m wind tunnel. The purpose of this test was to verify the capability of optical sensors in the detection of the airfoil characteristics over a wing model. This wing model had an NACA 4415 airfoil with a span of 4 ft (1.2 m) and a chord of 18 inch (0.4572 m), and was fitted with nine pressure taps, four optical sensors and one Kulite sensor. The optical sensors signals were compared with the pressure taps and Kulite sensor signal in order to validate the correct measurements of the sensors.

The post-processing of the aerodynamic data (pressures) presented in this article was mainly done by me in collaboration with the other co-authors from LARCASE and IAR-NRC. My main contribution in this paper was the conception of the new algorithm for optical sensors measurements corrections with temperatures.

At the first visualization of the pressure signals, we observed an offset between the pressures tap values and optical sensors values. The offsets between the mean values measured by optical sensors and pressure values measured by pressure taps followed a uniform rule variation with Mach number and angle of attack, which led to the conclusion that the optical

sensors had calibration errors. We also observed a match between the static temperature variations during the tests and the offset values. The article shows the new correction made to the pressure value recorded by predicting the local temperature of the airflow where the pressure was measured by the optical sensors.

The conclusion drawn from this test was that the optical sensors have an offset reading proportional to the local temperature, which changed on the boundary layer during experiments in wind tunnel tests by changing Mach number or angle of attack. It was possible to correct this drift if the optical sensors were equipped with thermocouples that compensate pressure variation readings in real time.

The optical sensors signals were studied through spectral analysis in order to verify the sensors' ability to detect the transition, as shown in the Section 3.2.3, *Modeling and simulation of optical sensor measurements*. This analysis determined that the optical sensors' sampling rate of 1000 samples/sec was too low to detect the Tolmien-Schlichting waves frequencies. The sensors spectra showed only the background noise in the 0–500 Hz frequency band. It was concluded that in the future test, we need to use optical sensors with higher sampling rates (10 or 20 kHz, if possible) and to apply temperature compensation to the pressure reading because of the high sensitivity of these types of sensors to temperature variations.

## **Résumé**

Dans cet article sont présentés les enregistrements effectués dans les tests en soufflerie par des capteurs optiques de pression. Vingt et un tests ont été effectués pour des différents nombres de Mach, angles d'incidence et nombres de Reynolds dans la soufflerie de 2 m × 3 m de l'Institut de Recherche Aérospatiale du Conseil National de Recherche du Canada. Une demi-aile rectangulaire d'envergure finie, avec un profil NACA 4415 a été utilisée pour l'installation des capteurs de pression, capteurs optiques et un capteur Kulite. Le nombre de Mach a été varié entre 0.1 et 0.3 et l'angle d'incidence a été varié entre -3 et 3 degrés. Les

valeurs de pressions non-stationnaires ont été enregistrées et les coefficients de pression moyenne des trois types de capteurs ont été comparés. Des corrections de température ont été effectuées pour les enregistrements de capteurs optiques de pression. Des comparaisons ont été effectuées entre les prédictions théorétiques calculées par le logiciel XFoil, et on a obtenu des erreurs moyennes petites de moins de 10% entre les valeurs mesurées et prédites.

### **Abstract**

In this paper, wind-tunnel measurements are presented for the airflow fluctuation detection using pressure optical sensors. Twenty-one wind-tunnel test runs for various Mach numbers, angles of attack, and Reynolds numbers were performed in the  $6 \times 9 \text{ ft}^2$  wind tunnel at the Institute for Aerospace Research at the National Research Council Canada. A rectangular finite aspect ratio half-wing, having a NACA4415 cross section, was considered with its upper surface instrumented with pressure taps, pressure optical sensors, and one Kulite transducer. The Mach number was varied from 0.1 to 0.3 and the angle of attack range was within  $-3$  to  $3$  deg. Unsteady pressure signals were recorded and a thorough comparison, in terms of unsteady and mean pressure coefficients, was performed between the measurements from the three sets of pressure transducers. Temperature corrections were considered in the pressure measurements by optical sensors. Comparisons were also performed against theoretical predictions using the XFoil computational fluid dynamics code, and mean errors smaller than 10% were noticed between the measured and the predicted data.

### **6.1 Introduction**

The modern era of aviation opened a new horizon of research for drag reduction through morphing an adaptive wing, which is motivated by rising fuel costs and environmental concerns. The concept relies on delaying the transition location toward the wing trailing edge by morphing the upper surface of the wing. Several authors have studied this concept from a theoretical point of view [1,2]. The main objective of this concept is to promote large laminar regions on the wing surface, thus reducing drag over an operating range of flow conditions characterized by Mach numbers, airspeeds, and angles of attack [3]. The airborne

modification of an aircraft wing airfoil shape can be realized continuously to maintain laminar flow over the wing surface as flight conditions change. To achieve such a full operating concept, a closed control system has to be developed to link the flow fluctuations over the wing surface to the deformation mechanism (actuators). The flow fluctuation signals can be detected by conventional pressure transducers or the new emerging pressure optical sensors. Linked to a controller system, the collected data would be treated in real time aiming to identify the location of transition and then sending a signal to the actuator system to adjust the wind surface to delay the transition location. Several measurement techniques for transition detection were developed in the past using various pressure transducers such as microphones [4], hot films [5–8], and piezoelectric [9] and Kulite sensors [10]. Usually, this type of transducer could be intrusive to the flow past the wing. In this paper, to avoid such transducer and flow interaction, optical sensors are chosen as they can be mounted right on the model surface with sealed taps.

In the present theoretical and experimental investigation, the performance of the pressure optical sensors is assessed in static and dynamic modes. Unsteady pressure signals were recorded and reduced for wind-tunnel wall interference. The measured data were confronted against pressure tap and Kulite transducers data. Flow simulations, using XFOIL code, were also performed for the same wind-tunnel flow conditions and the predicted results, obtained in terms of pressure coefficients and transition location, were compared with the measured data, for various Mach numbers, angles of attack, and Reynolds numbers.

## **6.2 Experimental setup description**

The wind-tunnel tests were performed at the Institute for Aerospace Research at the National Research Council Canada Uplands facilities in Ottawa. The purpose of these tests was to verify the capabilities of optical sensors to detect the pressures and flow transition on a half-wing in a wind tunnel. This wing had a NACA 4415 airfoil with a span of 4 ft (1.2 m) and a chord of 18 in. (0.4572 m), and was equipped with nine pressure taps (PT) connected to a Scanivalve ZOC™ Kulite, one Kulite (KU) sensor, and four optical sensors (OS). Their positions on the wing are shown in Fig. 1. The Kulite sensor was connected through the

Precision Filter 27000. The filter provides a 6-pole Butterworth function and the sampling rate was set to 1 kHz for the entire test. The Kulite has a sensitivity of 18.14 mV/psi at 5 V excitation. The Precision Filter gain was set to 100 providing a full scale voltage at 2.5 psi of 4.535 V to the electrical interface module. The optical sensors were set to provide 1 V/0.5 psi out of the analog output port which corresponds to 5V at 2.5 psi.

The optical sensors used in this experiment are micro-electromechanical systems based fibre optic pressure sensors of 2.5 mm, diameter of 10 mm, range of 5 psid, resolution less than 0.0005 psi, and precision of  $\pm 0.005$  psi. The pressure taps and Kulite sensor were referenced to the wind-tunnel static pressure during the test runs, whereas the optical sensors were not referenced. The optical sensors were set to zero before the test was run, their indications giving a gage pressure with respect to the static pressure value of the wind off air.

The pressure information for pressure taps, Kulite sensor, and optical sensors was recorded through 18 channels; for redundancy two channels were used for each optical sensor. Optical sensors OS2, 3, and 4 were installed at the same chord position  $x/c$  as two pressure taps; PT2, OS2, and PT3 were installed at the same  $x/c = 0.3$ ; PT4, KU, and PT5 were installed at the same  $x/c = 0.4$ ; PT6, OS3, and PT7 were installed at the same  $x/c = 0.5$ ; and PT8, OS4, and PT9 were installed at the same  $x/c = 0.625$ . Only the first optical sensor was installed at different  $x/c$  as follows: PT1 was installed at  $x/c = 0.2$ , OS1 was installed at  $x/c = 0.25$ , and PT2 was installed at  $x/c = 0.3$ .

The model was installed vertically in the wind tunnel for 21 airflow cases characterized by three Mach numbers  $M = 0.1, 0.15, \text{ and } 0.2$  and seven angles of attack  $\alpha = 3, 2, 1, 0, -1, -2, \text{ and } -3$  deg. The wind-tunnel tests were conducted as follows: for each angle-of attack  $\alpha$  setting, a “run” was recorded during which the airspeed was varied from Mach number  $M = 0.1$ , which was recorded as “point number 1,” to Mach number  $M = 0.15$ , which was recorded as “point number 2,” and finally to Mach number  $M = 0.2$ , which was recorded as “point number 3.” Figure 6.1 shows the positions of the sensors on the upper surface airfoil of the wing.

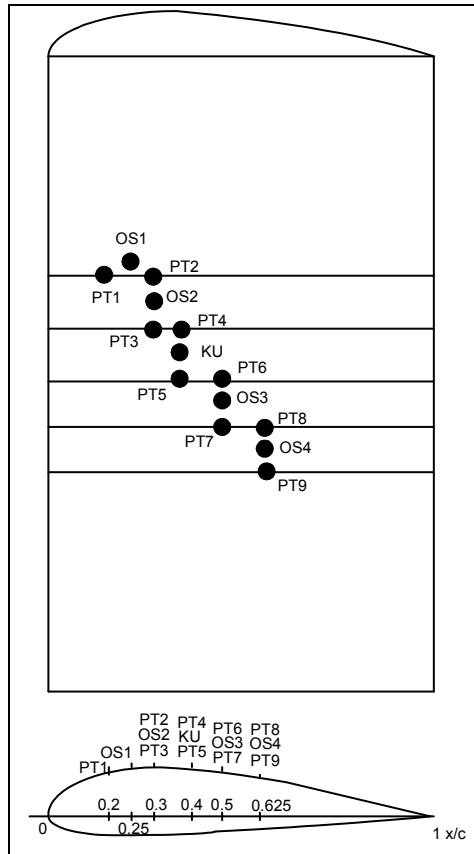


**Figure 6.1** Positions of the sensors on the upper surface airfoil during a wind-tunnel test.

### 6.3 Wind-Tunnel Data Post-processing Details

An offset was observed between the pressures taps and the optical sensors values, as gage pressure signals were first visualized as shown in Fig. 6.2. It was found that three pressure taps gave wrong signals, as their tubes were pinched during installation. The pinched tube pressure signals could be identified as signals with the least oscillations, whereas they (the pinched tube signals) show the highest offsets from the theoretical calculated pressures (predicted pressure values). Figure 6.2 shows the time history for a pinched tube signal PT7, a correct pressure tap signal PT6, and an optical sensor signal OS3.

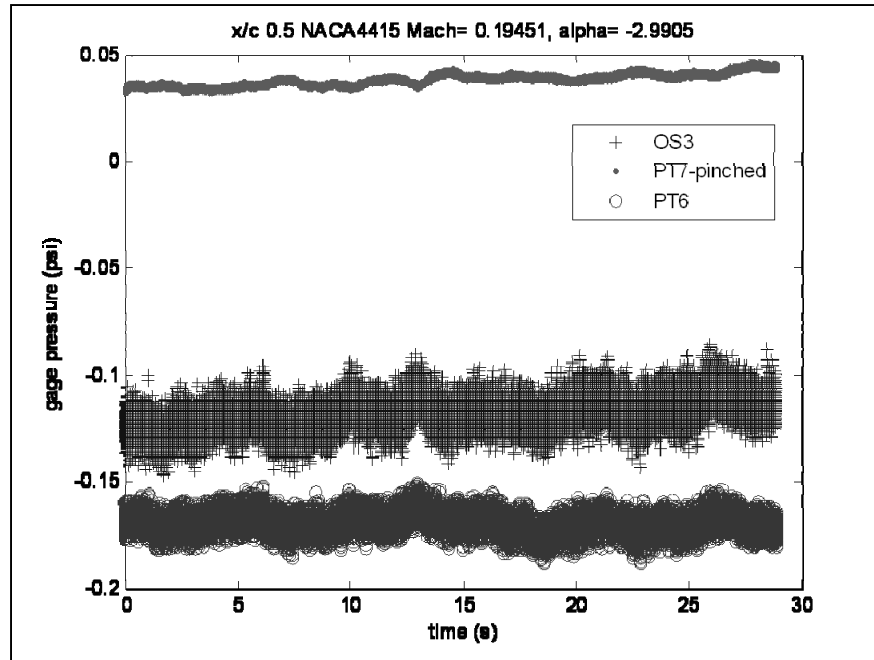


**Figure 6.2** Gage pressure signals recorded by optical sensors and pressure taps during 29 s.

We observed that the offsets between the mean pressure values of OS and PT followed uniform rule variations with Mach number  $M$  and angle of attack  $\alpha$ , as shown in Fig. 6.3, which led to the conclusion that calibration errors of optical sensors were done. We observed that these offsets shown in Fig. 6.3 have the same shape as the static temperature variations during the 21 tests shown in Fig. 6.4. In both Figs. 6.3 and 6.4, the abscise axes showed the run numbers in chronological order from 1 to 21 (Table 6.1).

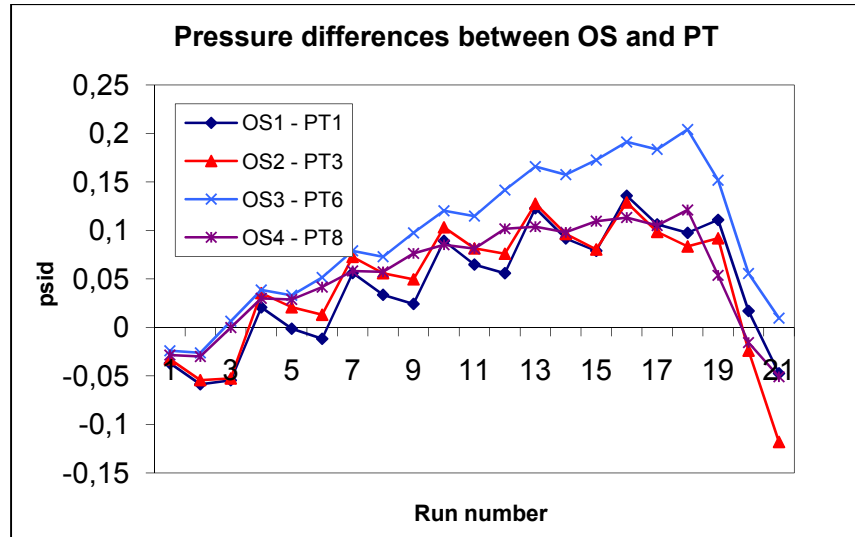


Figure 6.3 Differential pressures between gage pressures measured by optical sensors OS and gage pressures measured by pressure taps PT.

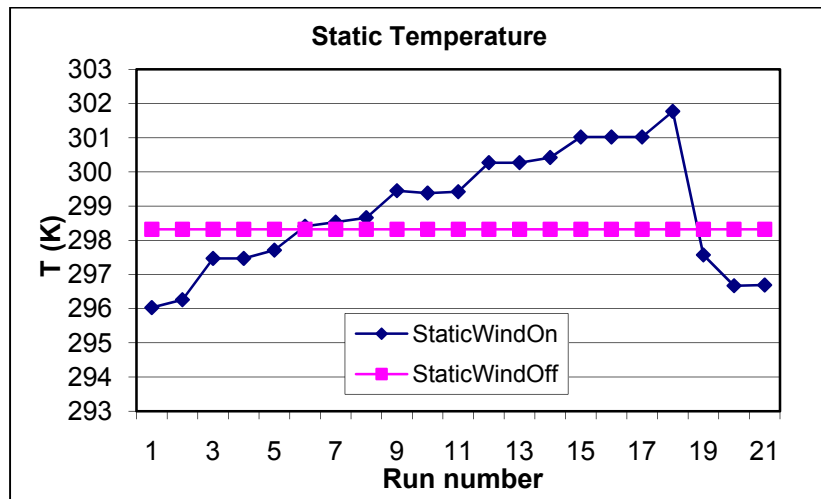


Figure 6.4 Static air temperatures variations during 21 runs in the Wind Tunnel.

Table 6.1 Airflow cases dependent of angles of attack  $\alpha$ , Mach numbers  $M$ , Reynolds numbers  $Re$  and static temperatures wind on  $T_{static}$

<b>Airflow case</b>	<b>Angle of attack <math>\alpha</math> (deg)</b>	<b>Mach number</b>	<b>Reynolds number</b>	<b>Static Temperature Wind On (deg K)</b>
1	0.1842	0.1020	1.04e+06	296.03
2	0.1691	0.1546	1.58e+06	296.26
3	0.172	0.1951	1.98e+06	297.47
4	-2.98	0.1014	1.03e+06	297.64
5	-2.98	0.1542	1.57e+06	297.71
6	-2.99	0.1945	1.96e+06	298.41
7	-1.92	0.1014	1.03e+06	298.53
8	-1.92	0.1534	1.55e+06	298.66
9	-1.92	0.1947	1.96e+06	299.45
10	-0.87	0.1005	1.02e+06	299.38
11	-0.87	0.1534	1.55e+06	299.42
12	-0.87	0.1946	1.95e+06	300.27
13	1.242	0.1007	1.01e+06	300.27
14	1.237	0.1534	1.54e+06	300.42
15	1.236	0.1942	1.94e+06	301.02
16	2.279	0.1006	1.01e+06	301.02
17	2.275	0.1532	1.53e+06	301.02
18	2.275	0.1937	1.93e+06	301.77
19	3.317	0.1008	1.03e+06	297.57
20	3.313	0.154	1.57e+06	296.67
21	3.312	0.1958	1.99e+06	296.69

When the temperature recorded during these 21 runs was verified, a static temperature increase was observed when the wind was on. The first run static temperature was found below the static air temperature when the wind was off, but during the next runs, due to the air friction with the tunnel walls and screens, the static temperature increased as shown in Fig. 6.4. At the 19<sup>th</sup> test point, the automatic cooling system of the wind tunnel activated, causing a static temperature sudden decrease from 302 to 296.7°C.

Each optical sensor was calibrated at the beginning of the tests at the static temperature wind off  $T_0$ , which corresponds to the total air temperature. The static temperature  $T_0$  at each optical sensor position was calculated with the following equation:

$$T_0 = T_{s\infty} (1 + 0.2M_{\infty}^2) = T_{sOS} (1 + 0.2M_{OS}^2) \quad (6.1)$$

The optical sensor pressure coefficients  $C_{pOS}$  were calculated from their recorded mean pressures in the wind tunnel by use of Eq. (6.2). The airflow speeds  $V_{OS}$  at the location of optical sensors were calculated with Eq. (6.3) from their pressure coefficients. Then, the local Mach number  $M_{OS}$  was further calculated for the airflow at the location of each optical sensor from the knowledge of their correspondent airflow speeds  $V_{OS}$  by Eq. (6.4):

$$C_{pOS} = \frac{\Delta p_{OS}}{Q_{\infty}} \quad (6.2)$$

$$V_{OS} = U_{\infty} \sqrt{1 - C_{pOS}} \quad (6.3)$$

$$M_{OS} = \frac{V_{OS}}{a(T_{\infty})} \quad (6.4)$$

The optical sensor static temperature  $T_{sOS}$  was further calculated with Eq. (6.1), in which  $T_{s1}$  was the air static temperature when the wind was on. The correction was made by use of optical sensor pressure variation with temperature provided by the sensor manufacturer (Table 6.2) as follows:

$$\Delta p = \frac{dp}{dT} \Delta T + \Delta_r p \quad (6.5)$$

where  $\Delta T$  was the difference between the temperature calculated at the sensor location  $T_{sOS}$  and the temperature of its calibration from the test beginning  $T_s$ . We used the value of static temperature of 296 K (23°C) as reference temperature for sensor correction. Each optical sensor has a pressure deviation with the temperature  $\Delta p/\Delta T$  of 0.026–0.037 psi/°C and a temperature reading deviation  $\Delta_r p$  (see Table 6.2).

Table 6.2 Optical sensor readings with respect to temperature and pressure variations given by the manufacturer

<b>Optical Sensor OS no.</b>	<b>Temperature deviation psi / deg C</b>	<b>Reading deviation of mean pressure psi</b>
OS1	0.037	- 1.11%
OS2	0.030	- 0.65%
OS3	0.037	- 1.02%
OS4	0.026	- 0.62%

#### 6.4 Results Analysis

Each airflow case was simulated in Xfoil code to predict the  $C_p$  distribution and transition point position.  $N_{cr} = 7$  was used in the simulation to match the turbulence level of 0.14% measured in the wind tunnel using Mack's correlation [11]. The simulated gage pressures on the NACA 4415 airfoil calculated by use of the Xfoil code were traced versus the gage pressures measured by pressure taps PT, by optical sensors, by corrected optical sensors OS by use of Eq. (6.5), and by Kulite sensors KU. These types of results were traced for each airflow case from 1 to 21. An example of the plotted results is shown in Fig. 6.5. The optical and Kulite sensor's gage pressures were compared versus the gage pressures measured by

pressure taps for all 21 runs by use of relative error calculations. The gage pressure is defined as follows:

$$P_{gage} = P_{abs} - p_0 = \frac{\rho V_{\infty}^2}{2} (C_p - 1) \quad (6.6)$$

where  $p_0$  is the total pressure defined in Eq. (6.7) and  $C_p$  is defined as the pressure coefficient in Eq. (6.8).

$$p_0 = p_{\infty} + \frac{\rho V_{\infty}^2}{2} \quad (6.7)$$

$$C_p = \frac{P_{abs} - P_{\infty}}{\frac{\rho V_{\infty}^2}{2}} \quad (6.8)$$

Then, the gage pressure relative error is defined in following equation (6.9):

$$error_{gage} = \frac{|P_{gageOS} - P_{gagePT}|}{P_{gagePT}} \quad (6.9)$$

The relative errors for gage pressure measured by optical sensors versus the gage pressure measured by pressure taps are given in Table 6.3. Gage pressure of the first optical sensor cannot be compared to gage pressure for the first pressure tap as they are not at the same chord position  $x/c$ . From Table 6.3, only results obtained for case 19 are the worst, which is the case when the cooling system of the wind tunnel automatically activated. These results are visualized in Fig. 6.6. The relative errors for gage pressures measured by optical sensors versus the gage pressures calculated with the XFOIL computational fluid dynamics code at the same chord positions are given in Table 6.4.

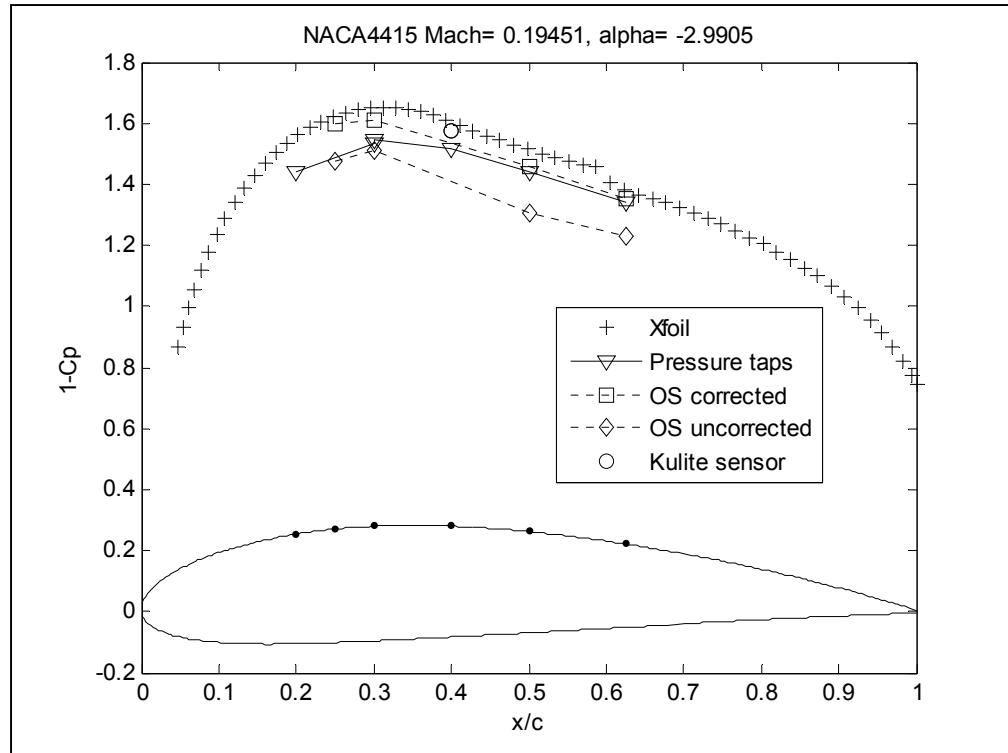


**Figure 6.5 Pressure coefficients distribution plotted over the wind-tunnel model airfoil's upper surface.**

### 6.5 Transition detection

From the direct visualization of signals recorded during wind-tunnel tests, it was observed that optical sensors' signals were much noisier than the pressure taps and Kulite sensors. The turbulent waves begin to develop in the range of Tollmien–Schlichting frequency of  $\sim 1000$  Hz [9, 12]. Therefore, the optical sensors acquisition unit, according to the Shannon–Nyquist theorem, should have the minimum sampling rate frequency of 2000 Hz to detect the flow transition, and the optimum sampling rate should be 4000 Hz [9, 13]. Because of the fact that the optical sensors acquisition unit had the sampling frequency of 1000 Hz, it was not possible to detect the airflow transition.

Table 6.3 Relative errors between OS and PT measured results for 21 airflow cases

<b>Run no.</b>	<b><math>\alpha</math></b>	<b><math>M</math></b>	<b>OS2 – PT2</b>	<b>OS3 – PT6</b>	<b>OS4 – PT8</b>
1	0.17	0.102	12.51%	7.92%	15.03%
2	0.17	0.154	9.15%	3.06%	6.54%
3	0.17	0.195	9.13%	1.83%	3.26%
4	-2.98	0.101	5.52%	7.60%	4.81%
5	-2.98	0.154	3.82%	2.49%	1.39%
6	-2.98	0.195	4.87%	1.09%	0.79%
7	-1.92	0.101	0.51%	3.06%	1.44%
8	-1.92	0.153	1.89%	1.12%	0.31%
9	-1.92	0.195	3.98%	0.40%	0.73%
10	-0.87	0.101	3.88%	2.95%	1.87%
11	-0.87	0.153	0.69%	2.41%	1.13%
12	-0.87	0.195	3.39%	2.68%	1.53%
13	1.24	0.101	3.30%	10.00%	0.93%
14	1.24	0.153	3.53%	4.16%	1.09%
15	1.24	0.194	4.95%	3.61%	0.15%
16	2.28	0.101	6.08%	8.95%	6.78%
17	2.28	0.153	6.23%	5.27%	3.11%
18	2.28	0.194	6.93%	4.36%	1.29%
19	3.31	0.101	25.13%	53.49%	11.33%
20	3.31	0.154	4.02%	12.62%	4.91%
21	3.31	0.196	12.40%	3.52%	7.53%
Mean error of OS versus PT pressures for 21 cases			<b>6.28%</b>	<b>6.79%</b>	<b>3.62%</b>

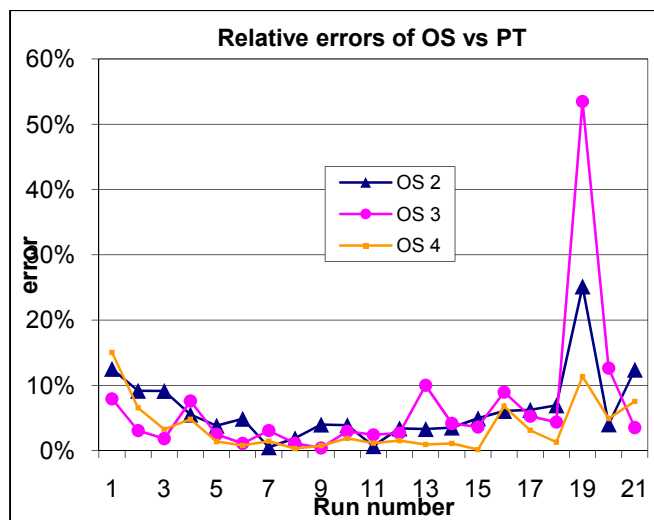


**Figure 6.6** Visualization of relative errors of optical sensors versus pressure taps during 21 runs in the wind tunnel.

Table 6.4 Mean error between OS measured and XFoil calculated results for 21 airflow cases

Run no.	$\alpha$	$M$	OS1 vs XFoil	OS2 vs XFoil	OS3 vs XFoil	OS4 vs XFoil
1	0.17	0.102	4.53%	2.32%	2.61%	5.57%
2	0.17	0.154	7.94%	4.84%	6.82%	0.87%
3	0.17	0.195	8.37%	5.23%	5.49%	4.07%
4	-2.98	0.101	3.08%	5.13%	1.24%	1.16%
5	-2.98	0.154	1.77%	4.21%	1.96%	3.63%
6	-2.98	0.195	1.55%	2.41%	3.72%	1.98%
7	-1.92	0.101	3.13%	8.68%	1.58%	3.16%
8	-1.92	0.153	0.66%	4.79%	2.86%	2.95%
9	-1.92	0.195	1.11%	2.90%	4.99%	3.66%
10	-0.87	0.101	2.71%	14.80%	9.72%	5.16%
11	-0.87	0.153	6.48%	9.91%	10.17%	6.33%
12	-0.87	0.195	5.35%	6.52%	8.17%	6.21%
13	1.24	0.101	6.53%	16.11%	17.79%	6.60%
14	1.24	0.153	8.71%	10.40%	10.70%	5.97%
15	1.24	0.194	9.93%	9.34%	10.60%	7.10%
16	2.28	0.101	1.95%	8.46%	13.41%	1.02%
17	2.28	0.153	8.88%	9.08%	12.74%	4.66%
18	2.28	0.194	10.40%	8.75%	12.41%	6.62%
19	3.31	0.101	41.65%	35.96%	56.87%	18.18%
20	3.31	0.154	21.72%	11.98%	20.49%	3.70%
21	3.31	0.196	15.28%	4.46%	11.27%	1.02%
Mean error of OS gage versus XFoil computed pressures for 21 cases			<b>8.18%</b>	<b>8.87%</b>	<b>10.74%</b>	<b>4.74%</b>

## 6.6 Conclusions

It was found that optical sensors can be used for the pressure measurements on the surface of the model, provided that each sensor has a thermocouple installed at the same position. These thermocouples should provide the optical sensor static temperatures for an accurate reading of their pressures. A new feature in this paper is the correction of the optical sensor readings using the static temperature recorded in the airflow upstream of the wind-tunnel test section.

In the absence of thermocouples, the local temperature at the position of each optical sensor was estimated as shown in the previous paragraph. By taking into account the various elements that might introduce errors, fairly accurate pressure readings were obtained.

The turbulent boundary-layer investigation demonstrated that optical sensors were found to be a good alternative to the classical present technologies using Kulite sensors or piezoelectric or hot film sensors, provided the acquisition unit of the optical signal has a minimum sampling rate of 2000 Hz.

## References

- [1] Jacob, J. D., 1998, *On the Fluid Dynamics of Adaptive Airfoils*, Proceedings of ASME International Mechanical Engineering Congress and Exposition, American Society of Mechanical Engineers, Fairfield, NJ, 15–20 Nov. 1998, pp. 1–10.
- [2] Driver, J., and Zingg, D. W., 2006, *Optimized Natural-Laminar-Flow Airfoils*, 44th AIAA Aerospace Sciences Meeting and Exhibit, AIAA, Reston, VA, 9–12 Jan. pp. 1–16; also AIAA Paper 2006-247, 2006.
- [3] Zingg, D.W., Diosady, L., and Billing, L., 2006, *Adaptive Airfoils for Drag Reduction at Transonic Speeds*, 24th Applied Aerodynamics Conference, AIAA, Reston, VA, 5–8 June 2006, pp. 1–15; also AIAA Paper 2006-3656.
- [4] Rioual, J.-L., Nelson, P. A., and Fisher, M. J., 1994, *Experiments on the Automatic Control of Boundary-Layer Transition*, Journal of Aircraft, Vol. 31, No. 6, pp. 1416–1418.  
doi:10.2514/3.46668.

- [5] Mangalam, S. M., 2004, *Real-Time Extraction of Hydrodynamic Flow Characteristics Using Surface Signature*, IEEE Journal of Oceanic Engineering, Vol. 29, No. 3, July pp. 622–630.  
doi:10.1109/JOE.2004.833098.
- [6] Krishnan, V., Sundaram, S., and Viswanath, P. R., 2000, *Transition Related Studies on Two Low-Drag Airfoils*, Current Science, Vol. 79, No. 6, pp. 829–833.
- [7] Khalid, M., 1987, *The Use of Hot-Film Technique for Boundary Layer Studies on a 21% Thick Airfoil*, Aeronautical Note NAE-AN-45, NRC No. 27892, Ottawa, May.
- [8] Haussmann, F., and Schroder, W., 2006, *Coated Hot-Film Sensors for Transition Detection in Cruise Flight*, Journal of Aircraft, Vol. 43, No. 2, March–April pp. 456–465.  
doi:10.2514/1.14825.
- [9] Nitsche, T., Mirow, P., and Dorfler, T., 1990, *Investigations on Flow Instabilities on Airfoils by Means of Piezofilm-Arrays*, Laminar-Turbulent Transition IUTAM Symposium Toulouse, France 1989, Springer–Verlag, Berlin/Heidelberg, pp. 129–135.
- [10] Tang, F. C., and Brown, D., 1980, *Flow Quality Measurements in the NAE 5 FT × 5 FT Blowdown Wind Tunnel Using an Instrumented 10° Cone*, 53rd Semianual Meeting of the Supersonic Tunnel Association at the NASA Ames Research Center, 26–28 March.
- [11] Drela, M., 2003, *Implicit Implementation of the Full  $e^N$  Transition Criterion*, 21st Applied Aerodynamics Conference, AIAA, Reston, VA, 23–26 June pp. 1–8; also AIAA Paper 2003–4066.
- [12] Schubauer, G., and Skramstad, H., 1947, *Laminar Boundary Layer Oscillations and Transition on a Flat Plate*, NACA TR 909.
- [13] Lee, T., Petrakis, G., Kafyeke, F., and Mokhtarian, F., 1999, *Non-Intrusive Characterization of the Airfoil Boundary Layer at Low Reynolds Numbers*, Canadian Aeronautics and Space Journal, Vol. 45, No. 1, March pp. 9–16.

## **CHAPTER 7**

### **ARTICLE 4**

#### **DRAG REDUCTION BY IMPROVING LAMINAR FLOW PAST MORPHING CONFIGURATIONS**

Andrei Vladimir Popov, Ruxandra Mihaela Botez  
ETS, LARCASE, Notre Dame West, Montreal, Que., Canada, H3C-1K3

Mahmoud Mamou, Youssef Mébarki, Brian Jahrhaus and Mahmood Khalid  
Institute of Aeronautical Research - National Research Council Canada,  
Ottawa Ontario, Canada, K1A 0R6  
and Lucian Teodor Grigorie, ETS, LARCASE, Notre Dame West,  
Montreal, Que., Canada, H3C-1K3

This article was published in the conference proceedings at the AVT-168 NATO Symposium on the Morphing Vehicles, Evora, Portugal, 20 - 23 April 2009.

#### **Article presentation**

This article showed the finalized wing model that was built by LAMSI, IAR-NRC and LARCASE teams. The model was tested on 28-31 October 2008 at IAR-NRC wind tunnel without being controlled automatically or electrically using SMA actuators. The purpose of the test was to verify the capability of optical sensors in the detection of the airflow characteristics over the wing model. The wing model was designed, built and installed in the wind tunnel by the LAMSI team in collaboration with the IAR-NRC team and LARCASE team. In fact, LARCASE team, under the supervision of Dr Botez, has done the wind tunnel testing plan writing, and its scheduling in collaboration with IAR-NRC team, under the supervision of Dr. Mamou, the sensors and controller data post-processing and installation on the wing model, and the planning of the cabling systems related to the model integration in the wind tunnel. The references to the mechanical morphing system in this article are for the purpose of facilitating the reader understanding of the morphing wing concept.

Sixteen (16) optical sensors and sixteen (16) Kulite sensors were installed by me on the model flexible skin, and measured signals were recorded by Mr Brian Jahrhaus from IAR-NRC team and post-processed by me. The post-processing analysis showed that optical

sensors used were not capable of detecting the transition, unlike the Kulite sensors, which were able to. Moreover, the results showed that the optical sensors system used in this test could not determine the pressure distribution over the upper surface of the airfoil with a sufficient degree of accuracy due to the low accuracy of the sensors. The article demonstrated the success of the test, showed that Kulite sensors detected the location of transition for all the aerodynamic cases tested, which were all validated by infrared photos of the boundary layer flow over the wing model. The infrared photos in wind tunnel were performed by Dr. Mebarki Y. from IAR-NRC. The LARCASE and IAR-NRC teams works were realized under the supervision of Dr. Botez, and Dr. Mamou, respectively.

The signals recorded during the wind tunnel test were analysed by FFT decomposition in the post-processing phase. The Kulite sensor measurements showed that the transition was triggered by the Tolmien-Schlichting waves which had frequencies between 3 and 5 kHz. The magnitudes of pressure variations in the laminar flow boundary layer were of the order  $2 \times 10^{-4}$  Pa ( $3 \times 10^{-8}$  psi). The transition between laminar flow and turbulent flow was shown by an increase of the pressure variations of the order  $1 \times 10^{-3} \sim 3 \times 10^{-3}$  Pa ( $1.5 \times 10^{-7} \sim 4.4 \times 10^{-7}$  psi). In the turbulent flow, the magnitude of the pressure variations decreases by the same order value as in the laminar flow. For our application, in order to detect transition, we concluded that the optical sensors should be capable of measuring pressure with a resolution of about  $2 \times 10^{-4}$  Pa ( $3 \times 10^{-8}$  psi or 20dB SPL) with a sampling rate of 10 kHz, in order to at least match the sensitivity of Kulite sensors. This specification is required in order to allow a detection of small pressure fluctuations of the boundary layer, which shows the laminar flow and the transition from laminar to turbulent flow.

The previously tested optical sensors (presented in article 3), which had a rougher resolution and a lower sampling rate, would be blind to the detection of a transition, but should still be capable of measuring the  $C_p$  distribution over the wing airfoil. For this reason, we required that the next optical sensor manufacturer provides a full scale (FS) of 5 psi differential pressure, with a precision of 0.1% FS and a resolution  $<0.01$  % FS ( $5 \times 10^{-4}$  psi). Following the wind tunnel tests, the optical sensors were tested on bench in collaboration with Dr.

Grigorie L. The optical sensor system had a precision of 1% FS (0.15 psi) and a resolution of 0.1% FS (0.015 psi), which proved to be unsuitable for our application, which was the main reason why we abandoned the optical sensors in our project.

The minimum requirement specification allowing a generation of a  $C_p$  profile distribution over a wing airfoil should be a negative differential pressure of -2 psi FS, which is more than the maximum dynamic pressure encountered in wind tunnel at Mach number  $M = 0.3$ , a precision of less than 1% FS (0.02 psi) and a resolution of 0.1% FS (0.002 psi). The sampling rate is not important because at this resolution, the sensor is blind to the detection of a transition. Transition detection requires both the resolution and sampling rate to be very high, as shown above ( $2 \times 10^{-4}$  Pa and 10 kHz).

## Résumé

Dans cet article, les enregistrements des fluctuations de l'écoulement détectées par les capteurs Kulite effectués dans les tests en soufflerie ont été présentés. Plusieurs tests aux différents nombres de Mach et angles d'incidence ont été effectués dans la soufflerie de  $2\text{m} \times 3\text{m}$  de l'Institut de Recherche Aérospatiale du Conseil National de Recherche du Canada. Une aile à envergure finie, ayant un profil à forme variable causé par une peau flexible installée sur l'extrados de l'aile, a été équipée avec seize capteurs Kulite. Les nombres de Mach ont varié entre 0.2 et 0.3 et l'angle d'incidence a varié entre  $1^\circ$  et  $2^\circ$ . Les signaux de pression non-stationnaires ont été enregistrés; les coefficients moyens de pressions entre les enregistrements des capteurs de pression et leurs valeurs prédites en utilisant le logiciel XFoil ont été comparés. Les signaux de pression ont été analysés par décomposition spectrale en utilisant la transformée rapide de Fourier (Fast Fourier Transform) pour la détection des ondes Tollmien-Schlichting qui sont responsables du déclenchement de la transition dans la couche limite. Les positions du point de transition détectées par les capteurs Kulite ont été comparées avec les valeurs des points de transition prédites par le logiciel XFoil et validés par la détection visuelle à l'infrarouge des changements de température dans la couche limite.

## **Abstract**

In this paper, wind tunnel measurements are presented for the airflow fluctuation detection using Kulite pressure transducers. Several wind tunnel test runs for various Mach numbers and angles of attack were performed in the  $6 \times 9 \text{ ft}^2$  wind tunnel at the Institute for Aerospace Research at the National Research Council Canada. A rectangular finite aspect ratio wing, having a morphing airfoil cross section due to a flexible skin installed on the upper surface of the wing, was instrumented with sixteen Kulite transducers. The Mach number varied from 0.2 to 0.3 and the angle of attack range was within  $-1^\circ$  and  $2^\circ$ . Unsteady pressure signals were recorded and a thorough comparison, in terms of mean pressure coefficients, was performed between the measurements from the pressure transducers and theoretical predictions using the XFOIL computational fluid dynamics code. The unsteady pressure signals were analyzed through FFT spectral decomposition for detecting the Tollmien-Schlichting waves that trigger transition in the boundary layer. The transition point positions detected by Kulite transducers were compared to the predicted values by the XFOIL code and validated through infrared detection of the temperature changes in the boundary layer.

## **7.1 Introduction**

In this modern era due to earth climatic changes and shrinking of the fossil fuel reserves, the aerospace industry is motivated to reduce fuel consumption in large transport aircraft mainly by drag reduction. Drag reduction on a wing can be achieved by modifications of the airfoil shape which has an effect in the laminar flow to turbulent flow transition point position, which should move toward the trailing edge of the airfoil wing. The main objective of this concept is to promote large laminar regions on the wing surface thus reducing drag over an operating range of flow conditions characterized by mach numbers, airspeeds and angles of attack [1].

The airborne modification of an aircraft wing airfoil shape can be realized continuously to maintain laminar flow over the wing surface as flight conditions change. To achieve such a

full operating concept, a closed control system has to be developed to connect the flow fluctuations over the wing surface to the deformation mechanism (actuators) [2].

The flow fluctuation signals can be detected by conventional pressure transducers such as Kulite sensors. Linked to a controller system, the collected data would be treated in real time aiming to identify the location of transition and then sending a signal to the actuator system to adjust the wing surface to delay the transition location. Several measurement techniques for transition detection were developed in the past using various pressure transducers such as microphones [3], hot films [4-7] and piezoelectric [8]. The Kulite transducers have many advantages such as they are relatively small, have very good precision and accuracy [9].

In this paper, the possibility of the technological realization of a morphing wing which has to be tested in a wind tunnel is analyzed. The methodology used to analyse the unsteady pressure signals measured through the Kulite transducers in order to determine the transition location on the upper surface of the wing is shown. The transition point positions found by this method are compared to theoretical values calculated by the free licensed computational fluid dynamics code XFOIL [10]. Finally, the results recorded during the wind tunnel test using infrared technique will be shown, as the temperature differences will be detected in the boundary layer, therefore the validity of this methodology is proven.

## **7.2 Experimental setup description**

The wind tunnel tests were performed at the Institute for Aerospace Research at the National Research Council Canada. The purpose of these tests was the verification of the kulite sensors capabilities to detect small pressure variations on a morphing wing model in wind tunnel tests.

The wing had a span of 4 ft and a chord of 1.64 ft. This morphing wing concept consists of a rectangular wing model that incorporates two parts. One fixed part is built in aluminium and sustains all the resistance forces acting during wind tunnel tests and another part is flexible and consists in a flexible skin installed on the upper surface of the wing (see Fig. 7.1). The

flexible skin is required to change its shape through two action points in order to realise an optimised airfoil that is previously calculated for the airflow condition for which the test is performed.

As reference airfoil, a laminar airfoil WTEA [11] was used, and the optimised airfoils were previously calculated by modifying the reference airfoil for each airflow condition as a combination of angles of attack and Mach numbers such that the transition point position was found to be the nearest possible to the trailing edge. When the transition point position is close to the airfoil trailing edge, the drag is reduced. A number of thirty-six optimised airfoils for drag reduction were found for the airflow cases combinations of Mach numbers 0.2, 0.225, 0.25, 0.275, 0.3 and angles of attack -1, -0.5, 0, 0.5, 1 and 2 deg.

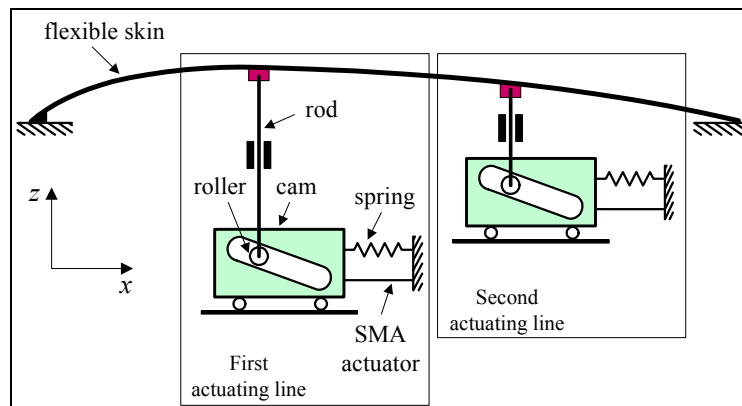


**Figure 7.1 Schematics of the flexible skin mechanical actuation, showing the mechanical principle of morphing.**

Two shape memory alloys actuators (SMA) created the displacement of the two control points on the flexible skin in order to realise the optimised airfoil shape.

The wing upper surface made of flexible skin – was equipped with sixteen Kulite transducers installed on a diagonal line at an angle of 15 deg to the center line of the wing being numbered as #1 the nearest to the leading edge and #16 nearest to the trailing edge in order to

avoid contamination of the downstream taps by the accidental leaking tap wedge shaped turbulence wake [12].

The Kulite sensors XCQ-062 series types have dimensions of 0.066 in diameter and 0.375 in length plus a flexible metallic reference tube of 0.016 in outside diameter and 1 in length. They also have a 5 psi differential pressure range with infinitesimal resolution and a natural frequency range up to 150 kHz. The data acquisition sampling rate was set to 10 kHz per channel by 16 channels due to acquisition system limitation of 160 kHz.

The model was installed vertically in the wind tunnel and for each airflow condition combination of angles of attack and Mach numbers a “run” was recorded for 30 seconds. The first set of runs was performed for all airflow conditions using the wing model with actuators in “zero” position i.e., which characterize the reference airfoil. The run is followed by a set of runs for all airflow conditions using the wing model with the actuators in the “optimised” position. Finally, several runs were performed using the wing model with the actuators in a fixed position to validate the pressure measurements with the infrared temperature detection on the wing model.

### **7.3 Wind tunnel data post-processing details**

After model disassembly, the Kulite sensors #2 and #4 were found to be defective, one had broken transducer wire and the other had pinched reference tube, and their mean pressure information was removed from the pressure coefficients distribution plots. The unsteady signal they recorded was still analysed and the results of this analysis is shown in the following paragraphs. In Figure 7.4, a pressure coefficient  $C_p$  distribution plot over the upper surface of the reference airfoil is shown. The measured Kulite pressure values are compared to the XFOIL code theoretical values. Also in the figure are shown the  $N$ -factor curve that is used by XFOIL as criteria to determine the transition occurrence versus the root mean square (RMS) pressure values of each Kulite sensor unsteady pressure signal.

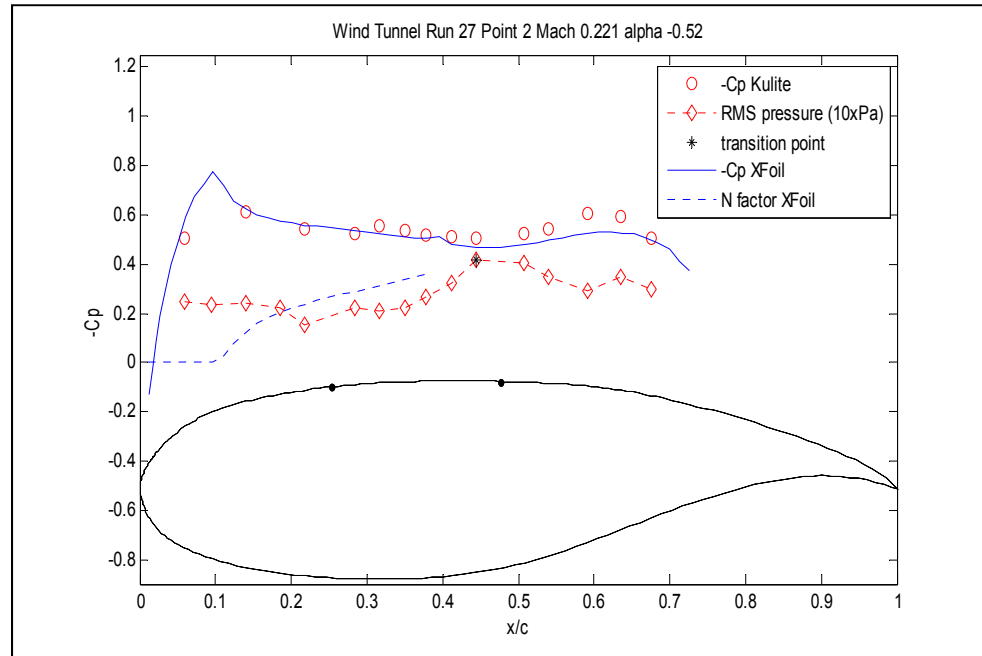


**Figure 7.2 Measured by Kulite transducers vs. theoretical XFOIL  $C_p$  values over the upper surface of the reference airfoil.**

The unsteady signal analysed through Fast Fourier Transform FFT spectral decomposition is shown in Fig. 7.5. It can be observed that the sensor #11 have a rise of the amplitudes in the neighbourhood of the 4 kHz frequency, which is an indication of the Tollmien-Schlichting waves occurrence that trigger the transition on the sensor location and subsequently the turbulent flow in the downstream of the sensor location. For the downstream sensors, the amplitudes of the pressure signal variations decrease but remain always greater than the pressure variations in the laminar flow. As a quantifier of the pressure signal variations amplitudes, the RMS which is the standard deviation of the pressure signal values with respect to the mean value for a high pass filtered signal at 1 kHz is used.

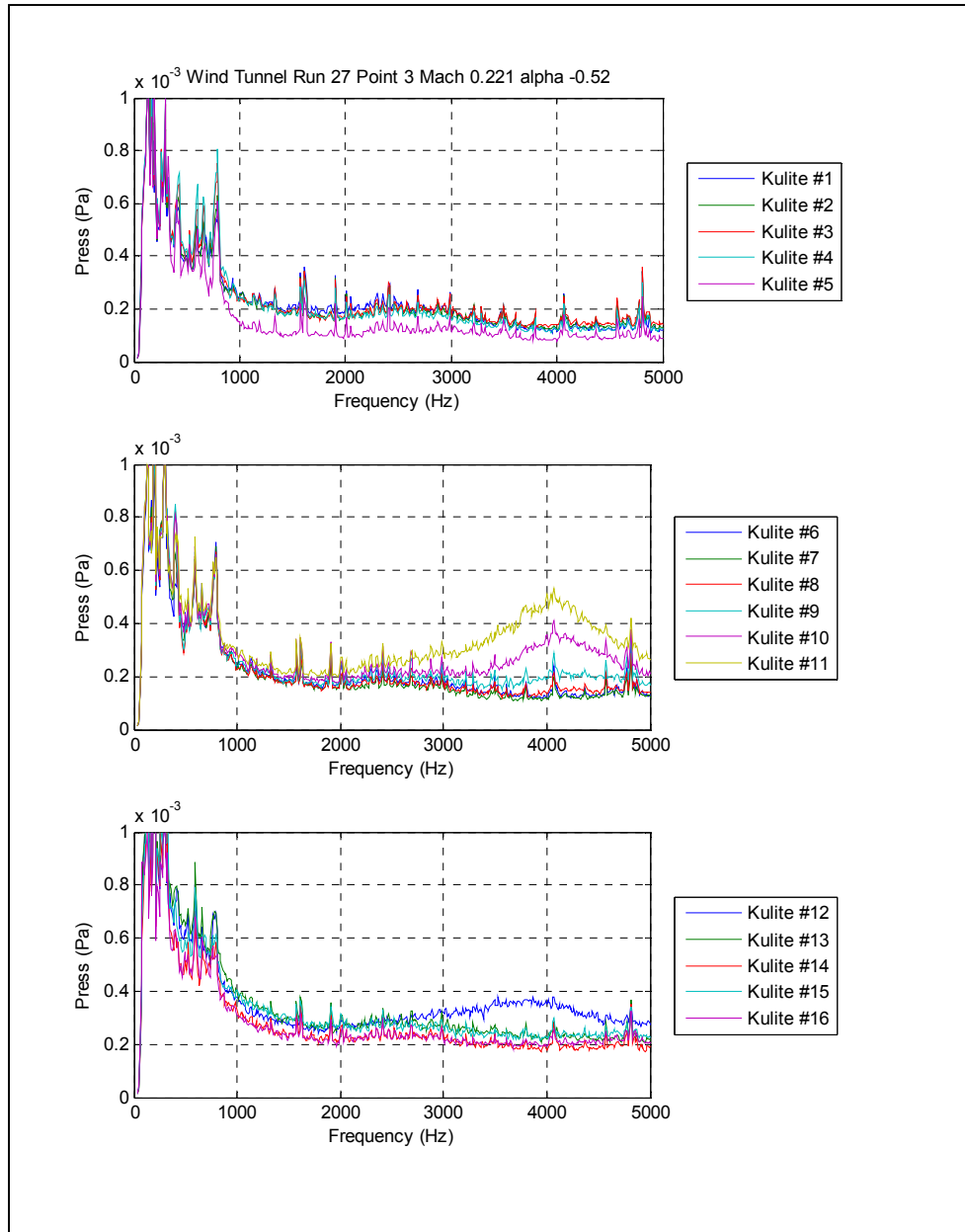


**Figure 7.3** FFT spectral decomposition of the 16 Kulite sensors channels.

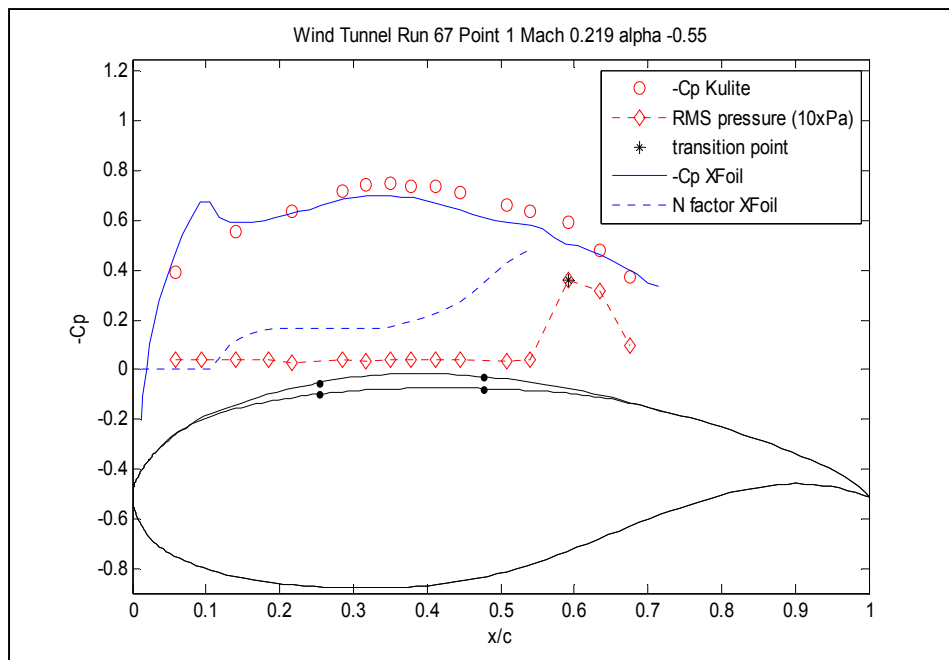


**Figure 7.4** Measured by Kulite transducers vs. theoretical XFOil pressure coefficient values over the upper surface of the optimized airfoil.

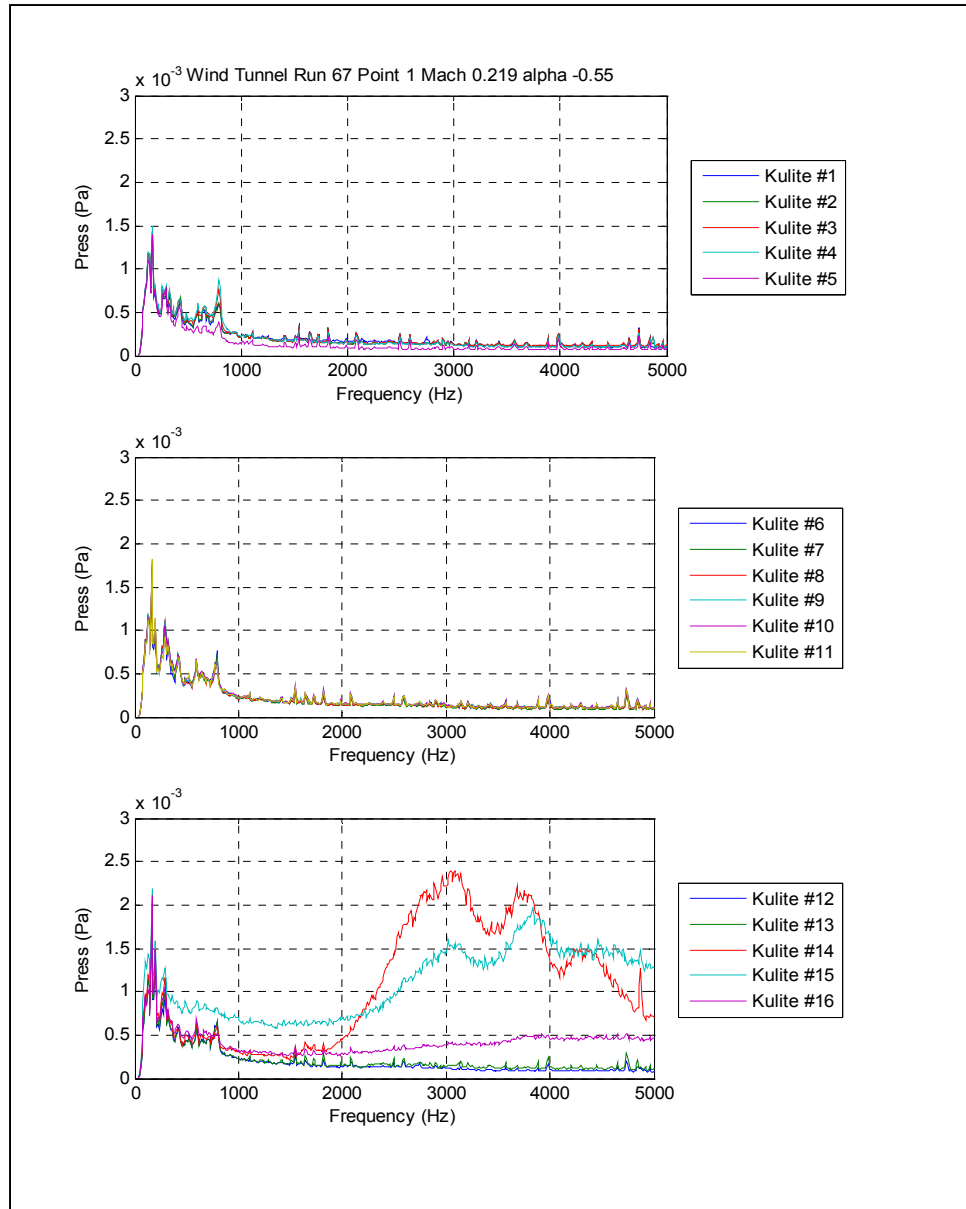


**Figure 7.5** FFT spectral decomposition of the 16 Kulite sensors channels.

#### 7.4 Results and discussion

Each airflow condition was simulated in XFOIL code to predict the pressure coefficient  $C_p$  distribution and transition point location on the upper surface of the airfoil. The critical value  $N_{cr} = 7.34$  was used in the simulation to match the turbulence level  $T = 0.14\%$  measured in the wind tunnel using Mack's correlation (7.1) [13].

$$N_{cr} = -8.43 - 2.4 \cdot \log(T) \quad (7.1)$$

The simulated  $C_p$  pressure distribution and the  $N$  factor plots were compared to the measured  $C_p$  distribution and pressures RMS (Fig. 7.2 and 7.4). The spectral analysis shows that the Tollmien-Schlichting waves occurred at 2 – 3 kHz up to 5kHz for Reynolds numbers of  $2 - 3 \times 10^6$  (Fig. 7.5 and 7.7). Also it was found that the magnitude of the pressure variations in the laminar flow boundary layer are of the order  $5 \times 10^{-4}$  Pa ( $7.25 \times 10^{-8}$  psi). The transition between laminar flow and turbulent flow is shown by an increase of the pressure variations of the order  $1 - 3 \times 10^{-3}$  Pa ( $1.45 - 4.4 \times 10^{-7}$  psi). In the turbulent flow, the pressure variations magnitude decreases at the same order value as in the laminar flow. In order to detect transition, a sensor able of measuring pressure with a resolution of about  $2 \times 10^{-4}$  Pa ( $3 \times 10^{-8}$  psi or 20dB SPL) and a sampling rate of 10 kHz could be used.

### 7.5 Transition detection validation

To validate the measurements using Kulite sensors, several measurements were performed using infra red camera that detects temperature differences in boundary layer. These temperature maps show the laminar boundary layer, turbulent boundary layer and the transition between laminar and turbulent regimes. In Fig. 7.6 the temperature map on the upper surface of the model – the flexible skin – is shown in which could be seen two vertical lines – the two SMA actuators that are installed along the span on the positions  $0.25 x/c$  and  $0.47 x/c$ , two rows of sensors arranged in a V with an angle of 30 deg between the two rows, each row having a 15 deg angle to the airflow direction; the upper row are the 16 Kulite sensors and the lower row are the 16 optical sensors that were tested in the same time with the Kulite sensors. The optical sensors proved to be blind to the small pressure variations in the boundary layer due to the precision and resolution inadequacy.

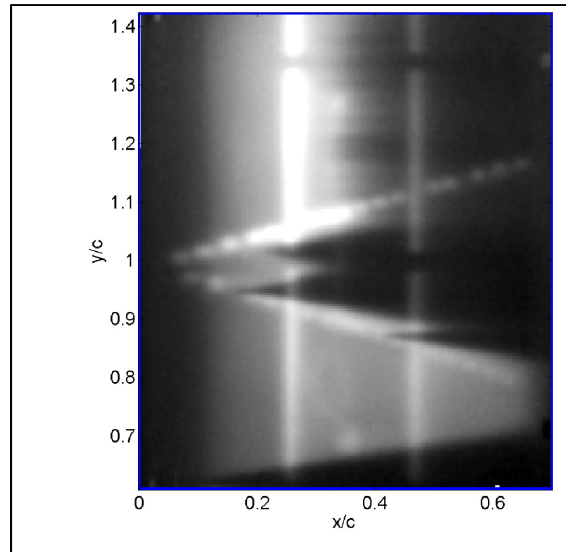


**Figure 7.6** Temperature map using infrared camera on the upper surface of the model for a flow of  $Re = 2.55 \times 10^6$ ,  $Mach = 0.224$  and  $\alpha = -0.53$  deg.

In Fig. 7.6 there are two zones, the lighter zone show the laminar flow and the darker zone show the turbulent flow. The line differentiating between the lighter and darker zone is the zone where transition occurs ( $0.35 - 0.4 x/c$ ). In this picture, three V turbulence wedges are shown which indicate three leaking sensors – Kulite sensor #4 and optical sensors #3 and #10.

The test were performed on an airfoil obtained by the actuator #1 deflection of 0.4 mm and actuator #2 deflection of 1.5 mm. The airfoils were scanned afterwards in this position as well as in “zero” position corresponding to the reference airfoil. The scanned airfoils were used in the pressure coefficient  $C_p$  distribution and  $N$  factor distribution computation using the XFOil free licensed software.

In figure 7.7 the  $C_p$  curve distributions calculated by the XFOil are shown, the  $C_p$  curve distribution measured by Kulite sensors and  $N$  factor curve calculated by XFOil compared to the pressure RMS of the Kulite sensors pressure signals. The maximum RMS value of the Kulite sensors pressure signal is considered to be an indication of the transition occurrence.

In this case, the sensor #10 (installed on the 0.41  $x/c$  position) shows the maximum value of the RMS.

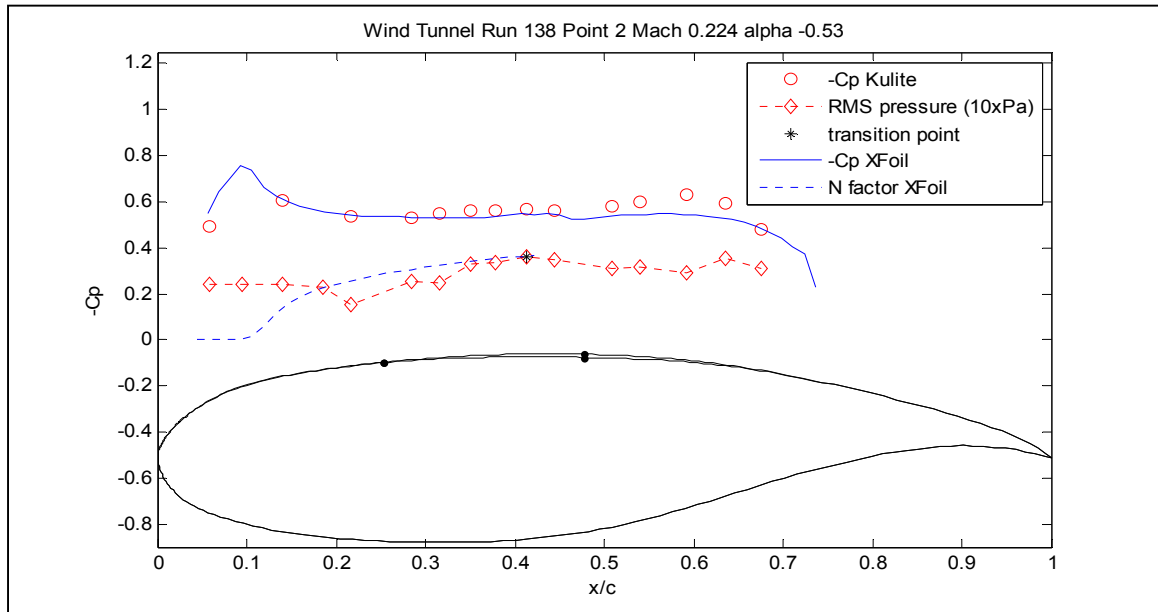


**Figure 7.7** Measured by Kulite transducers vs. theoretical XFOil  $C_p$  values over the upper surface of the model for airflow of  $Re = 2.55 \times 10^6$ , Mach = 0.224 and angle of attack = - 0.53 deg.

Figures 7.8 and 7.9 show another test visualised with infra-red camera for validation purposes in which the Reynolds number was  $2.55 \times 10^6$ , Mach = 0.225 and  $\alpha = 0.97^\circ$ . Figure 10 shows the same temperature map just that the color codes are reversed; the dark zones indicate the laminar flow while the lighter zones indicate turbulent flow. In the picture the transition occurs in the same position as the first SMA actuator, which is confirmed in Figure 7.9 through the RMS analysis. In Fig. 7.9 the maximum RMS value belongs to the sensor #6 which is installed at the position 0.28  $x/c$ .

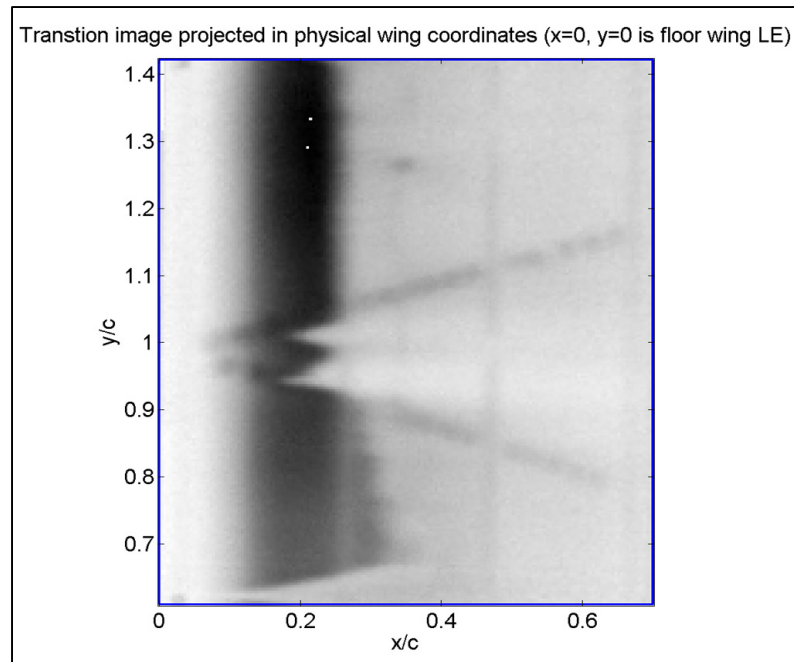


**Figure 7.8** Temperature map using infrared camera on the upper surface of the model for a flow of  $Re = 2.55 \times 10^6$ , Mach = 0.225 and  $\alpha = 0.97$  deg.

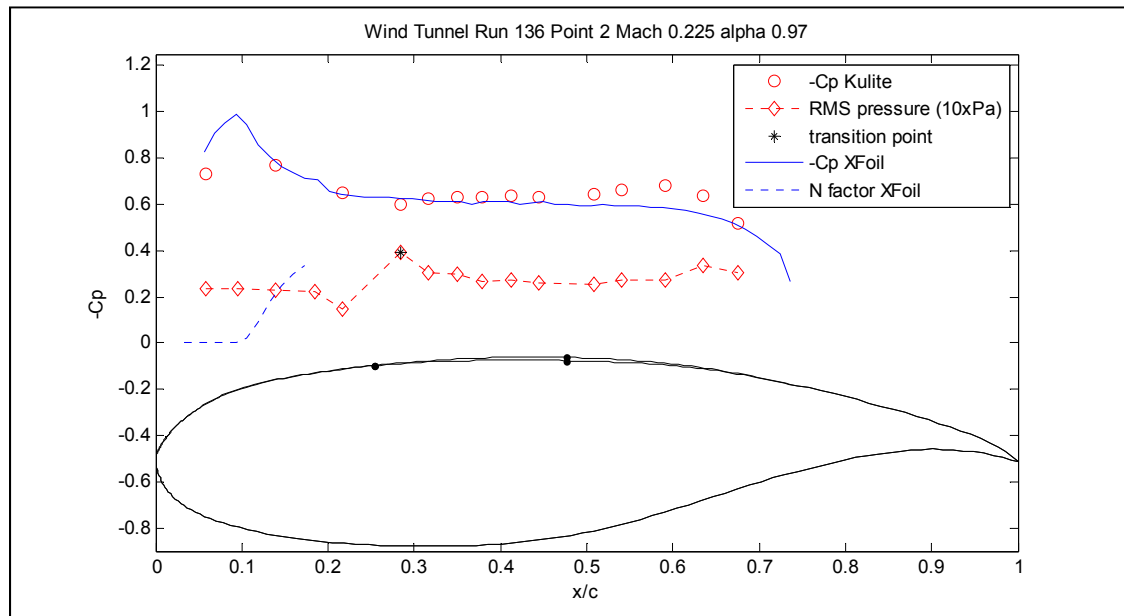


**Figure 7.9** Measured by Kulite transducers vs. theoretical XFOIL pressure coefficient values over the upper surface of the model for airflow of  $Re = 2.55 \times 10^6$ , Mach number = 0.225 and  $\alpha = 0.97$  deg.

## References

- [1] Zingg, D. W., Diosady, L., and Billing, L., 2006, *Adaptive Airfoils for Drag Reduction at Transonic Speeds*, AIAA paper 2006-3656.
- [2] Popov, A., V., Labib, M., Fays, J., Botez, R.M., 2008, *Closed loop control simulations on a morphing laminar airfoil using shape memory alloys actuators*, AIAA Journal of Aircraft, Vol. 45, No. 5, pp. 1794-1803.
- [3] Rioual, J.-L., Nelson, P. A., and Fisher, M. J., 1994, *Experiments on the Automatic Control of Boundary-Layer Transition*, Journal of Aircraft, Vol. 31, No. 6, pp. 1416-1418.
- [4] Mangalam, S. M., 2004, *Real-Time Extraction of Hydrodynamic Flow Characteristics Using Surface Signature*, IEEE Journal of Oceanic Engineering, Vol. 29, No. 3, pp. 622-630.
- [5] Krishnan, V., Sundaram, S., and Viswanath, P. R., 2000, *Transition Related Studies on Two Low-Drag Airfoils*, Current Science, Vol. 70, No. 6, pp. 829-833,.
- [6] Khalid, M., 1987, *The Use of Hot-Film Technique for Boundary Layer Studies on a 21% Thick Airfoil*, Aeronautical Note NAE-AN-45,NRC No. 27892, Ottawa, May.
- [7] Haussmann, F., and Schroder, W., 2006, *Coated Hot-Film Sensors for Transition Detection in Cruise Flight*, Journal of Aircraft, Vol. 43, No. 2.
- [8] Nitsche, T., Mirow, P., and Dorfler, T., 1990, *Investigations on Flow Instabilities on Airfoils by Means of Piezofoil-Arrays*, Laminar-Turbulent Transition IUTAM Symposium Toulouse, France 1989, Springer-Verlag, Berlin/Heidelberg, pp. 129-135.
- [9] Kulite pressure transducer XCQ-062 series data specifications  
[http://www.kulite.com/pdfs/pdf\\_Data\\_Sheets/XCQ-062.pdf](http://www.kulite.com/pdfs/pdf_Data_Sheets/XCQ-062.pdf).  
 Consulted November 6, 2009.
- [10] Drela, M., 2003, *Implicit Implementation of the Full  $e^N$  Transition Criterion*, AIAA paper 2003-4066.
- [11] Khalid, M., Navier Stokes 1993, *Investigation of Blunt Trailing Edge Airfoils using O-Grids*, AIAA Journal of Aircraft, vol. 30, no. 5, pp. 797-800.
- [12] Schubauer, G. B., Klebanoff, P. S., 1955, *Contributions on the Mechanics of the Boundary Layer Transition*, NACA TN 3489.
- [13] Mack, L. M., 1977, *Transition and Laminar Instability*, Jet Propulsion Laboratory Publication 77-15, Pasadena, CA.

## **CHAPTER 8**

### **ARTICLE 5**

#### **CONTROL OF A MORPHING WING IN BENCH TESTS**

Andrei Vladimir Popov

PhD student, Laboratory of Research in Active Controls, Avionics and AeroServoElasticity  
LARCASE, 1100 Notre-Dame West Street, Montreal, Quebec, H3C 1K3, Canada

Lucian Grigorie

Postdoctoral fellow, Laboratory of Research in Active Controls, Avionics and  
AeroServoElasticity

LARCASE, 1100 Notre-Dame West Street, Montreal, Quebec, H3C 1K3, Canada

Ruxandra Mihaela Botez

Professor, Laboratory of Research in Active Controls, Avionics and AeroServoElasticity  
LARCASE, 1100 Notre-Dame West Street, Montreal, Quebec, H3C 1K3, Canada.

This article was published in the conference proceedings at the CASI Aircraft Design and  
Development Symposium, Kanata, Ont., 5-7 May 2009.

#### **Article presentation**

The article showed the implementation and validation of the controller designed in the first stage of the project shown in Chapter 5, in a bench test. The bench test consisted in reproducing all the thirty five optimized airfoils previously calculated by Ecole Polytechnique and LAMSI teams, and its purpose was to validate the actual optimized airfoils realized by the morphing wing and to make comparisons with the theoretical coordinates obtained through simulations. The real airfoils were scanned by using a laser beam that measured the actual coordinates of the flexible skin deformed under the action of the two SMA actuators. The work presented in this article was performed in the LAMSI facility by me in collaboration with other members of LARCASE team (Dr. Lucian Grigorie) and LAMSI team (Thomas George and Morellon Emeric). The results obtained by the scanning were compared with the aerodynamically optimized airfoils and the morphed simulated airfoils using a finite element method (FEM) in the Patran/Nastran software. The dynamic behaviour of the SMA actuators was studied during the bench tests by recording their positions and temperatures in time histories. The time histories revealed that SMA actuators responded quickly when heated, the time being in the order of tenths of seconds;

however, it was also seen that they had a slow response when cooled, with a couple of minutes being required to bring them back to the reference position. This bench test was a preliminary test for the integration of the morphing wing control system before entering in the wind tunnel tests phase. The following articles discuss the control of the morphing wing under wind test conditions and with all subsystems (mechanical actuators electrical controlled, sensors and controllers) integrated.

### **Résumé**

Dans cet article, on a présenté la méthodologie de design et les résultats expérimentaux pour un contrôleur installé sur une aile à géométrie du profil variable. Une aile rectangulaire à envergure finie ayant un profil à géométrie variable munie d'une peau flexible installée sur l'extrados de l'aile a été équipée avec deux actionneurs utilisant les alliages à mémoire de forme qui déforment la peau flexible en deux points de control pour réaliser les formes des profils optimisées. Ces profils optimisés ont été calculés auparavant pour chaque condition d'écoulement d'air exprimée en fonction des nombres de Mach et des angles d'incidence, dans le but de positionner la transition le plus proche possible du bord de fuite de l'aile. Pendant les tests, les profils ont été scannés et validés en utilisant les profils théoriques optimisés par la méthode des éléments finis, en obtenant excellents résultats.

### **Abstract**

In this paper the design methodology and test results of a morphing wing controller are presented. A rectangular finite aspect ratio wing having different morphing airfoil cross sections due to flexible skin installed on the upper surface of the wing was instrumented with two shape memory alloys actuators which create the displacements of two control points on the flexible skin in order to realize the optimized airfoil shapes. These optimized airfoils were previously calculated for each airflow condition expressed in terms of angles of attack and Mach numbers combinations such that the transition point position was found to be located as nearest possible to the trailing edge. During the bench tests, the airfoil shapes were scanned by use of a laser beam and the scanned airfoils were verified and validated to the set

of theoretical optimized airfoils and to the set of simulated airfoils using the finite element method model. Thus, an excellent validation of our results was obtained.

## 8.1 Introduction

The work here presented is part of a global project CRIAQ 7.1 entitled *Improvement of laminar airflow on an aeroelastic wing* with the aim of reducing drag on the wing by controlling the transition point position to be closer to the wing airfoil trailing edge; this project was initiated by aerospace companies Thales Avionics and Bombardier Aerospace.

The main objective of this concept is to obtain large laminar regions on the wing surface, thus reducing drag over an operating range of flow conditions characterized by Mach numbers, airspeeds and angles of attack [1]. The airborne modification of an aircraft wing airfoil shape can be realized continuously to maintain laminar flow over the wing surface as flight conditions change. To achieve such a full operating concept, a closed loop control system concept was developed to link the flow fluctuations over the wing surface to the deformation mechanisms (actuators) [2].

The wing model has a rectangular plan is equipped with a flexible upper surface skin on which shape memory alloys actuators are installed. Two shape memory alloys actuators (SMA) create the displacement of the two control points on the flexible skin in order to realize the optimized airfoil shape.

As reference airfoil, a laminar flow airfoil WTEA was chosen, which aerodynamic performances were previously investigated at IAR-NRC in references [3, 4]; then, optimized airfoils were previously calculated by modifying the reference airfoils for each airflow condition considered as a combination of angles of attack and Mach numbers such that the transition point position was found to be located the nearest as possible to the trailing edge. A number of thirty five optimized airfoils were found for the airflow cases combinations of Mach numbers and angles of attack. Table I shows the angles of attack variations from -1 to

2 degrees, the Mach numbers variations from 0.2 to 0.3 and the Reynolds numbers variations from 2.2932 million to 3.3654 million for the denoted airfoils with C101 to C135.

Table 8.1 Test flow conditions for 35 wing airfoils.

<b>Mach</b>	<b>Re (mil.)</b>	<b>Angle of attack (degrees)</b>						
		<b>-1.00</b>	<b>-0.50</b>	<b>0.00</b>	<b>0.50</b>	<b>1.00</b>	<b>1.50</b>	<b>2.00</b>
0.200	2.2932	C101	C102	C103	C104	C105	C106	C107
0.225	2.5679	C108	C109	C110	C111	C112	C113	C114
0.250	2.8384	C115	C116	C117	C118	C119	C120	C121
0.275	3.1044	C122	C123	C124	C125	C126	C127	C128
0.300	3.3654	C129	C130	C131	C132	C133	C134	C135

## 8.2 Experimental setup description

The purpose of the bench tests was to verify the capabilities of SMA actuators to obtain the thirty five optimized airfoils to be used further in the wind tunnel tests. The morphing wing concept consisted of a rectangular wing model built with two parts (Fig. 8.1). The fixed inner wing surface part was built by IAR-NRC in aluminum and sustained all the resistance forces acting during wind tunnel tests while the upper flexible skin wing surface part was built by LAMSI team at ETS (Fig. 8.2). The flexible skin was required to change its shape through two action points in order to obtain the optimized airfoils for the airflow conditions in which the test were performed.

The actuators were basically composed of two oblique cams sliding rods that converted the horizontal movement along the span in vertical movement perpendicular to the chord. The position of each actuator was given by the mechanical equilibrium between the SMA wires that pulled the sliding rod in reverse direction. The role of the gas springs was to counteract the pulling effect of aerodynamic forces that acts in wind tunnel over the flexible skin when the SMA's were inactive (see Fig.8.1).

The architecture of the open loop control system of the wing model, SMA actuators and controller is shown in Figure 8.3. The two SMA actuators have six wires each which are supplied with power by the two AMREL SPS power supplies, controlled through analog signal by the QUANSER Q8 control board. The Q8 control board was programmed through Simulink/xPC. In Simulink a user interface was implemented which allow the user to choose the optimized airfoils and provide the values necessary for the SMA as shown in Figure 8.2.

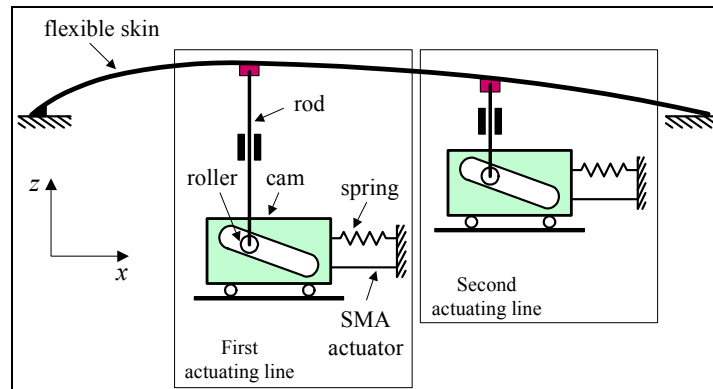


**Figure 8.1 Schematics of the flexible skin mechanical actuation.**

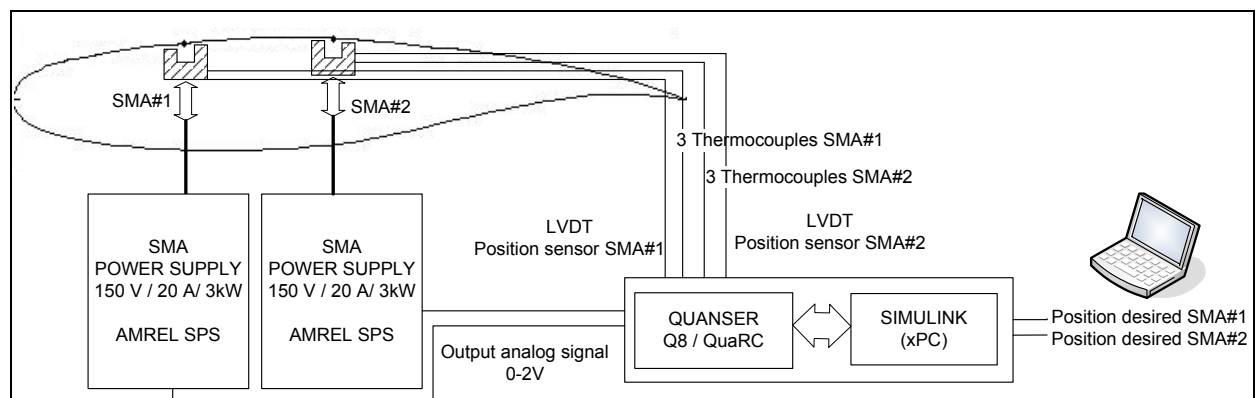


**Figure 8.2 SMA control architecture during the bench test.**

Each SMA actuator has its own controller that maintains the actuator in the desired position. The design concept of the controller consists of a PID and a switch that connects and

disconnects the SMA to a source of current (see Fig. 8.3) which heats and lets cooling the SMA to allow its change in its length, this concept was investigated in [2].

The initial input which is the optimized airfoil for any flow condition is chosen manually by the operator from the computer database through a user interface. Then the displacements ( $Y_1$  and  $Y_2$ ) that are required to be reproduced by the two control points on the flexible skin are sent to the controller. This controller sends an analog signal 0 – 2 V to the power supply that provide a current of 0 – 20 A / 20 V cc. to the SMA. The SMA will change its length according to the temperature of the wire due to the passing current and will change the position of the actuator which is sensed by a linear variable differential transducer (LVDT). The signal position received from the LVDT is compared to the desired position and the error obtained is fed back to the controller. The PID will control the dynamics of the heating process. If the realized position is greater than the desired position the switch will disconnect the control current letting the SMA wire to cool down. During the cooling down process the SMA will maintain its length due to the hysteretic behaviour. Also the controller uses three thermocouples signals from each SMA wire to monitor the temperature of the wires in order to maintain the temperature under 130 deg C limits.

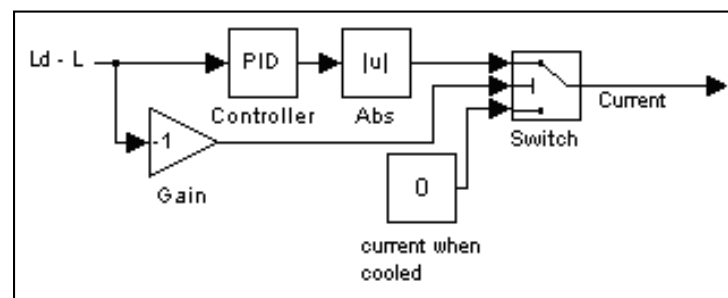


**Figure 8.3 Simulink controller schematics.**

### 8.3 Data analysis

During the bench tests at LAMSI, the functioning of the whole system was verified for the 35 optimized airfoil shapes, as for each of these cases, the controller adjusts the SMA actuators positions accordingly; the resulting shape of the flexible skin was measured through a laser scanner and compared with the desired airfoil shape coordinates. Figure 8.5 shows several examples of scanned airfoils versus theoretical airfoils. The scanned airfoils were not perfectly fitted on the theoretical coordinates due to the technological considerations, but it was found that for the whole batch of 35 airfoils the scanned airfoils were inside a tolerance of 0.5 mm deviation. With the exception of case C135 airfoil, the desired position of the second actuator could not be reached due to mechanical limits.

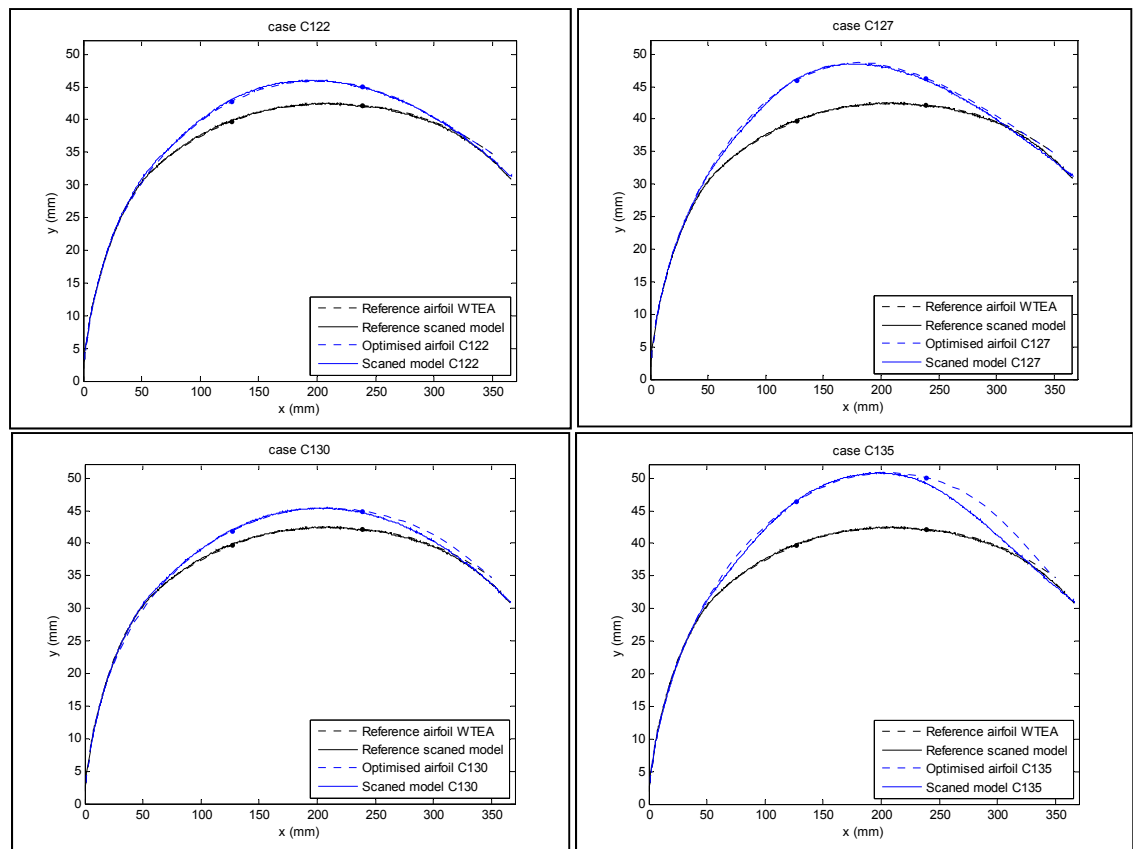


**Figure 8.4** Theoretical reference and optimized airfoils compared to scanned airfoils in bench test.

In Figure 8.5, an example of time history of the desired positions of the two SMA actuators is shown and their realized positions during bench tests are given for the case C127 airfoil. It is observed an overshoot of the real position which is immediately corrected by the controller switch. It is also observed in the temperatures time history that the temperature during the maintaining of desired position has a saw dents shape, which is due to the controller switching on and off of the heating current that controls the SMA's positions. In the temperature displacement diagram, a typical hysteresis is observed for all the SMA's functioning.

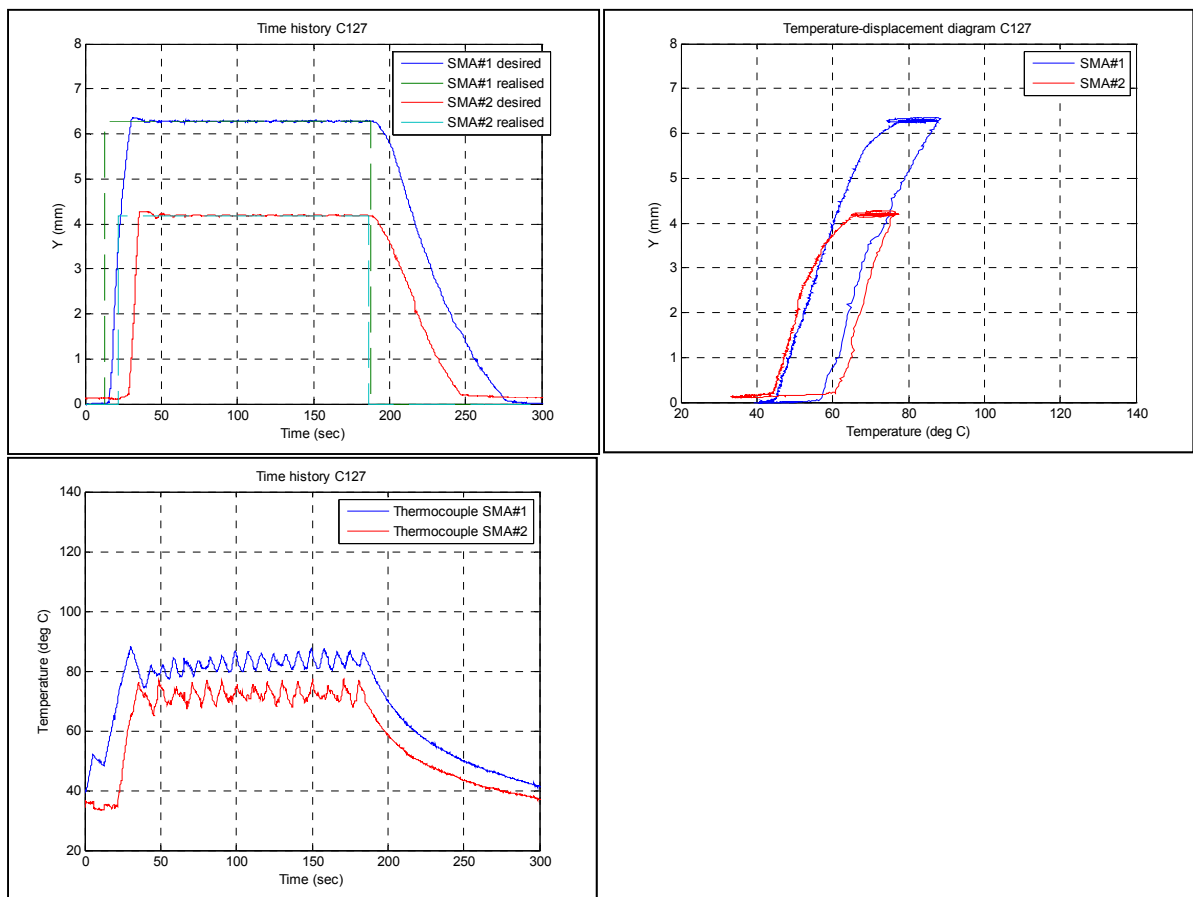


**Figure 8.5 Time histories and temperature displacement diagram of case C127 morphing airfoil in bench test.**

A particular case of time history of the desired positions of the two SMA actuators and their realized positions during bench tests for the case C135 airfoil are shown in Figure 8.6.

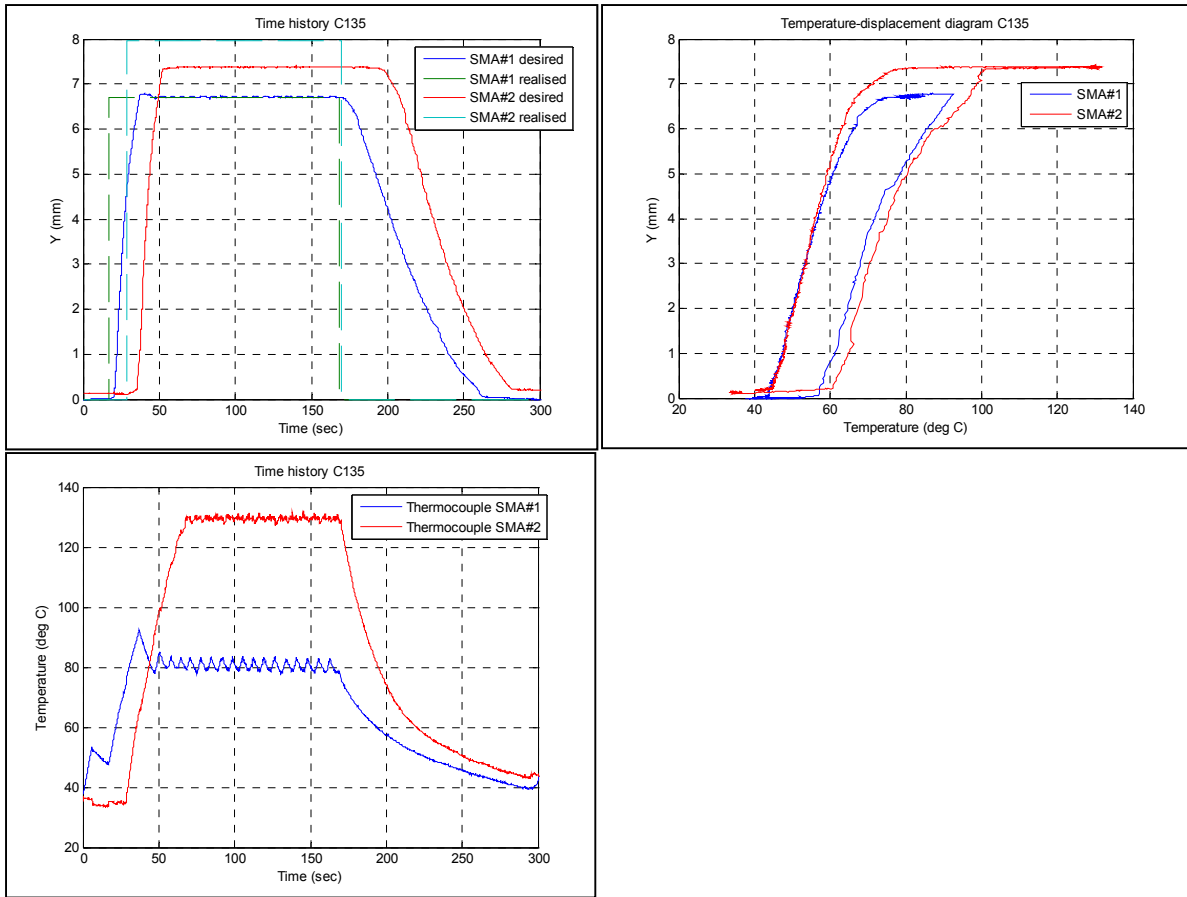


**Figure 8.6** Time histories and temperature displacement diagram of case C135 morphing airfoil in bench test.

#### 8.4 Conclusion

These preliminary tests were realized at the LAMSI laboratory and were extremely useful at the successful realization of the Wind Tunnel Tests closed loop controller in the CRIAQ 7.1 project.

## References

- [1] Zingg, D. W., Diosady, L., and Billing, L., 2006, *Adaptive Airfoils for Drag Reduction at Transonic Speeds*, AIAA paper 2006-3656.
- [2] Popov, A., V., Labib, M., Fays, J., Botez, R.M., 2008, *Closed loop control simulations on a morphing laminar airfoil using shape memory alloys actuators*, *AIAA Journal of Aircraft*, Vol. 45, No. 5, pp. 1794-1803.
- [3] Khalid, M., 1993, *Navier Stokes Investigation of Blunt Trailing Edge Airfoils using O-Grids*, *AIAA Journal of Aircraft*, vol. 30, no. 5, pp. 797-800.
- [4] Khalid, M., and Jones, D.J., 1993, *A CFD Investigation of the Blunt Trailing Edge Airfoils in Transonic Flow*, Inaugural Conference of the CFD Society of Canada, June 14-15, Montreal.

## **CHAPTER 9**

### **ARTICLE 6**

#### **MODELING AND TESTING OF A MORPHING WING IN OPEN LOOP ARCHITECTURE**

Andrei Vladimir Popov, Teodor Lucian Grigorie, Ruxandra Mihaela Botez  
ÉTS-LARCASE Laboratory of Active Controls, Aeroservoelasticity and Avionics,  
Department of Automated Production Engineering  
1100 Notre-Dame Street West, Montreal, QC, Canada, H3C 1K3

Youssef Mébarki, Mahmoud Mamou  
Institute for Aerospace Research, National Research Council,  
Ottawa, ON, Canada, K1A 0R6

This article was published in the conference proceedings at the  
AIAA Guidance, Navigation, and Control Conference,  
Chicago, Illinois, 10 – 13 August 2009,  
and submitted for publication at AIAA Journal of Aircraft.

#### **Article presentation**

The article shows the analysis of results obtained in wind tunnel tests performed in February 2009 at IAR-NRC Ottawa. The wing model was controlled by an open loop system driven automatically by computer. The paper shows the architecture of control, the control software and the real time pressure data acquisition and visualising realized at LARCASE by me in collaboration with Dr. Lucian Grigorie. The PID controller design and software programs presented in this article belongs to me, and the self-tuning controller using fuzzy logic design, testing and implementation belongs to Dr. Lucian Grigorie, and is the subject of a future article to be published. Dr. Botez is the supervisor of our works at LARCASE. Though the software was still in the testing and development phase, the operation of the morphing wing model in wind tunnel test was a validation success. The test proved that the controller can be further developed to improve its quality by closing the loop. The wing model mechanical and electrical design manufacture and installation in the wind tunnel was performed by LAMSI team in collaboration with IAR-NRC and LARCASE teams; in fact, LARCASE team has done the wind tunnel testing plan writing, and its scheduling in collaboration with Dr Mamou M. at IAR-NRC, the sensors and controller data post-

processing and installation on the wing model, and the planning of the cabling systems related to the model integration in the wind tunnel.

The references to the mechanical and electrical system in the paper have the purpose to facilitate the reader's understanding. The infrared measurements were performed during wind tunnel tests by Dr. Youssef Merbaki.

The pairs of actuators displacements values, and optimized airfoil shapes, used during the wind tunnel tests were calculated by École Polytechnique team in collaboration with LAMSI team, using CFD and FEM simulations commercial codes.

## **Résumé**

Cet article présente le modèle et les tests expérimentaux effectués sur une aile à géométrie variable dans une architecture en boucle ouverte. On présente la méthode utilisée pour l'acquisition des données de pression enregistrées de la surface extérieure de la peau flexible en utilisant les capteurs de pression Kulite ainsi que l'instrumentation du contrôleur pour changer la forme du profil. Les données enregistrées sont analysées par la transformée rapide de Fourier (Fast Fourier Transform) pour détecter la magnitude du bruit sur la surface d'écoulement. Suite au filtrage des données par un filtre passe-haut, les racines moyennes des carrés (Root Mean Square) sont calculées pour obtenir les graphiques de la distribution du bruit dans l'écoulement de l'air. Ces calculs sont nécessaires pour enlever les bruits électroniques induits par les installations électriques, et pour distinguer l'apparition des ondes Tollmien-Schlichting qui sont responsables pour le déclenchement de la transition entre l'écoulement laminaire et turbulent. La peau flexible change sa forme à l'aide de deux actionneurs pour obtenir les formes optimisés des profils calculés pour des conditions similaires d'écoulement que celles testées dans la soufflerie. Deux actionneurs avec des alliages à mémoire de forme ayant un comportement non-linéaire changent la forme de la peau flexible en deux points de contrôle. Chaque actionneur est alimenté avec d'énergie électrique par une source de puissance contrôlée à l'aide d'un logiciel conçu en

Matlab/Simulink en utilisant un contrôleur de logique floue avec autorégulation. La méthodologie et les résultats obtenus pendant les tests en soufflerie qui ont prouvé la validité du concept sont discutés dans l'article. L'acquisition en temps réel et l'analyse des données de pression est nécessaire pour le développement futur d'un contrôleur en boucle fermée pour obtenir un système de contrôle de l'aile à géométrie variable complètement automatique.

### **Abstract**

This paper presents the modeling and the experimental testing of the aerodynamic performance of a morphing wing in open-loop architecture. We show the method used to acquire the pressure data from the external surface of the flexible wing skin, using incorporated Kulite pressure sensors and the instrumentation of the morphing controller. The acquired pressure data is analyzed through Fast Fourier Transforms in order to detect the magnitude of the noise in the surface air flow. Subsequently, the data is filtered by means of high-pass filters and processed by calculating the Root Mean Square of the signal in order to obtain a plot diagram of the noise in the air flow. This signal processing is necessary to remove the inherent noise electronically induced from the Tollmien-Schlichting waves, which are responsible for triggering the transition from laminar flow to turbulent flow. The flexible skin is required to morph the shape of the airfoil through two actuation points in order to achieve an optimized airfoil shape based on the theoretical flow conditions similar to those tested in the wind tunnel. Two shape memory alloy actuators with a non-linear behavior drive the displacement of the two control points of the flexible skin towards the optimized airfoil shape. Each of the shape memory actuators is activated by a power supply unit and controlled using the Simulink/Matlab software through a self-tuning fuzzy controller. The methodology and the results obtained during the wind tunnel test that proved the concept and validity of the system in real time are discussed in this paper. Real-time acquisition and signal processing of pressure data is needed for further development of the closed-loop controller in order to obtain a fully automatic morphing wing system.

## 9.1 Morphing wing structure, objectives and testing conditions

To respond to the ever present need to reduce fuel and direct operating costs associated with new generations of aircraft, extensive research is underway to assess the performance of morphing wing technologies and concepts. These technologies will make it possible to enhance the aerodynamic performance of aircraft and to allow them to operate adaptively under a wide range of flight conditions. Moreover, the morphing technologies will be used to improve aircraft performance, expand the flight envelope, replace conventional control surfaces, reduce drag to improve range, and reduce vibrations and flutter [1]. Fly-by-wire and Active Control Technology can also be used to achieve even more benefits in terms of direct operating cost reduction. In the near future, morphing vehicle technology will likely focus in the design of small Unmanned Aerial Vehicles (UAV) [2]. Extremely complex, the interactions between aerodynamics, structures, controls, actuator power requirements, sensor integrations and all other components are studied as part of the multidisciplinary research on morphing wing projects. Active Control Systems (ACS) provides benefits in terms of reduced fuel consumption for morphing<sup>3</sup> and fly-by-wire aircraft. Their implementation requires knowledge of aero-servo-elasticity interactions (interactions between unsteady aerodynamics, structure and controls). In the MAW morphing wing research program [3,4], the aerodynamic benefits of smooth variable camber and automatic flight control modes were determined for the following systems: Maneuver Camber Control - MCC, Cruise Camber Control - CCC, Maneuver Enhancement/Gust Alleviation - ME/GA, and Maneuver Load Control - MLC. In the present paper, we perform the conceptual design and validation of an active control system for the transition flow control. Prior to this work, a new transition method was conceived based on XFOIL results and on the Matlab interpolation, tools PCHIP and SPLINE [5], and it was found to be quite effective for integration in a closed-loop real-time system. Various PID-based methods were used to produce the closed-loop controller for the transition from laminar to turbulent flow [6]. Optical sensors were measured on the rigid wing in order to validate their performances. Their dependence and relationship with respect to temperature variations were found and analyzed [7].

In this context, simulations and experimental multidisciplinary studies are performed through bench tests and wind tunnel measurements, for a morphing wing equipped with a flexible skin, smart material actuator SMAs, and optical sensors. The aim of these studies is to move the transition point from laminar to turbulent flow closer to the trailing edge by use of a controller in order to obtain a larger laminar flow region. During the research project, an investigation was performed on optical sensor selection and testing for laminar-to-turbulent flow transition validation (by use of Xfoil code and Matlab), smart material actuator controller methods, aero-elasticity wing studies by use of MSC/Nastran, open- and closed-loop transition position controller design, and integration and validation on the wing equipped with SMAs and optical sensors (simulation versus test results).

As seen in Fig. 9.1, a complex hardware system, which deforms the airfoil to its optimized shape in order to allow long laminar runs, was designed and manufactured. For different flight conditions (angles of attack  $\alpha$  and Reynolds number  $Re$ ), the closed-loop controller receives the airfoil upper surface pressure coefficient distribution  $C_p$  determined from the surface pressure measured by the optical sensors. The  $C_p$  distribution is compared with a computational fluid dynamics (CFD) database, which is generated such that for different airfoil types, the transition point is given as a function of the pressure coefficients distribution. Once an agreement is reached, the transition point is transferred to the loop controller by the CFD database, and then the controller will be able to decide whether or not the airfoil shape needs further adjustment. The adjustment of the airfoil shape is done in real time using the SMA actuators, which are used to deform the airfoil skin. The loop is closed by the airfoil shape, which communicates another surface pressure distribution to the optical sensors.

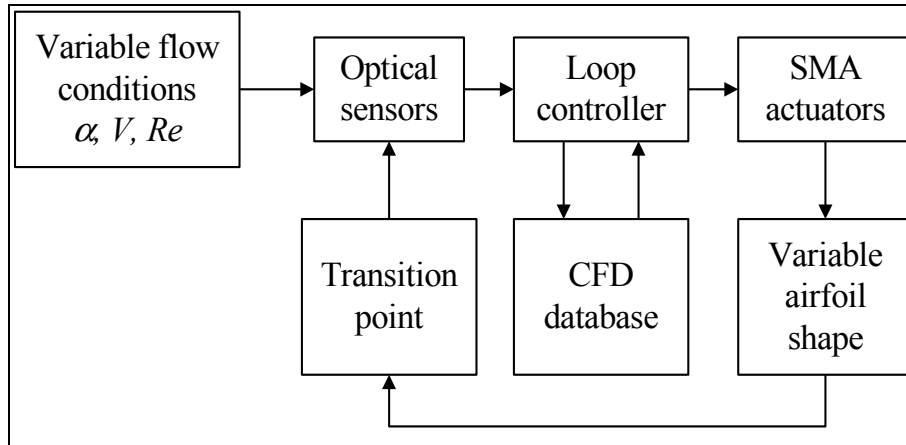


**Figure 9.1** Closed-loop morphing wing system.

This research project studies the possibility of the technological realization of a morphing wing followed by validation in a wind tunnel environment, and the possibility of detecting small pressure variations in the air flow boundary layer, and processing and analyzing the acquired signals in real time.

Thirty five (35) optimized airfoils were designed for the airflow case combinations of Mach number and angle of attack, and so 35 flight conditions were studied for the system: 7 values for the angle of attack, which was varied between  $-1^\circ$  and  $2^\circ$ , and 5 Mach number values, within range  $M [0.2, 0.3]$ ; see Table 9.1.

The configuration of the morphing wing wind tunnel model consists of a rectangular wing model that incorporates two parts: one rigid part built with a metal (aluminum alloy) designed to sustain all the aerodynamic and actuators loads, and one flexible part which consists of a flexible skin installed on the upper surface of the rigid wing part. As a reference airfoil, the NLF airfoil, WTEA, was chosen.

Table 9.1 Test flow conditions for 35 wing airfoils

	<b>Mach</b>	<b>1</b>	<b>2</b>	<b>3</b>	<b>4</b>	<b>5</b>
<b><math>\alpha</math> [°]</b>		<b>0.2</b>	<b>0.225</b>	<b>0.25</b>	<b>0.275</b>	<b>0.3</b>
1	-1°	C101	C108	C115	C122	C129
2	-0.5°	C102	C109	C116	C123	C130
3	0°	C103	C110	C117	C124	C131
4	0.5°	C104	C111	C118	C125	C132
5	1°	C105	C112	C119	C126	C133
6	1.5°	C106	C113	C120	C127	C134
7	2°	C107	C114	C121	C128	C135

The flexible skin is required to change the shape of the airfoil through two actuation points in order to realize an optimized airfoil for a given airflow condition under which the test is performed. Two rows of shape memory alloy actuators with a non-linear behaviour drive the displacement of the two control points on the flexible skin in order to obtain the optimized airfoil shape. Each of the shape memory actuators is activated by a power supply and controlled using Simulink/Matlab through a self-tuning fuzzy controller.

The optimized airfoils had previously been calculated by modifying the reference airfoils for each airflow condition such as to allow the transition point position to be located as close as possible to the trailing edge.

In this paper, the methods shown are used to acquire pressure data from the external surface of the flexible skin wing by means of optical and Kulite sensors, and by the instrumentation of the morphing controller. The acquired pressure data is analyzed through Fast Fourier Transforms in order to detect the magnitude of the noise in the air flow. This study is essential in reaching decisions concerning the minimal technical specifications for sensors that can be utilized in these applications. Subsequently, the data are run through high-pass filters and processed by calculating the RMS of the signal in order to obtain a plot diagram of

noise in the air flow. These processes are necessary to distinguish the inherent noise electronically induced from the Tollmien-Schlichting waves that are responsible for triggering the transition from laminar to turbulent flow.

## 9.2 Experimental set-up

From the initial studies related to the optimal configuration of the flexible structure [9], it can be concluded that the structure was conveniently designed to be operated by two actuation lines, respectively positioned at 25.3% and 47.6% of the chord from the leading edge of the airfoil (Fig. 9.2).

For this configuration, the aerodynamic forces coupled with the actuators can get the flexible skin to the position of maximum deflection, while the gas springs remind the SMA to return the flexible structure to its nominal position.

Under the aerodynamic loads for a given optimized airfoil shape and flight condition, the SMA actuation system would produce enough and sufficient force and displacement at the actuation line level. The vertical displacements induced by the two SMA actuators at the two actuation points are denoted by  $dY_1$  and  $dY_2$ , respectively. A sketch of the instrumented wing configuration is given in Fig. 9.3.

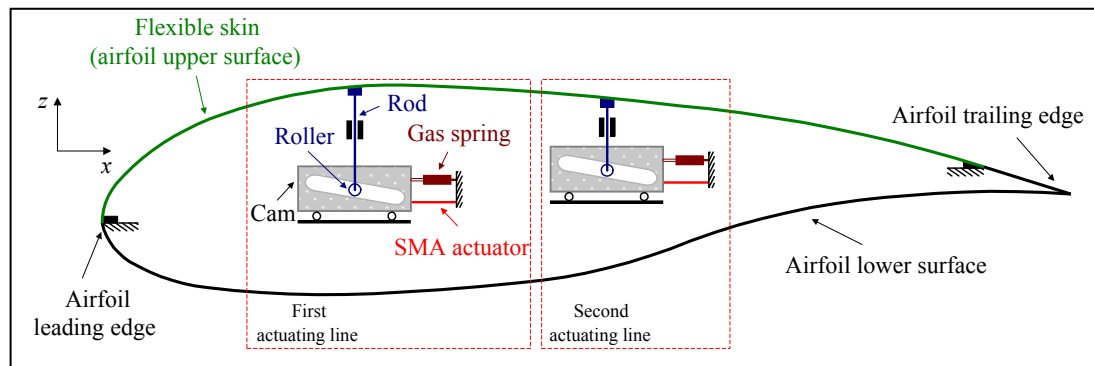


**Figure 9.2** Structure of the actuating system with SMAs.

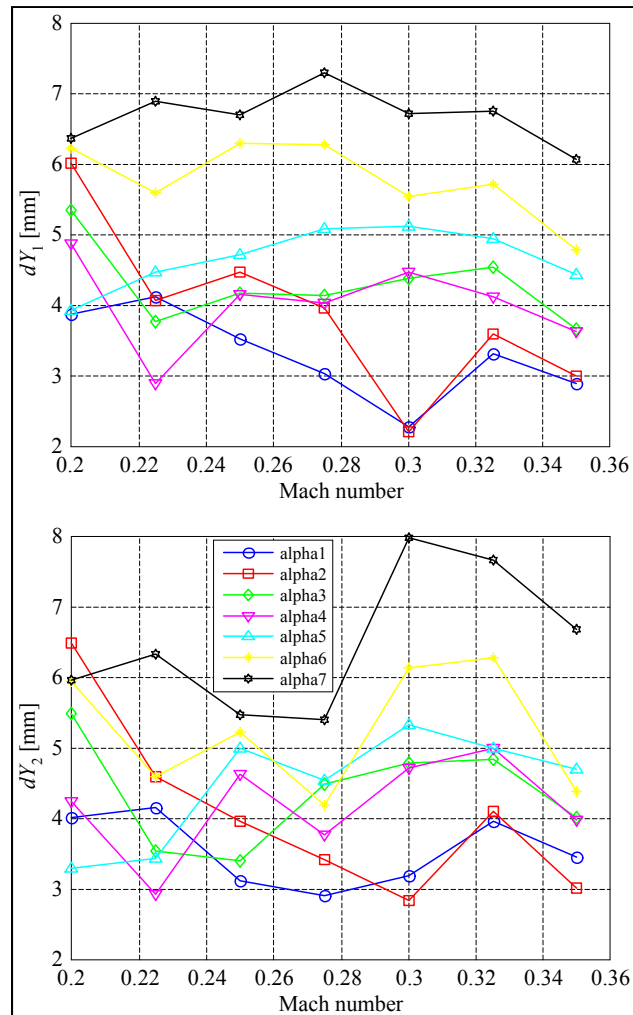


**Figure 9.3**  $dY_1$  and  $dY_2$  as functions of  $M$  for various  $\alpha$ .

Each actuating line of the system contains a cam, which moves in translation relative to the structure (in the  $x$ -axis direction in Fig. 9.2). The cam causes the movement of a rod linked to a roller and on the skin (in the  $z$ -axis direction) [9]. The initial position of the roller is restored by the compression gas spring. When the SMA is heated, the actuator contracts and the cam moves to the right, resulting in the rise of the roller and an upward vertical displacement of the skin. In contrast, the cooling of the SMA results in a movement of the cam to the left, and thus in a downward displacement of the skin (Fig. 9.4).

The architecture of the open-loop control system of the wing model, the SMA actuators and the controller are shown in Fig. 9.5. The two SMA actuators have six wires which are individually powered by two AMREL SPS power supplies, controlled through analog signals by a QUANSER Q8 control board, which was programmed through Simulink/xPC. In Simulink, a user interface was implemented allowing the user to choose the optimized airfoil shapes and to provide the necessary values for the SMA displacements,  $dY_1$  and  $dY_2$ , as shown in Fig. 9.2.

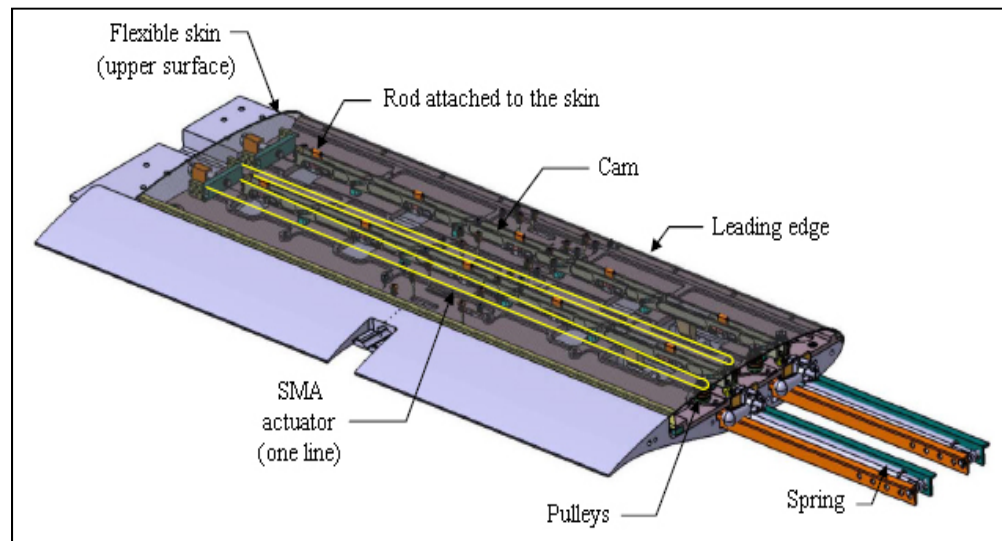


**Figure 9.4** Model of the flexible structure designed by LAMSI.

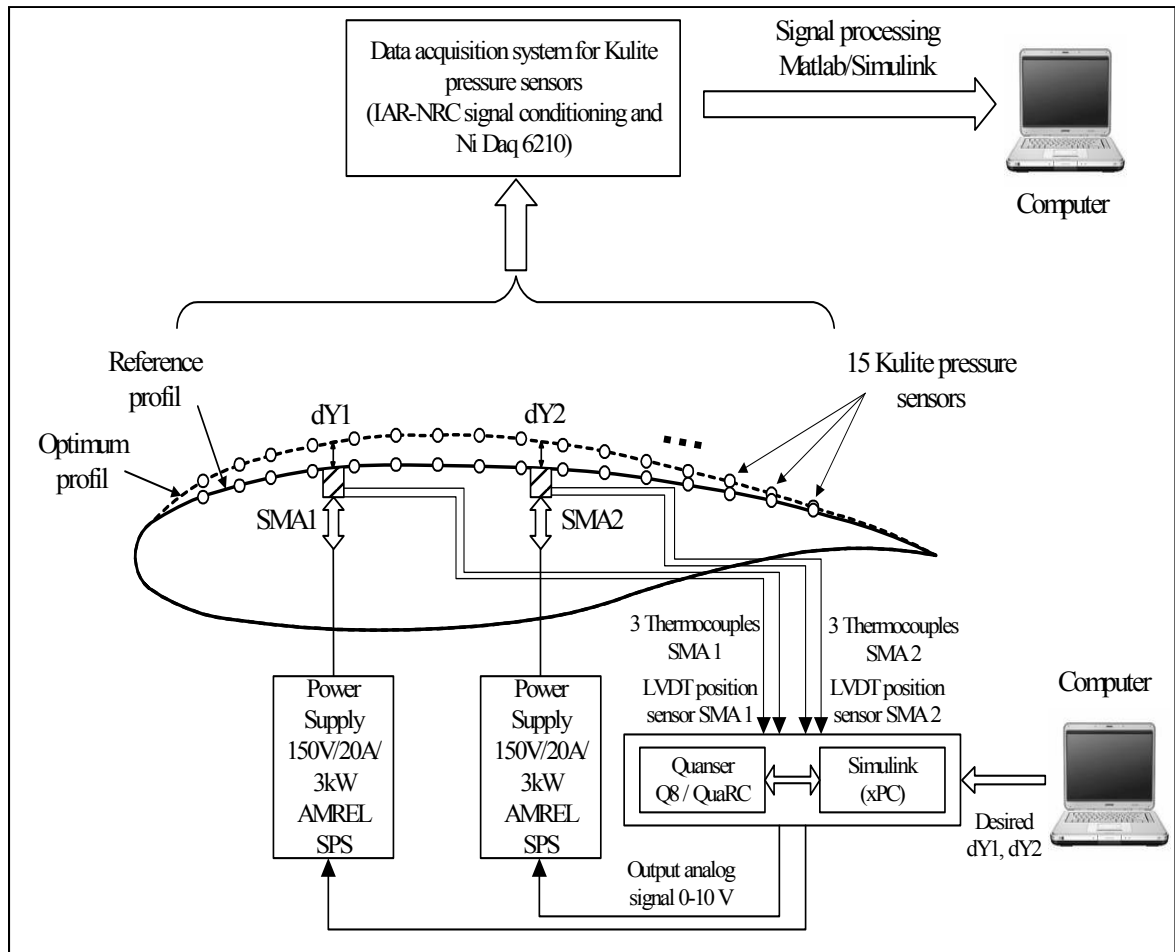


**Figure 9.5 SMA control architecture and sensor acquisition systems of the test in a wind tunnel for the morphing wing model.**

Each SMA actuator has its own controller which maintains the actuator in the desired position. The tested controller concept involves a self-tuning fuzzy controller. Furthermore, a classical PID controller was tested as well. The controllers act on the electrical current, which heats the SMA to allow it to change its length.

The initial input, which is the optimized airfoil for any flow condition, is chosen manually by the operator from the computer database through a user interface. Next, the displacements ( $dY_1$  and  $dY_2$ ) that need to be reproduced by the two control points on the flexible skin are sent to the controller. This controller sends an analog 0-2V signal to the power supply, which

provides a current of 0-20A/20V cc. to the SMA. The SMA responds accordingly, and changes its length according to the temperature of the wire. This results in the actuators changing positions, and the change is sensed by a linear variable differential transducer (LVDT). The signal position received from the LVDT is compared to the desired position, and the error obtained is fed back to the controller. If the realized position is greater than the desired position, the controller disconnects the control current, letting the SMA wire cool down. During the cooling down process, the SMA maintains its length due to the hysteretic behaviour, and this effect is taken into account for actuator displacement. Moreover, the controller uses three thermocouples signals from each SMA wire to monitor the temperature of the wires and maintains it below 130°C, which is the upper limit.

Typical measurements of turbulence in wind tunnels using microphones show that the noise level is about 20-40-60 dB SPL, depending on the wind speed and Reynolds number. The noise is converted into pressure RMS, which are about  $2e-4$ ,  $2e-3$ , and  $2e-2$  Pa, respectively. The reference pressure used in calculating the dB SPL is the value  $2e-5$  Pa, which is the standard value of the minimum sound pressure level detectable by the human ear. Usually, the noise level is calculated by RMS pressure values that show the noise density, which is constant at a given time interval. SI units were used and the conversion  $1\text{psi} = 6894.757$  Pa considered. The Kulite sensors have an “infinitesimal” resolution which is suitable for detecting such small variations. The signal sensitivity of the Kulite sensors is limited by the acquisition system used. As a consequence, 15 miniaturized pressure sensors are attached on the reference airfoil surface, as presented in Fig. 6, and the sensors are used to detect the transition point position of the airfoil by post-processing the pressure data.

The pressure data acquisition was performed using a NI-DAQ USB 6210 card with 16 analog inputs (Fig. 9.5), at a total sampling rate of 250 kS/s. The input channels were connected directly to the IAR-NRC analog data acquisition system, which in turn was connected to the 15 Kulite sensors. One extra channel was used for wind tunnel dynamic pressure acquisition and to calculate the pressure coefficient  $C_p$  from the pressure values measured by the 15 pressure sensors. The sampling rate of each channel was 15 kS/s which allowed a boundary

layer pressure fluctuation FFT spectral decomposition of up to 7.5 kHz for all channels. The signal was processed using Simulink, and displayed in real time.

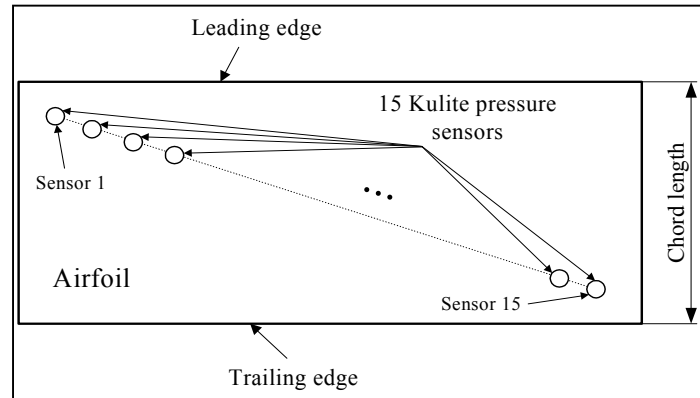


**Figure 9.6 Pressure sensor distributions on the morphing wing airfoil.**

### 9.3 Results and conclusions

The following proposed milestones were achieved (tests) during the wind tunnel tests performed at IAR-NRC:

- SMA open-loop control testing using a self-tuning fuzzy controller and a PID controller.
- Real-time pressure signal acquisition and processing tests using signal filtering, FFT spectral decomposition, RMS calculation and detection of the transition location, necessary for further development of closed-loop controller in order to obtain a fully automatic morphing wing system.
- Graphic User Interface (GUI) testing by keeping the dialog between the Matlab workspace and the Simulink schemes which were running in real time.

From the self tuning fuzzy versus PID open-loop control analysis, it was found that due to its in-built optimization algorithm, the self-tuning fuzzy controller needed less power than the PID controller for the same displacements. The PID controller uses a switch which connected and disconnected the power sources, and this had as consequence the saw teeth behaviour in the temperature time history plots, while the fuzzy controller kept a narrow control over the

temperature variations in the SMA wires. Fig. 9.7 shows the results for a wind tunnel run where the classical PID controller was used, while Fig. 9.8 shows the self-tuning fuzzy controller results for another wind tunnel run. As we can observe from the comparison of the results given in Figures 9.7 and 9.8, the time-response of the fuzzy controller is much better than that of the classical PID controller.

In Figures 9.7 and 9.8, the upper graph shows the displacement time histories, the middle graph shows the temperature time histories, and the lower graph shows the displacement temperature diagram.

Another test was conducted in order to prepare the closed-loop controller of the morphing wing system. The purpose of the test was to build a map of transition point locations and drag coefficients as functions of the two SMA displacements,  $dY_1$  and  $dY_2$ . The aerodynamic data was thus recorded while the  $dY_1$  and  $dY_2$  (keeping the same nomenclature and font) positions received a ladder input of 2, 4, 6 and 8 mm, respectively. In Fig. 9.9, one case is shown where the two actuators are controlled using a self-tuning fuzzy controller.

The next figures show the time history plots of the  $C_p$ , RMS and Power Spectra for the 15 pressure signals channels for various runs. Results obtained for sensors 11 and 12 were removed from the plots owing to their faulty dynamical signals. Sensor 5 showed a misalignment of the  $C_p$  values with respect to the  $C_p$  values of the other sensors, which meant that there was a leak or a pinched reference tube. On the other hand, the dynamic signal for sensor 5 was good, and as such, its value was retained on the plots.

The pressure data acquisition was performed using NI-DAQ USB 6210: 15 pressure signals from the Kulite sensors and the wind tunnel dynamic pressure.

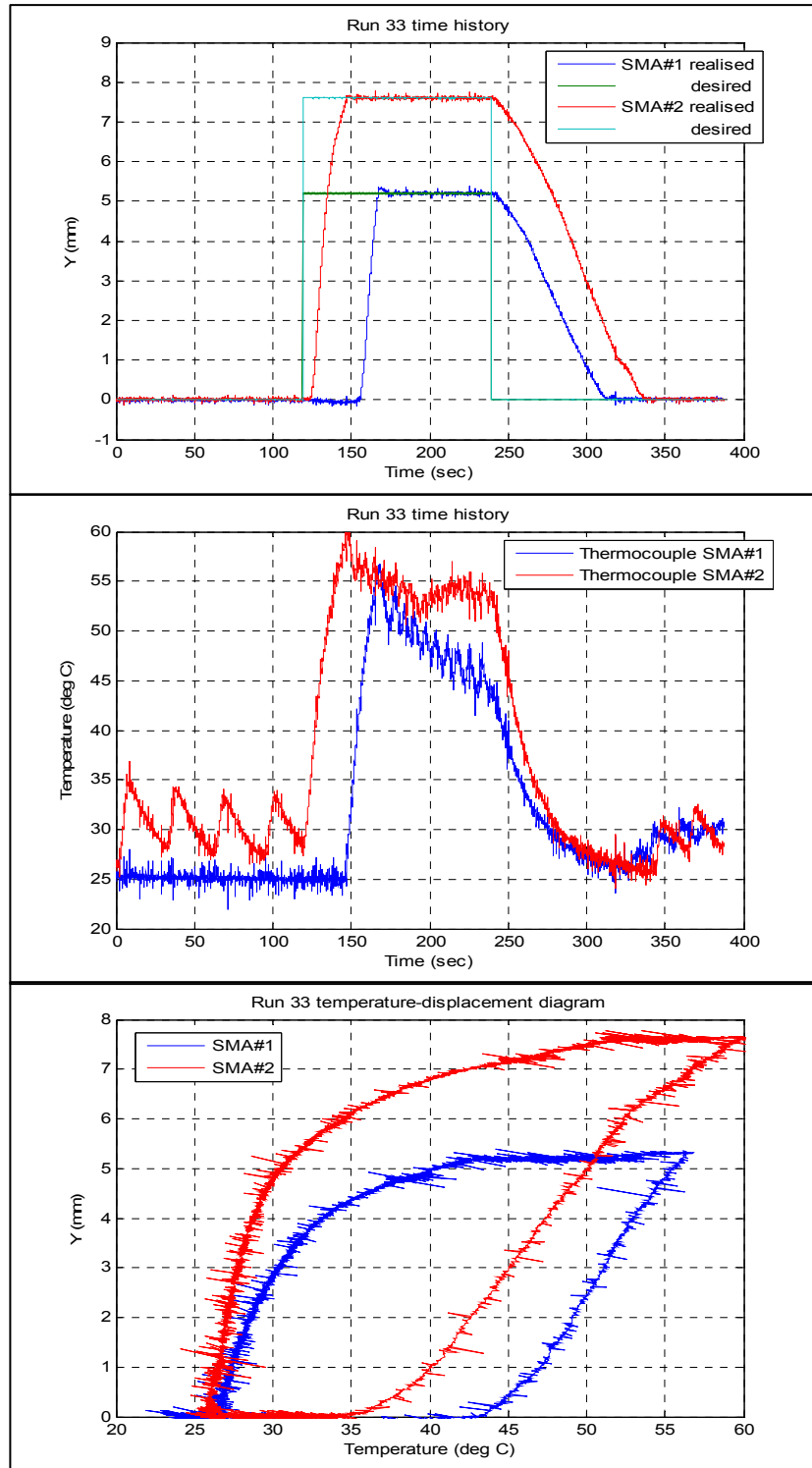


Figure 9.7 PID controller results for run 33.

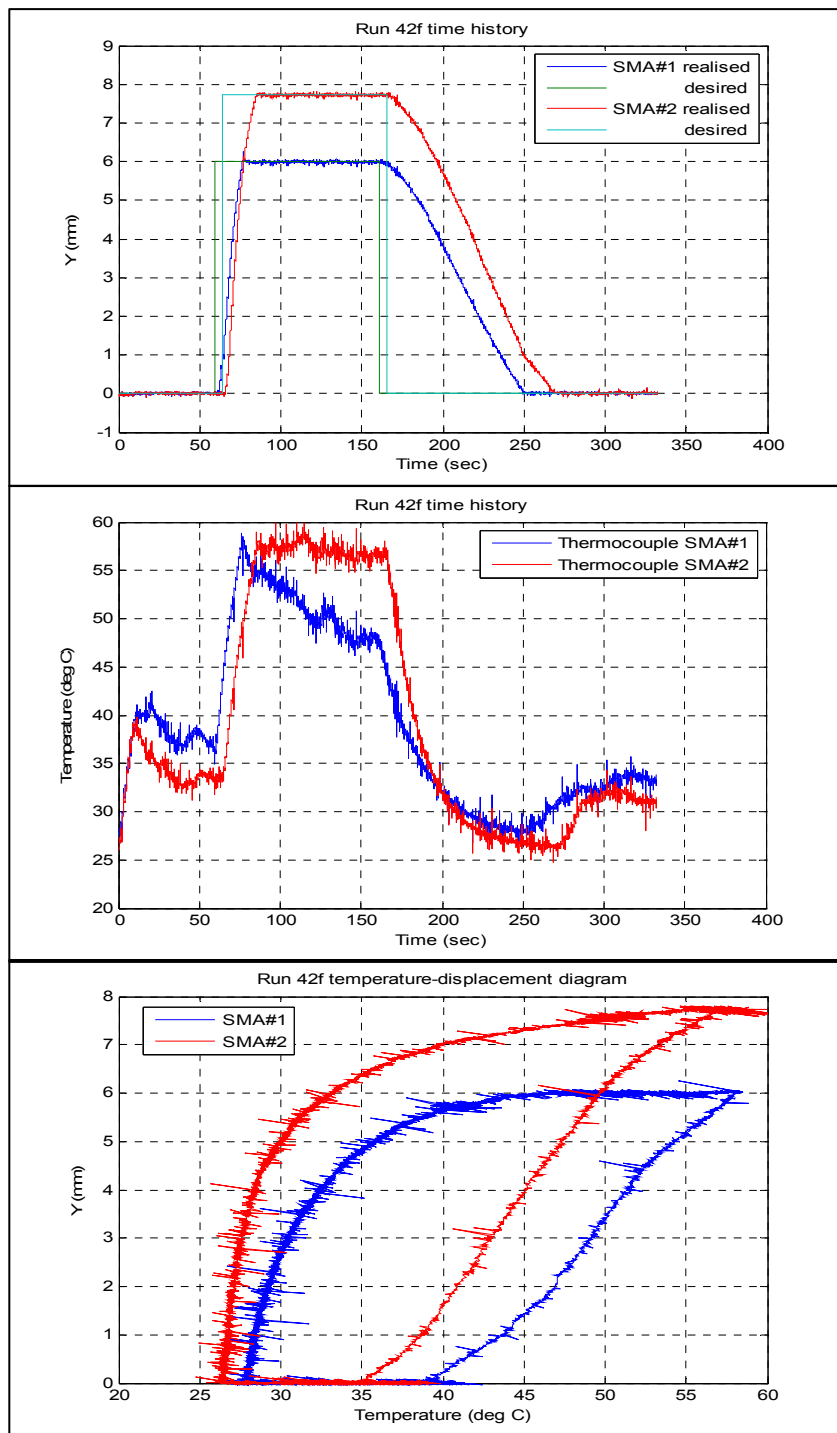
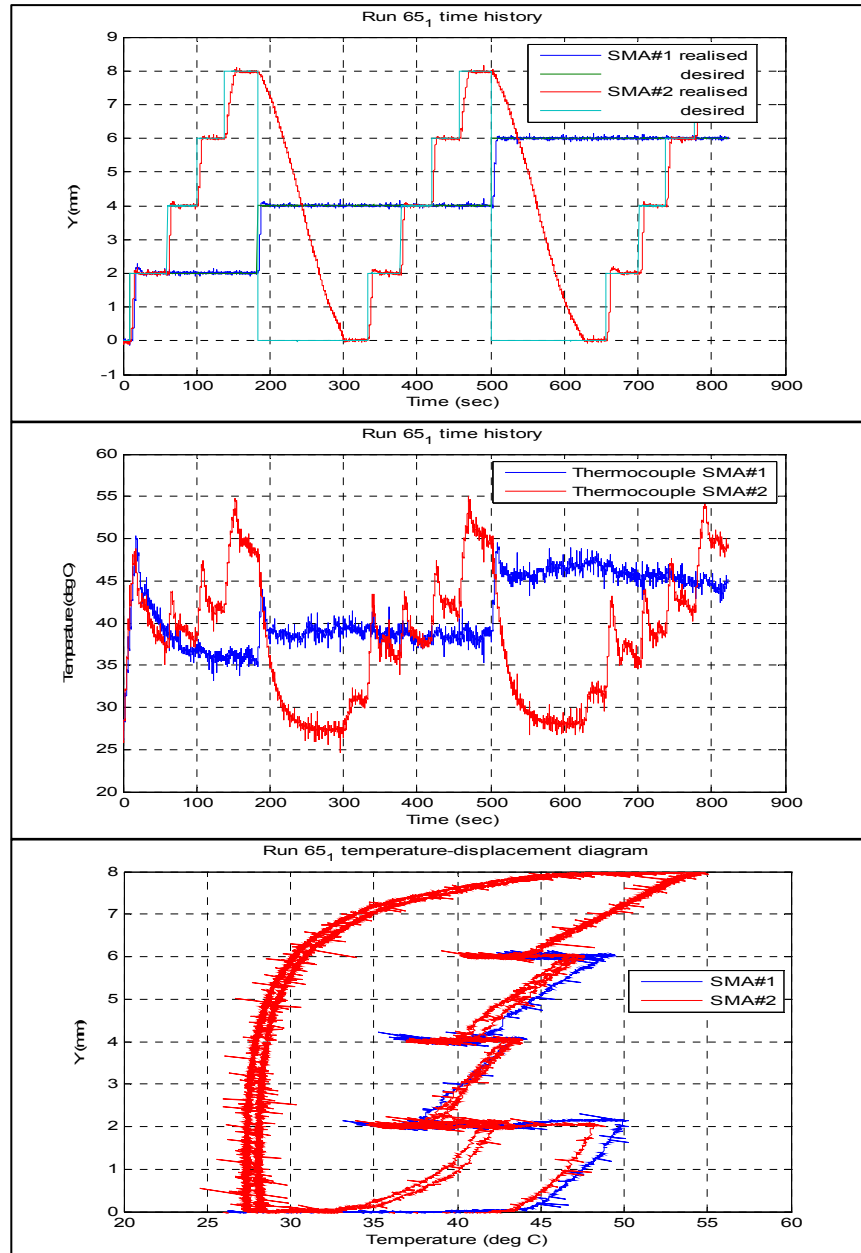


Figure 9.8 Self-tuning fuzzy controller results for run 42.



**Figure 9.9** Ladder command for SMA actuators using self-tuning fuzzy controller.

The middle left picture in Fig. 9.10 shows the Xfoil  $C_p$  values for the reference airfoil (black line and circles) and for the optimized airfoil (blue line and circles). The bottom picture shows the normalized RMS for 15 sensors for the reference un-morphed and optimized airfoils, while the pictures on the right show the FFT spectra for the 15 channels.

It is observed that for sensor 5, its  $C_p$  is not aligned with the  $C_p$  values of the other sensors, owing to the fact that the reference pressure tube was pinched, although its dynamic response is good. The transition is localized by sensor 14's maximum RMS and the highest noise band on the spectral plots (CH 2 magenta spectra on the lower right plot). The middle left picture in Fig. 9.11 shows the Xfoil  $C_p$  values for the reference airfoil (black line and circles) and for the optimized airfoil (blue line and circles). The bottom picture shows the normalized RMS for 15 sensors for the reference un-morphed and optimized airfoils. The pictures on the right show the FFT spectra for the 15 channels. The same observation was made for sensor 5 as in the above case. The transition is localized by sensor 13's maximum RMS and the highest noise band on the spectral plots (CH 1 light blue spectra on the lower right plot).

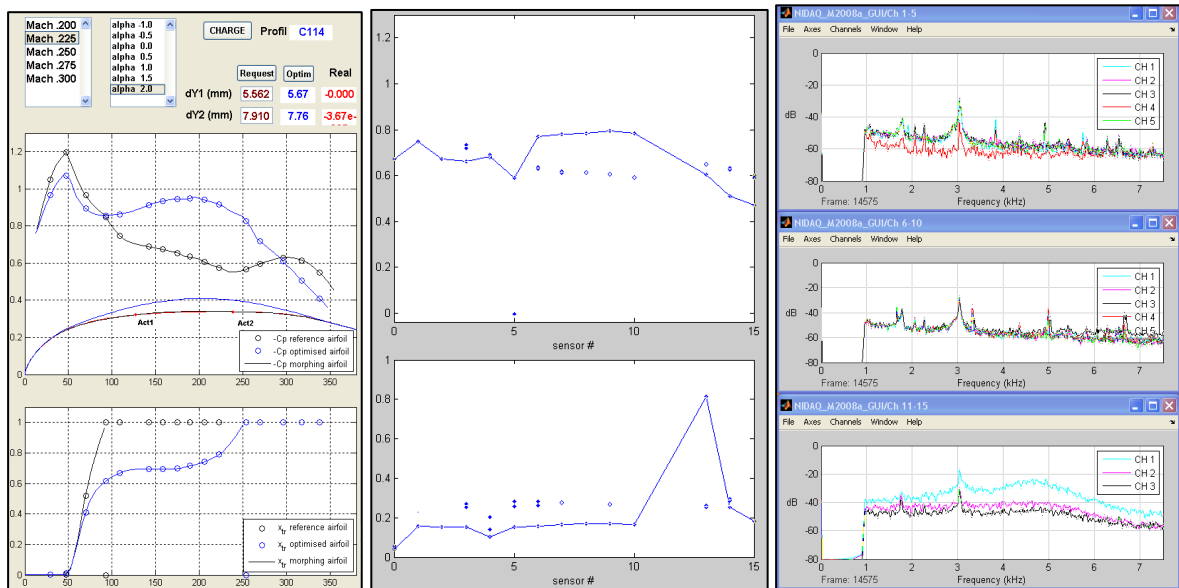
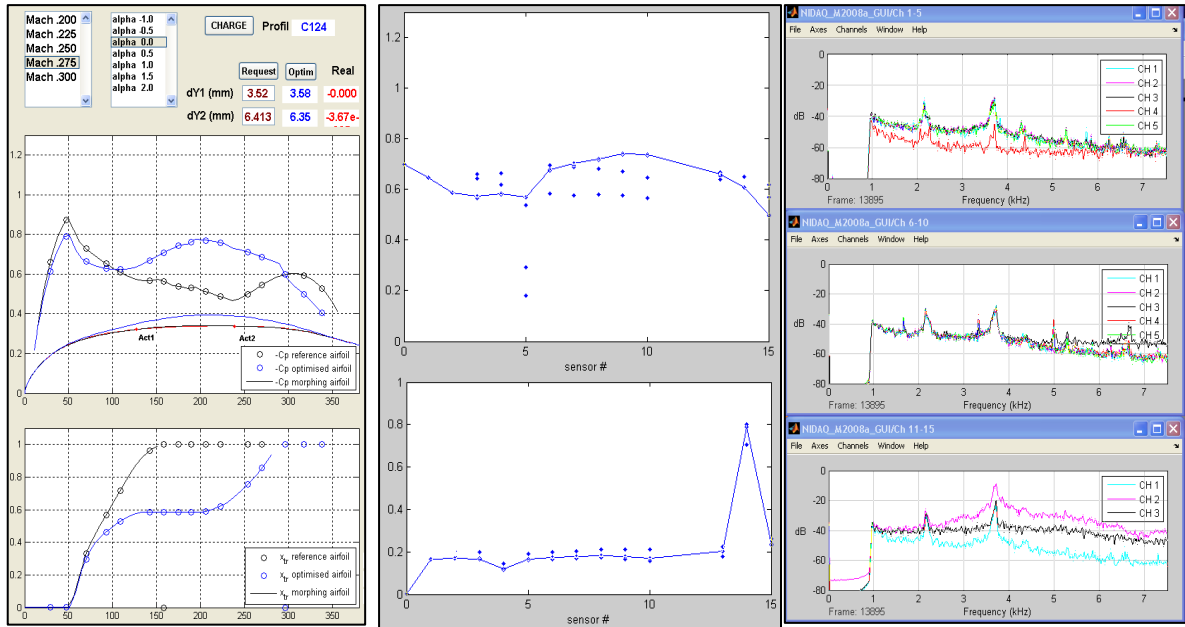


Figure 9.10 Airfoil case C124,  $M=0.275$  and  $\alpha=2^\circ$ .



**Figure 9.11** Airfoil case C114,  $M = 0.225$  and  $\alpha = 2^\circ$ .

The “CHARGE” push button runs a function that calculates the case number, such as “C129”, and further selects the reference and the optimized airfoils corresponding to this case from the database. With this button, the two airfoils (reference and optimized) are plotted starting from their leading edge ( $x$ -coordinate = 0 mm) to the end of flexible skin ( $x$ -coordinate = 380 mm). *XFoil* calculates the  $C_p$  distributions versus the chord for both airfoils. The distributions are plotted on the same graph, but with different colors (on the reference airfoil with black lines, and on the optimized airfoil, with blue lines).

On these graphs, the  $C_p$  values measured from various sensors are defined by *circles*, which will be used as “targets” in future versions of the closed-loop control software. In the lower figure, the  $N$  factor calculated with *XFoil* for both airfoils are plotted using the same colors as the above (blue and black, depending on whether the airfoil is optimized or reference).

In the left corner of the LHS (Left Hand Side) plots, three sets of actuator displacement values are shown in three columns: in the first column, the values requested by the user are transferred to the Simulink program by pressing the “Request” button; in the second column,

their values are optimized and automatically calculated from the difference between the database's optimized airfoil and reference airfoil values (these values are sent to the Simulink program by pressing the button "Optim"); in the third column, the real-time displacement values received from the actuator position sensors through the acquisition card are shown. In the right corner of the GUI figure from Fig. 9.12, there is a set of push-buttons that allow the user to control the Simulink program running.

The RHS (Right Hand Side) of plots contains a "Closed-loop" selection button which, when ON, calls a function to connect the entire system in a closed-loop controller which maintains the pressure distributions, such that the real values of the selected sensors remain in their respective targets. Another selector, "Find optim" is located below, which in the selected case, will call the function which will find the optimum configuration for the selected airflow case in real time.

The lower right corner of the LHS figures from Fig. 9.12 shows the number of the sensor located at the transition position calculated with XFoil for the reference airfoil (black), the number of the sensor located at the transition position calculated with XFoil for the optimized airfoil (blue), and the number of the sensor having the maximum noise level (maximum RMS of the filtered signal) that corresponds to the real transition position (red).

The power spectra plots on the right side of the Fig. 9.12 show the 15 channels as follows: the first 5 channels are shown in the upper figure named "Ch 1-5", the next 5 channels are shown in the middle figure named "Ch 6-10," and the next 5 channels, which are actually 3 because 2 of them were removed, are shown in the lower figure named "Ch 11-15".

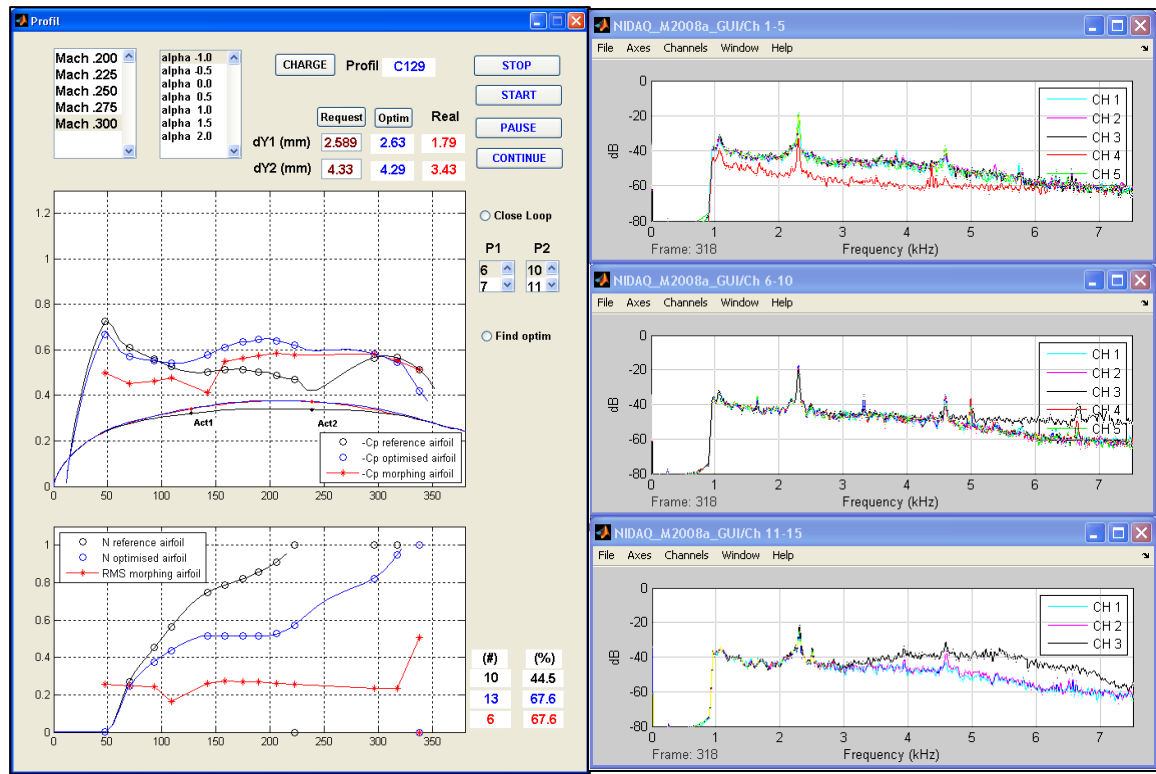


**Figure 9.12** Airflow case C129, Mach number = 0.3,  $\alpha = -1$  deg, reference (original) airfoil.

The realized tests show that the SMA actuators performed well, with the temperatures being lower than  $60^{\circ}\text{C}$  under maximal deployment. Moreover, the wind tunnel tests validated the self-tuning controller architecture for open-loop operation, and permitted the visualization of the transition which was controllable through Kulite sensors, which were able to detect the unsteady pressure coefficients  $C_p$  distributions as well as the noise signal distribution (RMS).

The paper presented a wind tunnel experimental testing of a morphing wing in open-loop architecture. The method used for acquiring the pressure data from the external surface of the flexible skin wing by means of Kulite pressure sensors and the instrumentation of the morphing controller were shown.

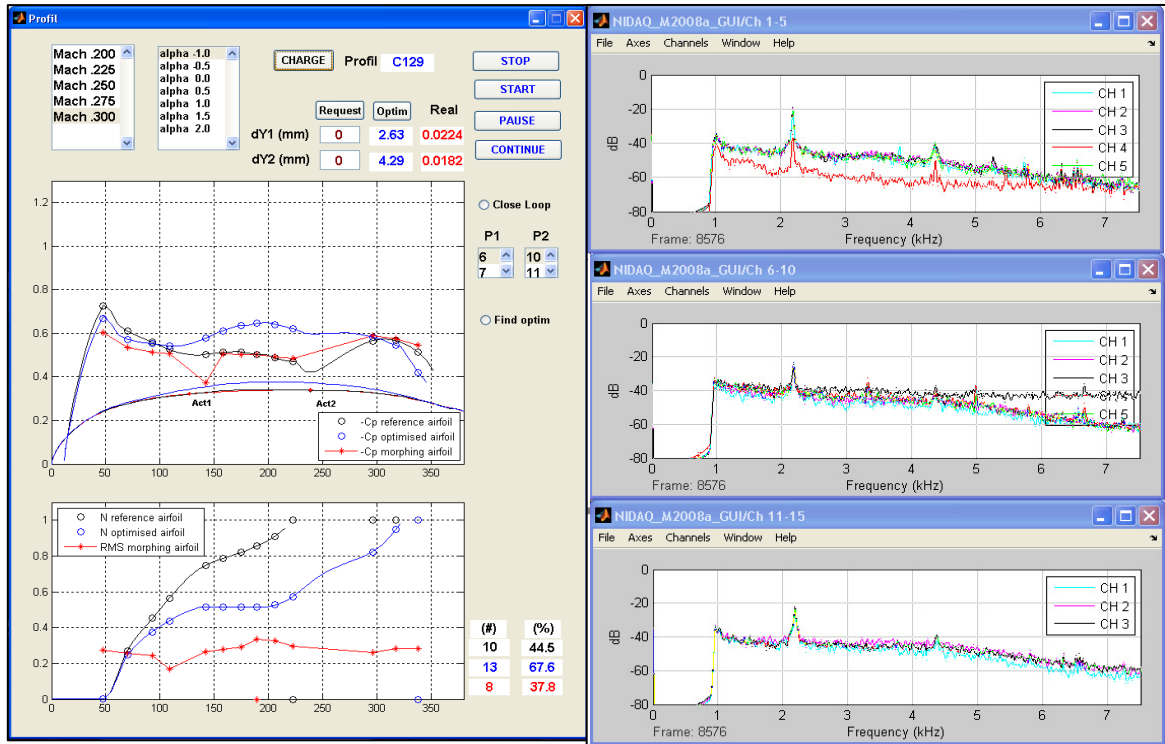


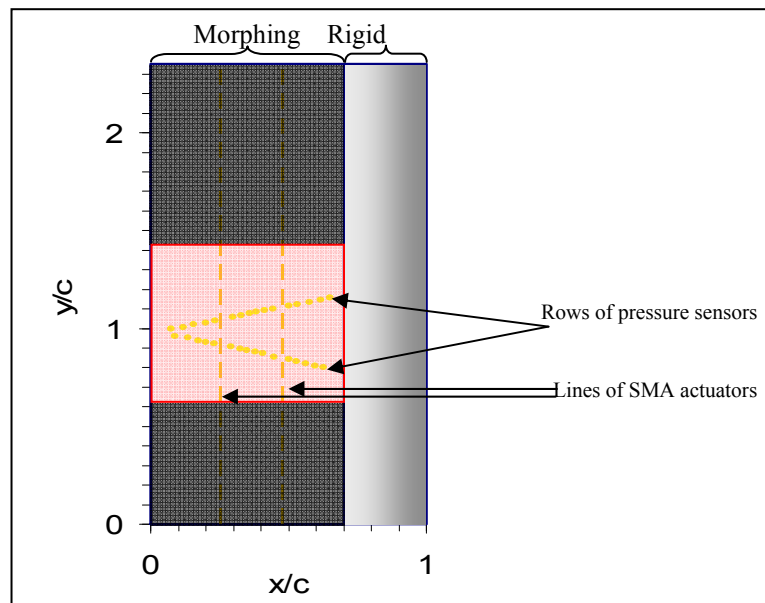
**Figure 9.13** Airflow case C129,  $M = 0.3$ ,  $\alpha = -1^\circ$  optimized (morphed) airfoil.

In support of the discrete pressure instrumentation, infrared thermography (IR) visualization was performed to detect the transition location on the upper surface of the morphing wing and to validate the pressure sensor analysis. The transition detection method using IR is based on the differences in laminar and turbulent convective heat transfer coefficient and was exacerbated by the artificial increase of model-air flow temperature differences. In the resulting images, the sharp temperature gradient separating high-temperature (white intensity in image) and low-temperature (dark intensity) regions indicates the transition location.

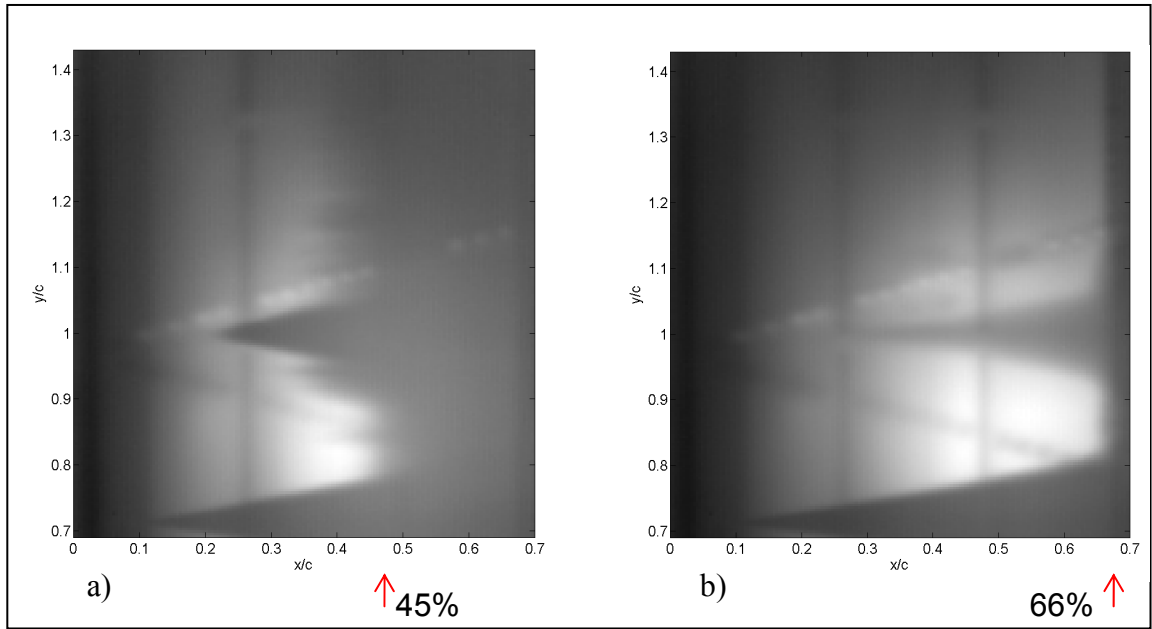
Figure 9.14 displays a wing schematics with the flexible portion in black ( $x/c < 0.7$ ), where the region of the morphing wing measured by the IR camera is highlighted in red. The aft rigid portion of the wing, made of aluminum, was not considered in the IR measurements. The rows of the powered pressure sensors are shown with the locations of the SMA actuators, which happen to be also visible in the IR images.

Figure 9.15 shows the IR transition images obtained for  $M = 0.3$  and  $\alpha = -1^\circ$ , in (a) the reference and (b) the optimized configurations. The transition, originally located at  $x/c = 45\%$  has been delayed to  $x/c = 66\%$  for the morphed wing configuration (case C129). The optimization has significantly extended the laminarity of the flow over the upper wing surface, as determined by the Kulite sensors. The optimization has also improved the apparent two-dimensionality of the flow: the transition appears vertical in the optimized case (b), except for the turbulent wedges triggered by some wing contamination near the leading edge (at  $x/c = 0.7$  and  $x/c = 1$ ).

Figure 9.16 shows the effect of optimization on the transition location at  $M = 0.275$  and  $\alpha = 0^\circ$ , in (a) the reference and (b) the optimized configurations (case C214). The transition was delayed from  $x/c = 33\%$  on average, for the reference case, to  $x/c = 57\%$ , for the optimized case. These results, which are in agreement with the Kulite data, confirm the use of discrete transducers as control parameters for wing shape optimization.



**Figure 9.14** 2-D Wing Model in normalized coordinates (chord  $c = 0.5\text{m}$ ). Morphing portion of the wing at  $0 < x/c < 0.7$ . Region measured by IR highlighted in red at  $0.69 < y/c < 1.46$ . The rigid part of the wing, made of aluminum, is not used in the IR data. Flow is from left to right.



**Figure 9.15** Infrared images at  $M = 0.3$ ,  $\alpha = -1^\circ$  for two wing shapes: a) Reference and b) Optimized shape C129. Transition location indicated with the red arrow. Flow is from left to right.

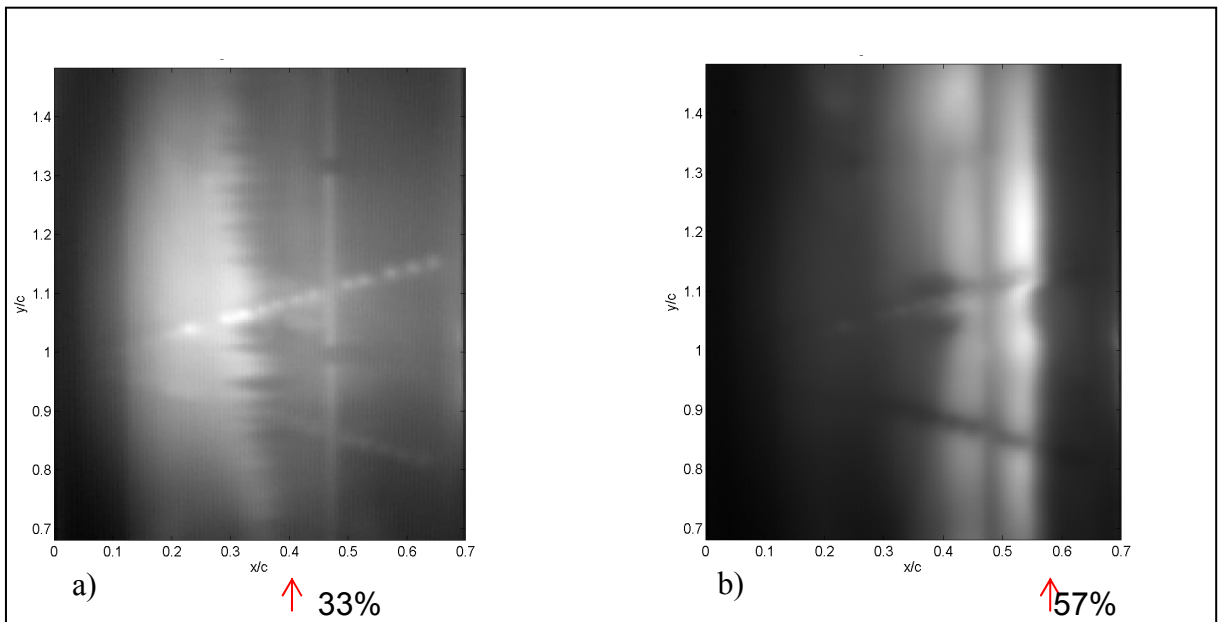


**Figure 9.16** Infrared images at  $M = 0.275$ ,  $\alpha = 0^\circ$  for two wing shapes: a) Reference and b) Optimized shape C124. Transition location indicated with the red arrow. Flow is from left to right.

In conclusion, the control and the pressure acquisition systems have proven their functioning during wind tunnel tests, using the wing model as hardware-in-the-loop. The next step in the control design was to close the loop using the pressure values measured by the pressure sensors as feedback control.

## References

- [1] Rodriguez, A. R., 2007, *Morphing aircraft technology survey*, Paper AIAA-2007-1258.
- [2] Livne, E., 2003, *Future of airplane aeroelasticity*, AIAA Journal of Aircraft, Vol. 40(6), pp. 1066-1092.
- [3] Moorhouse, D. et al., 2006, *Benefits and design challenges of adaptive structures for morphing aircraft*, The Aeronautical Journal, pp 157-162.
- [4] Carter, D.L., 2007, *The quest for efficient transonic cruise*, Paper AIAA-2007-7812, The 7<sup>th</sup> AIAA Aviation, Technology, Integration and Operations Conference ATIO, 18-20 September, pp. 1-17.
- [5] Popov, A.-V., Botez, R.M., Labib, M., 2008, *Transition point detection from the surface pressure distribution for controller design*, AIAA Journal of Aircraft, Vol. 45(1), pp. 23-28.
- [6] Popov. A-V., Labib, M., Fays, J., Botez, R.M., 2008, *Closed loop control simulations on a morphing laminar airfoil using shape memory alloys actuators*, AIAA Journal of Aircraft, Vol. 45(5), pp. 1794-1803.
- [7] Popov. A-V., Botez, R.M., Mamou, M., Grigorie, L. T., 2009, *Optical sensor pressure measurements variations with temperature in wind tunnel testing*, under print, AIAA Journal of Aircraft.
- [8] Grigorie, L. T., Botez, R. M., 2008, *The bias temperature dependence estimation and compensation for an accelerometer by use of the neuro-fuzzy techniques*, CSME Transactions, Vol. 32(3), pp. 383-400.
- [9] Brailovski, V., Terriault, P., Coutu, D., Georges, T., Morellon, E., Fischer, C., Berube, S., 2008, *Morphing laminar wing with flexible extrados powered by shape memory alloy actuators*, Proc. ASME Conf. Smart Materials, Adaptive Structures and Intelligent Systems (SMASIS 2008), Paper 337, Ellicott City, USA.

## CHAPTER 10

### ARTICLE 7

#### CLOSED LOOP CONTROL VALIDATION OF A MORPHING WING USING WIND TUNNEL TESTS

Andrei V. Popov, Lucian T. Grigorie and Ruxandra Botez  
École de Technologie supérieure, Montréal, Québec, H3C 1K3, Canada,  
Mahmoud Mamou, and Youssef Mebarki,

Institute of Aeronautical Research – NRC, Ottawa, Ontario, K1A 0R6, Canada

The article was submitted for publication at AIAA Journal of Aircraft on 20 September 2009.

#### Article presentation

The article shows the results obtained in wind tunnel tests performed on May 2009 at IAR-NRC, Ottawa. The wing model mechanical and electrical design manufacture and installation in the wind tunnel was performed by LAMSI, IAR-NRC and LARCASE team; in fact, LARCASE team, under Dr Botez supervision has done the wind tunnel testing plan writing, and its scheduling in collaboration with the IAR-NRC team under the supervision of Dr Mamou M., the sensors and controller data post-processing and installation on the wing model, and the planning of the cabling systems related to the model integration in the wind tunnel. The infrared measurements were performed during wind tunnel tests by Dr. Youssef Mebarki. The wing model was controlled by a closed loop system driven automatically by computer. The paper shows the control software and the real time pressure data acquisition and visualizing realized by me with the assistance of Dr. Lucian Grigorie at LARCASE. The references to the mechanical and electrical system in the paper have the purpose to facilitate the reader's understanding. The operation of the morphing wing model in wind tunnel tests was performed by me for all the test runs in wind tunnel using two control methods, an open loop control and a closed-loop control. The open loop method used a previously calculated database of  $Y_1$  and  $Y_2$  coordinates for each SMA actuator, while the closed-loop method used the aerodynamic information from pressure sensors to maintain the laminar flow over the upper surface of the airfoil. The pairs of actuators displacements

values, obtained for all optimised airfoils, as well as the coordinates of the morphed airfoil shapes used by my software during the wind tunnel tests were calculated by École Polytechnique team in collaboration with LAMSI team using CFD and FEM simulations commercial codes. Dr. Botez was my PhD advisor and Dr. Mamou was the responsible of the IAR-NRC wind tunnel tests. The paper discusses the differences between the two methods and proves that the functioning of the wing model in wind tunnel was a success.

## **Résumé**

Dans cet article, une aile rectangulaire avec une envergure finie, ayant un profil de référence WTEA a été considéré. La surface de l'extrados a été fabriquée en matériaux composites flexibles et équipée avec des capteurs de pression Kulite, et deux actionneurs avec alliages à mémoire de forme. Les signaux de pressions non-stationnaires ont été enregistrés et visualisés en temps réel, pendant que la forme de l'aile a été changée pour reproduire les formes optimisées à l'aide des deux actionneurs. La procédure de control a utilisée deux méthodes de contrôle présentés dans l'article. Plusieurs tests ont été effectués pour différentes valeurs des angles d'incidence et nombres de Reynolds dans la soufflerie de  $2\text{m} \times 3\text{m}$  de l'Institut de Recherche Aérospatiale du Conseil Nationale de Recherche du Canada. Les nombres de Mach ont varié entre 0.2 et 0.3, les nombres de Reynolds ont varié entre 2.29 millions et 3.36 millions, et les angles d'incidence ont varié entre  $-1^\circ$  et  $2^\circ$ . Les enregistrements des données dans la soufflerie pour la détection de la transition dans la couche limite en utilisant des capteurs de pression à haute fréquence d'échantillonnage sont présentés.

## **Abstract**

In this paper, a rectangular finite aspect ratio wing, having a WTEA reference airfoil cross-section, was considered. The wing upper surface was made of a flexible composite material and instrumented with Kulite pressure sensors, and two smart memory alloys actuators. Unsteady pressure signals were recorded and visualized in real time while the morphing wing was being deformed to reproduce various airfoil shapes by controlling the two

actuators displacements. The controlling procedure was performed using two methods which are described in the paper. Several wind tunnel test runs were performed for various angles of attack and Reynolds numbers in the  $6 \times 9$  foot wind tunnel at the Institute for Aerospace Research at the National Research Council Canada. The Mach number was varied from 0.2 to 0.3, the Reynolds numbers varied between 2.29 and  $3.36 \times 10^6$ , and the angle-of-attack range was within -1 to 2 degrees. Wind-tunnel measurements are presented for airflow boundary layer transition detection using high sampling rate pressure sensors.

### 10.1 Introduction

The present work was performed under the 7.1 Consortium for Research and Innovation in Aerospace in Quebec (CRIAQ) collaborative project between academia and industries. The project partners were the École de Technologie Supérieure (ETS), École Polytechnique of Montreal, the Institute for Aerospace Research at the National Research Council Canada (IAR-NRC), Bombardier Aerospace and Thales Avionics. In this project, the laminar flow behavior past aerodynamically morphing wing is improved in order to obtain significant drag reductions.

This collaboration calls for both aerodynamic modeling as well as conceptual demonstration of the morphing principle on real models placed in the wind tunnel. Drag reduction on a wing can be achieved by modification of the airfoil shape which has a direct effect on the laminar-to-turbulent flow transition location. The main objective of this concept is to promote large laminar regions on the wing surface, by delaying the transition location towards the trailing edge. Thus, the wing viscous drag could be reduced over an operating range of flow conditions characterized by a Mach number and angles of attack [1]. The airborne modification of an aircraft wing airfoil shape can be realized continuously to maintain laminar flow over the wing surface as flight conditions change. To achieve such a full operating concept, a closed-loop control system concept was developed to control the flow fluctuations over the wing surface with the airfoil skin deformation mechanisms (actuators) [2]. A similar automatic control of boundary layer transition using suction on a flat plane and microphones was presented by Rioual et al. [3].

The wing model had a rectangular plan form of aspect ratio of 2 and was equipped with a flexible upper surface skin on which shape memory alloys actuators were installed. The two shape memory alloys (SMA) actuators executed the displacement at the two control points on the flexible skin in order to realize the desired optimized airfoil shapes.

The flexible skin was manufactured in a 4 ply laminate structure in a polymer matrix, with 2 unidirectional Carbon fiber inner plies and 2 hybrid Kevlar/Carbon fiber outer plies. The hybrid Kevlar/Carbon fiber was used in the chord-wise direction, where flexibility was needed for profile modification, whereas the low-modulus unidirectional carbon fiber was spanwise installed, in which case rigidity was preferred. The total thickness of the skin was 1.3 mm, the total Young modulus was 60 GPa, the Poisson's ratios were 0.12 for Carbon/Kevlar hybrid and 0.25 for unidirectional Carbon [4].

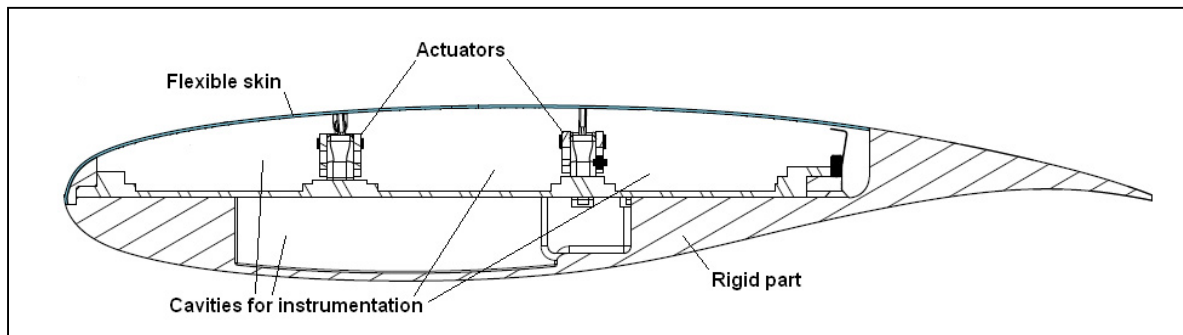


**Figure 10.1** Cross section of the morphing wing model.

As a reference airfoil, a laminar airfoil WTEA was considered; its aerodynamic performance was investigated at IAR-NRC in the transonic regime [5, 6]. The flow over the reference airfoil upper surface became turbulent in a certain point near the leading edge due to the separation bubble for each airflow case expressed by a combination of Mach number and angle of attack. The separation bubble (the transition between laminar and turbulent flow) appeared due to the steep curvature of the airfoil shape. The principle beyond moving the

separation bubble (the transition) towards trailing edge consisted in changing to a milder curvature of the airfoil shape, which was presented by Botez et al. [7]

The optimized airfoils were previously calculated by modifying the reference airfoil for each airflow condition as combinations of angles of attack and Mach numbers. The optimized airfoil shapes were realized using an optimizing routine that varied the vertical position of each actuator. The optimizing routine was coupled with a spline curve model of the flexible skin and the XFOIL CFD code, and then the first generation of optimized airfoils C1XX was obtained. The XFOIL CFD code is free software in which the  $e^N$  transition criterion is used [8, 9]. The imposed conditions of the first optimization were expressed in terms of the transition point position displacement as near as possible to the airfoil trailing edge, while maintaining a constant lift. The first generation of optimized airfoils was tested and validated by scanning using a laser during bench tests, as shown in Fig. 2 [10]. The second generation of optimized airfoils was obtained by coupling the optimizing routine with a finite element model (FEM) of the flexible skin [4] and the XFOIL CFD code, and the conditions imposed were to minimize the drag by moving the transition point as near as possible to the trailing edge while maintaining a constant lift [11].

Thirty five optimized airfoils were found for the airflow cases combinations of Mach numbers and angles of attack. Table 1 shows the optimized airfoils shapes denoted by C201-C235 for the angles-of-attack variations from -1 to 2 degrees, the Mach number variations from 0.2 to 0.3 and the Reynolds numbers variations from 2.29 to  $3.37 \times 10^6$ .

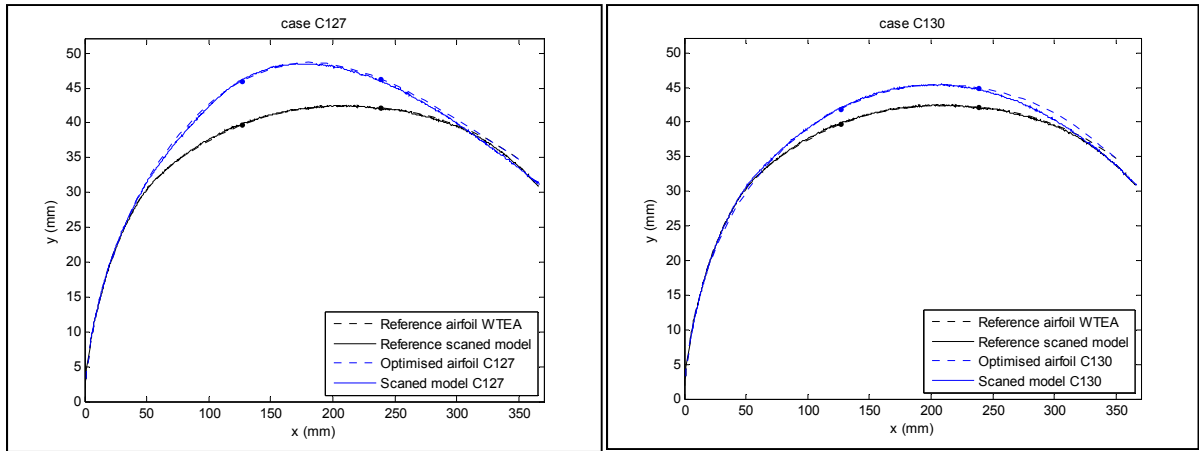


**Figure 10.2** Two examples of optimized airfoil shapes for the aerodynamic cases C127 ( $M=0.275$ ,  $\alpha=1.5$  deg) and C130 ( $M=0.3$ ,  $\alpha=-0.5$  deg).

## 10.2 Experimental setup description

### 1. Mechanical and electrical control system

The morphing wing model has a rectangular plan form (chord  $c = 0.5$  m and span  $b = 2.1$  m) and consists of two parts; one metal fixed part, which was designed to sustain the wing loads at a Mach number of 0.3 and an angle of attack up to 6 deg, and a morphing part, consisting of a flexible skin installed on the wing upper surface and the SMA actuator system (Fig. 10.1). The flexible skin was required to change its shape through two action points to realize the optimized airfoil for the airflow conditions under which the tests were performed.

The actuators were composed of two oblique cams sliding rods spanwise positioned that converted the horizontal movement along the span into vertical motion perpendicular to the chord (Fig. 10.2). The position of each actuator was given by the mechanical equilibrium between the Ni-Ti alloy SMA wires that pulled the sliding rod in one direction and the gas springs that pulled the sliding rod in the adverse direction. The gas springs role was to counteract the pulling effect of aerodynamic forces acting in wind tunnel over the flexible skin when the SMAs were inactive. Each sliding rod was actuated by means of three parallel SMA wires connected to a current controllable power supply which was the equivalent of six

wires acting together. The pulling action of the gas spring retracted the flexible skin in the undeformed-reference airfoil position, while the pulling action of the SMA wires deployed the actuators in the load mode i.e. morphed airfoil in the optimized airfoil position (see Fig. 10.3). The gas springs used for these tests were charged with an initial load of 225 lbf (1000 N) and had a characteristic rigidity of 16.8 lbf / in (2.96 N / mm).

Table 10.1 Test flow conditions for 35 wing airfoils

Mach	Re ( $\times 10^6$ )	Angle of attack (degrees)						
		-1.00	-0.50	0.00	0.50	1.00	1.50	2.00
0.200	2.2932	C201	C202	C203	C204	C205	C206	C207
0.225	2.5679	C208	C209	C210	C211	C212	C213	C214
0.250	2.8384	C215	C216	C217	C218	C219	C220	C221
0.275	3.1044	C222	C223	C224	C225	C226	C227	C228
0.300	3.3654	C229	C230	C231	C232	C233	C234	C235

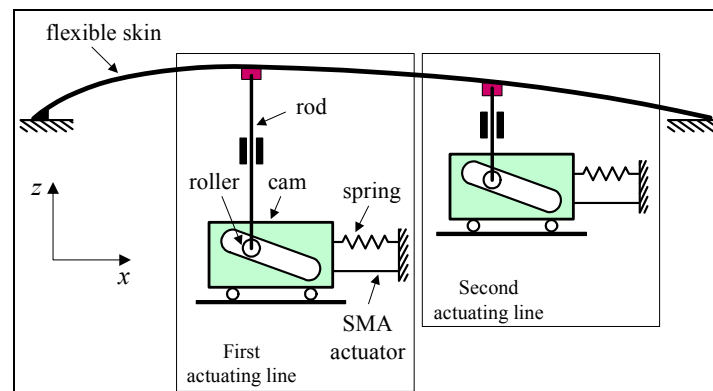
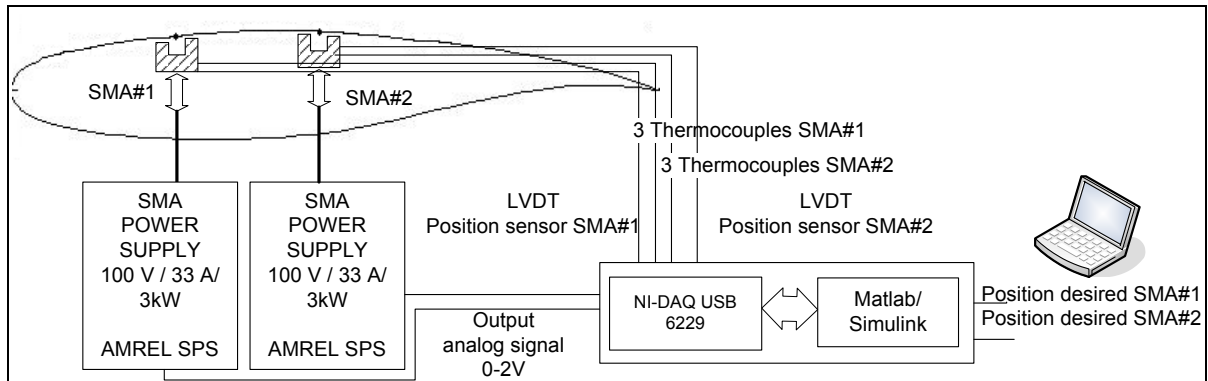


Figure 10.3 Schematics of the flexible skin mechanical actuation.

The mechanical SMA actuators system was controlled electrically through an open loop control system. The architecture of the wing model open loop control system, SMA actuators and controller are shown in Figure 10.4. The two SMA actuators have six wires each, which

are supplied with power by the two AMREL SPS power supplies, controlled through analog signals by the NI-DAQ USB 6229 data acquisition card. The NI-DAQ was connected to a laptop through a USB connection. A control program was implemented in Simulink which provided to the power supply unit the needed SMA current intensity through an analog signal as shown in Figure 10.4. The Simulink control program used as feedback three temperature signals coming from three thermocouples installed on each wire of the SMA actuator, and a position signal from a linear variable differential transducer (LVDT) sensor connected to the oblique cam sliding rod of each actuator. The temperature signals were used for the overheat protection system that disconnects the current supply to the SMA in case of wire temperature pass over the set limit of 130°C. The position signals served as feedback for the actuator desired position control. The oblique cam sliding rod had a horizontal versus vertical ratio 3:1; hence the maximum horizontal displacement of the sliding rod by 24 mm was converted into a maximum vertical displacement (8mm) of the actuator.



**Figure 10.4 Architecture of the morphing wing model control system.**

A user interface was implemented in Matlab/Simulink which allows the user to choose the optimized airfoils shape from database stored on the computer hard disk and provided to the controller the required vertical displacements to obtain the desired optimized airfoil shape. The controller activated the power supplies with the required SMA current intensities through an analog signal as shown in Figure 10.4. The control signal of 2 V corresponded to a SMA supplied current of 33 A. In practice, the SMA wires were heated at an approximate

temperature of 90°C with a current of 10 A. When the actuator reached the desired position the current was shut off and the SMA was cycled in endless heating/cooling cycles through the controller switching command on/off of the current to maintain the current position until another desired position or the entire system shut off was required.

In support of the discrete pressure instrumentation, infrared thermography (IR) visualization was performed to detect the transition location on the morphing wing upper surface and validate the pressure sensor analysis. The transition detection method using IR was based on the differences in laminar and turbulent convective heat transfer coefficient and was exacerbated by the artificial increase of model-air flow temperature differences. In the resulting images, the sharp temperature gradient separating high temperature (white intensity in image) and low temperature (dark intensity) regions is an indication of the transition location. The infrared camera used was an Agema SC3000 camera, equipped with a 240×320 pixels quantum well infrared photodetector (QWIP), operating in the infrared wavelength region of 8-9  $\mu\text{m}$  and cooled to 70°K to reduce thermal noise. The camera provided a resolution of 0.02°C and a maximum frame rate of 60 Hz. It was equipped with the default lens (FOV = 20 deg × 15 deg), and was installed 1.5 m away from the model with an optical axis oriented in the horizontal plane at about 30 deg with respect to the wing surface midchord normal. Optical access was provided through an opening on the side wall of the test section opposite to the upper surface. More details about the methodology and processing are from Mébarki and Mamou [12].

## **2. Aerodynamic detection system and graphical user interface**

The morphing wing goal was to improve laminar flows over the upper surface of the wing. To ensure that the improvement is achieved, a detection system was incorporated to the wing model that gives information about the flow characteristics. An array of 12 Kulite pressure sensors was installed on the flexible skin.

The pressure data acquisition was performed using a NI-DAQ USB 6210 card with 16 analog inputs, at a total sampling rate of 250 kilo samples/s. The input channels were connected directly to the wind tunnel analog data acquisition system which was connected to the 12 Kulite sensors. The data acquisition system served as an amplifier and conditioner of the signal at a sampling rate of 15 kilo samples/s. One extra channel was used for the wind-tunnel dynamic pressure acquisition to calculate the pressure coefficients  $C_p$ 's from the pressure values measured by the 12 pressure sensors. The signal was acquired at a sampling rate of 10 kilo samples/s in frames of 1024 points for each channel which allowed a boundary layer pressure fluctuations fast Fourier transform spectral decomposition up to 5 kHz for all channels, at a rate of 9.77 samples/s (Figure 10.5) using Matlab/Simulink software. The plot results were visualized in real time on the computer screen in dedicated windows (see Figure 10.6) at a rate of 1 sample/s. Figure 10.6 shows an example of graphical user interface in which all the aerodynamical and morphing shape information were centralized together with the control buttons of the controlling software. The window showed some data about the Mach number, the angle of attack, the airfoil shape of the morphing wing, and the two actuators vertical displacements needed to obtain the desired airfoil shape. Shown in the two plots, were the pressure coefficients distribution  $C_p$ 's of the 12 Kulite sensors and the noise of the signal (RMS) of each pressure signal. The left figure shows the wing unmorphed position, whereas the right figure shows the wing under its morphed position. The results obtained were qualitatively very similar to those obtained in previous studies [13, 14].

In Figure 10.5.a the 12 spectra of the pressure signals are shown, for the unmorphed wing. The noise amplitude of the signals is about the same for the whole bandwidth, with the exception being of the first signal channel which had obviously the smallest noise. The laminar-to-turbulent transition was detected by the slight peak of the fourth sensor positioned at 35% of the chord in the root mean squares (RMS) plot in Figure 10.6.a (star curve). The laminar-to-turbulent transition was not visible in signals spectra from Figure 10.5.a, but two peaks were visible at 1.7 kHz and 2.8 kHz, which may be due to electromagnetic-induced

noise by the wind-tunnel electrical system. The two peaks were visible all the time during wind tunnel tests, for both unmorphed and morphed configuration.

In Figure 10.5.b the 12 spectra of the pressure signals are shown when the wing was morphed. The noise amplitude of the 10<sup>th</sup> channel was the highest, showing that the laminar-to-turbulent transition occurred in that position. The spectra of the 11<sup>th</sup> and 12<sup>th</sup> channels show the turbulent flow noise which is higher than the laminar flow noise but is lower than transition flow noise. In Figure 10.6.b, the transition was detected by the peak of the 10<sup>th</sup> sensor positioned at 59.2% of the chord in the RMS plot (star curve).

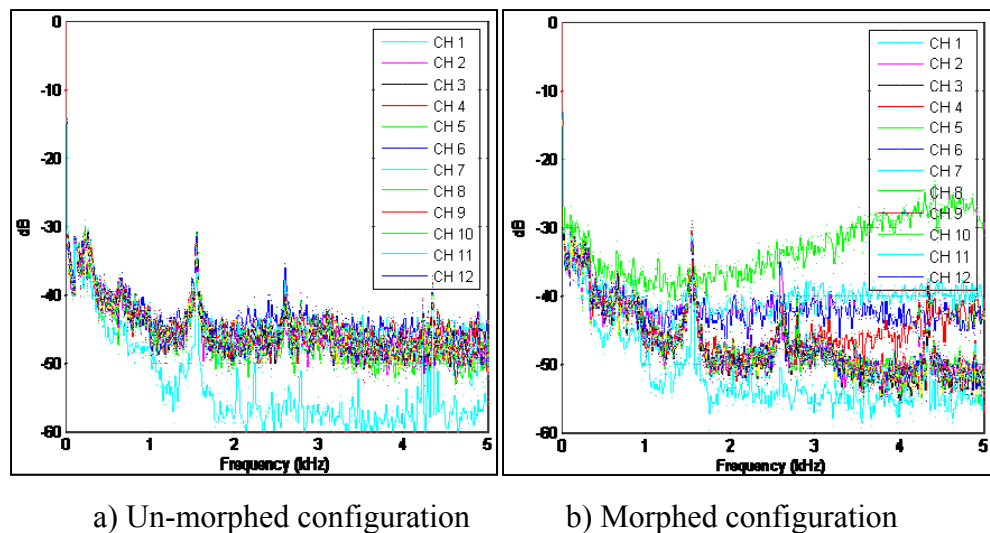
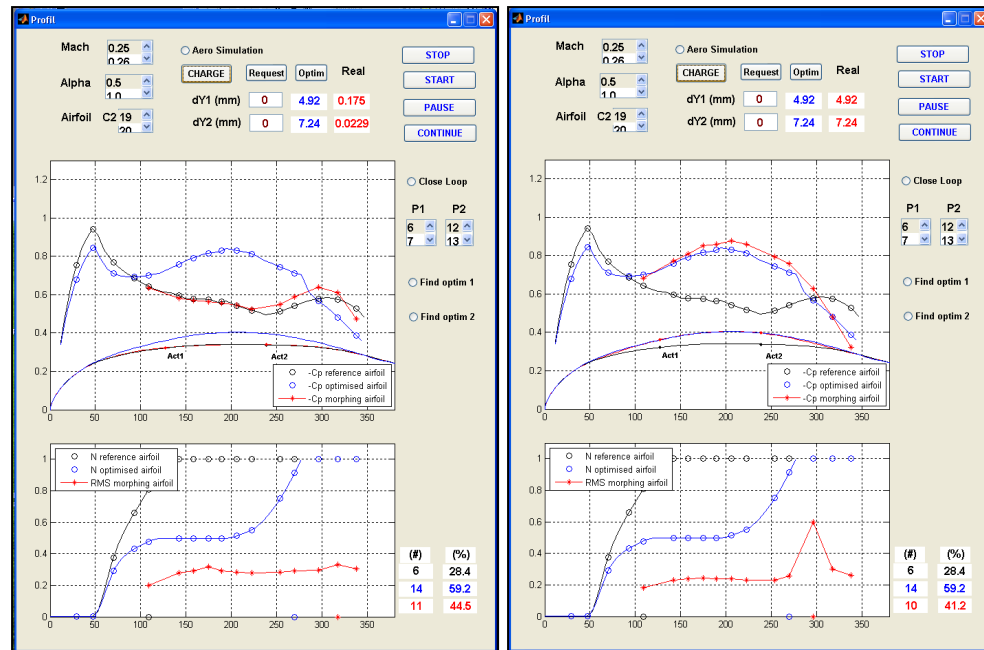


**Figure 10.5** FFT decomposition of the twelve channels pressure signals showing the transition development in the boundary layer over the morphing wing upper surface.



a) Un-morphed configuration

b) Morphed configuration

**Figure 10.6 Graphical User Interface (GUI) where all the aerodynamic and morphing shape information are centralized together with the control buttons of the software.**

In Figure 10.6.a, the data display graphical user-interface (GUI) is shown. Data for an unmorphed airfoil are illustrated. The actuators reference positions correspond to  $dY1 = 0$  mm and  $dY2 = 0$  mm, the  $C_p$  distribution calculated by XFOil for the reference airfoil (lower curve), and the  $C_p$  theoretical values of the sensors (circles) are displayed.

In the lower plot of Figure 10.6.a is shown the  $N$  factor used by XFOil to predict transition for the reference airfoil (higher curve). In the case of an unmorphed configuration, the predicted transition position was found to be at the sixth position of the 16 available sensors positions. In the beginning of wind-tunnel tests, a number of 16 sensors were installed but, due to their removal and re-installation during successive wind tunnel tests, four of them were found defective, therefore, a number of 12 sensors remained to be used during the last wind-tunnel tests. The  $C_p$  distribution and its RMS were illustrated in star symbols.

Results predicted for the morphed airfoil are shown in Figure 10.6.b. The morphed airfoil coordinates (higher curves), the  $C_p$  distribution calculated by XFOIL for the optimized airfoil (higher curve) and the  $C_p$  theoretical values of the sensors (circles) are displayed. In the lower plot of Figure 10.6.b, the  $N$  factor predicted by XFOIL for transition location prediction is shown for the optimized airfoil (lower circles curve). In this morphed configuration case, the position of the transition was predicted at the 14<sup>th</sup> sensor position positioned at 59.2% of the chord.

The unmorphed and morphed curves served as theoretical validations of the star curves reflecting the aerodynamic parameters ( $C_p$  and  $RMS$ ) provided by Kulite sensors plotted on screen in real time with a sampling rate of 1 sample/sec. In Figure 6.b is shown the actuated airfoil in the morphed position ( $dY1 = 4.92$  mm and  $dY2 = 7.24$  mm). The transition position was given by the sensor location where the maximum RMS was found, which in this case was the 10<sup>th</sup> Kulite sensor out of the 12 sensors. The instant visualization allowed us to find the exact position predicted by XFOIL. Figure 10.5.b allows to see the fast Fourier transform spectral distribution of the 10<sup>th</sup> sensor noise (higher spectra) having the highest noise in the frequency domain of 4-5 kHz.

### 3. Closed loop control methods

Two methods of closed-loop control were designed to obtain and maintain the optimized airfoil during the wind tunnel tests:

- 1) First method used a controller which took as a reference value the required displacement of the actuators from a database stored in the computer memory in order to obtain the morphing wing optimized airfoil shape. This method used the position signal feedback from the LVDT sensor connected to the oblique cam sliding rod of each actuator. This method was called open-loop control due to the fact that this control method does not take direct information from the pressure sensors concerning the wind flow characteristics. The design concept of the controller consists of a PID and an on/off switch that connects and disconnects

the SMA to a source of current which heats and lets cool the SMA to allow its change in its length, this concept was investigated by Popov et al. [2]. The initial input which is the optimized airfoil for any flow condition is chosen manually by the operator from the computer database through a user interface. Then the displacements ( $dY1$  and  $dY2$ ) that are required to be reproduced by the two control points on the flexible skin are sent to the controller. This controller sends an analog signal 0–2 V to the power supply that provide a current of 0–20 A / 20 V cc. to the SMA. The SMA will change its length according to the temperature of the wire due to the passing current and will change the position of the actuator which is sensed by a linear variable differential transducer (LVDT). The signal position received from the LVDT is compared to the desired position and the error obtained is fed back to the controller. The PID will control the dynamics of the heating process. If the realized position is greater than the desired position the switch will disconnect the control current letting the SMA wire to cool down. During the cooling down process the SMA will maintain its length due to the hysteretic behaviour. Also the controller uses three thermocouples signals from each SMA wire to monitor the temperature of the wires in order to maintain the temperature under 130 °C limits.

2) Second method used the same controller with the difference that took, as a reference value, the theoretical  $C_p$  value calculated by XFOIL in the position of the sensor connected through aerodynamic interdependence with the actuator position. The controller used as feedback the pressure signal coming from the 6<sup>th</sup> position of the 16 Kulite sensors which was connected to the first actuator, and the pressure signal coming from the 12<sup>th</sup> position of the 16 Kulite sensors which was connected to the second actuator. Their positions were visualized on Figure 6 at the two corresponding actuator points Act<sub>1</sub> and Act<sub>2</sub>. The theoretical  $C_p$  values were compared to the measured  $C_p$  values, while the control signal based on the difference between measured and theoretical  $C_p$  values was sent to the actuators power supplies. In this case, the method was called closed-loop control due to the fact that this control method used the pressure information from the Kulite sensors.

### A. Open-loop control

The schematics of the morphing wing open-loop control are shown in Figure 10.7. The input of the loop was the optimized airfoil corresponding to the airflow conditions in the wind tunnel, which was requested by the operator to be reproduced by the flexible skin. The optimized airfoil was selected by the operator from the computer database through the graphic interface listbox Airfoil and charged into the software by activating the button CHARGE (see Figure 10.6). The software sent actuators coordinates required to reproduce the airfoil displacements ( $dY1$  and  $dY2$ ) to the controller. When the operator selected the push button Optim, the controller adjusted the position of the actuators as required. The real position of the actuators was measured through the LVDT and compared with the desired  $dY1$  and  $dY2$  values. The horizontal displacement of the SMA oblique cam/actuator was converted in vertical displacement by division in 3. Figure 10.6 shows the optimized airfoil C219 obtained through open loop control of the two actuators displacements  $dY1 = 4.92$  mm and  $dY2 = 7.24$  mm. The new shape of the morphing wing obtained through the displacements of the SMA actuators was discussed in paper [10]. The return of the airfoil shape to the reference position was requested by filling up the dialog boxes  $dY1 = 0$  and  $dY2 = 0$  and afterwards using the push button Request. Any actuators displacements between 0 and 8 mm could be requested by the operator.

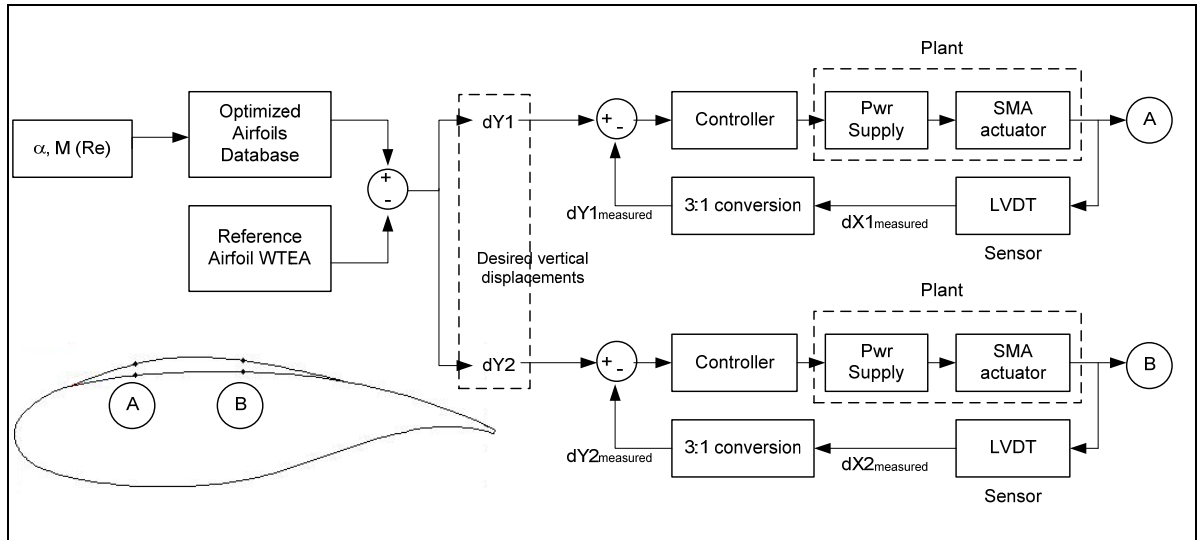


**Figure 10.7** Open-loop control using optimized airfoils database and actuator positions as feedback.

### B. Closed-loop control

In Figure 10.8, the schematic of the morphing wing closed-loop control is shown. The loop input was the optimized airfoil for each airflow conditions in the wind-tunnel, which was requested by the operator to be reproduced by the flexible skin. The optimized airfoil was selected by the operator from the computer database through the graphic interface list box Airfoil and was charged into the software by activating the button CHARGE (see Fig. 10.6). The software launched a subroutine calling the XFOIL code that calculated the  $C_p$  distribution for various airflow conditions  $\alpha$ ,  $M$  and  $Re$ ; they were entered as inputs. The operator selected the position of the sensors that were used to give feedback to the controller. In the example shown on Figure 10.6, the sensor located at the position No. 6 was selected to close the loop for the first actuator, and the sensor located at the position No. 12 was selected to close the loop for the second actuator.

When the close loop switch button was activated, the close loop control is activated. The two controllers gave commands to the power supplies that changed the actuators positions. The positions of the actuators had the effect of the shape changing, which had the effect of

change of the measured  $C_p$  values in the selected points. The controller used as targets the theoretical  $C_p$  values calculated by XFOIL. When the  $C_p$  values of the sensors reached the target values the controller stopped the SMA actuators activation and begun to maintain the  $C_p$  values around the target. The control principle was the same as in open-loop control case, even the controller was the same, with the exception that the  $C_p$  values errors were amplified by 10 and the feedback was given through two operator chosen pressure sensors instead of LVDT position sensors.

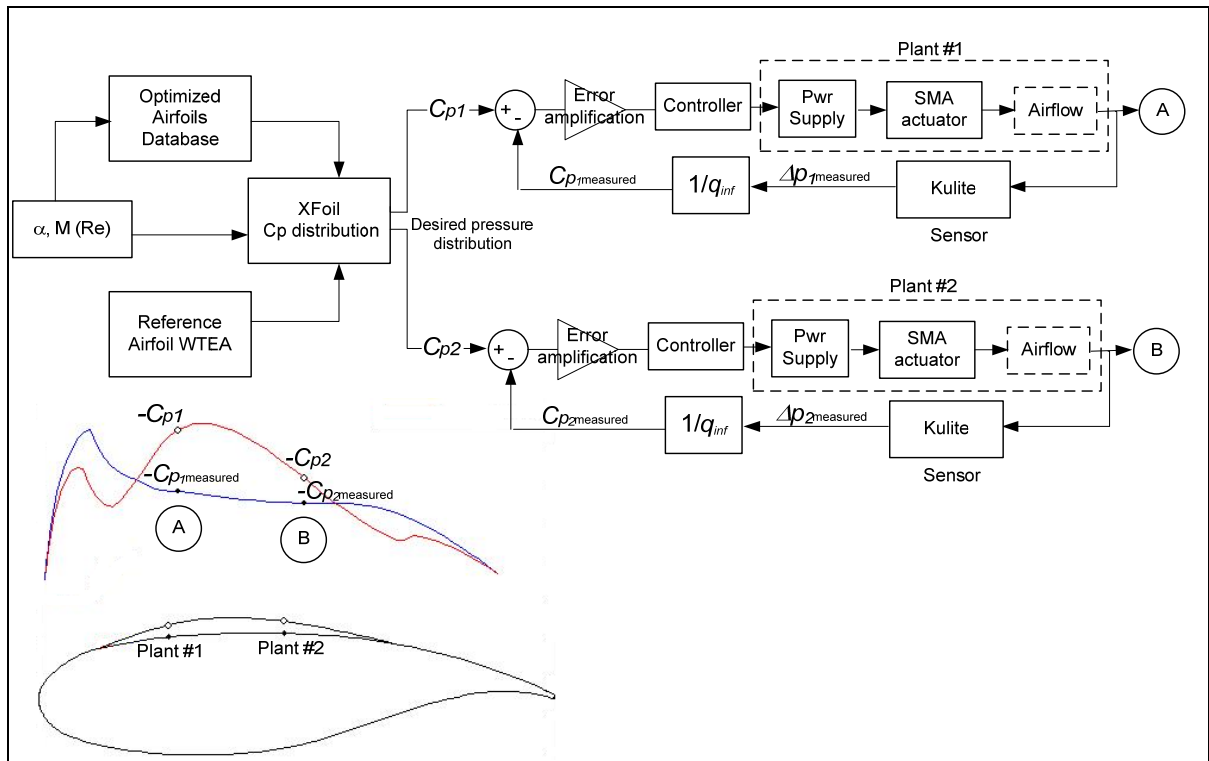


**Figure 10.8** Closed-loop control using optimized airfoils database and  $C_p$  values as feedback.

### 10.3 Experimental results obtained in the wind tunnel

The following sections outline the experimental results obtained during wind-tunnel tests. The tests were performed in the 6 × 9 ft subsonic wind tunnel at the IAR-NRC. The wind speed varied between Mach numbers 0.2 (223 ft/s) and 0.3 (335 ft/s) at Reynolds numbers between 2.29 and  $3.36 \times 10^6$  (see Table I).

## 1. Open loop control

The following figures show the morphing wing with the actuators at the zero position, i.e. the wing was the reference airfoil compared to the morphing wing with the actuator in the requested position to obtain the optimized airfoil C226.

In the Figure 10.9 the case  $M = 0.275$  and  $\alpha = 1$  deg is shown. On the left-hand side of Figure 10.8, there was a turbulent flow RMS pattern signature which appeared following a small peak in the second signal (CH 2). The typical RMS pattern signature of transition appeared when the morphing wing actuators were at the C226 optimized airfoil position. The RMS distribution peak at the ninth sensor is shown on the right-hand side fast Fourier transform decomposition as the highest signal (CH 9). These plots show that the transition location moved from sensor No. 2 to sensor No. 9.

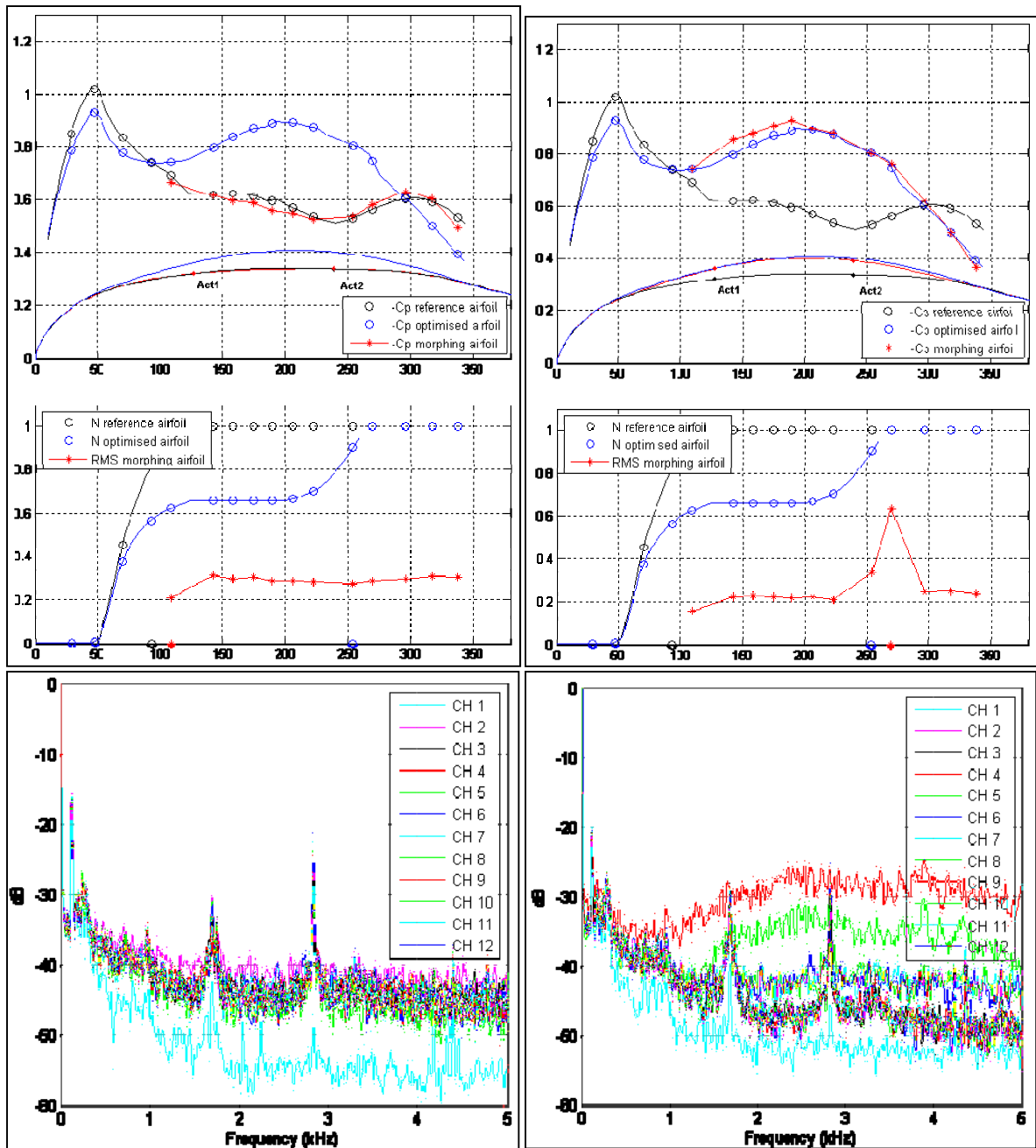
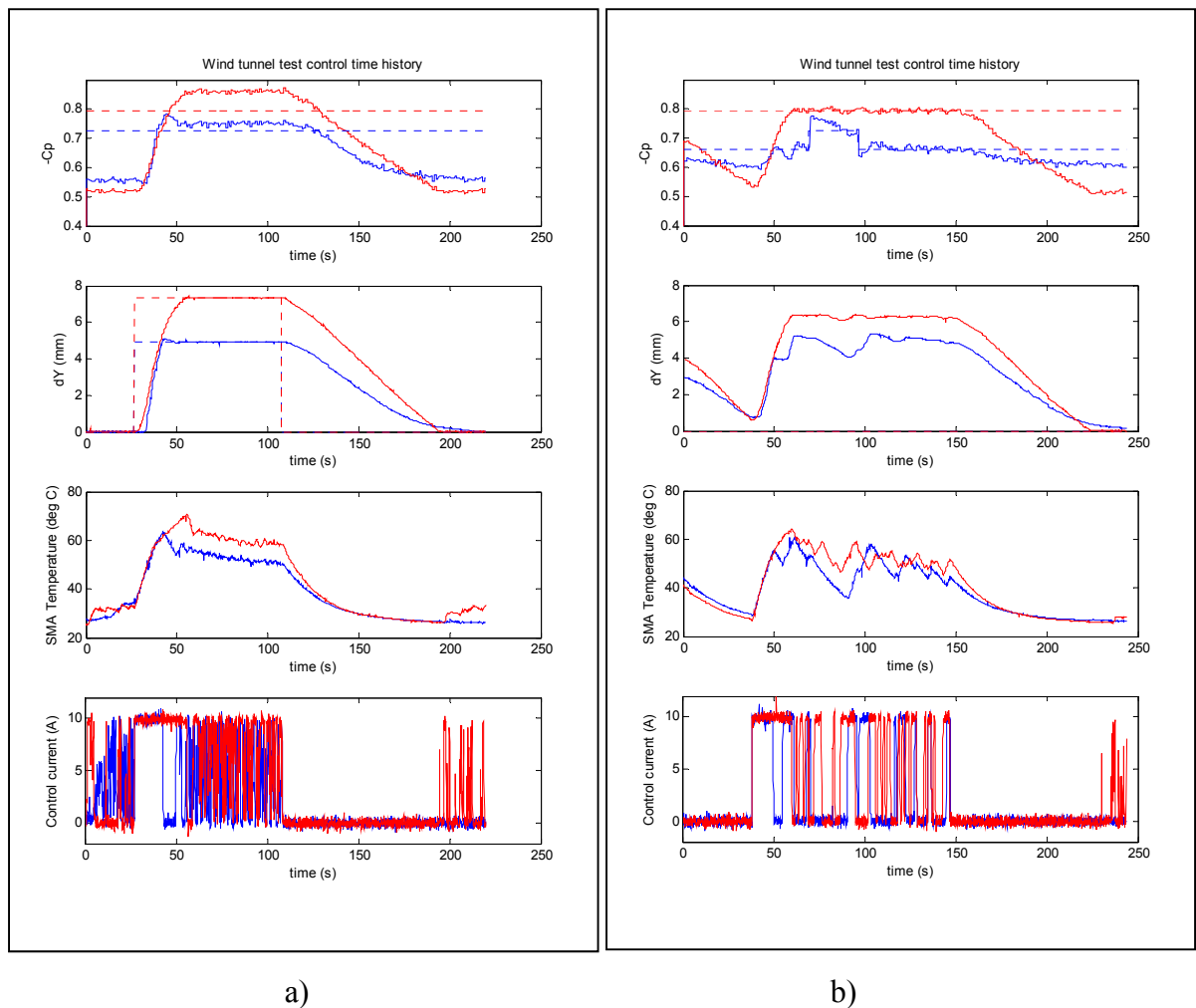


Figure 10.9 Reference airfoil versus C226 airfoil results for  $M = 0.275$  and  $\alpha = 1$  deg.

## 2. Closed loop control

Figure 10.9 shows the wing morphing configurations achieved by using two different control methods. The left-hand sides (LHS) of Figure 10.10 show the open-loop control, and the right-hand sides (RHS) show the closed-loop control data. The difference between the LHS graphs show the control having the actuator positions feedback, whereas the RHS curves show the control having the  $-C_p$  values as feedback.



**Figure 10.10** C232 airfoil results obtained in a) open loop, b) closed loop control

The time histories of the same critical parameters are shown in Fig. 10.10. The first plots at the top of Fig. 10.10.a and 10.10.b, show the theoretical (dashed lines) and measured  $C_p$

(solid lines) value for two sensors, No. 1 lower line and No. 8 higher line, located respectively at  $x = 38.1$  mm and  $x = 179.6$  mm on the airfoil. The second plots display the desired (dotted lines) and realized (solid lines) vertical displacements  $dY1$  and  $dY2$ , in millimeters, of the two actuators (first actuator, lower line; second actuator, upper line). The last two plots at the bottom of Fig. 10.10.a and 10.10.b give the SMA actuators wires temperatures in degrees C and control current intensity in A, respectively.

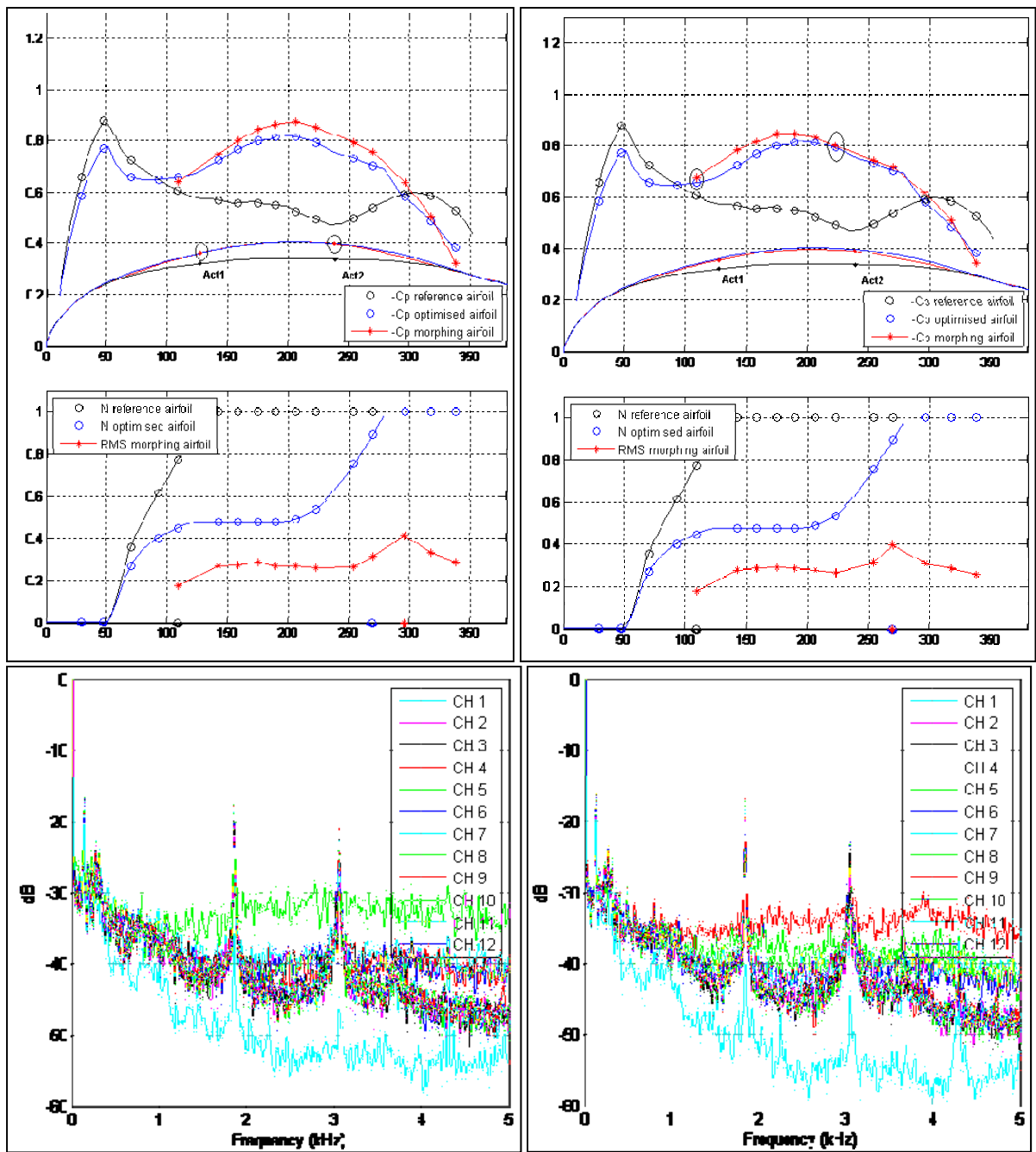
The LHS plots show the realization of the C232 optimized airfoil using the open-loop method, having the displacements  $dY1$  and  $dY2$  as feedback parameters, and using a PID coupled with an on/off switch method controller.

The RHS plots show the realization of the C232 optimized airfoil  $-C_p$  distribution using the close loop method having the sensors No.1 and No.7  $-C_p$  values as feedback parameters, using the same PID controller. The discontinuity in the  $-C_p$  desired value (lower line) was due to switching the control sensor from No.7 to No.8 and back. It is observed that the controller obeyed the command and achieved the desired results.

The aerodynamic effect of the control in open loop versus closed loop at the same airflow configuration and same optimized airfoil command for the C232 airfoil are shown on Figure 10.11.

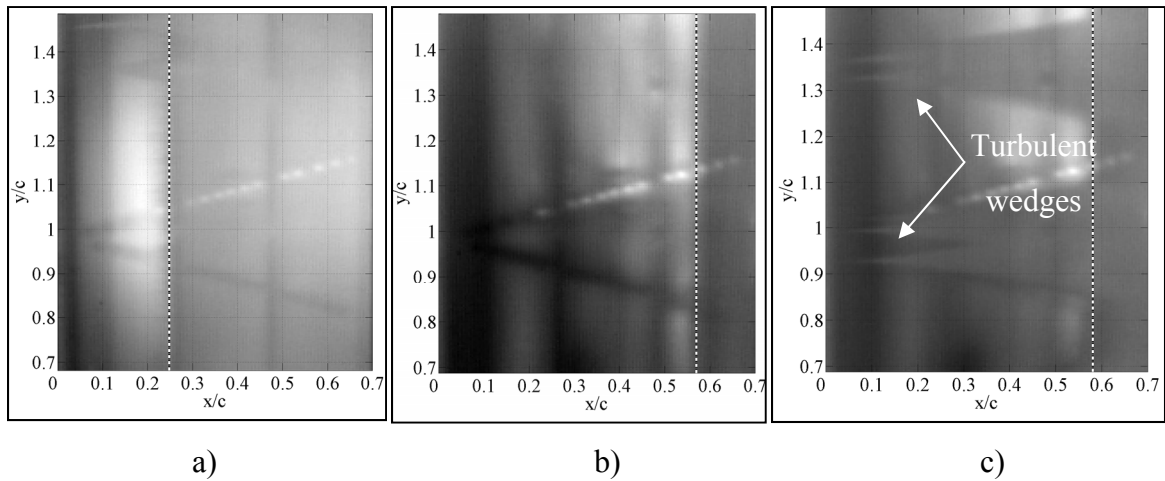
The LHS plots show the realization of the C232 optimized airfoil using the open loop method having the displacements  $dY1$  and  $dY2$  as feedback parameters (see the ovals in the figure). The RHS plots show the realization of the C232 optimized airfoil  $-C_p$  distribution using the closed-loop method having the sensors No.1 and No.7  $-C_p$  values as feedback parameters (see the ovals in figure). The slight differences in the aerodynamic configuration shown are due to zero calibration of the first actuator, which indicated its position with an error of 0.5 mm lower than in reality.

Figure 10.12 shows typical infrared results obtained at  $M = 0.3$ ,  $\alpha = 0.5$  deg for various configurations. Only the composite portion of the wing at  $x/c \leq 0.7$  is shown. The white spots on the wing were the electronically heated Kulite pressure transducers. The two lines of SMA actuators, colder than the model surface, were also visible at quarter chord and near mid-chord. The locations of the transition in the images have been highlighted using a white dashed line: it corresponds to the location of a large surface temperature gradient, the laminar region being about  $2^\circ\text{C}$  hotter than the turbulent region. The reference airfoil configuration (Figure 10.12.a) showed a transition location at  $x/c = 25\%$ . The open loop control (Figure 10.12.b) allowed a laminar boundary layer run to  $x/c = 57\%$ . In the case of the closed loop control (Figure 10.12.c), the transition location was  $x/c = 58\%$ , which represents a small improvement over the open loop control. Some turbulent wedges caused by leading edge contamination, due to dust particles in the flow, were visible in Figure 10.12.c. In addition to providing an on line verification of the Kulite dynamic pressure signals, the infrared measurement was particularly useful to detect those early triggered turbulent wedges. When the level of contamination was estimated to be unacceptable or likely to affect the drag or the Kulite measurements, the test was interrupted and the model was carefully cleaned.



a) b)

**Figure 10.11** C232 airfoil results obtained at  $M = 0.3$  and  $\alpha = 0.5$  deg in a) open loop, b) closed loop.



**Figure 10.12** C232 infrared results obtained at  $M = 0.3$  and  $\alpha = 0.5$  deg in a) reference, b) open loop control, c) closed loop control.

#### 10.4 Conclusion

The aerodynamic results of the wind-tunnel tests performed for morphing wing model were analyzed. Two control methods for obtaining optimized airfoil configurations for fixed wind flow conditions were studied. The first and the second control methods used a database of theoretical optimized airfoils using CFD codes. The first and the second control methods (open loop versus closed loop) were compared. It was observed that the first method (open loop) realized with more fidelity the imposed airfoil shape, and was more accurate from the point of view of aerodynamic results. The disadvantage of this method is its high sensitivity of the aerodynamic effects due to the zero calibration of the actuators. The second method (closed loop) has the advantage to reproduce the  $-C_p$  distribution that can change over time. The disadvantage of this method is the high sensitivity of the air flow external influences, which in real life scenarios could interfere with the aircraft flight, such as wind gusts.

## References

- [1] Zingg, D. W., Diosady, L., and Billing, L., 2006, *Adaptive Airfoils for Drag Reduction at Transonic Speeds*, AIAA paper 2006-3656.
- [2] Popov, A.-V., Labib, M., Fays, J., Botez, R.M., 2008, *Closed loop control simulations on a morphing laminar airfoil using shape memory alloys actuators*, AIAA Journal of Aircraft, Vol. 45(5), pp. 1794-1803.
- [3] Rioual, J.-L., Nelson, P., A., Fisher, M., J., 1994, *Experiments on the Automatic Control of Boundary-Layer Transition*, AIAA Journal of Aircraft, Vol. 31(6), pp. 1416-1419.
- [4] Coutu, D., Brailovski, V., Terriault, P., Fischer, C., *Experimental validation of the 3D numerical model for an adaptive laminar wing with flexible extradors*, 18<sup>th</sup> International Conference of Adaptive Structures and Technologies, Ottawa, Ontario, 3-5 October, 2007.
- [5] Khalid, M., 1993, *Navier Stokes Investigation of Blunt Trailing Edge Airfoils using O-Grids*, AIAA Journal of Aircraft, Vol.30, No.5, pp.797-800.
- [6] Khalid, M., and Jones, D.J., 1993, *A CFD Investigation of the Blunt Trailing Edge Airfoils in Transonic Flow*, Inaugural Conference of the CFD Society of Canada, June 14-15, Montreal.
- [7] Popov, A.-V., Botez, R.M., Labib, M., 2008, *Transition point detection from the surface pressure distribution for controller design*, AIAA Journal of Aircraft, Vol. 45(1), pp. 23-28.
- [8] Drela, M., 2003, *Implicit Implementation of the Full  $e^N$  Transition Criterion*, 21<sup>st</sup> Applied Aerodynamics Conference, AIAA paper 2003-4066, Orlando, Florida.
- [9] Drela, M., Giles, M., B., 1987, *Viscous-Inviscid Analysis of Transonic and Low Reynolds Number Airfoils*, AIAA Journal of Aircraft, Vol. 25(10), pp. 1347-1355.
- [10] Popov, A., V., Grigorie, L., T., Botez, R.M., 2009, *Control of a Morphing Wing in Bench Test*, 13<sup>th</sup> Canadian Aeronautical and Aerospace Institute CASI Aeronautics Conference, Kanata, Ontario, 5-7 May.
- [11] Sainmont, C., Paraschivoiu, I., Coutu, D., 2009, *Multidisciplinary Approach for the Optimization of a Laminar Airfoil Equipped with a Morphing Upper Surface*, NATO AVT-168 Symposium on "Morphing Vehicule", Evora, Portugal.
- [12] Mébarki, Y., Mamou, M. and Genest, M., 2009, *Infrared Measurements of Transition Location on the CRIAQ project Morphing Wing Model*, NRC LTR- AL-2009-0075.

- [13] Nitsche, W., Mirow, P., Dorfler, T., 1990, *Investigations on Flow Instabilities on Airfoils by Means of Piezofoil –Arrays*, Laminar-Turbulent Transition IUTAM Symposium, Toulouse, France, 11-15 September, 1989, pp.129-135. Springer-Verlag Berlin Heidelberg
- [14] Mangalam, S. M., 2004, *Real-Time Extraction of Hydrodynamic Flow Characteristics Using Surface Signature*, IEEE Journal of Oceanic Engineering, Vol. 29, No. 3, pp. 622-630.

## **CHAPTER 11**

### **ARTICLE 8**

#### **REAL TIME MORPHING WING OPTIMIZATION IN A SUBSONIC WIND TUNNEL**

Andrei V. Popov, Lucian T. Grigorie and Ruxandra Botez,  
École de technologie supérieure, Montréal, Québec, H3C 1K3, Canada  
Mahmoud Mamou, and Youssef Mebarki,  
Institute of Aeronautical Research - NRC, Ottawa, Ontario, K1A 0R6, Canada.  
This article was submitted for publication at AIAA Journal of Aircraft on 29 September  
2009.

#### **Article presentation**

The article shows the results obtained in wind tunnel tests performed on May 2009 at IAR-NRC Ottawa. The wing model mechanical and electrical design manufacture and installation in wind tunnel was performed by LAMSI team in collaboration with IAR-NRC team under the supervision of Dr. Mamou M., and with LARCASE team; in fact, the LARCASE team, under the supervision of Dr Botez, has done the wind tunnel testing plan writing and scheduling, the sensors and controller data post-processing and installation on the wing model, and the planning of the cabling systems related to the model integration in the wind tunnel. The references to the mechanical and electrical system in the paper have the purpose to facilitate the reader's understanding. The infrared measurements were performed during wind tunnel tests by Dr. Merbaki Y. The wing model was controlled by a closed loop system driven automatically by computer. The paper shows the real time optimization control software and the real time pressure data acquisition and visualizing realized in collaboration with Dr. Lucian Grigorie at LARCASE. The paper discusses the differences between the simulation and operation in real time with hardware-in-the-loop, and proves that the functioning of the wing model in wind tunnel was a success.

## Résumé

Dans cet article, une aile rectangulaire avec une envergure finie, ayant un profil de référence WTEA a été considéré. La surface de l'extrados a été fabriquée en matériaux composites flexibles et équipée avec des capteurs de pression Kulite, et deux actionneurs en alliages à mémoire de forme. Les signaux de pression non-stationnaires ont été enregistrés et visualisés en temps réel, pendant que la forme de l'aile a été changée pour reproduire les formes optimisés à l'aide des deux actionneurs. Plusieurs tests ont été effectués pour différentes valeurs des angles d'incidence et nombres de Reynolds dans la soufflerie de 2m × 3m de l'Institut de Recherche Aérospatiale du Conseil National de Recherche du Canada. Les nombres de Mach ont varié entre 0.2 et 0.3, les nombres de Reynolds ont varié entre 2.29 millions et 3.36 millions, et les angles d'incidence ont varié entre -1° et 2°. Les enregistrements des données dans la soufflerie pour la détection de la transition dans la couche limite en utilisant des capteurs de pression à haute fréquence d'échantillonnage sont présentés. Dans l'article on présente la méthode d'optimisation en temps réel implémentée dans le logiciel de contrôle qui permet que l'aile à géométrie variable trouve la configuration optimale pour une certaine condition de l'écoulement de l'air.

## Abstract

In this paper, wind-tunnel results of a real time optimization of a morphing wing in the wind tunnel for displacing the transition towards the trailing edge are presented. A morphing rectangular finite aspect ratio wing, having a WTEA reference airfoil cross-section, was considered, with its upper surface made of a flexible composite material and instrumented with Kulite pressure sensors, and two smart memory alloys actuators. Several wind-tunnel tests runs for various Mach numbers, angles of attack, and Reynolds numbers were performed in the 6 × 9 ft wind tunnel at the Institute for Aerospace Research at the National Research Council Canada. Unsteady pressure signals were recorded and used as feed back in real time control while the morphing wing was requested to reproduce various optimized airfoils by changing automatically the two actuators' strokes. This paper shows the

optimization method implemented into the control software code that allows the morphing wing to adjust its shape to an optimum configuration under the wind-tunnel airflow conditions.

### **11.1 Introduction**

The CRIAQ 7.1 project was a collaborative project between the teams from École de technologie supérieure (ETS), École Polytechnique, the Institute for Aerospace Research, National Research Canada (IAR-NRC), Bombardier Aerospace, and Thales Avionics. In this project, the laminar flow past aerodynamically morphing wing was improved to obtain important drag reductions.

This collaboration called for both aerodynamic modeling as well as conceptual demonstration of the morphing principle on real models placed inside the wind tunnel. Drag reduction on a wing could be achieved by modifications of the airfoil shape, which had an effect in the laminar-to-turbulent flow transition point position. The main objective of this concept was to promote large laminar regions on the wing surface by moving the transition point toward the trailing edge of the airfoil wing, thus reducing drag over an operating range of flow conditions characterized by Mach numbers, airspeeds and angles of attack [1].

The airborne modification of an aircraft wing airfoil shape could be realized continuously to maintain laminar flow over the wing surface as flight conditions changed. To achieve such a full operating concept, a closed-loop control system concept was developed to control the flow fluctuations over the wing surface with the deformation mechanisms (actuators) [2].

The wing model has a rectangular plan form of aspect ratio of 2 and was equipped with a flexible upper surface skin on which shape memory alloys actuators were installed [3, 4]. Two shape memory alloys (SMA) actuators created the displacement of the two control points on the flexible skin to realize the optimized airfoil shapes [5].

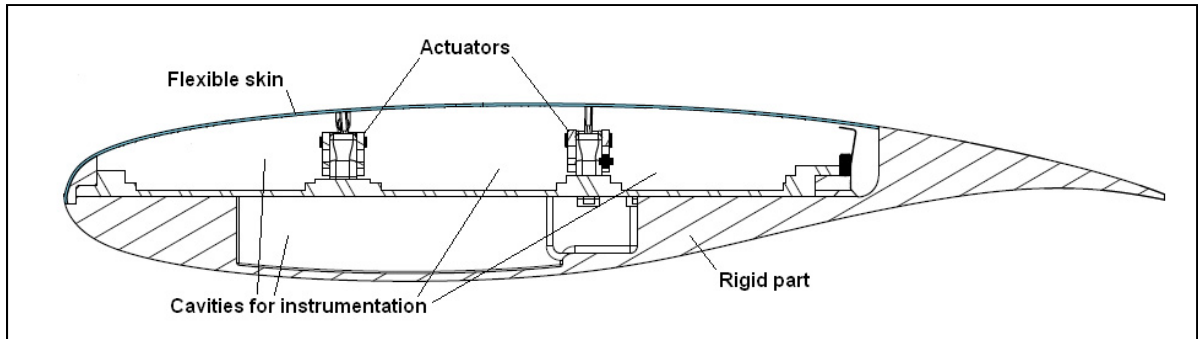


**Figure 11.1** Cross section of the morphing wing model.

As reference airfoil, the laminar airfoil WTEA was used because it was already optimized for laminar flow in the transonic regime. Its aerodynamic performance was investigated at IAR-NRC in [6, 7]. The optimized airfoils were previously calculated by modifying the reference airfoil for each airflow condition as combinations of angles of attack and Mach numbers such that the transition point position was found to be the nearest as possible to the airfoil trailing edge [5]. Several optimized airfoils were found for the airflow case combinations of Mach numbers and angles of attack. The optimized airfoils configurations were stored in the computer memory by means of a database and were selected as needed by the operator or computer to be realized by the morphing wing [8]. But this strategy relied on the previously calculated aerodynamic characteristics of the airfoils, which usually were determined by use of CFD codes and optimization algorithms.

The idea presented in this paper is to implement the same optimization algorithm into the computer controller that will search the optimal configuration with the real system, in real time and for real aerodynamic airflow conditions. The basic idea of optimization control is to bypass the necessity of a previously calculated optimized airfoils database, and to generate in real time the optimized airfoil for the exact conditions of the wind flow. For such a task it was necessary to develop a subroutine that optimized the airfoil shape in the same way in which the optimized airfoils database was generated. The method of optimization used in this case was a mixed method between the gradient ascent or hill climbing method and the simulated annealing, which is a metaheuristic search method.

The hill climbing method is a local search optimization algorithm. It considers a random poor solution, which improves slowly by iterations. When the solution cannot be further improved, it becomes the final solution and the algorithm ends. In our case, the searching domain is defined by the actuators' displacements as variables, and the cost function needed to be maximized is the transition point position  $x_{tr}$ . Normally the function is defined analytically and the maximum is searched along the lines with the maximum local derivatives or gradients. Although hill climbing would be very fast and simple to program, the solution found is not guaranteed to be the global maximum of the entire search domain [9]. Other local search algorithms such as stochastic hill climbing, random walks, and simulated annealing would overcome this problem. The characteristic of these methods is that the algorithm searches random solutions within the search domain to cover all the possible local maxima and to find the global maximum [10].

The reason why a mixed method was needed was because the cost function for such a complex problem (minimize the  $C_D$ , maximize the  $C_L/C_D$ , or maximize the transition point position  $x_{tr}$  for a morphing wing) was not defined analytically and the implementation of the gradient ascent method was not suitable. Also, due to time cost (very long time response of the SMA actuators due to heating but especially cooling time), a purely probabilistic metaheuristic search algorithm such as stochastic hill climbing, random walks, or simulated annealing was not suitable either.

The idea of the present algorithm was the mixture of the hill climbing method with the random walks or simulated annealing and the search within the defined domain nine points, one being the center of a circle and the other eight being situated on the circle with a predefined radius. When the maximum is found within the nine points, the algorithm reset the next searching step by iterating with eight points situated on smaller circles until the global maximum is found. This mixed method was found to be the fastest, that is, it considered the least number of points evaluated for converging to the transition point position  $x_{tr}$  maximum.

## 11.2 Experimental setup description

### 1. Mechanical and electrical control system

The concept of this morphing wing consisted of a rectangular wing model (chord  $c = 0.5$  m and span  $b = 2.1$  m) incorporating two parts. One fixed part was built in aluminum by the IAR-NRC team and sustained the resistance forces acting during wind-tunnel tests. The other part consisted of a flexible skin installed on a metallic structure on the wing upper surface and was designed and manufactured at ETS (Fig. 11.1). The flexible skin was required to change its shape through two action points to realize the optimized airfoil for the airflow conditions in which tests were performed.

The actuators were composed of two oblique cams sliding rods spanwise positioned that converted the horizontal movement along the span in vertical motion perpendicular to the chord (Fig. 11.2). The position of each actuator was given by the mechanical equilibrium between the Ni-Ti alloy SMA wires that pulled the sliding rod in one direction and the gas springs that pulled the sliding rod in the reverse direction. The gas springs role was to counteract the pulling effect of aerodynamic forces acting in wind tunnel over the flexible skin when the SMA's were inactive. Each sliding rod was actuated by means of three parallel SMA wires connected to a current controllable power supply which was the equivalent of six wires acting together. The pulling action of the gas spring retracted the flexible skin in the undeformed-reference airfoil position, and the pulling action of the SMA wires deployed the actuators in the load mode, that is, morphed airfoil in the optimized airfoil position (see Fig. 11.2). The gas springs used for these tests were charged with an initial load of 225 lbf (1000 N) and had a characteristic rigidity of 16.8 lbf / in (2.96 N / mm).

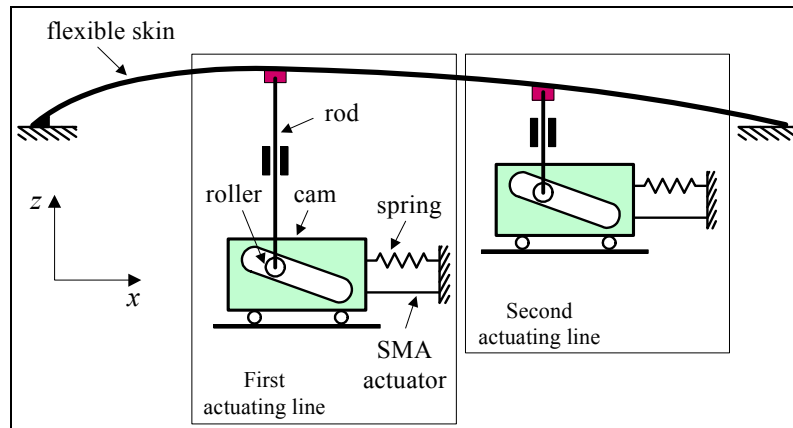


**Figure 11.2 Schematics of the flexible skin mechanical actuation.**

The mechanical SMA actuators system was controlled electrically through an open-loop control system. The architecture of the wing model open-loop control system, SMA actuators, and controller is shown in Figure 11.3. The two SMA actuators had six wires each, which were supplied with power by the two AMREL SPS power supplies, controlled through analog signals by the NI-DAQ USB 6229 data acquisition card. The NI-DAQ was connected to a laptop through a universal serial bus connection. A control program was implemented in Simulink that provided to the power supplies the needed SMA current values through an analog signal as shown in Figure 11.3. The control signal of 2 V corresponded to an SMA supplied current of 33 A. The Simulink control program used as feedback three temperature signals coming from three thermocouples installed on each wire of the SMA actuator, and a position signal from a linear variable differential transducer connected to the oblique cam sliding rod of each actuator. The temperature signals served in the overheat protection system that disconnected the current supply to the SMA in case of wire temperature passed over the set limit of 120°C. The position signals served as feedback for the actuator desired position control. The oblique cam sliding rod had a horizontal versus vertical ratio 3:1; hence, the maximum horizontal displacement of the sliding rod by 24 mm is converted into a maximum vertical displacement of the actuator and implicit of the flexible skin by 8 mm.

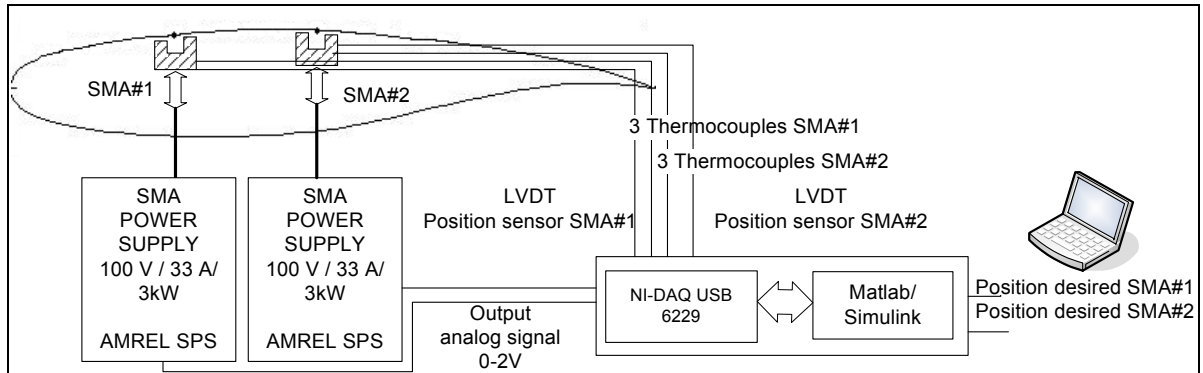


**Figure 11.3** Architecture of the morphing wing model control system.

A user interface was implemented in Matlab/Simulink that allowed the user to choose the optimized airfoils shape from a database stored on the computer hard disk and provided to the controller the vertical needed displacements to obtain the desired optimized airfoil shape. The controller activated the power supplies with the needed SMA current values through an analog signal as shown in Figure 11.3. In practice, the SMA wires were heated at an approximate temperature of  $90^{\circ}\text{C}$  with a current of 10 A. When the actuator reached the desired position the current was shut off and the SMA was cycled in endless heating/cooling cycles through the controller switching command on/off of the current to maintain the current position until another desired position or the entire system shut off was required.

In support of the discrete pressure instrumentation, infrared thermography (IR) visualization was performed to detect the transition location on the morphing wing upper surface and validate the pressure sensor analysis. The transition detection method using IR was based on the differences in the laminar and turbulent convective heat transfer coefficient and was exacerbated by the artificial increase of model airflow temperature differences. In the resulting images, the sharp temperature gradient separating high temperature (white intensity in image) and low-temperature (dark intensity) regions was an indication of the transition location. The infrared camera used was an Agema SC3000 camera, equipped with a  $240 \times 320$  pixels quantum well infrared photodetector (QWIP), operating in the infrared wavelength region of  $8\text{--}9 \mu\text{m}$  and cooled to  $70^{\circ}\text{K}$  to reduce thermal noise. The camera

provided a resolution of  $0.02^{\circ}\text{C}$  and a maximum frame rate of 60 Hz. It was equipped with the default lens ( $\text{FOV} = 20^{\circ} \times 15^{\circ}$ ), and was installed 1.5 m away from the model with an optical axis oriented in the horizontal plane at about 30 deg with respect to the wing surface midchord normal. Optical access was provided through an opening on the side wall of the test section opposite to the upper surface. More details about the methodology and processing are available in [11].

## 2. Aerodynamic detection system and graphical user interface

The morphing wing goal was the improvement of the laminar flow over the upper surface of the wing. To ensure that the improvement was real, we built a detection system that gave information about the flow characteristics. An array of 12 Kulite pressure sensors was installed on the flexible skin.

The pressure data acquisition was performed using a NI-DAQ USB 6210 card with 16 analog inputs, at a total sampling rate of 250 kilosamples/s. The input channels were connected directly to the IAR-NRC analog data acquisition system which was connected to the 12 Kulite sensors. The IAR-NRC served as an amplifier and conditioner of the signal at a sampling rate of 15 kilosamples/s. One extra channel was used for the wind-tunnel dynamic pressure acquisition to calculate the pressure coefficients  $C_p$ 's from the pressure values measured by the 12 pressure sensors. The signal was acquisitioned at sampling rate of 10 kilosamples/s in frames of 1024 points for each channel, which allowed a boundary-layer pressure fluctuations fast Fourier transform spectral decomposition up to 5 kHz for all channels, at a rate of 9.77 samples/s using Matlab/Simulink software. The plot results were visualized in real time on the computer screen in dedicated windows (see Figure 11.4) at a rate of 1 samples/sec. Figure 11.4 shows an example of graphical user interface in which all the aerodynamic and morphing shape information were centralized together with the control buttons of the controlling software. The window shows information about the Mach number, the angle of attack, the airfoil shape of the morphing wing, and the two actuators vertical displacements needed to obtain the desired airfoil shape. In the two plots, are shown the coefficients pressure distribution  $C_p$ 's of the 12 Kulite sensors, and the noise of the signal

(RMS) of each pressure signal. Figure 11.4.a shows the wing unmorphed position, and Figure 11.4.b shows the wing under its morphed position. The results obtained are qualitatively very similar to those obtained in previous studies [12, 13].

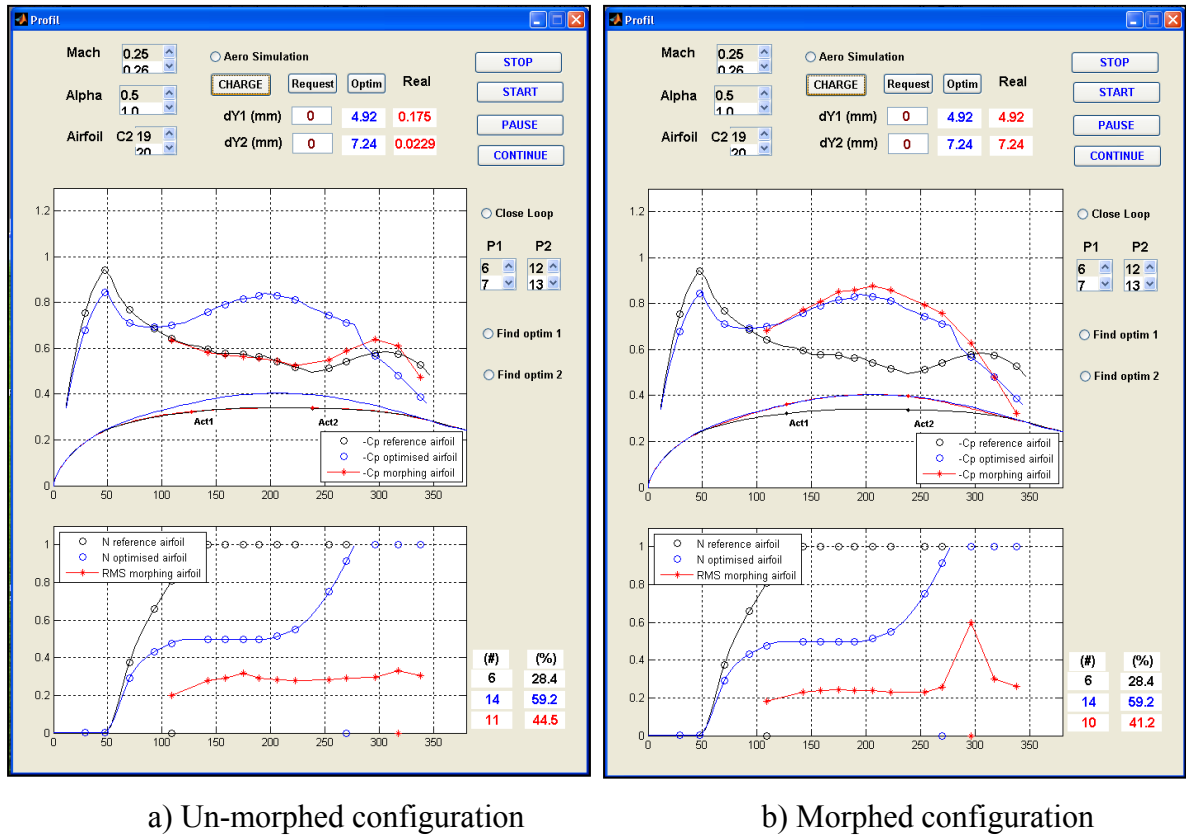


**Figure 11.4 Graphical user interface (GUI) with the control buttons of the software.**

The transition between laminar and turbulent flow was detected by means of each pressure signal’s RMS. The lower RMS plot given in Figure 11.4 shows the normalized quantity of the pressure signal noise from each Kulite sensor (star points curve). In the example shown in Figure 11.4, the RMS plot in the unmorphed configuration (Figure 11.4.a) the transition is shown in the fourth sensor due to the fact that it had the maximum RMS value.

In Figure 11.4.a, on the graphical user interface (GUI) an unmorphed airfoil is shown by use of a black color. The actuators’ reference positions correspond to  $dY1 = 0$  mm and  $dY2 = 0$

mm, the  $C_p$  distribution calculated by Xfoil for the reference airfoil (black curve), and the  $C_p$  theoretical values of the sensors shown as black circles on the  $C_p$  distribution curve.

In the lower plot of Figure 11.4.a the  $N$  factor used by Xfoil to predict transition for the reference airfoil (lower curve) is shown. The critical value  $N_{cr} = 7.34$  was used in the simulation to match the turbulence level  $T = 0.14\%$  measured in the wind tunnel using Mack's correlation Eq. (1), and the plotted values on the figure are normalized ( $N/N_{cr}$ ) [14]

$$N_{cr} = -8.43 - 2.4 \cdot \log(T) \quad (11.1)$$

In the case of an unmorphed configuration, the predicted transition position is found to be the 6<sup>th</sup> position of the 16 available sensors' positions. In the beginning of wind-tunnel tests, 16 sensors were installed, but due to their removal and reinstallation during the next two wind tunnel tests, four of them were found defective. Therefore, 12 sensors remained to be used during the last third wind-tunnel tests so that only 12 Kulite sensors were used for plotting the  $C_p$  distribution and RMS distribution (star plots).

Results predicted for the morphed airfoil are shown in the higher plot. The morphed airfoil coordinates are shown as higher curves in the upper part of Figure 11.4.b, the  $C_p$  distribution is calculated by Xfoil for the optimized airfoil (upper curve), and the  $C_p$  theoretical values of the sensors are shown as circles on the  $C_p$  distribution curve. In the lower plot of Figure 4.b, the  $N$  factor used by Xfoil to predict transition is shown for the optimized airfoil (higher curve). In this case of morphed configuration, the predicted position of transition is the 14<sup>th</sup> position of the 16 available sensors' positions.

These un-morphed (lower) and morphed (higher) curves served as theoretical validations of the measured values curves reflecting the aerodynamic parameters ( $C_p$  and  $RMS$ ) provided by Kulite sensors in real time with a sampling rate of 1 sample/sec. In Figure 4.b the actuated airfoil in the morphed position ( $dY1 = 4.92$  mm and  $dY2 = 7.24$  mm) is shown. The transition position was given by the sensor location where the maximum RMS was found, which in this

case is the 10<sup>th</sup> Kulite sensor out of 12 sensors. The instant visualization allows us to find the exact position predicted by XFOil.

### 11.3 Simulation and experimental results obtained in the wind tunnel

The simulation of the system used the Matlab/Simulink software as a programming platform. The simulation used the optimization subroutine exactly the same as in bench tests and wind-tunnel tests, except that in computer simulation and bench test the aerodynamic pressures that action upon the skin and stimulates the sensors were simulate by use of XFOil software. A mathematical model of the flexible skin used a *B*-spline with four flexion points. Two points were fixed where the skin was glued on the wing rigid structure and two points were mobile and were placed in the actuators' coordinates on the wing structure. The *B*-spline shape that define the airfoil's flexible skin did not have the same coordinates as the flexible skin but was a good approximation for the purpose of designing an optimization subroutine in closed loop with a CFD code. Laser scanning during bench tests showed that the differences between the scanned airfoils and the theoretical airfoils were less than 0.5 mm (less than 6.25% of the maximum actuators' deflection of 8mm) [15].

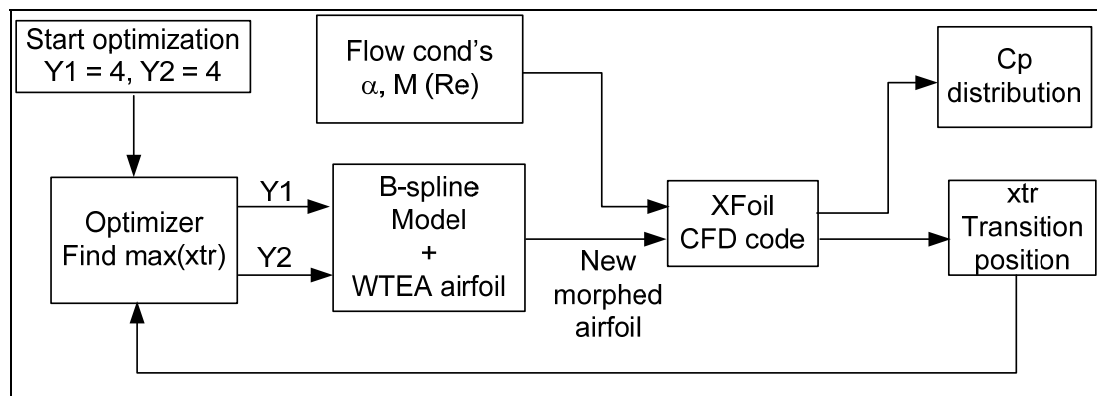


**Figure 11.5 Optimization logic schematic.**

The optimization initialized the algorithm with the values  $dY1 = 4$  mm and  $dY2 = 4$  mm. Afterward, the algorithm evaluated the transition point position in eight points of coordinates ( $dY1, dY2$ ) situated on a circle centered on the initial point with a radius of 4 mm within the

search domain defined by the bidimensional space of actuators strokes  $\{dY1 = [0, 8], dY2 = [0, 8]\}$ . For each evaluation point, the  $x_{tr}$  value was evaluated by use of XFOil and stored in the memory. After the first round of evaluations the optimizer decided which evaluating point had the maximum value of  $x_{tr}$ , which became the initial point for the next round of evaluations. The logic schematic of the optimization subroutine is shown in Fig. 11.5.

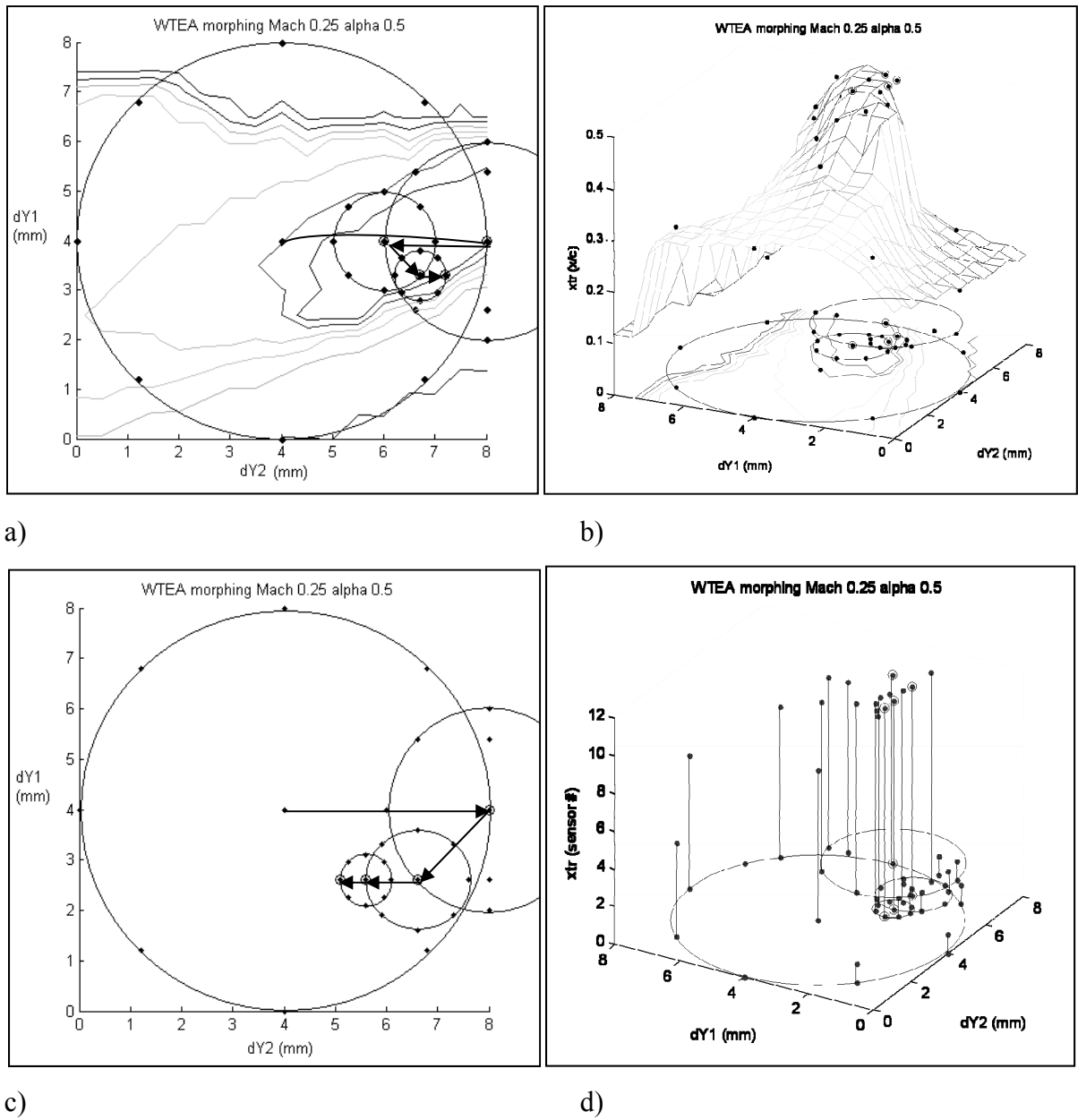
Figures 11.6.a, 11.6.b and 11.7 show the result of WTEA airfoil optimization after four evaluation rounds, first evaluation with a radius of 4 mm, second evaluation with a radius of 2 mm, third evaluation with a radius of 1 mm and fourth and last evaluation with a radius of 0.5 mm. As seen in Figure 11.6.b the last round of evaluation is almost unnecessary because the maximum  $x_{tr}$  was found inside a plateau of maximums with very small differences between them. Before doing the optimization a mapping of the search domain was performed, that is, for each combination of  $dY1$  and  $dY2$  in the interval (0 mm, 8 mm) with a step of 1 mm it was found the  $x_{tr}$  and was built the surface  $x_{tr} = f(dY1, dY2)$  for the purpose of visualizing the form of the hill and to validate the algorithm in the simulation. Figure 11.6.c and 11.6.d show the same optimization routine that ran during the wind tunnel tests in the same airflow conditions as the ones simulated except that there is no map of the searched function. The result was slightly different because the airfoil shape of the real flexible skin under wind-tunnel conditions was different than the airfoil shapes defined by use of  $B$ -splines. Still, the result was similar, in terms of actuator strokes  $dY1$  and  $dY2$  as well as the position of transition. Similarly there can be observed in Figure 11.6.d a plateau of evaluation points that had the transition occurrence on the 11<sup>th</sup> sensor.

Figure 11.7 shows the result of the airfoil shape optimization,  $C_p$  distribution, and  $x_{tr}$  transition point position on the upper surface of the airfoil obtained through simulation using XFOil and a  $B$ -splines model for the flexible skin. The values obtained for wind flow conditions of Mach = 0.25 and  $\alpha = 0.5$  degrees are  $dY1 = 3.3$  mm and  $dY2 = 7.2$  mm. Also in Figure 11.7 the  $N$  factor distribution is shown, which was the parameter used by XFOil to calculate the transition point position. When  $N$  factor reaches the  $N_{cr}$  critical value the

transition was triggered. This parameter was used in wind tunnel to validate the transition position found through the RMS measuring of the Kulite pressure sensors.

Figure 11.8 shows the optimized airfoil shape,  $C_p$  distribution, and  $x_{tr}$  transition point position on the upper surface of the airfoil in wind-tunnel test (star plots) compared to the optimal airfoil plots (upper circle continuous line) and reference airfoil plots (lower circle continuous line) obtained through simulation. Also in the lower subplot of Figure 11.8 the  $N$  factor used by XFOIL to detect the transition position was compared to the RMS of the Kulite sensors. Both the  $N$  factor and RMS were normalized and the purpose of the plots was to have a visual indicator of the transition position. The software considered the transition position in the coordinates of the sensor with the highest noise (RMS) as confirmed by previous studies [12]. The values obtained in the wind tunnel for wind flow conditions of Mach = 0.25 and  $\alpha = 0.5$  are  $x_{tr}/c = 0.635$  ( $x_{tr} = 317.5$  mm) for the actuator displacement values  $dY1 = 2.6$  mm and  $dY2 = 5.1$  mm.

Figure 11.9 shows the time history of the optimization process in the wind tunnel. Because of the long response of the SMA actuators ( the time of cooling from maximum displacement to zero was approx 2 min ), the entire process of optimum search converged to the optimum values in approximately 20 min. Also, it can be observed that the requested displacements of the actuators at the maximum displacement of 8 mm were not realized, due to the fatigue of the SMAs accumulated in previous testes. The maximum deflection was in fact 7 mm for the first actuator and 6.5 mm for second actuator.



**Figure 11.6** Optimization in simulation using XFOIL code (parts a and b) vs optimization in real time during wind tunnel tests ( parts c and d) for the same airflow conditions  $M = 0.25$  and  $\alpha = 0.5$  deg.

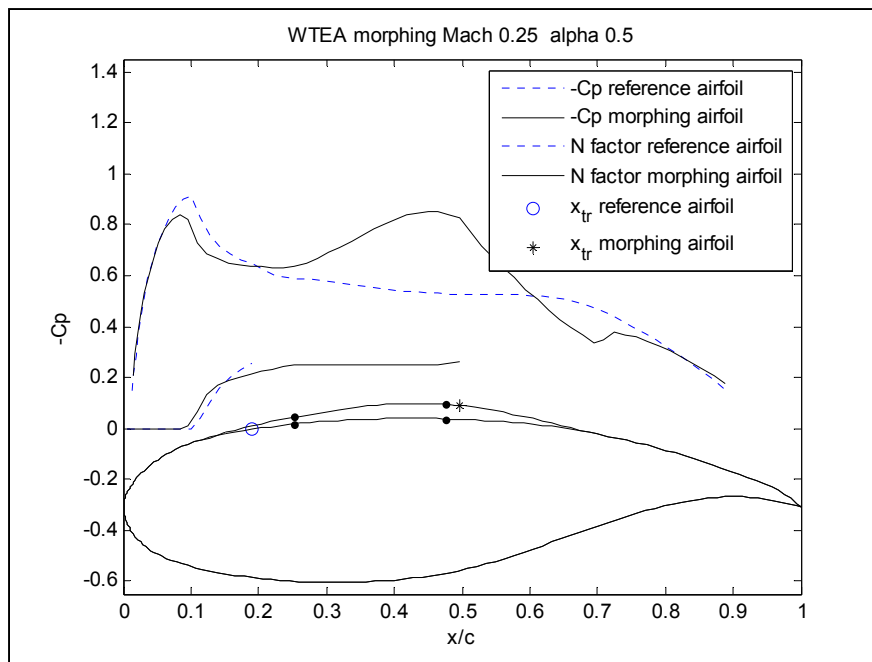


Figure 11.7 Optimization simulation results for  $M = 0.25$  and  $\alpha = 0.5$  deg.

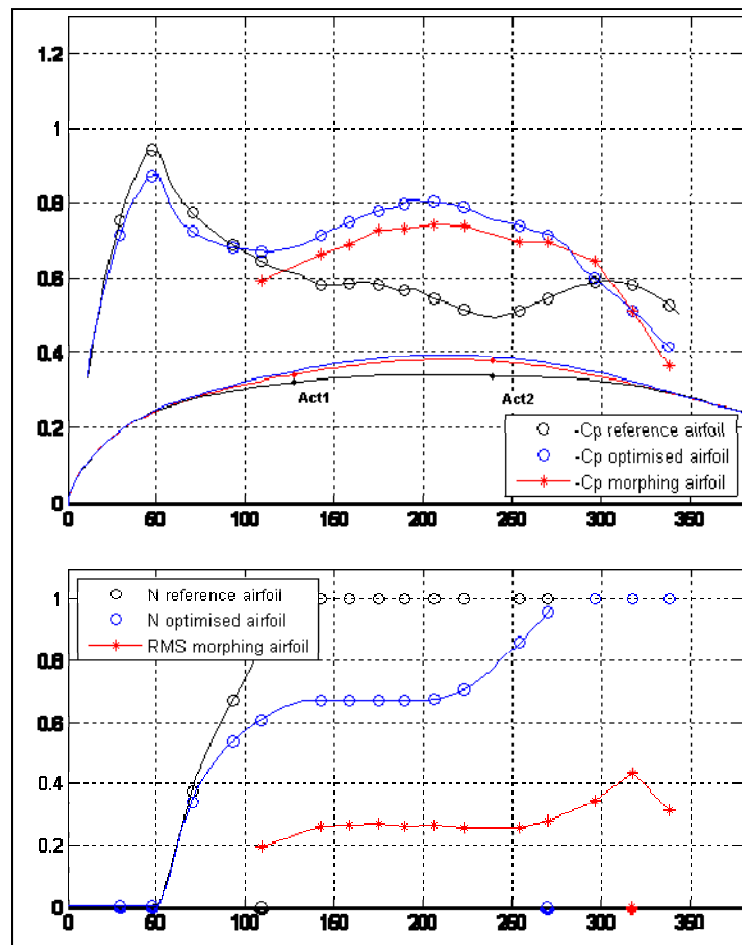
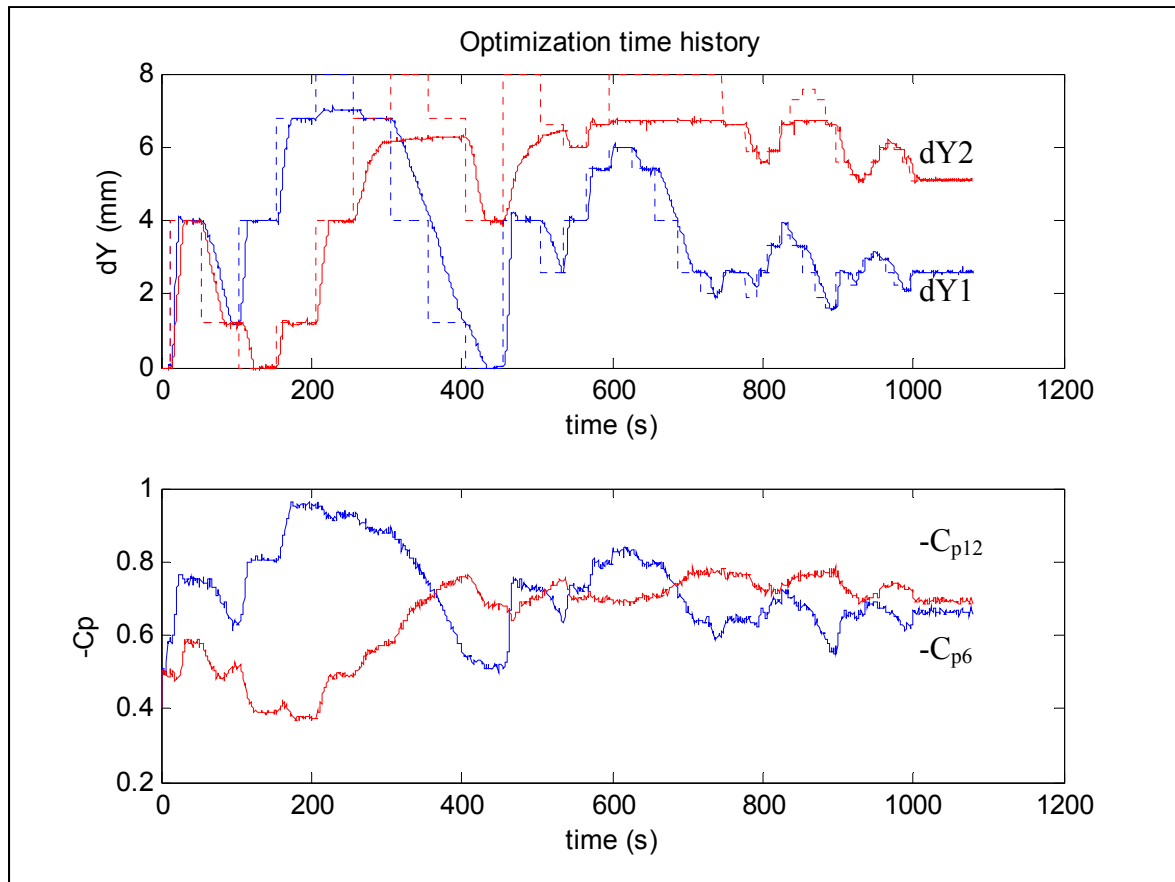


Figure 11.8 Optimization result during wind-tunnel test for  $M = 0.25$  and  $\alpha = 0.5$  deg.



**Figure 11.9 Optimization time history during wind-tunnel test for  $M = 0.25$  and  $\alpha = 0.5$  deg.**

Figure 11.10 shows typical infrared results obtained at  $M = 0.25$ ,  $\alpha = 0.5$  deg for various configurations. Only the composite portion of the wing at  $x/c \leq 0.7$  was shown. The white spots on the wing are the electronically heated Kulite pressure transducers. The two lines of SMA actuators, colder than the model surface, are also visible at quarter chord and near midchord. The locations of the transition in the images have been highlighted using a white dashed line; it corresponds to the location of a large surface temperature gradient, the laminar region being about  $2\text{--}3^\circ\text{C}$  hotter than the turbulent region. The reference airfoil configuration (Figure 11.10.a) showed a transition location at  $x/c = 26\%$ . The optimization (Figure 11.10.b) allowed a laminar boundary-layer run to  $x/c = 58\%$ , which represents a significant improvement over the reference case (Figure 11.10.a). Some turbulent wedges caused by leading-edge contamination, due to dust particles in the flow, were visible in Figure 11.10.a.

In addition to providing an on line verification of the Kulite dynamic pressure signals, the infrared measurement was particularly useful to detect those early artificial turbulent regions. When the level of contamination was estimated unacceptable or likely to affect the drag or the Kulite measurements, the test was interrupted and the model was carefully cleaned.

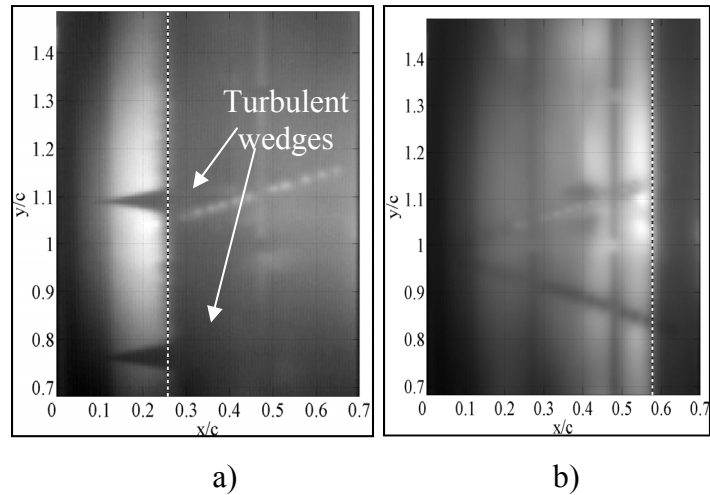


**Figure 11.10 Infrared results obtained at  $M = 0.25$  and  $\alpha = 0.5$  deg in a) reference, and b) after optimization.**

#### 11.4 Conclusion

The results of the tests performed in a wind tunnel using a morphing wing were shown. The optimization method did not use any CFD code but use the same optimization algorithm in real time. This optimization converged in approximately 20 minutes due to the slow response of the SMA actuators especially in the cooling phase of the cycle. It was observed that the airfoil realized by this method slightly differs from the optimization using CFD codes. This result was due to the fact that the cost function of the optimization (transition position) has discrete values (the sensor's positions) and the maximum of the function was a plateau of different  $dY1$  and  $dY2$  values. The optimizer stopped at a certain value in function of the number and magnitudes of the searching steps. It was observed that the last searching step (searching of the maximum in eight points situated on a circle with ray of 0.5 mm, see Figure 11.6) was not necessary due to the cost function plateau of maximums.

## References

- [1] Zingg, D. W., Diosady, L., and Billing, L., 2006, *Adaptive Airfoils for Drag Reduction at Transonic Speeds*, AIAA paper 2006-3656.
- [2] Popov, A-V., Labib, M., Fays, J., Botez, R.M., 2008, *Closed loop control simulations on a morphing laminar airfoil using shape memory alloys actuators*, AIAA Journal of Aircraft, Vol. 45(5), pp. 1794-1803.
- [3] Coutu, D., Brailovski, V., Terriault, P., 2009, *Promising benefits of an active-extrados morphing laminar wing*, AIAA Journal of Aircraft, Vol. 46(2), pp. 730-731.
- [4] Georges, T., Brailovski, V., Morellon, E., Coutu, D., Terriault, P., 2009, *Design of shape memory alloy actuators for morphing laminar wing with flexible extrados*, ASME Journal of Mechanical Design, Vol. 131(9), pp. 091006-1 – 091006-9.
- [5] Sainmont, C., Paraschivoiu, I., Coutu, D., 2009, *Multidisciplinary Approach for the Optimization of a Laminar Airfoil Equipped with a Morphing Upper Surface*, NATO AVT-168 Symposium on "Morphing Vehicule", Evora, Portugal.
- [6] Khalid, M., 1993, *Navier Stokes Investigation of Blunt Trailing Edge Airfoils using O-Grids*, AIAA Journal of Aircraft, Vol.30, No.3, pp.797-800
- [7] Khalid, M., and Jones, D.J., 1993, *A CFD Investigation of the Blunt Trailing Edge Airfoils in Transonic Flow*, Proceedings of the Inaugural Conference of the CFD Society of Canada, Montreal, June 14-15.
- [8] Popov, A-V., Botez, R. M., and Grigorie, L., 2009, *Morphing Wing Validation during Bench Tests*, 2009 Canadian Aeronautics and Space Institute Annual General Meeting, Aircraft Design & Development Symposium, Kanata, Ontario.
- [9] Hill climbing, From Wikipedia, the free encyclopedia [online], [http://en.wikipedia.org/wiki/Hill\\_climbing](http://en.wikipedia.org/wiki/Hill_climbing) [retrieved 26 November 2009]
- [10] Simulated annealing, From Wikipedia, the free encyclopedia [online], [http://en.wikipedia.org/wiki/Simulated\\_annealing](http://en.wikipedia.org/wiki/Simulated_annealing) [retrieved 26 November 2009]
- [11] Mébarki, Y., Mamou, M., and Genest, M., 2009, *Infrared Measurements of Transition Location on the CRIAQ project Morphing Wing Model*, NRC LTR- AL-2009-0075.
- [12] Nitsche, W., Mirow, P., and Dorfler, T., 1990, *Investigations on Flow Instabilities on Airfoils by Means of Piezofilm Arrays*, Laminar-Turbulent Transition Proceedings of the IUTAM Symposium, Ecole nationale Supérieure de l'Aéronautique et de l'Espace, Toulouse, France, Sept. 11-15, 1989, Berlin and New York, Springer-Verlag.

- [13] Mangalam, S. M., 2004, *Real-Time Extraction of Hydrodynamic Flow Characteristics Using Surface Signature*, IEEE Journal of Oceanic Engineering, Vol. 29, No. 3, pp. 622-630.
- [14] Mack, L. M., 1977, *Transition and Laminar Instability*, Jet Propulsion Laboratory Publication 77-15, Pasadena, CA,
- [15] Popov, A., V., Grigorie, L., T., Botez, R.M., 2009, *Control of a Morphing Wing in Bench Test*, 13<sup>th</sup> Canadian Aeronautical and Aerospace Institute CASI Aeronautics Conference, Kanata, Ontario, 5-7 May.

## CONCLUSION

In this thesis, the new methodology of a morphing wing controller was presented. The articles presented in chronological order the evolution of the controller from its theoretical description, numerical simulation, to the software realisation and implementation with hardware in the loop in wind tunnel conditions. The articles showed that the morphing wing model controlled in wind tunnel tests using several control strategies was a great success.

My overall contribution to this project was the control architecture and software design that allowed to the wing model to behave automatically in wind tunnel. The implementation of the software into the loop using the hardware was performed by me in collaboration with LARCASE and LAMSI colleagues, and the running of the software in wind tunnel was performed by me. The wind tunnel running conditions were supervised by Dr. Mamou from IAR-NRC. The collaboration of all those teams surpassing all the technological challenges was a success in itself leading to the finalization of such a complex and multidisciplinary project. This is a first realisation in the morphing aircraft research and design industry in Canada, and several research axes may be improved.

Firstly, the optical sensors technology could be improved in the future in order to be able to detect small pressure variations about 60 dB smaller than the average measured pressure values, as shown in the wind tunnel. Moreover, the sampling rate of the signal should be 10 kHz in order to allow the detection of the Tollmien-Schlichting waves. The actual optic to electric technology does not allow having at the same time measurements with high precision and high frequency sampling.

Second recommendation would regard the improvement of the SMA actuators control. In this project, the SMA actuators were supplied with uninterrupted power for the entire time of the wind tunnel tests. As this technology develops in the future, it would be recommended to design a controller and a mechanical blocking device that would allow the actuators to maintain the desired position without continuous electrical power consumption.

A third recommendation would be to improve the controller by integrating new control technologies such as an adaptive neural network and fuzzy logic, which are widely used today. The controller could be improved by a full automation of the closed loop control process, thus eliminating any human intervention, which could be done by introducing sensors for airflow speed, flow direction and pressure altitude in the control loop.

